Experimental analysis of two-point Navier-Stokes equations in non-homogeneous turbulence and application to Large Eddy Simulation

Paul Beaumard

CENTRALE LILLE

THÈSE

présentée en vue
d'obtenir le grade de

Docteur

en

Mécanique

par

Paul Beaumard

DOCTORAT DÉLIVRÉ PAR CENTRALE LILLE

Titre de la Thèse :

Analyse expérimentale des équations de Navier-Stokes à deux points dans la turbulence non homogène et application à la simulation numérique grandes échelles
Experimental analysis of two-point Navier-Stokes equations in non-homogeneous turbulence and application to Large Eddy Simulation

---

Soutenue le 5 décembre 2023 devant le jury d'examen :

Président	**Eric LAMBALLAIS**	Professeur, Université de Poitiers, Pprime
Rapporteur	**Mickaël BOURGOIN**	Directeur de Recherche, CNRS, ENS de Lyon
Rapporteur	**George PAPADAKIS**	Professeur, Imperial College London
Examinatrice	**Léonie CANET**	Professeure, Université Grenoble Alpes, LPMMC
Examinatrice	**Luminita DANAILA**	Professeure, Université de Rouen, M2C
Directeur	**Christos VASSILICOS**	Directeur de Recherche, CNRS, LMFL
Co-Directeur	**Jean-Marc FOUCAUT**	Professeur, Centrale Lille Institut, LMFL
Co-Encadrant	**Christophe CUVIER**	Maître de conférences, Centrale Lille Institut, LMFL

Thèse préparée au CNRS dans le Laboratoire de Mécanique des Fluides de Lille - Kampé de Fériet

École Doctorale ENGYS 632

Laboratoire de Mécanique des Fluides de Lille Kampé de Fériet

cnrs

centralelille

Région Hauts-de-France

I-SITE UNIVERSITÉ LILLE NORD-EUROPE

Page intentionally left blank

À mon épouse, Sixtine

Page intentionally left blank

Abstract

Time-resolved 2D2C PIV (Particle Image Velocimetry) measurements are carried out in a water tank agitated by four rotating blades. Different blade geometries with rectangular and fractal-like shapes are tested. In some runs, vertical bars (baffles) on the walls are used to break the rotation of the flow. This experimental set-up is used to generate and measure different non-homogeneous turbulent flows with different turbulent properties. The turbulent energy cascade is analyzed in a framework based on two-point Navier-Stokes equations which allows transfer rates of energy across scales and through space to be analysed in non-homogeneous flows without assumptions/approximations. For any length r, the Kármán-Howarth-Monin-Hill (KHMH) two-point equation is used to describe scales smaller than r and the Germano two-point equation is used for the first time to describe experimentally scales larger than r.

In non-homogenous flows where baffles break overall rotation, the Chen and Vassilicos 2022 theory is improved and used to explain theoretically the Kolmogorov-like results measured in the presence of significant non-homogeneity down to scales smaller than the Taylor length. This theory predicts that an intermediate range of length-scales exists where the interscale turbulence transfer rate, the two-point interspace turbulence transport rate and the two-point pressure gradient velocity correlation term in the two-point KHMH equation are all proportional to the turbulence dissipation rate and independent of length-scale. The PIV measurements in these flows support these predictions. The PIV measurements also suggest that the rate with which scales larger than r lose energy to the scales smaller than r in the two-point Germano equation behaves in a similar way. This result suggests a strong physical connection between the KHMH equation (scales smaller than r) and the Germano equation (scales larger than r) in our flows.

In non-homogeneous flows without baffles where the rotation is significant, structure function results are qualitatively different. Also, the two-point statistics from the KHMH and Germano equations are not proportional to the turbulence dissipation rate and not independent of length-scale. The assumptions of the Chen and Vassilicos 2022 theory are used in this case as a reference for identifying which assumptions fail and how under the action of rotation.

Finally, Germano's exact subfilter stress equation, which is part of the Germano two-point

framework used in this thesis to describe the physics at scales larger than a certain r, is used as the basis of a new Large Eddy Simulation (LES) model. As this model is a simplification/approximation and modeling of two different parts of an exact subfilter stress equations, it lends itself to controlled future improvements by refining the mathematical approximations and by implementing future physical findings into a preexisting mathematical framework. This new model is tested in a simulated Taylor-Green flow both *a priori* and *a posteriori*. It is found to capture well the large local energy transfer between filtered scales and residual scales including large backscatter and large forward transfer events.

Page intentionally left blank

Acknowledgments

First of all, I am very grateful to Christos for his guidance and support during these years and for sharing his deep knowledge about turbulence. I learned a lot from his commitment for accuracy and research of physical truth through his advises and comments during these years. I will keep this inspiration with me during my scientific journey as well as his motivation to always aim for the highest standards.

Then, I want to thank the experimental team: Jean-Marc, Christophe and Pierre for introducing me into the practical world of experiments. They helped me not to get lost by confronting the real world where a leak of water must be treated with equal care as the diffraction spot of the PIV particles illuminated by the laser beam. I learned a lot from them about experiments in general and more precisely about PIV methods. Thank you also for the nice discussions we had during these years. A special thanks to Christophe for his very helpful training for teaching.

I want to thank also Jean-Philippe Laval for his availability and patience to help for any subject all along my PHD. He introduced me to the numerical world and provided me very useful numerical datasets. Thank you for the help and the significant contribution to the Large Eddy Simulation part of the project.

I want to thank all the members of the laboratory and particularly Sarp for his kind friendship and Felipe for his really helpful support during the PHD and during conferences abroad.

Finally, I want to thank Sixtine who encouraged me to do this PHD and supported me at every moment. She commuted during two years from Lille to Paris for that with early trains and late returns so that she truly deserves credit for the existence of this PHD thesis.

The CNRS Research Federation on Ground Transports and Mobility, in articulation with the Elsat2020 project supported by the European Community, the French Ministry of Higher Education and Research, the Hauts de France Regional Council are acknowledged for the founding of the PIV equipements used in this study. This work was directly supported by JCV's Chair of Excellence CoPreFlo unded by I-SITE-ULNE (grant number R-TALENT-19-001-VASSILICOS), MEL (grant number CONVENTION_219_ESR_06) and Region Hauts de France (grant number 20003862). Centrale Lille Institute is also acknowledged for the funding of the equipments of our mixer experiment.

Page intentionally left blank

Contents

Page intentionally left blank

Chapter 1

Introduction

1.1 Why looking at turbulence ?

Turbulence describes a specific state of the flow when it is moving fast or when it is disturbed by a large or complex geometry. The flow can be the one of any fluid such as air or water. Turbulent flows are easily identified by their unsteadiness and irregularity. Most of flows which surround us in our everyday life are turbulent. If air was not transparent, turbulence would be visible everywhere.

Turbulent flows are also present in many industrial applications: aeronautical (flight mechanics, aircraft design, engines design,...), industries (industrial mixers, turbines,...), geophysics (weather prediction,...). The behavior of these flows is very difficult to understand and to predict because of the complexity of their equations. However, their understanding and prediction is critical for the applications mentioned above.

For example, there is a need for a better understanding of turbulent flow equations in aeronautical industry because of the actual trend to design very complex geometries (such as new rotors or fuselages) while using 'model based design' process. It requires accurate predictions of the flow to model the main aerodynamic effects such as lift, drag, thrust, in all situations.

Industries tackle the aerodynamic modeling problem by using numerical methods called 'Reynolds Averaging Navier Stokes simulation' or more recently 'Large Eddies Simulation', in collaboration with research, which require large computational resources such as high performance computers. Research goes a step further by using 'Direct Numerical Simulation'. This latter numerical method is much more accurate but requires also much larger computational resources and is limited to low-speed turbulence due to the computational cost or is used on very small regions of the flow. Neither of these methods are fully satisfactory because

the numerical methods are complex, require too much computational resources or require a calibration for each application case. Therefore, long and expensive experiments are needed before a new design. The solution chosen often contains large simplifications and inaccuracies.

This is why turbulence and more generally aerodynamic understanding and prediction remains an open problem to be resolved.

One of the main directions to solve this problem is to increase the turbulence equations knowledge and understanding. This should be done in situations close to practical ones: disturbed flows whose properties change in space and where velocity evolves from low to large speed.

Practically, a better understanding of the turbulence equations, called the Navier-Stokes equations, should lead to:

- More efficient flow predictions through the use of physical simplifications to reduce the numerical computations cost
- Better prediction of aerodynamic / hydrodynamic effects through development of new numerical models
- Design of new geometries more aerodynamically / hydrodynamically efficient
- New applications using turbulent flow energy and properties

1.2 Why studying especially non-homogeneity in turbulence?

A scientific consensus exists about a turbulence theory developed by Kolmogorov in 1941. This theory was developed for homogeneous, equilibrium turbulence. It is a theoretical state of the flow which might exist at very high Reynolds number (high speed, large geometry, low viscosity) when turbulence is fully developed. In that case, the flow properties do not change in space and in direction: it is homogeneous and isotropic.

The theory remains to be extended for non-equilibrium/ non-homogeneous turbulence. Indeed, the theoretical framework used to derive Kolmogorov theory is not applicable for most of complex flows. This is for example the case for non-homogeneous turbulence present in mixers, rotors, sails, storms,...

1.3 What was done during this PHD ?

First, turbulence is analyzed with experimental datasets recorded during the PHD project. The flow is stimulated by four blades rotating inside a mixer full of water.

This set-up generates a rotating or non-rotating flow depending on the experimental configuration. The flows generated are non-homogeneous because of the complex geometry of the problem.

This experiment reproduces specific turbulent flow properties which exist in practical applications such as highly developed turbulence or rotating turbulence stimulated by blades. The turbulence properties understanding in this experiment provides insights about the turbulence existing in practical applications while keeping a relative experimental simplicity.

A recent (two-points) theoretical framework is applied on the experimental dataset and some physical understanding is captured. Moreover, an extension of this framework is analyzed with experiments and its physical relevance is confirmed. From a simplified point of view, this mathematical extension describes mainly the large 'scales' of turbulent flow.

In the last chapter of this PHD, the theoretical results obtained in the previous chapters are used in a more practical way. Indeed, the large scale extension of the two points framework is used to build a simulation model for Large Eddy Simulation. The idea of this part is to bring some fundamental research knowledge to applicative research through modelling improvements. A new simulation model with mathematical and physical justifications is developed from exact equations through simplifications. Doing that way, the previous and future findings from fundamental research about the two-points framework can be applied to Large Eddy Simulation through the connection described in this study.

Chapter 2

State of the art

2.1 General turbulence results

2.1.1 Navier-Stokes equations

This equation is the result of successive discoveries of researchers from different nationalities. Euler introduced first a fluid momentum conservation equation in the middle of 18th century. Navier added the viscous effects into this momentum conservation in 1822 so that all the physical effects are captured. Finally, Stokes carried out extensive research on this equation and wrote it in its final form in 1845:

$$\frac{\partial \boldsymbol{u}}{\partial t} + (\boldsymbol{u}.\boldsymbol{\nabla})\boldsymbol{u} + \frac{1}{\rho}\boldsymbol{\nabla} p = \nu \nabla^2 \boldsymbol{u} \tag{2.1}$$

for incompressible flows where $\nabla.\boldsymbol{u} = 0$ and ∇ is the gradient operator.

This equation is used in this thesis as a tool to understand turbulent flow behavior. It is assumed to describe perfectly the flow in real conditions as it has never been disapproved in extensive previous research over two centuries.

2.1.2 Kolmogorov theory

Kolmogorov theory often called 'K41' because of the three famous papers (Kolmogorov 1941a, Kolmogorov 1941b and Kolmogorov 1941c) is the most important turbulence theory. It is derived for 'very large Reynolds number'. The main points of the first paper are reminded below with simplifications.

The spatial velocity increment $\delta u_i = u_i(X) - u_i(X^0)$ is introduced where X is the spatial coordinate vector and X^0 is fixed. The second moment $B_{i,j}\left(Y^1, Y^2\right) = \overline{\delta u_i(Y^1)\delta u_j(Y^2)}$ is

also defined where $Y_i^k = X_i^k - X_i^0 - u_i(X^0, t)(t - t_0)$ where the dependence on the random variable u_i implies that Y_i is also a random variable. Finally, $r = |Y^2 - Y^1|$.

Assumptions used

Local homogeneity

The distribution law of δu_i is independent of X^0, t^0 and $u_i(X^0)$.

Local isotropy

The distribution laws of δu_i are 'invariant with respect to rotations and reflections of the original system of coordinate axes'.

This later assumption is considered by Kolmogorov as a 'rather far approximation of reality even for small domains [...] and very large Reynolds numbers' except for particular cases such as turbulence generated behind a grid.

First hypothesis of similarity

'For the locally isotropic turbulence the distributions [of δu_i] are uniquely determined by the quantities ν and $\bar{\epsilon}$', where $\bar{\epsilon}$ is the mean turbulence dissipation rate ('dispersion of energy').

The Kolmogorov length scale is deduced: $\eta = \frac{\nu^{3/4}}{\bar{\epsilon}^{1/4}}$.

Second hypothesis of similarity

'If the moduli of the vector Y^k and of their differences $Y^k - Y^{k'}$ (where $k \neq k'$) are large in comparison with η, then, the distribution laws [of δu_i] are uniquely determined by the quantity $\bar{\epsilon}$ and do not depend on ν'.

Main results

The second moment can be expressed as:

$$B_{i,j}(Y, Y) = (B_{dd}(r) - B_{nn}(r))\, cos(\theta_i) cos(\theta_j) + \delta_{i,j} B_{nn}(r) \tag{2.2}$$

where $Y_i = r cos(\theta_i)$, $B_{dd}(r) = \overline{(\delta u_1(r, 0, 0))^2}$ and $B_{nn}(r) = \overline{(\delta u_2(r, 0, 0))^2}$.

For r large compared to η the following very important results are obtained where C is a dimensionless constant:

$$B_{dd}(r) \sim C \bar{\epsilon}^{2/3} r^{2/3} \tag{2.3}$$

$$B_{nn}(r) \sim \frac{4}{3} B_{dd}(r) \tag{2.4}$$

Comments about this theory

These results are commonly related to the energy cascade described by Richardson 1922 in his well known poem 'Big whirls have little whirls that feed on their velocity, and little whirls have lesser whirls and so on to viscosity'.

The Kolmogorov theory range of validity is called the inertial range. This range contains scales small enough ($r << L$, where L is the integral scale which describes the largest scales of the flow) so that local homogeneity and isotropy assumptions might be valid but also large enough so that it is not affected by viscosity as assumed by Kolmogorov. The eddies present in the inertial range are expected to depend only on their local interactions and to cascade toward smaller scales at the dissipation rate (Kolmogorov 1941a). This theory is an important achievement as it provides a universal law to describe energy distribution among scales of turbulent flows in spite of their irregular behavior.

In most researches, the verification of this theory is done with energy spectrum analysis. Indeed, the equivalent results of equations 2.3 and 2.4 in Fourier space is the Kolmogorov-Obukhov $k^{-5/3}$ evolution of energy spectrum in the inertial range where k is the Fourier wavenumber.

Over the last 80 years, Kolmogorov prediction for the wavenumber dependence $k^{-5/3}$ was verified with experiments in a large variety of flows. These results were already questioned in Kraichnan 1974: 'Kolmogorov's 1941 theory has achieved an embarrassment of success. The '-5/3' -spectrum has been found not only where it reasonably could be expected but also at Reynolds numbers too small for a distinct inertial range to exist and in boundary layers and shear flows where there are substantial departures from isotropy, and such strong effects from the mean shearing motion that the stepwise cascade appealed to by Kolmogorov is dubious'.

Nearly 50 years after this quote, there is still no consensus to explain this contradiction. With Kolmogorov theory, basic research attention has been focusing a long time on homogeneous turbulence as reported in Alves Portela 2017, Gomes-Fernandes, Ganapathisubramani, and Vassilicos 2015 and Alves Portela, Papadakis, and Vassilicos 2017 and might have been diverted from an important feature of real flows: their non-homogeneity.

Turbulence scales

A common property of turbulent flows is that they contain a large range of scales. The smallest scales are often less than 1 millimeter while the largest ones can be of the order of the kilometer for atmospheric flows. Therefore, reference scales are defined and are important to describe turbulence. The integral scale is characteristic of the largest motions of the flow: its interpretation is quite straightforward. Its estimation is described directly in the chapters concerned.

The Kolmogorov scale is defined in Kolmogorov 1941c as 'the scale of the finest pulsations, whose energy is directly dispersed'. It can be interpreted as the 'smoothness scale'. It

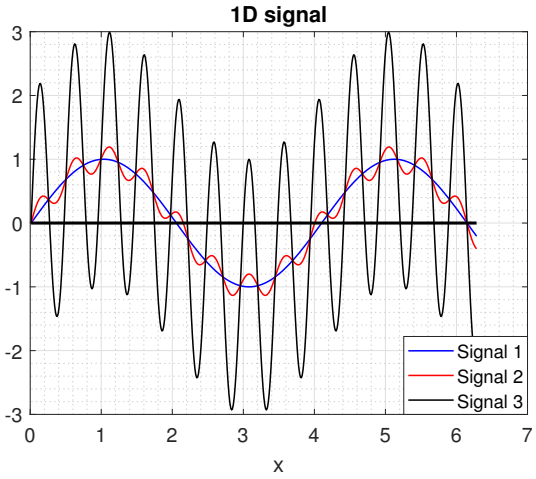

Figure 2.1: Taylor scale and zero-crossing in a theoretical signal

means the signal is smooth for scales smaller than η so that Taylor series can be applied to approximate derivatives.

Another important scale is the Taylor 1935 scale: λ. This scale is first defined in relation with correlation function and is computed as: $\lambda = \sqrt{\frac{15\nu\overline{|\boldsymbol{u}'|^2}}{\bar{\epsilon}}}$. However, Liepmann 1949, Liepmann and Robinson 1952 and Mazellier and Vassilicos 2008 derived $\lambda = \frac{1}{C\pi}\widetilde{l}$ where $\widetilde{l}$ is the mean zero crossing distance of the signal and C a constant. This latter definition and the work in Goto and Vassilicos 2009 which relates λ with the stagnation points helps understanding physically this scale.

Simple periodic signals in one dimension are plotted in figure 2.1. This signal is not representative of a turbulent signal but it is a way to have a first intuition of the Taylor scale. The first signal contains only one harmonic so the mean zero crossing distance is just the signal half spatial length. The second signal contains two harmonics but the high frequency harmonic has a small magnitude so it does not affect significantly the mean zero-crossing: $\lambda_2 \approx \lambda_1$. The third signal is dominated by the second harmonic so that the mean zero crossing is nearly unaffected by the first harmonic: $\lambda_3 << \lambda_1$.

In this theoretical signal (not turbulence), we understand that Taylor scale is mainly defined by the dominant structures of the signal. These structures may be called the 'coherent structures' as they stand out from the 'background randomness' to impact significantly the mean zero crossing distance. In turbulence, a large number of scales can also co-exist without a clear domination of one with respect to the others. In that case, the mean zero crossing / Taylor scale represents the scales average weighted by their energy representation. The main difference compared to the previous simplified example is the impact of viscosity on the results which affects the smallest scales and therefore the Taylor scale computation.

2.1.3 Two-point Navier-Stokes equations

The turbulence framework introduced previously involves dimensional and scale analysis. On the other hand, the two-point framework, described in this section, allows turbulence analysis directly from Navier-Stokes equations in real space. This very powerful tool requires expensive computations to evaluate the different terms from datasets. However, it allows to quantify mathematically complex physical phenomena such as the energy cascade. This framework does not require periodicity assumption as is the case in Fourier space. Furthermore, the results are local in space which is not the case for spectral results. Therefore, this framework is very useful for turbulence analysis in non-homogeneous flows.

Presentation of the equation

This framework requires two points in physical space as for Kolmogorov theory: $\boldsymbol{\zeta}^- = \boldsymbol{X} - \boldsymbol{r}$ and $\boldsymbol{\zeta}^+ = \boldsymbol{X} + \boldsymbol{r}$ (figure 2.2). $\boldsymbol{X}$ is the centroid and $2\boldsymbol{r}$ is the two-point separation vector.

The velocity half difference $\boldsymbol{\delta u}(\boldsymbol{X}, \boldsymbol{r}, t) = \frac{\boldsymbol{u}(\boldsymbol{\zeta}^+) - \boldsymbol{u}(\boldsymbol{\zeta}^-)}{2}$ and velocity half sum $\boldsymbol{u_X}(\boldsymbol{X}, \boldsymbol{r}, t) = \frac{\boldsymbol{u}(\boldsymbol{\zeta}^+) + \boldsymbol{u}(\boldsymbol{\zeta}^-)}{2}$ are defined.

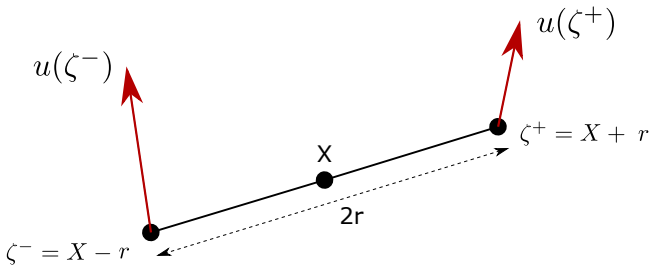

Figure 2.2: Schematic of fluid velocities at points $\boldsymbol{\zeta}^- = \boldsymbol{X} - \boldsymbol{r}$ and $\boldsymbol{\zeta}^+ = \boldsymbol{X} + \boldsymbol{r}$.

Following Hill 2001 and Hill 2002b, a two-point equation for $\boldsymbol{\delta u}$ is derived from Navier-Stokes equation:

$$\frac{\partial \boldsymbol{\delta u}}{\partial t} + (\boldsymbol{u_X}.\boldsymbol{\nabla_X})\,\boldsymbol{\delta u} + (\boldsymbol{\delta u}.\boldsymbol{\nabla_r})\,\boldsymbol{\delta u} = -\frac{1}{\rho}\boldsymbol{\nabla_X}\delta p + \frac{\nu}{2}\boldsymbol{\nabla_X}^2\boldsymbol{\delta u} + \frac{\nu}{2}\boldsymbol{\nabla_r}^2\boldsymbol{\delta u} \tag{2.5}$$

where incompressibility gives $\boldsymbol{\nabla_X}.\boldsymbol{\delta u} = \boldsymbol{\nabla_r}.\boldsymbol{\delta u} = 0$. The mathematical relations: $\frac{\partial}{\partial X_k} = \frac{\partial}{\partial \zeta_k^+} + \frac{\partial}{\partial \zeta_k^-}$, $\frac{\partial}{\partial r_k} = \frac{\partial}{\partial \zeta_k^+} - \frac{\partial}{\partial \zeta_k^-}$ and $\frac{\partial^2}{\partial \zeta_k^{+2}} + \frac{\partial^2}{\partial \zeta_k^{-2}} = \frac{1}{2}\frac{\partial^2}{\partial X_k^2} + \frac{1}{2}\frac{\partial^2}{\partial r_k^2}$ are used. $\nabla_{\mathbf{X}}$ and $\boldsymbol{\nabla_X}^2$ are the gradient and Laplacian in $\mathbf{X}$ space; $\nabla_{\mathbf{r}}$ and $\boldsymbol{\nabla_r}^2$ are the gradient and Laplacian in $\mathbf{r}$ space; ν is the kinematic viscosity; $\delta p = \frac{p(\boldsymbol{\zeta}^+) - p(\boldsymbol{\zeta}^-)}{2}$ and $P_X = \frac{p(\boldsymbol{\zeta}^+) + p(\boldsymbol{\zeta}^-)}{2}$.

Similarly and following Germano 2007b, a two-point equation for $\boldsymbol{u_X}$ is derived for the velocity sum:

$$\frac{\partial \boldsymbol{u_X}}{\partial t} + (\boldsymbol{u_X}.\boldsymbol{\nabla_X})\,\boldsymbol{u_X} + (\boldsymbol{\delta u}.\boldsymbol{\nabla_r})\,\boldsymbol{u_X} = -\frac{1}{\rho}\boldsymbol{\nabla_X}P_X + \frac{\nu}{2}\boldsymbol{\nabla_X}^2\boldsymbol{u_X} + \frac{\nu}{2}\boldsymbol{\nabla_r}^2\boldsymbol{u_X} \tag{2.6}$$

were incompressibility gives $\boldsymbol{\nabla_X}.\boldsymbol{u_X} = \boldsymbol{\nabla_r}.\boldsymbol{u_X} = 0$.

Two-point energy equations are now derived and are used in this thesis to quantify the different physical effects. Equation 2.5 is multiplied by $2\boldsymbol{\delta u}$ to obtain the small scale Kármán-Howarth-Monin-Hill equation as derived in Hill 2001 and Hill 2002a (see also the procedure in Danaila et al. 2001):

$$\frac{\partial|\boldsymbol{\delta u}|^2}{\partial t} + \boldsymbol{\nabla_X}.(\boldsymbol{u_X}|\boldsymbol{\delta u}|^2) + \boldsymbol{\nabla_r}.(\boldsymbol{\delta u}|\boldsymbol{\delta u}|^2) = -\frac{2}{\rho}\boldsymbol{\nabla_X}.(\boldsymbol{\delta u}\delta p) + \frac{\nu}{2}{\boldsymbol{\nabla_X}}^2|\boldsymbol{\delta u}|^2 + \frac{\nu}{2}{\boldsymbol{\nabla_r}}^2|\boldsymbol{\delta u}|^2 - \epsilon \tag{2.7}$$

Where $\epsilon = \frac{1}{2}\epsilon^+ + \frac{1}{2}\epsilon^-$; $\epsilon^+ = \nu\frac{\partial u_i^+}{\partial\zeta_k^+}\frac{\partial u_i^+}{\partial\zeta_k^+}$ and $\epsilon^- = \nu\frac{\partial u_i^-}{\partial\zeta_k^-}\frac{\partial u_i^-}{\partial\zeta_k^-}$.

Equation 2.6 is multiplied by $2\boldsymbol{u_X}$ to obtain the Germano 2007b equation:

$$\frac{\partial|\boldsymbol{u_X}|^2}{\partial t}+\boldsymbol{\nabla_X}.(\boldsymbol{u_X}|\boldsymbol{u_X}|^2)+\boldsymbol{\nabla_r}.(\boldsymbol{\delta u}|\boldsymbol{u_X}|^2) = -\frac{2}{\rho}\boldsymbol{\nabla_X}.(\boldsymbol{u_X}P_X)+\frac{\nu}{2}{\boldsymbol{\nabla_X}}^2|\boldsymbol{u_X}|^2+\frac{\nu}{2}{\boldsymbol{\nabla_r}}^2|\boldsymbol{u_X}|^2-\epsilon \tag{2.8}$$

This latter equation is related by Germano to the work of Hill and is described as a large scale equation. It was derived to study Large Eddy Simulation. In the present work, the physical analysis of this equation is developed.

Finally, the kinematic equation:

$$\boldsymbol{\nabla_r}.(\boldsymbol{\delta u}|\boldsymbol{u_X}|^2) + \boldsymbol{\nabla_r}.(\boldsymbol{\delta u}|\boldsymbol{\delta u}|^2) = 2\boldsymbol{\nabla_X}.(\boldsymbol{\delta u}(\boldsymbol{\delta u}.\boldsymbol{u_X})) \tag{2.9}$$

derived in Germano 2007b relates the small scale and the large scale equations.

Interpretation of the equations

A Reynolds decomposition can be applied to these equations and is used later in this thesis. However, the equations are presented here without this decomposition to match their initial derivation and to simplify their understanding. Interpretation refinements associated to the decomposition are done directly in the chapters concerned.

Equation 2.7 (resp. 2.8) is an energy equation for $|\boldsymbol{\delta u}|^2$ (resp. $|\boldsymbol{u_X}|^2$) written at the location $\boldsymbol{X}$ and for the separation vector $\boldsymbol{r}$. The different terms are interpreted separately.

$\boldsymbol{\nabla_X}.\left(\boldsymbol{u_X}|\boldsymbol{\delta u}|^2\right)$: it can also be written as $\left(\boldsymbol{u_X}.\boldsymbol{\nabla_X}\right)|\boldsymbol{\delta u}|^2$. It corresponds to the transport in space of the energy $|\boldsymbol{\delta u}|^2$.

This term is written as a divergence in $\boldsymbol{X}$ space. Therefore, if the equation is integrated over a local domain (V_X) in $\boldsymbol{X}$ space, it corresponds to a flux on the sides (S_X) of the domain which is consistent with the spatial transport interpretation:

$$\int_{V_X}\boldsymbol{\nabla_X}.\left(\boldsymbol{u_X}|\boldsymbol{\delta u}|^2\right)d^3X = \oint_{S_X}\left(\boldsymbol{u_X}|\boldsymbol{\delta u}|^2\right).\boldsymbol{n}d^2X \tag{2.10}$$

Similarly, $\boldsymbol{\nabla_X}.\left(\boldsymbol{u_X}|\boldsymbol{u_X}|^2\right)$ is the transport in space of the energy $|\boldsymbol{u_X}|^2$.

$\frac{2}{\rho}\boldsymbol{\nabla_X}.(\boldsymbol{\delta u}\delta p)$**:** it corresponds to the pressure contribution to the energy balance. It is also a divergence in $\boldsymbol{X}$ space so it can be interpreted as the small scale pressure energy contribution on the sides of a local domain.

Similarly, $\frac{2}{\rho}\boldsymbol{\nabla_X}.(\boldsymbol{u_X}P_X)$ is the large scale pressure energy contribution.

$\frac{\nu}{2}{\boldsymbol{\nabla_X}}^2|\boldsymbol{\delta u}|^2+\frac{\nu}{2}{\boldsymbol{\nabla_r}}^2|\boldsymbol{\delta u}|^2$**:** These two terms correspond to the viscous diffusion in $\boldsymbol{X}$ space and in $\boldsymbol{r}$ space of the small-scale energy $|\boldsymbol{\delta u}|^2$. The viscous diffusion is important at small r because $\frac{\nu}{2}{\boldsymbol{\nabla_r}}^2|\boldsymbol{\delta u}|^2$ does not vanish when $r\to 0$ (Valente and Vassilicos 2011) as opposed to the other terms (except the dissipation).

Similarly, $\frac{\nu}{2}{\boldsymbol{\nabla_X}}^2|\boldsymbol{u_X}|^2+\frac{\nu}{2}{\boldsymbol{\nabla_r}}^2|\boldsymbol{u_X}|^2$ correspond to the viscous diffusion of the large scale energy $|\boldsymbol{u_X}|^2$.

$-\frac{1}{2}\epsilon^+-\frac{1}{2}\epsilon^-=-\frac{\nu}{2}\frac{\partial u_i^+}{\partial\zeta_k^+}\frac{\partial u_i^+}{\partial\zeta_k^+}-\frac{\nu}{2}\frac{\partial u_i^-}{\partial\zeta_k^-}\frac{\partial u_i^-}{\partial\zeta_k^-}$**:** This term is a sink of energy, it corresponds to the turbulent dissipation rate. It acts similarly both in the small scale and large scale energy equations.

$|\boldsymbol{\delta u}|^2$**:** This term is a three dimensional quantity equal to $\delta u_x\delta u_x+\delta u_y\delta u_y+\delta u_z\delta u_z$. Therefore, there is a direct connection with the second moments introduced by Kolmogorov.

Moreover, inspired by Nie and Tanveer 1999, Zhou and Vassilicos 2020 and Chen and Vassilicos 2022 integrate this quantity in r space to provide a physical interpretation of this term:

$$E_{\delta u}(R)=\frac{1}{\frac{4}{3}\pi R^3}\int_{|\boldsymbol{r}|<R}|\boldsymbol{\delta u}|^2d^3r \tag{2.11}$$

It can be derived that $E_{\delta u}(R\to 0)\to 0$ and $E_{\delta u}(R\to\infty)\to\frac{1}{4}\boldsymbol{u}(\boldsymbol{\zeta}^+)^2+\frac{1}{4}\boldsymbol{u}(\boldsymbol{\zeta}^-)^2$. $E_{\delta u}(R)$ is also a monotonically increasing function of R. Therefore, $E_{\delta u}(R)$ can be interpreted as an average kinetic energy at scales smaller than R.

$|\boldsymbol{\delta u}|^2$ is the density function in $\boldsymbol{r}$ space related to the quantity $E(R)$ so it is related to the turbulent energy at scale $\boldsymbol{r}$.

Similarly, a large scale energy quantity can be defined:

$$E_{u_X}(R)=\frac{1}{\frac{4}{3}\pi R^3}\int_{|\boldsymbol{r}|<R}|\boldsymbol{u_X}|^2d^3r \tag{2.12}$$

The sum of the small scale quantity and large scale quantity is related to the total kinetic energy present in the spatial sphere around $\boldsymbol{X}$ and of radius R:

$$E_{\delta u}(R) + E_{u_X}(R) = \frac{2}{\frac{4}{3}\pi R^3} \int_{|\boldsymbol{r}|<R} \frac{\boldsymbol{u}(\boldsymbol{X}+\boldsymbol{r})^2}{2} d^3r \tag{2.13}$$

Therefore, E_{u_X} is deduced to contain the energy of the scales larger than R which confirms its interpretation as a large scale quantity. This latter interpretation is consistent with the analysis of Mouri and Hori 2010.

$\boldsymbol{\nabla_r}.\left(\boldsymbol{\delta u}|\boldsymbol{\delta u}|^2\right)$: The interpretation of this term is easier when simplifications are introduced in equation 2.7. Homogeneity assumption is used so that all spatial derivatives vanish. The diffusion term is neglected for $r >> \lambda$ as derived in Valente and Vassilicos 2015. Equation 2.7 is also integrated in $\boldsymbol{r}$ space so that it describes $E_{\delta u}(R)$ which has a clear physical interpretation:

$$\frac{\partial}{\partial t} < E_{\delta u}(R) > + \frac{1}{\frac{4}{3}\pi R^3} \oint_{|\boldsymbol{r}|=R} < \boldsymbol{\delta u}|\boldsymbol{\delta u}|^2 > .\boldsymbol{n} d^2r \approx - < \epsilon > \tag{2.14}$$

where the notation $< . >$ is used to describe spatial averaging (over infinite/periodic space). Equation 2.14 is a conservative equation in $\boldsymbol{r}$ space where the variation in time of $E_{\delta u}(R)$ balances an energy flux in $\boldsymbol{r}$ space across a closed surface and a sink term $< \epsilon >$ which dissipates energy.

$\frac{1}{\frac{4}{3}\pi R^3} \oint_{|\boldsymbol{r}|=R} < \boldsymbol{\delta u}|\boldsymbol{\delta u}|^2 > .\boldsymbol{n} d^2r$ can therefore be interpreted as the energy flux received by the scales smaller than R. When it is negative in average, the energy cascade is direct from large scales to small scales. This is consistent with the interpretation of $\boldsymbol{\nabla_r}.\left(\boldsymbol{\delta u}|\boldsymbol{\delta u}|^2\right)$ as the energy interscale transfer rate across scales (Alves Portela, Papadakis, and Vassilicos 2017, Chen and Vassilicos 2022).

Similarly, $\boldsymbol{\nabla_r}.\left(\boldsymbol{\delta u}|\boldsymbol{u_X}|^2\right)$ can be interpreted as the large scale interscale transfer rate. When the flow is homogeneous, the small scale and large scale cascades are exactly connected as derived from equation 2.9:

$$\boldsymbol{\nabla_r}. < \boldsymbol{\delta u}|\boldsymbol{u_X}|^2 >= -\boldsymbol{\nabla_r}. < \boldsymbol{\delta u}|\boldsymbol{\delta u}|^2 > \tag{2.15}$$

Indeed, the large scale interscale transfer balances the small scale interscale transfer with a minus sign consistently with the large scale (resp. small scale) interpretation of these quantities. When the flow is non-homogeneous, there is permeability (or lack of impermeability) between the two interscale transfer rates described by the term $2\boldsymbol{\nabla_X}.(\boldsymbol{\delta u}(\boldsymbol{\delta u}.\boldsymbol{u_X}))$ in equation 2.9.

Links with Kolmogorov theory

In homogeneous turbulence, the Kolmogorov 1941c theory uses the hypothesis of equilibrium for $r << L$ which can be written as:

$$\frac{\partial}{\partial t} < E_{\delta u}(R) > \quad << \quad < \epsilon > \tag{2.16}$$

As explained previously the viscous diffusion can be neglected for $\lambda << r$. Therefore, for $\lambda << r << L$, we can derive:

$$\frac{1}{\frac{4}{3}\pi R^3} \oint_{|\boldsymbol{r}|=R} < \boldsymbol{\delta u}|\boldsymbol{\delta u}|^2 > .\boldsymbol{n}d^2r \approx - < \epsilon > \tag{2.17}$$

This result is the mathematical description of the so called inertial range where the energy cascades on average towards smaller scales at the turbulence dissipation rate. The range of validity of this homogeneous result is non-zero if $\lambda << L$ which requires large Reynolds number but not necessarily isotropy.

Following Chen and Vassilicos 2022, equation 2.17 supports the first and second similarity assumption of Kolmogorov. Therefore, the small scale energy behavior in the inertial range can be derived based on dimensional analysis for $\lambda << r << L$:

$$< |\boldsymbol{\delta u}|^2 > \sim < \epsilon >^{2/3} r^{2/3} \tag{2.18}$$

This result is very useful as the interscale transfer rate of energy can be evaluated to see if equation 2.17 is verified or not in real flows. This might helps to understand the Kolmogorov prediction's validity in some non-homogeneous flows where the theory is not supposed to hold.

2.1.4 Recent studies of the cascade in this framework

Recent energy cascade analyses using this mathematical framework give a new picture of the turbulent cascade. Indeed, Yasuda and Vassilicos 2018 describe very intense energy transfers across scales with events going both in direct and reverse directions. These events are much more energetic than the mean value. Once averaged in time, the classical energy cascade, from large scale to small scale appears where interscale energy transfer rate is close to turbulence dissipation rate. This is reminiscent of the Richardson 1922 cascade. However, it is only a time averaged picture which means that it is meaningless to see the turbulence cascade that way locally at a fixed time and a fixed point in space.

Anisotropy of the time-averaged interscale energy transfer rate was observed in Danaila et al. 2012 where a simplified expression of this term is derived in axisymmetric turbulence and whose reduced form is evaluated with PIV measurements in the impact zone of two opposed jets. This reduced form is measured to be significant in the in-plane direction (perpendicular to the axisymmetric axis) while it is inhibited in the axisymmetric direction. These measurements prove that non-homogeneous flows can exhibit a strong anisotropy of the cascade. In this experiment, the sign of the reduced form of the axisymmetric interscale transfer rate is measured to be negative at small r (direct cascade) and positive at large r which is interpreted

as the 'signature of large-scale inhomogeneity'. In Danaila et al. 2001, generalized forms of the Kolmogorov equation were derived where non-homogeneous terms were added. These terms were measured, with hot-wire measurements, to improve significantly the balance of the Kolmogorov equation in the central region of a channel flow. This result underlines the importance of the non-homogeneity in turbulent flows which is not present in the Kolmogorov theory. The non-homogeneity quantification and the understanding of its impact on energy cascade is therefore important for the understanding of turbulent flows present in practical applications.

Also, as opposed to classical energy cascade description, Gomes-Fernandes, Ganapathisubramani, and Vassilicos 2015 and Alves Portela, Papadakis, and Vassilicos 2017 observed significant interscale transfer rate variations in space even when averaged in time. Gomes-Fernandes, Ganapathisubramani, and Vassilicos 2015 identified a local inverse cascade in the near field behind a fractal grid where the energy spectrum has a classical power law slope close to -5/3. They observed, however, that the energy transfer rate averaged over orientation remains from large to small scales.

Alves Portela, Papadakis, and Vassilicos 2017 observed also similar results with energy transfers going backward and forward depending on the direction, coexisting with a $-5/3$ energy spectrum power law slope. More generally, the scale orientation of the time averaged energy transfer rate varies significantly depending on the spatial location.

In this latter publication, an even more disturbing result is observed: the flow is non-homogeneous on average but the time and direction averaged interscale transfer rate balances exactly dissipation over a significant range of scales. This results can be derived for time averaged homogeneous flows but it is not supposed to coexist with non-homogeneity as it requires a complex compensation between the non-homogeneous terms. This result is observed for the first time with this accuracy but it suggests that non-homogeneous energy balance laws might exist.

Knutsen et al. 2020 described also very clearly the non-homogeneity and anisotropy of the interscale energy transfer rate in a Von-Kármán experiment. In this study, the interscale transfer is also locally backward once averaged over time. The root cause of the locally inverse cascade that they identified seems to be associated with the mean flow. Therefore, the mean flow non-homogeneity and its interaction with turbulence plays a direct role in non-homogeneous cascades.

These papers support the use of the two-point framework as the cascade process is actually very different compared to the simplified Richardson 1922 picture. This latter picture may only be valid once averaged in time in specific flows where non-homogeneity does not affect the results.

More recently, Chen and Vassilicos 2022 started to generalize Kolmogorov's predictions with a new theory compatible with non-homogeneous flows. In this paper, the non homogeneous terms are present but behave similarly once averaged in time through similarity assumptions.

This theory is described and improved in chapter 4.

2.2 Rotation and non-Kolmogorov cascades

2.2.1 Non-Kolmogorov cascades

Even though most of energy spectrum measured comply with Kolmogorov predictions in the inertial range, some of them have different shapes. Therefore, different theories exist to explain these differences observed in very specific flows. Examples of non-Kolmogorov cascades are provided in the next sections to give an overview of the main research directions.

Helicity cascade

Non-Kolmogorov energy spectra are possible theoretically, based on various type of dimensional analysis. Brissaud et al. 1973 introduced the idea of helicity cascade. Helicity H is an invariant of inviscid, incompressible flow similarly to the energy:

$$H = \int_V \boldsymbol{u}.\left(\nabla \times \boldsymbol{u}\right) dV \tag{2.19}$$

With this concept, there is no energy cascade because the energy distribution in scales is driven by helicity cascade. Under several assumptions based on this helicity cascade concept, the energy spectrum scales as $k^{-7/3}$.

Kessar et al. 2015 suggest, on the basis of a dimensional analysis, that the helicity and the energy spectra depend both on energy and helicity injection rates, but their slopes can vary with two free parameters. In that case, there is a combined cascade of helicity and energy. In this formulation, the -5/3 and -7/3 slopes of the energy spectrum are only two specific solutions of the general formula:

$$E(k) \sim \epsilon^{7/3-a}\eta^{a-5/3}k^{-a}, \quad H(k) \sim \epsilon^{4/3-b}\eta^{b-2/3}k^{-b} \tag{2.20}$$

Kurien, Taylor, and Matsumoto 2004 introduce, using Kraichnan like arguments, an helicity transfer time scale τ_H and an energy transfer time scale τ_E. Using these time scales, they conclude that helicity cascade is dominating at small scales while the energy cascade is dominating at large scales. These results comply with the energy spectrum slopes evaluated in a DNS of homogeneous isotropic turbulence where a $k^{-5/3}$ slope is followed, at the higher wavenumbers, by a $k^{-4/3}$ slope which is another possible solution of equation 2.20.

Helicity cascade is therefore a non-Kolmogorov theoretical cascade. In the next section, we briefly summarize experimental results by Herbert et al. 2012 where a non-Kolmogorov cascade appears to be measured and is justified by the authors in term of an helicity cascade.

Rotating flow and helicity

Herbert et al. 2012 measured a non-Kolmogorov spectrums with PIV measurements in a Von-Kármán tank. A k^{-1} behavior was identified in the spatial energy spectrum followed by a steeper logarithmic slope at smaller scales. This steep slope was observed over a large range of scales. The slope was around k^{-2} at low Reynolds ($\sim 10^4$) and transitions to around $k^{-2.2}$ at higher Reynolds ($\sim 10^5$). The k^{-1} behavior was identified as an inverse cascade while the steep logarithmic slope as a direct cascade. In their paper, the results are interpreted using Beltrami assumption which maximize helicity. The Beltrami assumption means the velocity is aligned with vorticity so that $\boldsymbol{u} \times \boldsymbol{\omega} \approx 0$.

This argument links experimental results with helicity developments introduced previously. It leads to an inverse energy cascade (at large scales) and direct helicity cascade (at small scales). The two energy spectrum slopes obtained with helicity cascade are derived theoretically with Kraichnan-like arguments assuming local an non-local scenarios. The non-local scenario predicts k^{-2} energy spectrum and is associated with relatively low Reynolds numbers. The local scenario predicts a $k^{-7/3} \approx k^{-2.3}$ energy spectrum and is associated with high Reynolds numbers.

The helicity cascade and its dimensional analysis prediction are therefore a way to explain deviations from the Kolmogorov energy spectrum but it requires the Beltrami assumption to be valid in real flows.

Rotating flow and wave turbulence

Sagaut and Cambon 2018 relate rapidly rotating flow with wave turbulence. To do so, Navier-Stokes equations are written in a rotating frame and non-dimensionalized by a reference velocity U, a reference length scale L and a reference time scale $\frac{1}{\Omega}$ characterizing rotation rate. The equation in the rotating frame is written as:

$$\frac{\partial \widetilde{\boldsymbol{u}}}{\partial \widetilde{t}} + \boldsymbol{n} \times \widetilde{\boldsymbol{u}} - \frac{Ro}{Re}\widetilde{\nabla}^2 \widetilde{\boldsymbol{u}} + \frac{1}{2\Omega U}\nabla \widetilde{\boldsymbol{p}} = -Ro(\widetilde{\boldsymbol{u}}.\widetilde{\nabla})\widetilde{\boldsymbol{u}} \tag{2.21}$$

where $Ro = \frac{U}{2\Omega L}$ is the Rossby number and the tilde notation is used for quantities in rotating axis system.

In the limit $Ro \to 0$, the geostrophic balance $\widetilde{\nabla}\widetilde{\boldsymbol{p}} = \boldsymbol{n} \times \widetilde{\boldsymbol{u}}$ is obtained. Similar simplifications can be done in the vorticity equation to derive the Proudman theorem. It describes a 2D state where the velocity does not depend on the axial coordinate (Sagaut and Cambon 2018).

With this analysis, the energy cascade is deduced to be affected by rotation through the simplifications done with the Rossby number which appears during the non-dimensionalization of the equation. Baroud et al. 2002 measure for example a k^{-2} energy spectrum in a rapidly rotating flow and they relate it to quasi two-dimensionalisation of the flow. However, the

results are observed only for very small Rossby numbers (in the later study $Ro \approx 0.06$).

The linearized equation (zero Rossby number) associated to the inviscid assumption can lead to the existence of wave solutions in rotating axis system. This is the basis of wave turbulence theory which also predicts non-Kolmogorov spectra in some regions. Some elements of wave turbulence theory are confirmed with experiments dedicated for that. The flow in these experiments is far from practical applications as it needs to be very smooth without any disturbance except the ones introduced to test the theory.

This wave turbulence theory is not studied in the present thesis because the mixer rotation speed used is not very high and the highly turbulent flow present in the tank suggests that the non linear term of the Navier-Stokes equation plays a dominant role. Moreover, the experimental set up used in this project does not allow the camera rotation needed to measure turbulence in rotating axis system which is required in this theoretical framework. However, we can keep in mind the possibility that the flow present in the mixer might, in certain cases, be in an intermediate regime between non rotating flow, possibly described by Kolmogorov/Kolmogorov-like theory, and rapidly rotating turbulence, possibly described by wave turbulence theory.

2.2.2 Previous work on the mixer used for the PHD project

A mixer is used in this PHD thesis to produce various turbulent flows. The mixer is not used to mix the flow but as a scientific tool to generate turbulence. Therefore, we do not review the wide scientific literature about mixers but we focus on the research previously done with our mixer tank to describe its flow properties. When mixer knowledge is needed, the book from Nagata 1975 is used for reference.

The mixer tank experiment used during this PHD research was previously designed and used at Imperial College by Kostas Steiros to analyse the fractal blades impact on mixing quality and efficiency. He found that fractal blades reduce significantly the torque during mixing (Steiros et al. 2017a). This torque decrease is associated with weaker coherent vortices on the blades' sides compared to the rectangular blade configuration. The torque decrease seems to be associated to interactions of these coherent structures with the wall (Steiros et al. 2017b). A more precise flow understanding was developed in Başbuğ, Papadakis, and Vassilicos 2018 with a DNS of a similar mixing tank. According to this study, the fractal blades break the coherent structures. The strength reduction of these coherent structures is associated to a smaller recirculation region behind the propeller which can explain the torque decrease.

Therefore, the turbulence properties in the mixer tank are expected to change with blade configurations especially with their fractal dimension. This might have an impact on energy cascade and dissipation so we test fractal and non-fractal blades.

Also, preliminary experiments in the mixer done at Imperial College by K.Steiros suggest that energy spectra in the frequency domain measured in the bulk of the flow might have a different shape compared to one predicted by Kolmogorov theory (section 2.1.2). This work was not published so it should be confirmed with our experiments in collaboration with K. Steiros.

2.3 Turbulence modeling

There is a strong connection between the large scale two-point Navier-Stokes equations and Large Eddy simulation as introduced in Germano 2007b. Therefore, a review about Large Eddy Simulation methods is done in this section to introduce chapter 6. However, the detailed links between two-point equations and Large Eddy Simulation (LES) is done directly in the chapter. The following review is mainly based on Moser, Haering, and Yalla 2021 and Pope 2000.

Flow simulations require huge computational resources to be accurate. Indeed, the turbulent flow smallest scales have non-negligible impact on the largest ones. These accurate simulations are called Direct Numerical Simulations (DNS). They are so resource-consuming that the vast majority of existing industrial cases cannot be resolved with such a method even with high performance computers. This is why industrial companies mainly use Reynolds Averaged Navier Stokes (RANS) equations resolution where only the mean flow is resolved and the fluctuating flow is modeled with turbulence models. This resolution method is much more efficient but some modeling uncertainty is introduced and no information is provided about non-stationary effects. Moreover, the modeling is complex and not directly related to the physics so that it is not fully reliable. Another method is the Large Eddy Simulation where only the largest scales of the flow are resolved and the smallest scales are modeled. This method allows the simulation of non-stationary effects and is probably a good way to have physically supported results if the small scale model is based on physics. Therefore, this method is expected to be more reliable while still having a computational cost around an order of magnitude less than DNS (Moser, Haering, and Yalla 2021). The computational resources increase with the years could make this technology available to various industrial problems in the medium to large term.

The LES description formulated in Reynolds 1990, Pope 2000 and Dairay et al. 2017 is used to separate the physical modeling error from the numerical error. The Navier-Stokes

equation is first filtered without approximation:

$$\frac{\partial \widetilde{\boldsymbol{u}}}{\partial t} + (\widetilde{\boldsymbol{u}}.\nabla)\widetilde{\boldsymbol{u}} + \left[\widetilde{(\boldsymbol{u}.\nabla)\boldsymbol{u}} - (\widetilde{\boldsymbol{u}}.\nabla)\widetilde{\boldsymbol{u}}\right] = -\frac{1}{\rho}\nabla\widetilde{p} + \nu\nabla^2\widetilde{\boldsymbol{u}} \tag{2.22}$$

where the filter is defined as:

$$\widetilde{\boldsymbol{u}}(\boldsymbol{x},t) = \int G(\boldsymbol{r},\boldsymbol{x})\boldsymbol{u}(\boldsymbol{x}-\boldsymbol{r},t)d\boldsymbol{r} \tag{2.23}$$

Where $\int G(\boldsymbol{r},\boldsymbol{x})d\boldsymbol{r} = 1$ over the domain and the residual velocity field is defined as $\boldsymbol{u}'(\boldsymbol{x},t) = \boldsymbol{u}(\boldsymbol{x},t) - \widetilde{\boldsymbol{u}}(\boldsymbol{x},t)$. The function solved during resolution is the filtered velocity field.

The derivative commutes with the filter when the filter is homogeneous. In this thesis, only homogeneous filters are used to simplify results. Equation 2.22 is therefore re-written in a more classical form:

$$\frac{\partial \widetilde{\boldsymbol{u}}}{\partial t} + (\widetilde{\boldsymbol{u}}.\nabla)\widetilde{\boldsymbol{u}} = -\frac{\partial}{\partial x_j}\tau_{ij} - \frac{1}{\rho}\nabla\widetilde{p} + \nu\nabla^2\widetilde{\boldsymbol{u}} \tag{2.24}$$

where $\tau_{ij} = \widetilde{u_i u_j} - \widetilde{u}_i\widetilde{u}_j$. This quantity is called the residual stress.

This quantity is replaced by a model $\widehat{\tau_{ij}}$ based on resolved quantities to obtain the new equation:

$$\frac{\partial \widetilde{\boldsymbol{u}}}{\partial t} + (\widetilde{\boldsymbol{u}}.\nabla)\widetilde{\boldsymbol{u}} = -\frac{\partial}{\partial x_j}\widehat{\tau_{ij}} - \frac{1}{\rho}\nabla\widetilde{p} + \nu\nabla^2\widetilde{\boldsymbol{u}} \tag{2.25}$$

The difference between these two equations is called the modeling error. The error associated to the numerical resolution of equation 2.25 is called the numerical error. It can be evaluated through mesh convergence for example.

Many LES models have already been developed since the 60's, for example: Smagorinsky 1963 model, Clark, Ferziger, and Reynolds 1977 model, Bardina, Ferziger, and Reynolds 1980 model, Métais and Lesieur 1992 model and Dairay et al. 2017 model. The most famous ones are the eddy diffusivity models inspired by RANS modeling. The idea is to model the small scale effects by a turbulent viscosity as if turbulence was changing the flow viscosity. This physical justification for LES modeling is however questionable. The Smagorinsky 1963 model is the most famous one from this category as it is easy to implement. The model is defined as:

$$\widehat{\tau_{ij}} = -2\nu_T\widetilde{S_{ij}} \tag{2.26}$$

where Δ is the LES mesh width,

$$\widetilde{S_{ij}} = \frac{1}{2}\left(\frac{\partial\widetilde{u_i}}{\partial x_j} + \frac{\partial\widetilde{u_j}}{\partial x_i}\right) \tag{2.27}$$

is the resolved strain rate tensor and

$$\nu_T = C_S \Delta^2 \sqrt{2\widetilde{S_{ij}}\widetilde{S_{ij}}}. \tag{2.28}$$

This model predicts rather well the mean dissipation of residual scales but has a very poor correlation with real subfilter stress when evaluated on real turbulent flows according to Meneveau and Katz 2000. This model is designed for 'homogeneous', isotropic turbulence.

The Germano et al. 1991a, Germano et al. 1991b and Lilly 1992 method can be used to adapt the dissipation introduced depending on local flow properties. This is done by replacing the global coefficient C_S by a dynamic coefficient computed locally. This method was designed to extend the use of the Smagorinsky model to non-homogeneous flows. It improves significantly the results in specific situations. For example, it cancels dissipation near walls where Smagorinsky model produces unwanted dissipation (Germano et al. 1991a). It is just a correction and it does not solve all problems. This method is famous as it is now used as a tool to compute dynamic coefficients for many models.

Many other dissipation models exist and good performance is obtained to predict mean dissipation in homogeneous turbulence. A state of the art dissipation model is for example the implicit model developed by Dairay et al. 2017. With this method, the dissipation is introduced through the numerical scheme specifically designed to reproduce some physical properties during the resolution. This method is 'equivalent to the use of spectral vanishing viscosity' with an implementation in real space. This method is based on a Kolmogorov spectrum so it is also designed for homogeneous turbulence. This methodology converges to the right solution when the mesh is refined as opposed to Smagorinsky model. Therefore, the numerical error goes to zero when the resolution is chosen accordingly and the modeling error understanding is much easier.

One main issue about LES identified by Moser, Haering, and Yalla 2021 is that 'exact subgrid term determined from NS exhibits variations in the local dissipation (energy transfer rate) that can be much larger than the mean transfer rate. This necessarily includes large local transfers of energy from small to large scales, commonly called backscatter.' This feature is not captured well by dissipation models in general and more particularly by Smagorinsky model. This feature is not new as it was already identified in Piomelli et al. 1991.

Other models were introduced to take into account this effect. This is for example the case of wall adapted LES which are widely developed these years to capture non dissipative effects close to walls.
However, more universal models were already developed to capture such phenomenon in general. This is for example the case of the scale similarity model introduced by Bardina,

Ferziger, and Reynolds 1980. According to Meneveau and Katz 2000, this model correlates much better than Smagorinsky model with exact subfilter stress once evaluated on real turbulence data. However, the mean dissipation is not well captured which leads to poor simulation results. This is why this model is often used as a complement to a dissipation model such as Smagorinsky:

$$\widehat{\tau_{ij}} = -2C_S\Delta^2\sqrt{2\widetilde{S_{ij}}\widetilde{S_{ij}}}\widetilde{S_{ij}} + \widetilde{u_i}\check{\widetilde{u_j}} - \check{\widetilde{u_i}}\check{\widetilde{u_j}} \tag{2.29}$$

where $\check{(.)}$ is a filter applied on the resolved quantities during LES. The similarity model idea is to evaluate a subfilter stress with resolved quantities by over-filtering the resolved terms. Then, these results are extrapolated to smaller scales. This method is expected to give good results when the filtering cutoff frequency is in the inertial range. Indeed, the inertial range similarity may legitimate the extrapolation to smaller scales.

More generally the mixed model configuration allows to tune the two parts of the model separately: one mainly taking into account dissipation and the other energy transfer fluctuations and backscatter.

A remaining work regarding LES modeling is to improve understanding and modeling of this energy transfer fluctuations including backscattering. The good understanding of this phenomenon is important to improve non-homogeneous flow modeling. Indeed, in flows where strong mean flow gradients exist such as channel flows, backscatter can even prevail over dissipation (Cimarelli and De Angelis 2014). Therefore, residual scales might locally provide energy in average to resolved scales.

2.4 Objectives and thesis Outline

The small scale and large scale two-point Navier-Stokes equations are very powerful tools to analyze non-homogeneous turbulence. The small scale equation is more related to the small scale physics and therefore to turbulence cascade theories. The large scale equation is strongly related to the small scale equation and was never analyzed either numerically or experimentally to our group's knowledge. Moreover, it is related to Large Eddy Simulation. Therefore, the experimental analysis of both equations and their relations in different classes of non-homogeneous steady flows is needed to improve their physical understanding as well as the turbulence physics itself. Eventually, the links with Large Eddy Simulation are to be analyzed to see how these fundamental equations can be useful for turbulence modeling.

In chapter 3, we introduce the mixer experiment used to produce different turbulent flows. The Particles Image Velocimetry measurements methods and settings are described as well as the main post-processing methods.

In chapter 4, a first class of non-homogeneity is identified where Kolmogorov-like results are measured in non-homogeneous turbulence. Theoretical elements are used to analyze these results.

In chapter 5, non-Kolmogorov turbulence results are measured when the flow is rotating. More information is obtained through two-point statistics to understand why the chapter 4 theoretical elements do not hold in this flow.

In chapter 6, the links between Large Eddy Simulation and the large scale two-point equation are analyzed. A new physically supported LES model is derived and tested.

Chapter 3

Experiments and processing methods

3.1 Mixer presentation

Experiments are carried out with water in the same octagonal shaped, acrylic tank used in (Steiros et al. 2017a) and refurbished for this project (figure 3.1). The octagonal shape is used to minimize optical distortion during measurements. The water used during experiments is highly pure (resistivity of 18 MΩ.cm) to improve measurements quality.

The impeller has a radial four-bladed flat blade turbine, mounted on a stainless steel shaft at the mid-height of the tank. The impellers are driven by a stepper motor (Motion Control Products, UK) in microstepping mode (25, 000 steps per rotation), to ensure smooth movement, which is controlled by a function generator (33600A, Agilent, US). The rotation speed and torque signal are measured with the Magtrol torquemeter TS 106/011. The torque accuracy is 0.1 % of the rated torque (5Nm). The dimensions of the mixer are presented in figure 3.2 where D_T is the tank diameter (45cm) and H its height ($H = D_T$), C is the rotor height ($H/2$) and D is the rotor diameter (about $DT/2$).

3.2 Different experiment configurations

Different configurations are tested to change the turbulence properties. The main geometrical change is the use of the octagonal tank with baffles (figures 3.3b and 3.4) or without baffles (figure 3.3a). The baffles (four vertical bars on the sides of the tank) are used to break the flow rotation. These baffles are designed based on Nagata 1975 specifications for close to fully baffled conditions which maximize power consumption and minimize rotation. For a circular tank, this condition is achieved with four baffles of width around $0.12D_T$ where D_T is the tank diameter (see D_T in figure 3.2). Therefore, four baffles of mixer tank height and

Figure 3.1: Mixing tank installation without baffles
1: Mixer tank, 2: Camera, 3: Stepper motor, 4: Torquemeter, 5: Blades, 6: Stepper motor controller

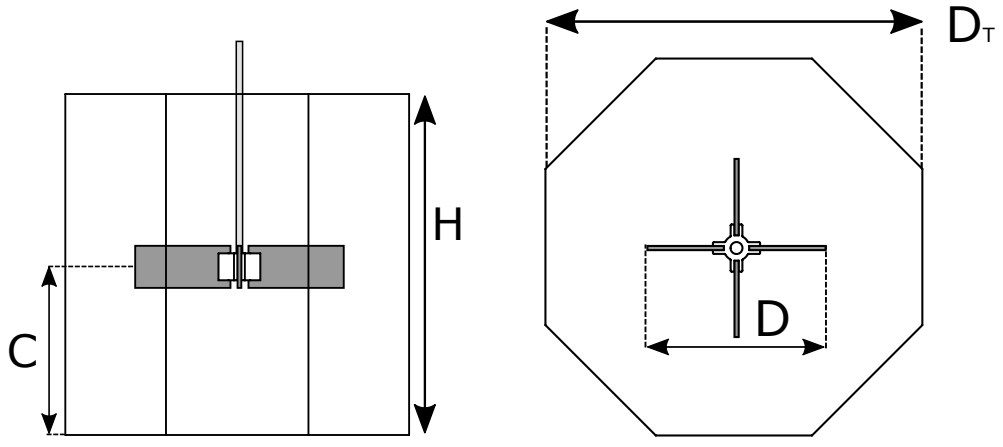

(a) (b)

Figure 3.2: Mixer dimensions. Figures modified from Steiros et al. 2017b

(a) Mixing tank without baffles (b) Mixing tank with baffles

Figure 3.3: Mixer with and without baffles

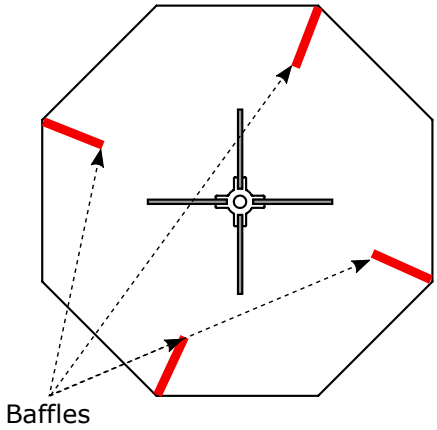

Figure 3.4: Top view of baffles

58mm width are used.

To test the robustness of our results we run experiments with two different types of blade geometry which stimulate the turbulence differently: rectangular blades of $44mm \times 99mm$ size (figure 3.5a) and fractal-like/multiscale blades (figure 3.5b) of the exact same frontal area $44 \times 99mm^2$ but much longer perimeter. This blade difference affects turbulence properties substantially as the resulting turbulence dissipation rate differs by 30% to 40% at equal rotation speed (see table 3.3). We use here the two-iteration 'fractal2' blade described in Steiros et al. 2017b and shown in figure 3.5b. The blades are machined with laser cutting machine of $15\mu m$ accuracy so the second fractal iteration is the maximal one which can be manufactured easily.

Eventually, different rotation speeds are tested to evaluate Reynolds number effect. The

(a) Rectangular blades (b) Fractal blades

Figure 3.5: Mixer blades

rotor speed is limited for practical reasons. First, the rotation torque shall be limited to not break the 3D printed piece which hold the blades. Then, high rotation speed bring air bubbles inside the water which can affect PIV measurements quality. For the configurations without baffles, a vortex appears (figure 3.3a) and brings air bubbles deep inside the mixer so that it can enter the field of view. For these configurations, the maximal rotation speed is set to 3Hz for rectangular blades and 2.5Hz for fractal blades to limit the presence of air bubbles in the field of view. For these configurations, the mixing tank is not filled to the top to prevent water leaks occurring at high rotation speed with centrifugal forces. There is a 2.5cm space between the lid and water surface when the rotor is at rest.

For the baffled configurations, there is no rotation vortex at the center but the mixing is so efficient that air at the surface is easily mixed inside water. Therefore, water is filled to the top of the sealed container to minimize air bubbles. Even with this care, the rotation speed can not be increased more than 1.5Hz. This is already a high speed for these configurations because the torque is more than 1 N.m.

The water filling difference between baffled and non-baffled configurations is not a problem because the baffles are used to break the flow rotation. The drag added by the lid in the baffled configurations is also a way to reduce rotation. On the other hand, the small air gap in the non-baffled configurations allows the rotation to develop freely.

3.3 Axis system conventions

All results are computed in non-rotating axis system (figure 3.6).

- The reference point is defined on the mixer centerline at a distance of 0.118m from the bottom of the mixer (which corresponds to the center of the PIV field of view).
- The z axis is coincident with the centerline and directed toward the top.
- The mixer tank is octagonal so different plans exist. One of them is chosen for reference and the camera is set parallel to this plan (P1).
- The x axis is defined in the plan P1 and perpendicular to the axis z. x is directed toward the right side when looking the mixer at the camera point of view.

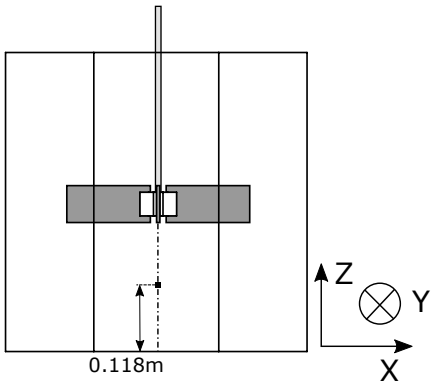

Figure 3.6: Axis system (camera view)

- The y axis is deduced to have a direct axis system.

3.4 PIV resolution

The PIV resolution of the experiment (i.e. interrogation window size) is presented in table 3.1. In terms of the Kolmogorov length $\eta = (\nu^3/\langle\overline{\epsilon'}\rangle)^{1/4}$, where the angular brackets signify a space-average over the PIV field of view, the resolution is between 2.3η and 5.1η depending on the configuration. For those configurations where the interrogation window size is larger than 3η the turbulence dissipation rate might be underestimated when denoised properly (Foucaut et al. 2021). However, this underestimation remains acceptable for interrogation window size smaller than 5η where less than 30 % of uncertainty (filtering effect) is expected according to Laizet, Nedić, and Vassilicos 2015 and Lavoie et al. 2007.

	F (Hz)	Mf ($\mu m/px$)	IW size (mm)	IW size/η
Rectangular blades	2	14	0.45	2.3
Rectangular blades	3	14	0.45	3.2
Fractal blades	2	14	0.45	2.8
Fractal blades	2.5	14	0.45	3.1
Rectangular blades with baffles	1	14	0.45	4.1
Rectangular blades with baffles	1.5	14	0.45	5.1
Fractal blades with baffles	1	14	0.45	3.4
Fractal blades with baffles	1.5	14	0.45	4.4

Table 3.1: PIV resolution where Mf is the magnification factor and IW the interrogation window.

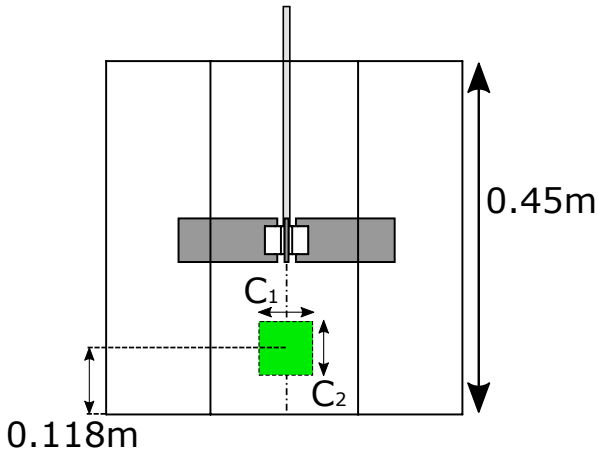

Figure 3.7: Measurement plane location

3.5 Presentation of the measurement planes

Two measurement planes are used during experiments. They are located at the same place (figure 3.7) but their size is not the same as described in table 3.2. All the results presented in this thesis are computed with the small field of view to have good resolution. The large field of view was only used for checks but the quality of the measurements is not comparable. Therefore, the results of this dataset are mentioned for information but are not presented explicitly in the thesis because of their low quality.

Measurement plan size	C_1	C_2
Small field of view	27mm	28mm
Large field of view	64mm	67mm

Table 3.2: Measurement planes size

The aim of the experiment was to have the field of view center coincident with the reference point defined in section 3.3. In practice, some positioning uncertainty was introduced when doing the experiment. Indeed, the mixer tank is not exactly symmetrical by construction and the set-up is slightly flexible. The measurement plane positioning uncertainty is around 1mm in all directions.

In addition to this small uncertainty, the small field of view measurement plan is offseted by 3mm in the y direction to be at the same location as preliminary experiments done at the beginning of the project. Therefore, for the non baffle cases there is a small but non zero mean flow in the measurement plan associated to this offset. Indeed, for these configurations there is a close to solid rotation of the flow around the centerline. A small constant mean flow over the measurement plan is expected through the projections computed in equation

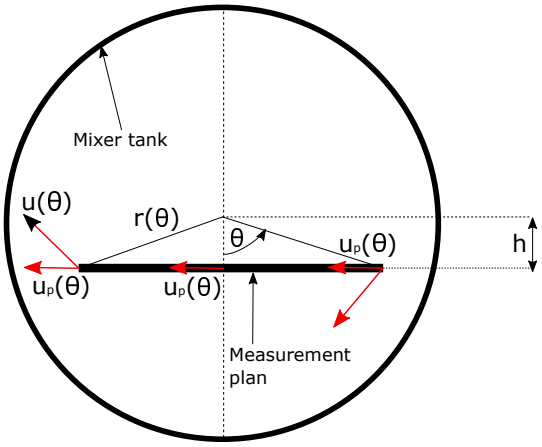

Figure 3.8: Measurement plane (top view)

3.1 and presented in figure 3.8. The measured mean flow variation with rotation frequency is consistent with this analysis.

$$u_p(\theta) = u(\theta)cos(\theta) = \omega r(\theta)cos(\theta) = \Omega\frac{h}{cos(\theta)}cos(\theta) = h\Omega \tag{3.1}$$

3.6 Particule Image Velocimetry settings

The PIV set up is composed of a camera, a laser, a set of lenses and mirrors to shape the laser beam into a thin light sheet (figure 3.9), a Lavision PTU synchronisation unit and a recording computer with Davis 10 from Lavision.

3.6.1 Camera

The camera used is the Phantom v2640 with full sensor image ($2048px \times 1952px$). A Nikon macro Nikkor 200mm lens is used with f#8. The extremity of the lens is at 93 mm from the glass. The field of view size is $C_1 \times C_2 \approx 27mm \times 28mm$ for the high resolution experiments (see figure 3.7) with a magnification factor of $14.1\mu m/px$.

The acquisition is done by packets of five time-resolved images. The packet acquisition frequency is 6Hz to ensure decorrelation between successive packets. The acquisition frequency for the five images within each packet varies from 1.25kHz to 3kHz depending on type of blade and rotor speed. This parameter is specifically set for each configuration to ensure a turbulent fluctuation displacement between two frames of around 5px (corresponding to about 1 standard deviation) and rarely above 10px (observed with samples during the experiments).

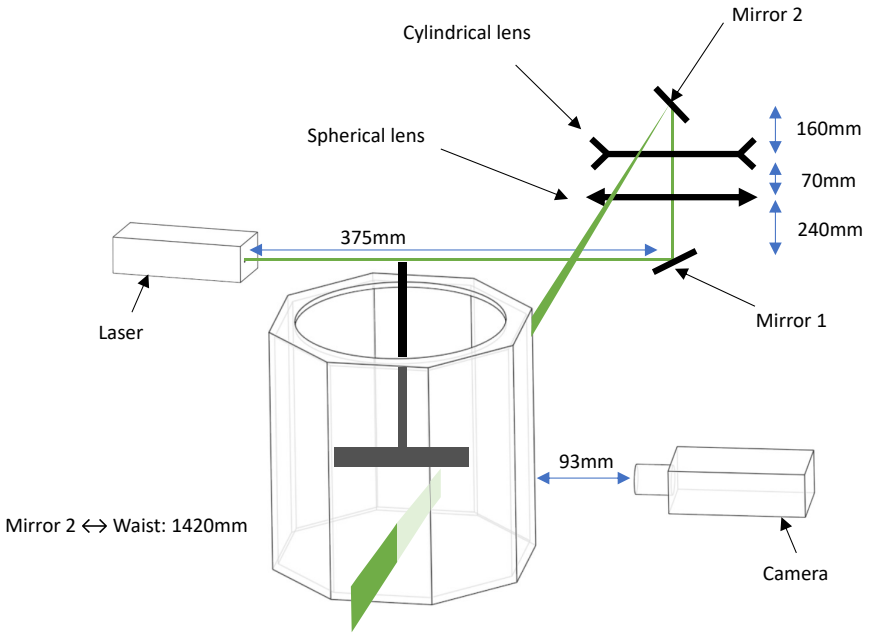

Figure 3.9: PIV set-up

3.6.2 Laser

The laser used is the Blizz 30W high speed frequency laser from InnoLas. The laser is optimized at 40kHz with $750\mu J/pulse$ at $532nm$ wavelength and $M^2 < 1.3$. For the experiments it was set to around $500\mu J/pulse$ because of the smaller frequency used. The laser frequency is set according to the camera time-resolved recording frequency. The focal lengths of the spherical and the cylindrical lenses are +800mm and -80mm respectively (beam-waist set in the centre of field of view). The laser sheet height obtained is around 60mm and its width is 0.6mm at the waist (which is close to the centerline of the mixer) with a Rayleigh length of 400 mm. Therefore, the width of the laser is constant over the field of view.

3.6.3 Seeding

Mono-disperse polystyrene particles from Spherotech of diameter $5.33\mu m$ are used. They maximise the concentration in the flow and lead to enough particles within each interrogation window. The background noise is around 30 counts. There are on average about 10 particles per interrogation window of $32px \times 32px$ if a threshold of 50 counts is used to select most particles. This is consistent with the criteria of Keane and Adrian 1991. Among these particles, there is on average 6.5 particles higher than 100 counts per interrogation window.

3.6.4 Processing

The calibration is done with LaVision 058-5 plate. The PIV processing is done with the Matpiv toolbox modified at LMFL. It is a classical multigrid and multipass cross-correlation algorithm (Willert and Gharib 1991, Soria 1996). Here four passes are used, starting with $64px \times 64px$ then, $48px \times 48px$ and finishing with two $32px \times 32px$ passes. Before the final pass, image deformation is used to improve the results (Scarano 2001, Lecordier and Trinité 2004). An overlap between IW of 62% is used, leading to vector spacing of about 0.17mm. The final grid has then 159 points in the horizontal direction and 167 in the vertical one.

3.7 Computation of the turbulence parameters

The following conventions are used to compute the different turbulent parameters.

3.7.1 Viscosity

The temperature is measured before and/or after each experiment. The variation during an experiment does not exceed 1°C. This is approximately the uncertainty associated to this measure. The water viscosity is recomputed through a variant of the empirical Guzman Andrade law which depends on temperature:

$$\mu = A \times 10^{B/(T-C)} \tag{3.2}$$

where T is the temperature in Kelvin, $A = 2.415 \times 10^{-5} Pa.s$, $B = 247.8K$ and $C = 140K$.

The kinematic viscosity is deduced from the equation:

$$\nu = \frac{\mu}{\rho} \tag{3.3}$$

assuming $\rho \approx 1000 Kg/m^3$.

3.7.2 Dissipation

The axisymmetric dissipation formulation is used (George and Hussein 1991) where the rotation axis is z:

$$< \overline{\epsilon'} >= \nu < \overline{\left(- \left(\frac{\partial u'_z}{\partial z} \right)^2 + 2 \left(\frac{\partial u'_z}{\partial x} \right)^2 + 2 \left(\frac{\partial u'_x}{\partial z} \right)^2 + 8 \left(\frac{\partial u'_x}{\partial x} \right)^2 \right)} >. \tag{3.4}$$

The dissipation is averaged both in space and time to obtain a converged estimate over the field of view. The notation $< . >$ is used for space averaging and $\overline{(.)}$ for time averaging.

Different estimates are tested to check the robustness of the results with respect to the choice estimate. One of them inspired by isotropic formula is defined as

$$< \overline{\epsilon'_\tau} >= \frac{\nu}{3} \overline{< \left(2 \times 15 \frac{\partial u'_x}{\partial x}^2 + 15 \frac{\partial u'_z}{\partial z}^2 \right) >} \tag{3.5}$$

and is evaluated in table 3.3 after signal denoising (method explained in the next paragraph).

The results are different by less than 10% but more importantly the evolution from one configuration to the other is consistent. Therefore, the variation of the results does not seems to be significantly dependent on the estimate choice so that dissipation scalings can be evaluated accurately. However, the value itself might contains some uncertainty.

The dissipation computation from experimental data is difficult because PIV introduces random noise during the measurements. This noise contaminates significantly the dissipation (Foucaut et al. 2021). Indeed, the turbulent energy is small at small scales so that noise can dominate at these scales. This result is directly visible on experimental energy spectrum (see figure 3.10) where a squared cardinal sine function modulation is observed (Foucaut, Carlier, and Stanislas 2004). In Foucaut et al. 2021, the product of the derivatives used to compute dissipation is overestimated by 70% before denoising. The best way to denoise dissipation is to perform the experiment with two different PIV set-ups so that the noise of both measurements are decorrelated. The product of the derivatives obtained from the two systems cancel the random noise contribution:

$$\begin{aligned} &< \frac{\partial u'}{\partial x}|_{s1} \times \frac{\partial u'}{\partial x}|_{s2} > \\ &=< \widehat{\frac{\partial u'}{\partial x}}|_{s1} \times \widehat{\frac{\partial u'}{\partial x}}|_{s2} > + < \beta_{s1} \times \widehat{\frac{\partial u'}{\partial x}}|_{s2} > + < \widehat{\frac{\partial u'}{\partial x}}|_{s1} \times \beta_{s2} > + < \beta_{s1} \times \beta_{s2} > \\ &=< \widehat{\frac{\partial u'}{\partial x}}|_{s1} \times \widehat{\frac{\partial u}{\partial x}}|_{s2} > \end{aligned} \tag{3.6}$$

where $< . >$ is used for realization averaging here, s_1 (resp. s_2) refers to system 1 (resp. system 2), β is the random PIV noise and $\widehat{(.)}$ refers to denoised data (i.e. without noise but with PIV interrogation window filtering effect).

Indeed, the noise is not correlated with the true signal and the noise of the two cameras is decorrelated so it cancels out once averaged.

This double measurement was not possible for this experiment because of practical limitations. Therefore, a simplified denoising method is used. The idea is to use the high resolution of the measurements (in space or in time) and shift the two derivatives by a small offset. This method introduces a small filtering of the true signal but the noise cancels out. The experimental measurements are highly resolved in time so time denoising is used:

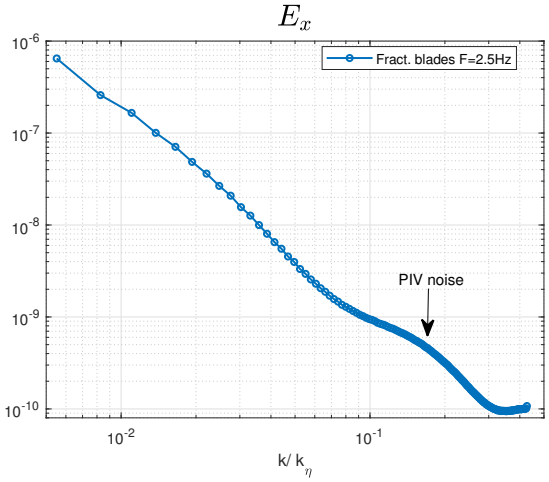

Figure 3.10: Energy spectrum from experimental results contaminated by PIV noise

$$
\begin{aligned}
&< \frac{\partial u'}{\partial x}|_t \times \frac{\partial u'}{\partial x}|_{t+dt} > \\
&=< \widehat{\frac{\partial u'}{\partial x}}|_t \times \widehat{\frac{\partial u'}{\partial x}}|_{t+dt} > + < \beta_t \times \widehat{\frac{\partial u'}{\partial x}}|_{t+dt} > + \widehat{\frac{\partial u'}{\partial x}}|_t \times \beta_{t+dt} > + < \beta_t \times \beta_{t+dt} > \\
&=< \widehat{\frac{\partial u'}{\partial x}}|_t \times \widehat{\frac{\partial u'}{\partial x}}|_{t+dt} > \\
&\approx< \widehat{\frac{\partial u'}{\partial x}}|_t \times \widehat{\frac{\partial u'}{\partial x}}|_t >
\end{aligned}
\tag{3.7}
$$

where β_t and β_{t+dt} are uncorrelated because the new particles entering the interrogation window (IW) at t +dt change the peak shape, so the peak fit random noise is then completely different. This method is valid if dt (the time increment between two velocity fields) is small enough so that the denoised quantities do not change significantly between two time steps but not too small (otherwise there would be no new particles inside the IW). In the experiments carried out, dt is chosen to have time resolved results which means the particle displacement between two frames is less than 10 pixels: it is between 0.02τ and 0.08τ where $\tau = \sqrt{\frac{\nu}{<\overline{\epsilon'}>}}$ is the Kolmogorov time scale. The PIV processing (final pass) is done with a window size of 32 pixels $\times$ 32 pixels so that there is already a spatial filtering of the data. Therefore, the filtering introduced by shifting the two derivatives by a maximum of 10 pixels is comparable or smaller than the already existing PIV filtering so that the results should not change significantly. This method can be used to denoise experimental data without losing too much information of the true signal. This method might however slightly underestimate the dissipation. The same procedure can also be used in space by selecting different points in the derivative, i.e. multiplying the

	F (Hz)	$<\overline{\epsilon'}>$ (1)	$\widehat{<\overline{\epsilon'}>}$ (2)	$\widehat{<\overline{\epsilon'}>}$ (3)	$\widehat{<\overline{\epsilon'_\tau}>}$ (4)
Rectangular blades	2	1.4×10^{-3}	7.4×10^{-4}	6.0×10^{-4}	5.7×10^{-4}
Rectangular blades	3	4.4×10^{-3}	2.3×10^{-3}	2.1×10^{-3}	2.1×10^{-3}
Fractal blades	2	2.5×10^{-3}	1.5×10^{-3}	1.3×10^{-3}	1.3×10^{-3}
Fractal blades	2.5	4.7×10^{-3}	2.6×10^{-3}	2.3×10^{-3}	2.3×10^{-3}
Rectangular blades with baffles	1	5.2×10^{-3}	3.5×10^{-3}	3.6×10^{-3}	3.7×10^{-3}
Rectangular blades with baffles	1.5	1.7×10^{-2}	1.1×10^{-2}	1.2×10^{-2}	1.3×10^{-2}
Fractal blades with baffles	1	4.2×10^{-3}	2.6×10^{-3}	2.4×10^{-3}	2.5×10^{-3}
Fractal blades with baffles	1.5	1.3×10^{-2}	8.2×10^{-3}	8.2×10^{-3}	8.6×10^{-3}

Table 3.3: Dissipation computation (m^2/s^3). $<\overline{\epsilon'}>$ (1) is computed with noise; $\widehat{<\overline{\epsilon'}>}$ (2) is computed with spatial denoising process; $\widehat{<\overline{\epsilon'}>}$ (3) is computed with time denoising process; and $\widehat{<\overline{\epsilon'_\tau}>}$ (4) is also computed with time denoising process.

derivative at x and at x+dx computed with a centred scheme, where dx is the vector spacing whose value is between 2.3η and 5.1η. As a 62% overlap is used, the three points used are separated by 36px which corresponds to a second filter which has about the same filter size as the IW. However, the spatial denoising may filter more than time denoising.

The denoising process is tested both in space and in time to check the results consistency (table 3.3). The results are close so that the two methods seems to be reliable. There is a significant decrease of the dissipation associated to the denoising process (around a factor 2). These results seems to be consistent because the mixer PIV measurements are expected to be more noisy than typical air experiments. Indeed, this noise is amplified by the remaining presence of small air bubbles in water and the difficulty to obtain the optimal particle concentration (of very bright particles) linked to this high magnification measurement. These results underline also the importance to denoise dissipation. The energy spectra and two-point statistics do not need to have the same denoising process because the noise is known to be non-negligible (or even dominant) only at small scales. Therefore, only the small scale part of the results (large k in Fourier space or small r in two-point space) are non-negligibly contaminated by this PIV noise.

Finally, the PIV resolution affects significantly the dissipation results and a small underestimation is expected in our results as explained in section 3.4.

Overall, the dissipation computation is a difficult problem where resolution, noise and convergence affect significantly the results. For these experiments, the resolution is acceptable, the noise impact is removed through denoising process and the convergence is achieved through an averaging over 100,000 velocity fields (corresponding to 50,000 uncorrelated) and space averaging over the field of view. The dissipation estimate is expected to slightly underestimate the true one. For simplicity the notation $\widehat{(.)}$ is not used in the thesis but all the

dissipation results are denoised.

3.7.3 Kolmogorov micro scale

The Kolmogorov micro scale is computed from dissipation:

$$\eta = \left(\frac{\nu^3}{< \overline{\epsilon'} >} \right)^{1/4} \tag{3.8}$$

This scale represents the smallest pulsation presents in the flow. Indeed, at this scale the dissipation is dominant so these pulsations dies out with viscosity.

3.7.4 Taylor length scale and Taylor Reynolds number

The following formulation of the Taylor micro-scale is used based on the available data:

$$\lambda = \sqrt{\frac{15\nu}{< \overline{\epsilon'} >}} \sqrt{\frac{< \overline{u_x'^2 + u_z'^2} >}{2}} \tag{3.9}$$

The value of the Taylor scale can vary significantly with the formulation choice. However, the variation from one configuration to the other should remain consistent whatever the formulation. The following formulation is also tested:

$$\widetilde{\lambda} = \sqrt{\frac{15\nu}{< \overline{\epsilon'} >}} \sqrt{\frac{< \overline{2u_x'^2 + u_z'^2} >}{3}} \tag{3.10}$$

This formulation overestimates the value by a close to constant proportion between 20% and 25% compared to 3.9. The plots collapse is nearly unchanged when this later estimate is used to non-dimensionalize r.

The Reynolds number based on the Taylor length is calculated:

$$Re_\lambda = \frac{\lambda \sqrt{< \overline{u_x'^2 + u_z'^2} >}}{\nu} \tag{3.11}$$

This number is used to quantify the turbulence development. The following formulation is also tested:

$$\widetilde{Re_\lambda} = \frac{\widetilde{\lambda} \sqrt{< \overline{2u_x'^2 + u_z'^2} >}}{\nu} \tag{3.12}$$

This formulation overestimates the value by a close to constant proportion between 45% and 55% compared to 3.11. This magnitude difference is significant but the main risk is to overestimate the Taylor Reynolds number. Therefore, the formulation with the smallest values is retained.

3.7.5 Rossby number

The Rossby non-dimensional number:

$$Ro = \frac{U_{turb}}{2\Omega L} \tag{3.13}$$

quantifies the rotation effect on turbulence. $\Omega = 2\pi F$ is the rotation speed. L is the integral scale which is estimated by the rotor radius ($L \approx R = 11.25cm$). U_{turb} is a characteristic turbulence velocity scale. The maximal fluctuating velocity is taken for U_{turb} following Baroud et al. 2002. There is no impact of the rotation if $Ro > 1$ and the flow is said rapidly rotating for $Ro << 1$. The Rossby number values are evaluated directly in chapters 4 and 5.

3.8 Error bars computations

For each configuration, $150,000$ velocity fields are recorded in time including around $50,000$ fully uncorrelated velocity field samples for convergence. Averaging over time is not sufficient for convergence and we therefore also apply averaging over space which greatly improves it. It corresponds to $150,000 \times 164 \times 78 \approx 1.9 \times 10^9$ points for one-point statistics where 164×78 is the number of points associated with the vector spacing. For two-point statistics, some spatial points are not available depending on the separation vector size and direction. For zero separation vector, $150,000 \times 164 \times 78 \approx 1.9 \times 10^9$ points are available for convergence but for the largest separation vector in r_x direction there are only $150,000 \times 164 \approx 2.4 \times 10^7$ points available and in r_z direction only $150,000 \times 78 \approx 1.2 \times 10^7$ are available.

The most important results in this paper are reported with error bars quantifying convergence and computed with a bootstrapping method.

The convergence quantification is a classical problem in turbulence and it is usually evaluated with the formula from Benedict and Gould 1996 for a 95% confidence interval:

$$\frac{\Delta \bar{f}}{\bar{f}} = \frac{2}{\sqrt{N}} \frac{\sigma_f}{\bar{f}} \tag{3.14}$$

where N is the number of independent samples.

Regarding the two-point quantities it is not as easy to estimate the convergence because the quantities are computed at different two-point separations r. Therefore, the number of independent points is difficult to estimate and depends on r. Moreover, there is a double averaging in time and in space which make things even more complicated. This is why a more direct and robust method is used to estimate the convergence: the bootstrapping method. This method gives more accurate results than formula 3.14 because it does not need to estimate the number of independent samples.

This method is based on the central limit theorem which states that 'irrespective of a

random variable's distribution if large enough samples are drawn from the population then the sampling distribution of the mean for that random variable will approximate a normal distribution.'

For each quantity and at every separation value r, 600 sub-groups are defined. Each sub-group contains 83 successive time steps with at least 167 spatial points. The spatial and temporal average of these sub-groups are computed and noted $(m_i(r))_{i\in[1:N]}$. According to the central limit theorem, $(m_i(r))_{i\in[1:N]}$ has a normal distribution. Therefore, a confidence interval can be easily defined for this distribution with 95% of reliability:

$$I_{95\%} = \left[\bar{m} - t_{95}\frac{\sigma_m}{\sqrt{N}}, \bar{m} + t_{95}\frac{\sigma_m}{\sqrt{N}}\right] \tag{3.15}$$

where $t_{95\%} = 1.96$, $\bar{m} = \lim_{N\to\infty} \frac{\sum_1^N m_i}{N}$ and $\sigma_m = \sqrt{\lim_{N\to\infty} \frac{\sum_1^N (m_i-\bar{m})^2}{N-1}}$

Only a standard deviation estimate of $(m_i(r))_{i\in[1:N]}$ is known because of the limited number of sub-groups. Therefore, following Neuilly and Fréjacques 1998, the following correction is used to be more accurate:

$$I_{95\%} = \left[\bar{m} - \left(1+\frac{t_{95}}{2N}\right) t_{95}\frac{Std((m_i(r))_{i\in[1:N]})}{\sqrt{N}}, \bar{m} + \left(1+\frac{t_{95}}{2N}\right) t_{95}\frac{Std((m_i(r))_{i\in[1:N]})}{\sqrt{N}}\right] \tag{3.16}$$

A test is carried out with a badly converged quantity to check the error bars reliability. The time derivative estimate is not used in this thesis but it can be evaluated from the dataset. This quantity can only be computed with $50,000$ different velocity fields out of $150,000$ because of the time differentiation. Therefore, this quantity is much less converged than others. This quantity should also converge to zero when averaged in time by definition. Therefore, it is a good test to check the error bars. The results are averaged both in time and in space. The results of several configurations including the less converged one are presented in figure 3.11. The error bars are small at small scales and increase with r. This is expected because there are more samples available at small r than at large r on the spatial domain. The error bars always include 0 (the expected value) even for the large deviations of the mean value. Therefore, the error bars are confirmed to be robust and to provide accurate uncertainty estimate.

The error bars of a third order quantity are then computed (an estimate of the energy interscale transfer rate) and are presented in figure 3.12. It is a third order quantity so it is very difficult to converge as its distribution law is highly non-Gaussian. The uncertainty estimated is non-negligible but acceptable to conclude on the shape and on the value when r is not too large. It confirms the good results convergence. For the most important results, the error bars are estimated in the results sections.

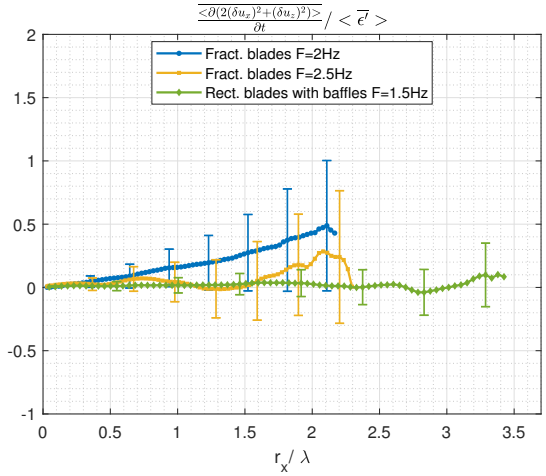

Figure 3.11: Error bars test for time derivative

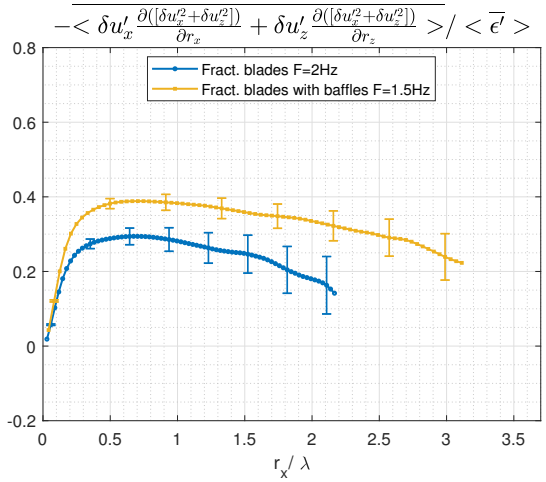

Figure 3.12: Error bars used for an estimate of interscale transfer rate

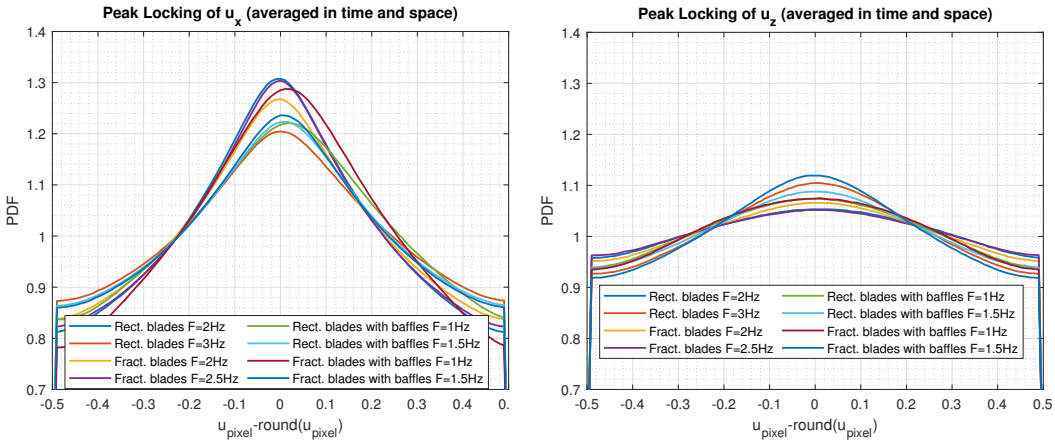

(a) u_x decimal part (b) u_z decimal part

Figure 3.13: Probability distribution function of the velocity components u_x and u_z decimal part

3.9 Peak-locking

When a particle is too small, its correlation peak position fit results are biased towards integer values. Therefore, the displacement between two images is more likely to be an integer number of pixels. This peak-locking error (as it is called, Raffel et al. 2018) is systematic (bias error) and is therefore visible on the velocity probability distribution functions (sine modulation) but does not usually impact first order mean quantities of turbulent flow if enough dynamic is used (here high dynamic is selected of about 5px for one standard deviation, see Christensen 2004). Peak-locking can be reduced by increasing particles diffraction spot using camera lens aperture F#. However, an increased F# reduces the brightness of the particles and therefore the number of visible particles. In this experiment, F#8 is used (diffraction spot of $1.4px$) as a compromise and some peak locking is still visible. The impact on the results is analyzed in this section.

3.9.1 Peak locking quantification

The experimental PIV measurements introduce a random error which respect a Gaussian distribution law. This distribution law has a zero mean and usually a standard deviation around 0.1 - 0.2 px (Raffel et al. 2018). It introduces also the peak locking systematic error as explained previously. This latter error can be quantified through the probability distribution function (PDF) of the particle displacement in pixel: $u_{pixel} - round(u_{pixel})$. A constant PDF means there is no peak locking. The results are presented in figure 3.13. Some peak-locking is observed in the results. This error is similar for all configurations and is more important in the x direction.

The peak locking error can be modeled as $-a.sin(2\pi(u_{true} - round(u_{true}))$ so that $u_{measured} = u_{true} - a.sin(2\pi(u_{true} - round(u_{true})) + \epsilon_{Gaussian}$, where $\epsilon_{Gaussian}$ is the random noise and u_{true} the true displacement with IW filtering effect. However, the peak locking can only be estimated in the measurements as $a.sin(2\pi(u_{measured} - round(u_{measured}))$ according to Cholemari 2007. The coefficient represents the peak-locking magnitude and it can be evaluated from experimental data using the previous approximation. A correction is added to the contaminated data until the PDF of the rounded part of the displacement is nearly flat. The coefficient a used for this correction gives a good estimate of the peak locking magnitude. For all configurations, the maximal value of a is estimated to be $0.02px$ which corresponds to a weak peak locking.

It means that the peak locking error order of magnitude is around 10 times smaller than the Gaussian PIV noise. However, this error does not necessarily disappear when averaged because it is a systematic error. This is why the consequences of this phenomenon on the results of this study are quantified.

3.9.2 Peak locking impact on spatial energy spectrums

The peak locking impact on spatial energy spectrums is evaluated by introducing artificial peak locking into Direct Numerical Simulations (DNS).

The DNS dataset was computed by Jean-Philippe Laval from LMFL. It is a $512 \times 512 \times 512$ pseudo-spectral periodic simulation with $Re_\lambda \approx 140$. The resolution is around 1.6η. The energy spectrum is computed directly from the simulation results and from the results affected by a modeled peak locking:

$$u_{peaklocking} = u_{simulation} - a \times sin(2\pi(u_{simulation} - round(u_{simulation})) \tag{3.17}$$

with $a = 0.02px$.

The results are presented in figure 3.14. The peak-locking does not have any consequence on the spatial energy spectrum except at the very high wavelengths where in reality it will be much more polluted by the PIV noise. Therefore, the experimental results can be used to compute energy spectrums without restrictions.

3.9.3 Peak-locking impact on two-point statistics

The peak locking impact on averaged two-point statistics is quantified by introducing a peak locking correction in the experimental data. Then, we evaluate the results evolution after the correction. The correction defined in Cholemari 2007 is used:

$$u_{corrected} = u_{measured} + a_{estimated} \times sin(2\pi(u_{measured} - round(u_{measured})) \tag{3.18}$$

where a is estimated for each configuration in x and y direction.

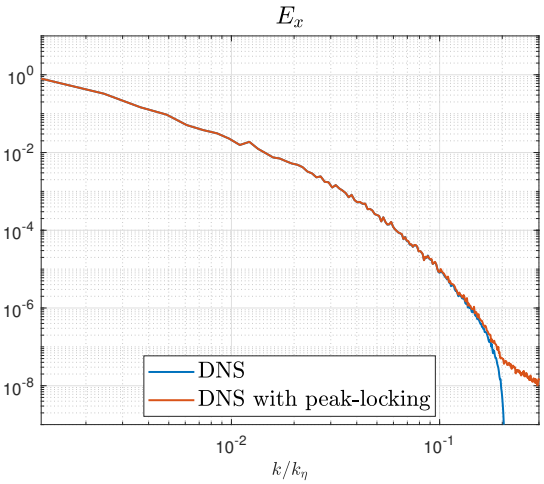

Figure 3.14: Peak locking impact on spatial energy spectrum from DNS.

The results are presented in figure 3.15. No difference is observed between the results with and without peak locking correction. Therefore, the experimental results can be used to compute two-point statistics without restrictions. The results presented in the report do not contain peak locking correction.

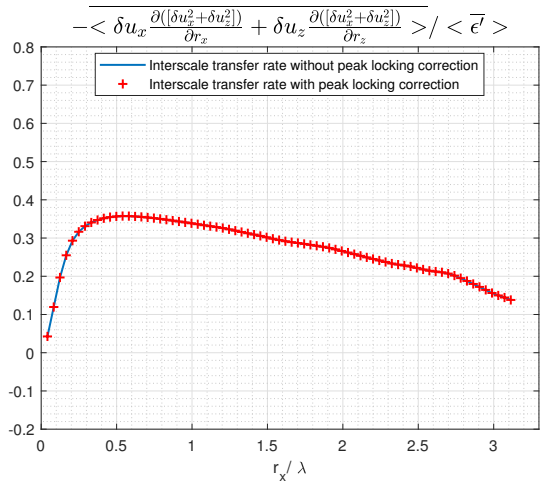

Figure 3.15: Peak-locking impact on an estimate of the interscale energy transfer rate

Chapter 4

Scale-by-scale non-equilibrium with Kolmogorov-like scalings in non-homogeneous stationary turbulence

Most of the material presented in this chapter is submitted as a publication in the Journal of Fluid Mechanics.

4.1 Introduction

The Kolmogorov 1941 theory of statistically homogeneous turbulence (see Frisch 1995, Pope 2000) predicts that the interscale transfer rate of turbulent kinetic energy is approximately balanced by the turbulence dissipation rate across a wide range of length scales in the inertial range as the Reynolds number tends to infinity. This prediction of scale-by-scale equilibrium holds for statistically stationary forced homogeneous turbulence (see Frisch 1995) but is also made for decaying homogeneous turbulence on the basis of a small-scale stationarity hypothesis (see Frisch 1995, Pope 2000 and section 2 of Chen and Vassilicos 2022). A widely held view is that the turbulence is always statistically homogeneous at small enough length-scales if the Reynolds number is large enough. But what if the Reynolds number, even if high, is not high enough for homogeneity to exist at the smallest scales? And if, in such circumstances, one finds simple scalings and scale-by-scale balances which appear independent of the details of the non-homogeneity, would these non-homogeneity laws survive as the Reynolds is taken to infinity? Or would they locally tend to Kolmogorov scale-by-scale equilibrium, in which case Kolmogorov scale-by-scale equilibrium would, in some sense, be an asymptotic case of

these non-homogeneity laws?

In this chapter we address statistically stationary non-homogeneous turbulence at moderate to high Reynolds numbers and we attempt to provide some partial answer to the first one of these questions: can simple scale-by-scale turbulence energy balances exist in non-homogeneous turbulence? The questions concerning the limit towards infinite Reynolds numbers cannot be answered at present and may, perhaps, never be answered unless one can some day answer them by rigorous mathematical analysis of the Navier-Stokes equations. The problem with claims made for Reynolds numbers tending to infinity is that one can always argue that the Reynolds number is not large enough if an experiment or simulation does not confirm the claims.

We chose to study the turbulent flow under the turbulence-generating rotating impellers in a baffled tank where the baffles break the full rotation of the flow. This is a flow where the turbulence is statistically stationary, where Taylor length-based Reynolds numbers up to 650 can be achieved, where different types of impeller can produce significantly different turbulent flows and where we can use a two-dimensional two-component (2D2C) Particle Image Velocimetry (PIV) that is highly resolved in space and capable to access estimates of turbulence dissipation rates as well as parts of various interscale and interspace turbulent transfer/transport rates. Only full three-dimensional three-component highly resolved PIV measurements can, in principle, access the turbulence dissipation and these transfer/transport rates in full, but such an approach is currently beyond our reach over the significant range of length scales needed to establish scale-by-scale energy balances. The truncated transfer/transport rates obtained by our 2D2C PIV do, nevertheless, exhibit interesting properties, in particular because they are concordant with a recent non-equilibrium theory of non-homogeneous turbulence (Chen and Vassilicos 2022) which we also further develop here.

In the following section we present the two-point scale-by-scale equations which form the basis of this study's theoretical framework. In section 4.3, we discuss interscale turbulent energy transfers and the special case of freely decaying statistically homogeneous turbulence as a point of reference. Section 4.4 presents the main 2D2C PIV measurements' results. We use our PIV measurements to assess two-point turbulence production in section 4.5 and linear transport terms (e.g. mean advection) in section 4.6. In section 4.7 we present intermediate similarity predictions and PIV measurements of second order structure functions of turbulent fluctuating velocities. Section 4.8 presents theoretical predictions of non-equilibrium small-scale turbulent energy budgets for non-homogeneous turbulence and related 2D2C PIV measurements. Finally, section 4.9 presents measurements and a theoretical discussion of elements of the large-scale turbulent energy budget, section 4.10 proposes a small-scale homogeneity hypothesis that is extended in a more theoretical way in appendix A.2 and we conclude about this chapter in section 4.11.

4.2 Theoretical framework based on two-point Navier-Stokes equations

Interscale turbulence transfers for incompressible turbulent flows can be studied in the presence of all other co-existing turbulence transfer/transport mechanisms in terms of two-point equations exactly derived from the incompressible Navier-Stokes equations (see Hill 2001, Hill 2002b and Germano 2007b) without any hypotheses or assumptions, in particular no assumptions of homogeneity or periodicity. In chapter 2, the small scale two-point equation 2.7 was introduced without Reynolds decomposition. Here a Reynolds decomposition is used: $\boldsymbol{\delta u} = \overline{\boldsymbol{\delta u}} + \boldsymbol{\delta u'}$, $\boldsymbol{u_X} = \overline{\boldsymbol{u_X}} + \boldsymbol{u_X}'$, $\delta p = \delta\overline{p} + \delta p'$ where the overline signifies an average over time. Under the assumption of statistical stationarity, this general two-point energy equation leads to the following pair of two-point energy equations:

$$\begin{aligned}&(\overline{\boldsymbol{u_X}}.\boldsymbol{\nabla_X} + \boldsymbol{\delta\overline{u}}.\boldsymbol{\nabla_r})\,\frac{1}{2}|\boldsymbol{\delta\overline{u}}|^2 + P_r + P^s_{Xr} + \frac{\partial}{\partial x_j}(\delta\overline{u_i}\overline{u'_{Xj}\delta u'_i}) + \frac{\partial}{\partial r_j}(\delta\overline{u_i}\overline{\delta u'_j\delta u'_i})\\ &= -\boldsymbol{\nabla_X}.(\boldsymbol{\delta\overline{u}}\delta\overline{p}) + \frac{\nu}{2}{\boldsymbol{\nabla_X}}^2\frac{1}{2}|\boldsymbol{\delta\overline{u}}|^2 + \frac{\nu}{2}{\boldsymbol{\nabla_r}}^2\frac{1}{2}|\boldsymbol{\delta\overline{u}}|^2 - \frac{\nu}{4}\frac{\partial\overline{u_i}^+}{\partial\zeta_k^+}\frac{\partial\overline{u_i}^+}{\partial\zeta_k^+} - \frac{\nu}{4}\frac{\partial\overline{u_i}^-}{\partial\zeta_k^-}\frac{\partial\overline{u_i}^-}{\partial\zeta_k^-}\end{aligned} \tag{4.1}$$

$$\begin{aligned}&(\overline{\boldsymbol{u_X}}.\boldsymbol{\nabla_X} + \boldsymbol{\delta\overline{u}}.\boldsymbol{\nabla_r})\,\frac{1}{2}\overline{|\boldsymbol{\delta u'}|^2} - P_r - P^s_{Xr} + \boldsymbol{\nabla_X}.\overline{(\boldsymbol{u_X}'\frac{1}{2}|\boldsymbol{\delta u'}|^2)} + \boldsymbol{\nabla_r}.\overline{(\boldsymbol{\delta u'}\frac{1}{2}|\boldsymbol{\delta u'}|^2)}\\ &= -\boldsymbol{\nabla_X}.\overline{(\boldsymbol{\delta u'}\delta p')} + \frac{\nu}{2}{\boldsymbol{\nabla_X}}^2\frac{1}{2}\overline{|\boldsymbol{\delta u'}|^2} + \frac{\nu}{2}{\boldsymbol{\nabla_r}}^2\frac{1}{2}\overline{|\boldsymbol{\delta u'}|^2} - \frac{\nu}{4}\overline{\frac{\partial u_i'^+}{\partial\zeta_k^+}\frac{\partial u_i'^+}{\partial\zeta_k^+}} - \frac{\nu}{4}\overline{\frac{\partial u_i'^-}{\partial\zeta_k^-}\frac{\partial u_i'^-}{\partial\zeta_k^-}}\end{aligned} \tag{4.2}$$

where $P_r = -\overline{\delta u'_j\delta u'_i}\frac{\partial\delta\overline{u_i}}{\partial r_j} = -\overline{\delta u'_j\delta u'_i}\frac{1}{2}[\Sigma_{ij}(\mathbf{X}+\mathbf{r})+\Sigma_{ij}(\mathbf{X}-\mathbf{r})]$ and $P^s_{Xr} = -\overline{u'_{Xj}\delta u'_i}\frac{\partial\delta\overline{u_i}}{\partial X_j}$, with $\Sigma_{ij} \equiv \frac{1}{2}(\frac{\partial\overline{u_i}}{\partial X_j} + \frac{\partial\overline{u_j}}{\partial X_i})$, are two-point turbulence production rates. Indeed, being proportional to mean flow gradient terms and to averages of products of fluctuating velocities, they represent linear turbulence fluctuation processes and they exchange energy between $|\boldsymbol{\delta\overline{u}}|^2$ and $\overline{|\boldsymbol{\delta u'}|^2}$ because they appear with opposite signs in equations (4.1) and (4.2) as already noted by Alves Portela, Papadakis, and Vassilicos 2017.

The two-point turbulence production terms P_r and P^s_{Xr} differ. P_r results from the product of the two-point small-scale Reynolds stress $\overline{\delta u'_j\delta u'_i}$ with the two-point half sum of mean strain rates $\frac{1}{2}(\Sigma_{ij}(\mathbf{X}+\mathbf{r}) + \Sigma_{ij}(\mathbf{X}-\mathbf{r}))$ both of which are symmetric in (i,j). On the other hand, P^s_{Xr} results from the product of non-symmetric small/large-scale correlation $\overline{u'_{Xj}\delta u'_i}$ with the two-point gradient $\frac{\partial\delta\overline{u_i}}{\partial X_j}$. To better set the context for the two-point turbulence production rate P^s_{Xr} one needs to consider the evolution equation for the two-point velocity half sum ${\boldsymbol{u_X}}^2(\boldsymbol{X},\boldsymbol{r},t)$.

This equation (2.8) was first obtained by Germano 2007b and was already introduced in chapter 2. A pair of Reynolds averaged two-point energy equations follows (using $p_X =$

$\overline{p_X} + p'_X$):

$$\begin{aligned}&(\overline{\boldsymbol{u}_{\boldsymbol{X}}}.\boldsymbol{\nabla}_{\boldsymbol{X}} + \boldsymbol{\delta}\overline{\boldsymbol{u}}.\boldsymbol{\nabla}_{\boldsymbol{r}})\,\frac{1}{2}|\overline{\boldsymbol{u}_{\boldsymbol{X}}}|^2 + P_X + P^l_{Xr} + \frac{\partial}{\partial x_j}(\overline{u_{Xi}}\,\overline{u'_{Xi}u'_{Xj}}) + \frac{\partial}{\partial r_j}(\overline{u_{Xi}}\,\overline{\delta u'_j u'_{Xi}}) \\ &= -\boldsymbol{\nabla}_{\boldsymbol{X}}.(\overline{\boldsymbol{u}_{\boldsymbol{X}}\,p_X}) + \frac{\nu}{2}\boldsymbol{\nabla}_{\boldsymbol{X}}{}^2\frac{1}{2}|\overline{\boldsymbol{u}_{\boldsymbol{X}}}|^2 + \frac{\nu}{2}\boldsymbol{\nabla}_{\boldsymbol{r}}{}^2\frac{1}{2}|\overline{\boldsymbol{u}_{\boldsymbol{X}}}|^2 - \frac{\nu}{4}\frac{\partial\overline{u_i}^+}{\partial\zeta_k^+}\frac{\partial\overline{u_i}^+}{\partial\zeta_k^+} - \frac{\nu}{4}\frac{\partial\overline{u_i}^-}{\partial\zeta_k^-}\frac{\partial\overline{u_i}^-}{\partial\zeta_k^-}\end{aligned} \tag{4.3}$$

$$\begin{aligned}&(\overline{\boldsymbol{u}_{\boldsymbol{X}}}.\boldsymbol{\nabla}_{\boldsymbol{X}} + \boldsymbol{\delta}\overline{\boldsymbol{u}}.\boldsymbol{\nabla}_{\boldsymbol{r}})\,\frac{1}{2}\overline{|\boldsymbol{u}'_{\boldsymbol{X}}|^2} - P_X - P^l_{Xr} + \boldsymbol{\nabla}_{\boldsymbol{X}}.(\overline{\boldsymbol{u}_{\boldsymbol{X}}{}'\frac{1}{2}|\boldsymbol{u}_{\boldsymbol{X}}{}'|^2}) + \boldsymbol{\nabla}_{\boldsymbol{r}}.(\overline{\boldsymbol{\delta u}'\frac{1}{2}|\boldsymbol{u}_{\boldsymbol{X}}{}'|^2}) \\ &= -\boldsymbol{\nabla}_{\boldsymbol{X}}.(\overline{\boldsymbol{u}_{\boldsymbol{X}}{}'p'_X}) + \frac{\nu}{2}\boldsymbol{\nabla}_{\boldsymbol{X}}{}^2\frac{1}{2}\overline{|\boldsymbol{u}'_{\boldsymbol{X}}|^2} + \frac{\nu}{2}\boldsymbol{\nabla}_{\boldsymbol{r}}{}^2\frac{1}{2}\overline{|\boldsymbol{u}'_{\boldsymbol{X}}|^2} - \frac{\nu}{4}\overline{\frac{\partial u_i'^+}{\partial\zeta_k^+}\frac{\partial u_i'^+}{\partial\zeta_k^+}} - \frac{\nu}{4}\overline{\frac{\partial u_i'^-}{\partial\zeta_k^-}\frac{\partial u_i'^-}{\partial\zeta_k^-}}\end{aligned} \tag{4.4}$$

where $P_X = -\overline{u'_{Xj}u'_{Xi}}\frac{\partial\overline{u_{Xi}}}{\partial X_j} = -\overline{u'_{Xj}u'_{Xi}}\frac{1}{2}[\Sigma_{ij}(\mathbf{X}+\mathbf{r}) + \Sigma_{ij}(\mathbf{X}-\mathbf{r})]$ and $P^l_{Xr} = -\overline{\delta u'_j u'_{Xi}}\frac{\partial\overline{u_i}}{\partial X_j}$. These two-point turbulence production rates represent linear turbulence fluctuation processes and an exchange of energy between $|\overline{\boldsymbol{u}_{\boldsymbol{X}}}|^2$ and $\overline{|\boldsymbol{u}'_{\boldsymbol{X}}|^2}$ because they appear with opposite signs in equations (4.3) and (4.4).

Once again, the two-point turbulence production terms P_X and P^l_{Xr} differ. P_X results from the product of the two-point large-scale Reynolds stress $\overline{u'_{Xj}u'_{Xi}}$ with the two-point half sum of mean strain rates $\frac{1}{2}(\Sigma_{ij}(\mathbf{X}+\mathbf{r}) + \Sigma_{ij}(\mathbf{X}-\mathbf{r}))$ both of which are symmetric in (i,j). This is similar to P_r except that the two-point Reynolds stress is now large-scale rather than small-scale because it is defined in terms of the fluctuating velocity half sum rather than half difference. On the other hand, P^l_{Xr} results from the product of non-symmetric small/large-scale correlation $\overline{u'_{Xi}\delta u'_j}$ with the two-point gradient $\frac{\partial\delta\overline{u_i}}{\partial X_j}$, which is similar to P^s_{Xr}. However, the sum of both, i.e. $P_{Xr} \equiv P^s_{Xr} + P^l_{Xr}$, results from the product of a symmetric small/large-scale correlation $\overline{u'_{Xi}\delta u'_j} + \overline{u'_{Xj}\delta u'_i}$ with $\frac{1}{2}[\Sigma_{ij}(\mathbf{X}+\mathbf{r}) - \Sigma_{ij}(\mathbf{X}-\mathbf{r})]$ and contributes to the linear transfer of energy by total production rate $P_X + P_r + P_{Xr}$ between $\frac{1}{2}|\overline{\boldsymbol{u}}^+|^2 + \frac{1}{2}|\overline{\boldsymbol{u}}^-|^2$ and $\frac{1}{2}\overline{|\boldsymbol{u}'^+|^2} + \frac{1}{2}\overline{|\boldsymbol{u}'^+|^2}$.

4.3 Interscale turbulent energy transfers

Besides two-point turbulent production terms, the two-point energy equations of the previous section involve important interscale and interspace transport terms. Germano 2007b interpreted his equations 2.6 and 2.8 in the context of large eddy simulations (LES). He showed that the term $(\boldsymbol{\delta u}.\boldsymbol{\nabla}_{\boldsymbol{r}})\,\boldsymbol{u}_{\boldsymbol{X}}$ in equation 2.6 can be interpreted as the gradient of a subgrid stress. This term gives rise to the term $\boldsymbol{\nabla}_{\boldsymbol{r}}.(\boldsymbol{\delta u}|\boldsymbol{u}_{\boldsymbol{X}}|^2)$ in equation 2.8 which is therefore an energy transfer rate between large-scale velocities (velocity half sum) and small-scale velocities (velocity half difference). Germano 2007b also derived the kinematic equation 2.9

previously introduced in chapter 2 and reminded here for ease of reading:

$$\boldsymbol{\nabla_r}.(\boldsymbol{\delta u}|\boldsymbol{u_X}|^2) + \boldsymbol{\nabla_r}.(\boldsymbol{\delta u}|\boldsymbol{\delta u}|^2) = 2\boldsymbol{\nabla_X}.(\boldsymbol{\delta u}(\boldsymbol{\delta u}\cdot\boldsymbol{u_X})) \tag{4.5}$$

This equation relates $\boldsymbol{\nabla_r}.(\boldsymbol{\delta u}|\boldsymbol{u_X}|^2)$ to $\boldsymbol{\nabla_r}.(\boldsymbol{\delta u}|\boldsymbol{\delta u}|^2)$ in equation 2.7 where $\boldsymbol{\nabla_r}.(\boldsymbol{\delta u}|\boldsymbol{\delta u}|^2)$ accounts for non-linear interscale energy transfer and the turbulence cascade, e.g. see Chen and Vassilicos 2022.

It must be stressed, however, that the term $\boldsymbol{\nabla_r}.(\boldsymbol{\delta u}|\boldsymbol{\delta u}|^2)$ in equation 2.7 does not only include non-linear interscale transfer responsible for the turbulence cascade, it also includes two-point turbulence production and interscale energy transfer by mean flow differences. Indeed, it gives rise in equation 4.2 to the two-point turbulence production rate P_r, to the linear average interscale turbulent energy transfer rate by mean flow differences $\boldsymbol{\delta\overline{u}}.\boldsymbol{\nabla_r}\overline{|\boldsymbol{\delta u'}|^2}$ and to the non-linear average interscale turbulent energy transfer rate $\boldsymbol{\nabla_r}.(\overline{\boldsymbol{\delta u'}|\boldsymbol{\delta u'}|^2})$ relating to the turbulence cascade. The other terms in the energy equation 4.2 arise from the pressure gradient, the viscous terms and the advection of small-scale velocity $\boldsymbol{\delta u}$ by the large-scale velocity $\boldsymbol{u_X}$ in equation 2.5. In particular, this advection term gives rise to P^s_{Xr} and to the interspace turbulent transport rate of smaller-scale turbulence energy, i.e. $\boldsymbol{\nabla_X}.(\overline{\boldsymbol{u_X}'|\boldsymbol{\delta u}'|^2})$.

Similar observations can be made for the large-scale energy equations 2.8 and 4.4 where $\boldsymbol{\nabla_r}.(\boldsymbol{\delta u}|\boldsymbol{u_X}|^2)$ in 2.8 gives rise in 4.4 to the two-point production rate P^l_{Xr} (not P_X), to the linear average turbulent energy transfer rate by mean flow differences $\boldsymbol{\delta\overline{u}}.\boldsymbol{\nabla_r}\overline{|\boldsymbol{u'_X}|^2}$ and to the fully non-linear average turbulent energy transfer rate $\boldsymbol{\nabla_r}.(\overline{\boldsymbol{\delta u'}|\boldsymbol{u'_X}|^2})$. The other terms in the energy equation 4.4 arise from the pressure gradient, the viscous terms and the self-advection of large-scale velocity $\boldsymbol{u_X}$ in equation 2.6. In particular, this self-advection term gives rise to P_X (not P^l_{Xr}) and to the interspace turbulent transport rate of larger-scale turbulence energy, i.e. $\boldsymbol{\nabla_X}.(\overline{\boldsymbol{u_X}'|\boldsymbol{u_X}'|^2})$

Returning to the two-point turbulence production terms, P_r and P^s_{Xr} appear in the small-scale energy equation 4.2 whereas P_X and P^l_{Xr} appear in the large-scale energy equation 4.4. All four terms vanish if the mean flow is homogeneous but P_r represents turbulence production by mean flow non-homogeneities at small scales whereas P_X represents turbulence production by mean flow non-homogeneities at large scales. It is worth noting that P_X tends to the usual one-point turbulence production rate $-\overline{u'_j u'_i}\Sigma_{ij}$ in the limit $\mathbf{r}\to\mathbf{0}$ ($\boldsymbol{u'}$ is the fluctuating turbulent velocity at one point) whereas P_r tends to zero in that limit. P^l_{Xr} and P^s_{Xr} also tend to zero in that limit but they represent turbulence production by mean flow non-homogeneities that is cross-scale as they involve correlations between the fluctuating velocity half differences and fluctuating velocity half sums. The hypothesis that large and small scales may be uncorrelated leads to the suggestion that P^l_{Xr} and P^s_{Xr} may be increasingly negligible for decreasing $|\mathbf{r}|$, as indeed found for P^s_{Xr} in the intermediate layer of fully developed turbulent channel flow by Apostolidis, Laval, and Vassilicos 2023.

Applying Reynolds averaging to the kinematic identity 4.5 we obtain

$$\begin{aligned}
&\boldsymbol{\nabla_r}.(\overline{\boldsymbol{\delta u}}|\overline{\boldsymbol{\delta u}}|^2) + \boldsymbol{\nabla_r}.(\overline{\boldsymbol{\delta u}}\overline{|\boldsymbol{\delta u'}|^2}) + \boldsymbol{\nabla_r}.(\overline{\boldsymbol{\delta u'}|\boldsymbol{\delta u'}|^2}) + 2\boldsymbol{\nabla_r}.(\overline{\boldsymbol{\delta u'}(\boldsymbol{\delta u'}\overline{\boldsymbol{\delta u}})}) \\
&+ \boldsymbol{\nabla_r}.(\overline{\boldsymbol{\delta u}}|\overline{\boldsymbol{u_X}}|^2) + \boldsymbol{\nabla_r}.(\overline{\boldsymbol{\delta u}}|\overline{\boldsymbol{u_X}'|^2}) + \boldsymbol{\nabla_r}.(\overline{\boldsymbol{\delta u'}|\boldsymbol{u_X}'|^2}) - 2P^l_{Xr} \\
&= 2\boldsymbol{\nabla_X}.(\overline{\boldsymbol{\delta u}}(\overline{\boldsymbol{\delta u}}.\overline{\boldsymbol{u_X}})) + 2\boldsymbol{\nabla_X}.(\overline{\overline{\boldsymbol{\delta u}}(\boldsymbol{\delta u'}.\boldsymbol{u'_X})}) \\
&+ 2\boldsymbol{\nabla_X}.(\overline{\boldsymbol{\delta u'}(\boldsymbol{\delta u'}.\boldsymbol{u'_X})}) + 2\boldsymbol{\nabla_X}.(\overline{\boldsymbol{\delta u'}(\overline{\boldsymbol{\delta u}}.\boldsymbol{u'_X})}) - 2P_r
\end{aligned} \tag{4.6}$$

which demonstrates that, in general, the average interscale turbulent energy transfer rate $\boldsymbol{\nabla_r}.(\overline{\boldsymbol{\delta u'}|\boldsymbol{\delta u'}|^2})$ reflecting the turbulence cascade does not trivially relate with the average turbulent energy transfer $\boldsymbol{\nabla_r}.(\overline{\boldsymbol{\delta u'}|\boldsymbol{u_X}'|^2})$ reflecting work by subgrid stresses (see Germano 2007b).

A notable exception is statistically homogeneous turbulence where $\overline{\boldsymbol{\delta u}} = \mathbf{0}$, $P_r = 0$, $P^l_{Xr} = 0$ and derivatives with respect to $\mathbf{X}$ of third order fluctuating velocity statistics such as $\boldsymbol{\nabla_X}.(\overline{\boldsymbol{\delta u'}(\boldsymbol{\delta u'}.\boldsymbol{u'_X})}$ vanish (we cannot assume that $\overline{\boldsymbol{u_X}}.\boldsymbol{\nabla_X}\overline{|\boldsymbol{\delta u'}|^2}$ vanishes), in which case 4.6 reduces to

$$\boldsymbol{\nabla_r}.\overline{\boldsymbol{\delta u'}|\boldsymbol{u'_X}|^2} = -\boldsymbol{\nabla_r}.\overline{\boldsymbol{\delta u'}|\boldsymbol{\delta u'}|^2}. \tag{4.7}$$

Under such statistical homogeneity conditions (note that the terms involving pressure fluctuations in equations 4.2 and 4.4 are derivatives with respect to $\mathbf{X}$ of third order fluctuating velocity statistics given the Poisson equation relating pressure and velocities), and by considering scales $|\mathbf{r}|$ large enough to neglect viscous diffusion, fluctuating energy equations 4.2 and 4.4 become, respectively,

$$\overline{\boldsymbol{u_X}}.\boldsymbol{\nabla_X}\overline{|\boldsymbol{\delta u'}|^2} + \boldsymbol{\nabla_r}.(\overline{\boldsymbol{\delta u'}|\boldsymbol{\delta u'}|^2}) \approx -\overline{\epsilon'} \tag{4.8}$$

and

$$\overline{\boldsymbol{u_X}}.\boldsymbol{\nabla_X}\overline{|\boldsymbol{u'_X}|^2} + \boldsymbol{\nabla_r}.(\overline{\boldsymbol{\delta u'}|\boldsymbol{u_X}'|^2}) \approx -\overline{\epsilon'} \tag{4.9}$$

where $\overline{\epsilon'}$ is the average turbulence dissipation rate. Kolmogorov's small-scale stationarity hypothesis adapted to these equations states that $\overline{\boldsymbol{u_X}}.\boldsymbol{\nabla_X}\overline{|\boldsymbol{\delta u'}|^2}$ is much smaller in magnitude than $\overline{\epsilon'}$ at small enough scales $|\mathbf{r}|$. With this hypothesis it follows that

$$\boldsymbol{\nabla_r}.\overline{\boldsymbol{\delta u'}|\boldsymbol{\delta u'}|^2} \approx -\overline{\epsilon'}, \tag{4.10}$$

$$\boldsymbol{\nabla_r}.\overline{\boldsymbol{\delta u'}|\boldsymbol{u'_X}|^2} \approx \overline{\epsilon'} \tag{4.11}$$

and

$$\overline{\boldsymbol{u_X}}.\boldsymbol{\nabla_X}\overline{|\boldsymbol{u'_X}|^2} \approx -2\overline{\epsilon'} \tag{4.12}$$

in an intermediate range of scales large enough to neglect viscous diffusion and small enough to neglect small-scale non-stationarity. Relation 4.10 is Kolmogorov's scale-by-scale equilibrium and relation 4.11 was first derived by Germano 2007b. (Hosokawa 2007 assumed isotropy

and derived the equivalent of 4.11 for homogeneous isotropic turbulence).

Turbulence is rarely homogeneous. Therefore, the natural question to ask is whether energy transfer balances which may be different from but nevertheless in the same spirit as 4.10 and 4.11 exist in non-homogeneous turbulence. And if they do, how different are they and what determines the difference?

Various different classes of non-homogeneity exist. Apostolidis, Laval, and Vassilicos 2023 developed a scale-by-scale turbulent kinetic energy balance theory for the intermediate layer of fully developed turbulent channel flow where interspace turbulent transport rate and two-point pressure-velocity transport are negligible but small-scale production is not. A theory of scale-by-scale turbulent kinetic energy for non-homogeneous turbulence was recently proposed by Chen and Vassilicos 2022 who's approach allowed them to treat equation 4.2 when small-scale interspace turbulent transport and spatial gradients of two-point pressure-velocity correlations are not negligible. In the present chapter we study the turbulent flow under the rotating blades in a baffled container (mixer) where the baffles break the rotation in the flow and enhance turbulence. We start by assessing two-point production to determine whether we need to take it into account when applying the theory of Chen and Vassilicos 2022 to equation 4.2. Even if P_r and P^s_{Xr} are negligible, large-scale two-point production is necessarily present at some scales if one-point production is present in the flow.

In the following section we present the main experimental measurements' results which we use in subsequent sections to estimate various terms in equations 4.2 and 4.4.

4.4 Experimental measurements

The experimental measurements are presented in detail in chapter 3. Only the baffle configurations results are used in this chapter.

Defining parameters

The defining parameters of the experiment are presented in table 4.1. The rotation frequency F is either 1Hz or 1.5Hz. The global Reynolds number is $Re = \frac{2\pi F R^2}{\nu}$. where $R = D/2 \approx 11.25cm$ is an estimate of the rotor radius. Re is large, higher than 8.10^4, and the flow is therefore turbulent.

The Rossby number is estimated as defined in section 3.7.5. Our values of Ro range between 10^{-1} and 1 and are therefore intermediate between fast rotating and non-rotating turbulence. However, the rotor rotation speed Ω is not representative of flow rotation because the baffles break the flow rotation as explained in Nagata 1975. Therefore, the Rossby number is probably severely underestimated and the rotation is not expected to affect significantly the turbulence behavior in our experiment.

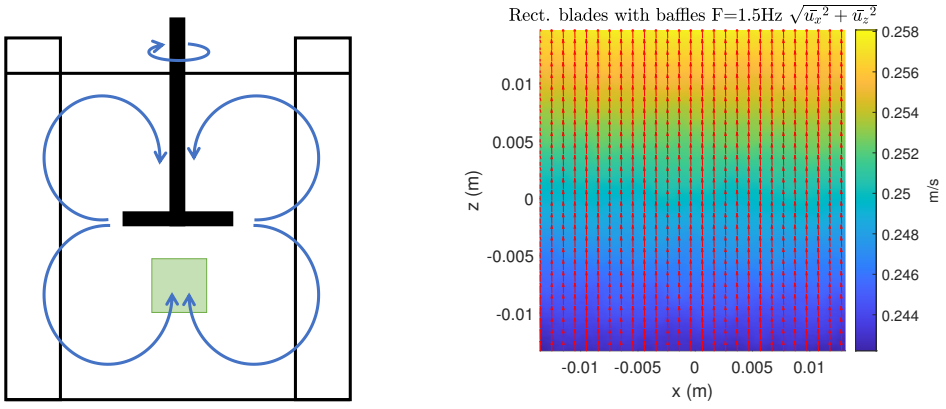

(a) (b)

Figure 4.1: (a): Schematic of mean flow in a mixer with baffles (Nagata 1975). (b): Mean flow measurement within the measurement plane shown as a green square in (a).

Basic turbulent flow properties

The main turbulent parameters are presented in table 4.2. They include the turbulence dissipation rate $\langle\overline{\epsilon'}\rangle$ averaged over time (overbar) and over space in our field of view (brackets), the resulting Kolmogorov length-scale η (computed with $\langle\overline{\epsilon'}\rangle$) and the Taylor length λ. These parameters are provided as reference and are used in the chapter to non-dimensionalise results.

The Taylor length-based Reynolds number Re_λ (see discussion on its estimation in chapter 3) is larger than 480 in all four configurations. All the four flows that we study are therefore highly turbulent.

In figure 4.1b we plot the mean flow velocity for one of our four configurations but the plot is representative of all four configurations. The mean flow velocity is oriented vertically from bottom to top and is not negligible in magnitude. Within our field of view, it is horizontaly uniform and accelerates by about 7% from bottom to top. These observations are consistent with the overall mean flow structure identified by Nagata 1975 and shown in figure 4.1a.

	$F(Hz)$	Re	vel rms (m/s)	Ro	Mean torque (N.m)
Rectangular blades with baffles	1	9.8×10^4	1.0×10^{-1}	3.6×10^{-1}	5.3×10^{-1}
Rectangular blades with baffles	1.5	1.3×10^5	1.6×10^{-1}	4.0×10^{-1}	1.1
Fractal blades with baffles	1	8.6×10^4	9.1×10^{-2}	3.2×10^{-1}	4.1×10^{-1}
Fractal blades with baffles	1.5	1.2×10^5	1.4×10^{-1}	3.4×10^{-1}	8.1×10^{-1}

Table 4.1: Main parameters of the experiment: vel rms (m/s) stands for $\sqrt{\overline{< u_x'^2 >} + \overline{< u_z'^2 >}}$

	$F(Hz)$	$\langle\overline{\epsilon'}\rangle$ (m^2/s^3)	$\eta(m)$	$\lambda(m)$	Re_λ
Rectangular blades with baffles	1	3.6×10^{-3}	1.1×10^{-4}	4.1×10^{-3}	5.1×10^2
Rectangular blades with baffles	1.5	1.2×10^{-2}	8.8×10^{-5}	3.7×10^{-3}	6.5×10^2
Fractal blades with baffles	1	2.4×10^{-3}	1.3×10^{-4}	4.9×10^{-3}	4.8×10^2
Fractal blades with baffles	1.5	8.2×10^{-3}	1.0×10^{-4}	4.1×10^{-3}	5.8×10^2

Table 4.2: Main turbulence parameters. The Kolmogorov length scale is calculated as $\eta = (\nu^3/\langle\overline{\epsilon'}\rangle)^{1/4}$. The Taylor length and the Reynolds number Re_λ are calculated as in chapter 3.

2D2C truncations and estimates of 3D3C statistics

The various terms in the equations of the previous sections require three-component (3C) velocity fields in three-dimensional (3D) space to be calculated. However, our measurements are performed with 2D2C PIV. We can therefore only calculate 2D2C truncations of 3D3C statistics and in a few cases (section 4.5 and section 4.6) we estimate 2D2C surrogates of 3D3C terms.

4.5 Two-point turbulence production rates

We start our data analysis with an assessment of two-point turbulence production rates. We define our coordinate system such that components $i = 1$, $i = 2$ and $i = 3$ correspond to the x, y and z directions respectively and therefore $(r_1, r_2, r_3) = (r_x, r_y, r_z)$ and $(X_1, X_2, X_3) = (X_x, X_y, X_z)$. The sums defining $P_r = -\overline{\delta u'_j \delta u'_i}\frac{\partial \overline{\delta u_i}}{\partial r_j}$, $P^s_{Xr} = -\overline{u'_{Xj}\delta u'_i}\frac{\partial \overline{\delta u_i}}{\partial X_j}$, $P_X = -\overline{u'_{Xj}u'_{Xi}}\frac{\partial \overline{u_{Xi}}}{\partial X_j}$ and $P^l_{Xr} = -\overline{\delta u'_j u'_{Xi}}\frac{\partial \overline{\delta u_i}}{\partial X_j}$ are sums of nine terms of which our 2D2C PIV has access to four. Our data therefore allow only truncations to be calculated directly and we start with the truncation of P_r:

$$\widetilde{P_r} = -\overline{\delta u'_x \delta u'_x}\frac{\partial \overline{\delta u_x}}{\partial r_x} - \overline{\delta u'_x \delta u'_z}\frac{\partial \overline{\delta u_z}}{\partial r_x} - \overline{\delta u'_z \delta u'_x}\frac{\partial \overline{\delta u_x}}{\partial r_z} - \overline{\delta u'_z \delta u'_z}\frac{\partial \overline{\delta u_z}}{\partial r_z} \tag{4.13}$$

with $\overline{\delta u'_y \delta u'_y}\frac{\partial \overline{\delta u_y}}{\partial r_y} + \overline{\delta u'_x \delta u'_y}\frac{\partial \overline{\delta u_y}}{\partial r_x} + \overline{\delta u'_x \delta u'_y}\frac{\partial \overline{\delta u_x}}{\partial r_y} + \overline{\delta u'_z \delta u'_y}\frac{\partial \overline{\delta u_y}}{\partial r_z} + \overline{\delta u'_z \delta u'_y}\frac{\partial \overline{\delta u_z}}{\partial r_y}$ being the difference between $\widetilde{P_r}$ and P_r. We know from our measurements and from Nagata 1975 that the mean flow is vertical in our field of view which is small and very close to the centreline of the tank. Hence, we can readily neglect all the terms making the difference between $\widetilde{P_r}$ and P_r except $\overline{\delta u'_z \delta u'_y}\frac{\partial \overline{\delta u_z}}{\partial r_y}$. Making the assumption that $\overline{\delta u'_z \delta u'_y}\frac{\partial \overline{\delta u_z}}{\partial r_y} \approx \overline{\delta u'_z \delta u'_x}\frac{\partial \overline{\delta u_z}}{\partial r_x}$ we form the following surrogate estimate of P_r:

$$\widetilde{\widetilde{P_r}} = -\overline{\delta u'_x \delta u'_x}\frac{\partial \overline{\delta u_x}}{\partial r_x} - 2\overline{\delta u'_x \delta u'_z}\frac{\partial \overline{\delta u_z}}{\partial r_x} - \overline{\delta u'_z \delta u'_x}\frac{\partial \overline{\delta u_x}}{\partial r_z} - \overline{\delta u'_z \delta u'_z}\frac{\partial \overline{\delta u_z}}{\partial r_z}. \tag{4.14}$$

Similarly, we have the following truncations and surrogate estimates for the other three two-point turbulence production rates:

$$\widetilde{P^s_{Xr}} = -\overline{u'_{Xx}\delta u'_x}\frac{\partial\overline{\delta u_x}}{\partial X_x} - \overline{u'_{Xx}\delta u'_z}\frac{\partial\overline{\delta u_z}}{\partial X_x} - \overline{u'_{Xz}\delta u'_x}\frac{\partial\overline{\delta u_x}}{\partial X_z} - \overline{u'_{Xz}\delta u'_z}\frac{\partial\overline{\delta u_z}}{\partial X_z} \tag{4.15}$$

and

$$\widetilde{\widetilde{P^s_{Xr}}} = -\overline{u'_{Xx}\delta u'_x}\frac{\partial\overline{\delta u_x}}{\partial X_x} - 2\overline{u'_{Xx}\delta u'_z}\frac{\partial\overline{\delta u_z}}{\partial X_x} - \overline{u'_{Xz}\delta u'_x}\frac{\partial\overline{\delta u_x}}{\partial X_z} - \overline{u'_{Xz}\delta u'_z}\frac{\partial\overline{\delta u_z}}{\partial X_z}; \tag{4.16}$$

$$\widetilde{P_X} = -\overline{u'_{Xx}u'_{Xx}}\frac{\partial\overline{u_{Xx}}}{\partial X_x} - \overline{u'_{Xx}u'_{Xz}}\frac{\partial\overline{u_{Xz}}}{\partial X_x} - \overline{u'_{Xz}u'_{Xx}}\frac{\partial\overline{u_{Xx}}}{\partial X_z} - \overline{u'_{Xz}u'_{Xz}}\frac{\partial\overline{u_{Xz}}}{\partial X_z} \tag{4.17}$$

and

$$\widetilde{\widetilde{P_X}} = -\overline{u'_{Xx}u'_{Xx}}\frac{\partial\overline{u_{Xx}}}{\partial X_x} - 2\overline{u'_{Xx}u'_{Xz}}\frac{\partial\overline{u_{Xz}}}{\partial X_x} - \overline{u'_{Xz}u'_{Xx}}\frac{\partial\overline{u_{Xx}}}{\partial X_z} - \overline{u'_{Xz}u'_{Xz}}\frac{\partial\overline{u_{Xz}}}{\partial X_z}; \tag{4.18}$$

$$\widetilde{P^l_{Xr}} = -\overline{\delta u'_x u'_{Xx}}\frac{\partial\overline{\delta u_x}}{\partial r_x} - \overline{\delta u'_x u'_{Xz}}\frac{\partial\overline{\delta u_z}}{\partial r_x} - \overline{\delta u'_z u'_{Xx}}\frac{\partial\overline{\delta u_x}}{\partial r_z} - \overline{\delta u'_z u'_{Xz}}\frac{\partial\overline{\delta u_z}}{\partial r_z} \tag{4.19}$$

and

$$\widetilde{\widetilde{P^l_{Xr}}} = -\overline{\delta u'_x u'_{Xx}}\frac{\partial\overline{\delta u_x}}{\partial r_x} - 2\overline{\delta u'_x u'_{Xz}}\frac{\partial\overline{\delta u_z}}{\partial r_x} - \overline{\delta u'_z u'_{Xx}}\frac{\partial\overline{\delta u_x}}{\partial r_z} - \overline{\delta u'_z u'_{Xz}}\frac{\partial\overline{\delta u_z}}{\partial r_z}. \tag{4.20}$$

We calculate space averages over the field of view of the four truncated and the four surrogate two-point production rates in the eight equations above. In figures 4.2, 4.3, 4.4 and 4.5 we plot, versus $r_1 \equiv r_x$ and $r_3 \equiv r_z$, the four average surrogate two-point production rates $\langle\widetilde{\widetilde{P_r}}\rangle$, $\langle\widetilde{\widetilde{P^l_{Xr}}}\rangle$, $\langle\widetilde{\widetilde{P_X}}\rangle$ and $\langle\widetilde{\widetilde{P^l_{Xr}}}\rangle$ where the brackets signify space-averaging. We plot them normalised by $\frac{\langle\overline{\epsilon'}\rangle}{2}$ where $\epsilon' \equiv \nu\frac{\partial u'_i}{\partial\zeta_j}\frac{\partial u'_i}{\partial\zeta_j}$ is estimated on the basis of our 2D2C PIV data using its axisymmetric formulation (see chapter 2 where we also report that we did not find very significant differences in the values of $\langle\overline{\epsilon'}\rangle$ calculated either on the basis of small-scale axisymmetry or on the basis of small-scale isotropy). $\frac{\langle\overline{\epsilon'}\rangle}{2}$ is used to non-dimensionalize results instead of $\langle\overline{\epsilon'}\rangle$ because the turbulence dissipation term in equation 4.2, once averaged in space, is $< \frac{\nu}{4}\overline{\frac{\partial u'^+_i}{\partial\zeta^+_k}\frac{\partial u'^+_i}{\partial\zeta^+_k}} + \frac{\nu}{4}\overline{\frac{\partial u'^-_i}{\partial\zeta^-_k}\frac{\partial u'^-_i}{\partial\zeta^-_k}} > \approx \frac{1}{2} < \epsilon' >$.

In the plots in figures 4.2 and 4.3, $\langle\widetilde{\widetilde{P_r}}\rangle$ is relatively small and $\langle\widetilde{\widetilde{P^s_{Xr}}}\rangle$ is negligible, irrespective of experimental configuration, for most values of r_x and r_z that our field of view allows us to access. Plots, not shown here for economy of space, of the corresponding truncations $\langle\widetilde{P_r}\rangle$ and $\langle\widetilde{P^s_{Xr}}\rangle$ are very similar. The largest absolute values of $\langle\widetilde{\widetilde{P_r}}\rangle$ are obtained at relatively large scales $r_z = 5\lambda \approx R/5$ with values around $0.15\frac{\langle\overline{\epsilon'}\rangle}{2}$ which is not negligible but still relatively small. These values decrease with decreasing two-point separation lengths as $\langle\widetilde{\widetilde{P_r}}\rangle$ tends to zero when $\boldsymbol{r}$ tends to zero. Furthermore, the increase of $\langle\widetilde{\widetilde{P_r}}\rangle$ with increasing two-point

separation is also much smaller than the increase of two-point turbulence production in the intermediate layer of fully developed turbulent channel flow found by Apostolidis, Laval, and Vassilicos 2023.

We are therefore encouraged to hypothesise that two-point turbulence production by mean flow non-homogeneities at small scales and cross-scale two-point turbulence production are negligible in the small-scale energy equation 4.2 for the present turbulent flows.

Looking at figure 4.5, we can equally hypothesise that cross-scale two-point production is also negligible in the large-scale energy equation 4.4, and a similar conclusion arises from respective plots of the average surrogate $\langle \widetilde{P^l_{Xr}} \rangle$ (not shown given the very close resemblance with figure 4.5). However, unlike $\langle \widetilde{\widetilde{P_r}} \rangle$, $\langle \widetilde{P_r} \rangle$, $\langle \widetilde{\widetilde{P^l_{Xr}}} \rangle$, $\langle \widetilde{P^l_{Xr}} \rangle$, $\langle \widetilde{\widetilde{P^l_{Xr}}} \rangle$ and $\langle \widetilde{P^l_{Xr}} \rangle$ which are all close to zero over a wide range of scales r_x and r_z for all four experimental configurations, $\langle \widetilde{\widetilde{P_X}} \rangle$ and $\langle \widetilde{P_X} \rangle$ do not decrease towards 0 with decreasing two-point separation and can even be comparable to $\frac{\langle \overline{\epsilon'} \rangle}{2}$ at the very smallest separations.

Figure 4.4 shows this clearly for $\langle \widetilde{\widetilde{P_X}} \rangle$ and the corresponding plots (not shown here) for $\langle \widetilde{P_X} \rangle$ are qualitatively similar but with different quantitative values. In particular, $\langle \widetilde{\widetilde{P_X}} \rangle$ and $\langle \widetilde{P_X} \rangle$ do not tend to zero as $\mathbf{r}$ tends to 0 in agreement with the point made in section 4.2 that P_X tends to $-\overline{u'_j u'_i}\Sigma_{ij}$ in the limit $\mathbf{r} \to \mathbf{0}$ and therefore does not tend to zero if there is non-vanishing one-point turbulence production present in the flow. However, the ratios $2\langle \widetilde{\widetilde{P_X}} \rangle / \langle \overline{\epsilon'} \rangle$ and $2\langle \widetilde{P_X} \rangle / \langle \overline{\epsilon'} \rangle$ differ between configurations, and in particular for different types of blade, suggesting that there are non-homogeneity differences between the four configurations considered here. In spite of these differences, $\langle \widetilde{\widetilde{P_X}} \rangle$ and $\langle \widetilde{P_X} \rangle$ are typically negative in all configurations suggesting that energy is transferred from the fluctuations to the mean.

Overall, our data support the hypothesis that, for the turbulent flows considered here and for scales small enough compared to the flow's large scales, two-point production may be neglected in the small-scale energy equation 4.2 even if P_X cannot be neglected in the large-scale energy equation 4.4. This is not a trivial hypothesis because P_r was found by Apostolidis, Laval, and Vassilicos 2023 not to be negligible at scales comparable to and larger than the Taylor length in the intermediate layer of fully developed turbulent channel flow where the turbulence is also non-homogeneous.

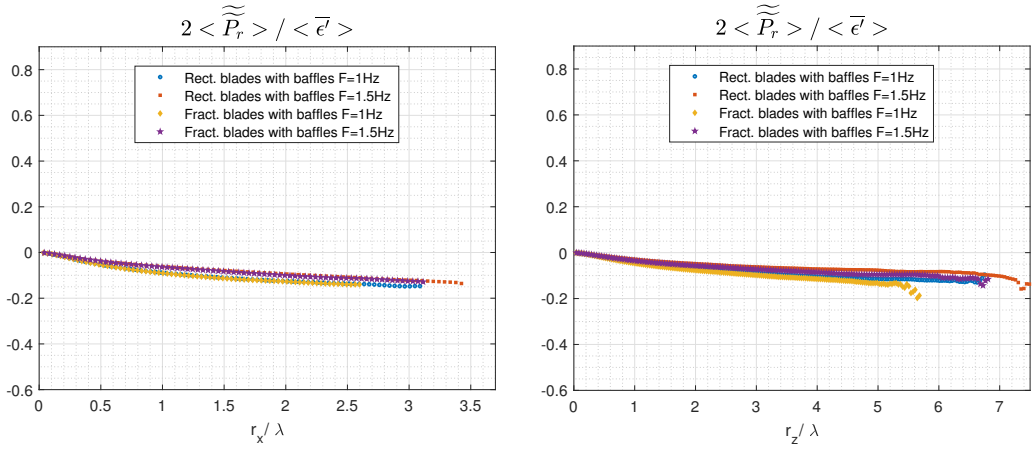

(a) r_x direction (b) r_z direction

Figure 4.2: Production surrogate defined in equation 4.14 along two radial directions

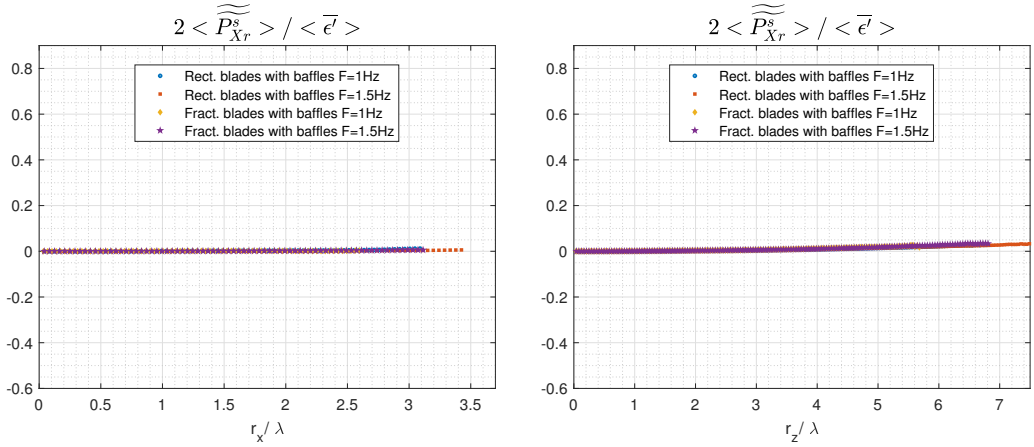

(a) r_x direction (b) r_z direction

Figure 4.3: Production surrogate defined in equation 4.16 along two radial directions

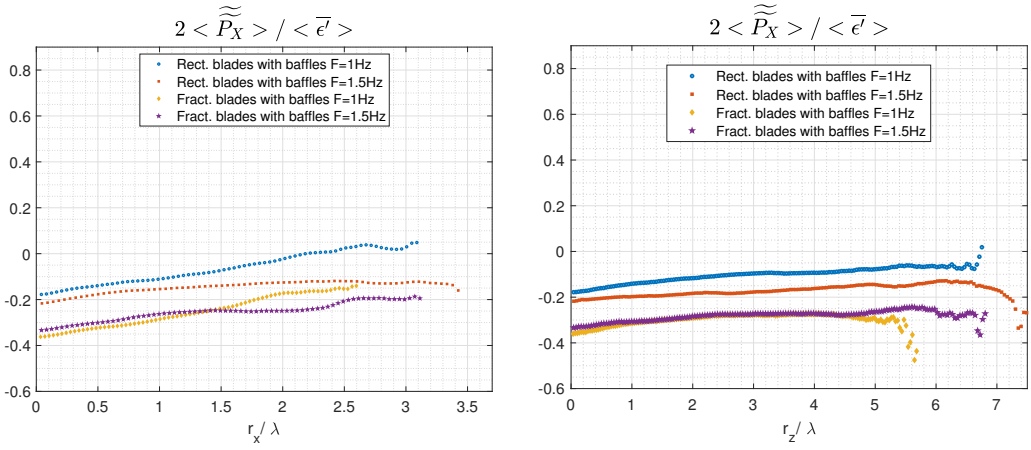

(a) r_x direction (b) r_z direction

Figure 4.4: Production surrogate defined in equation 4.18 along two radial directions

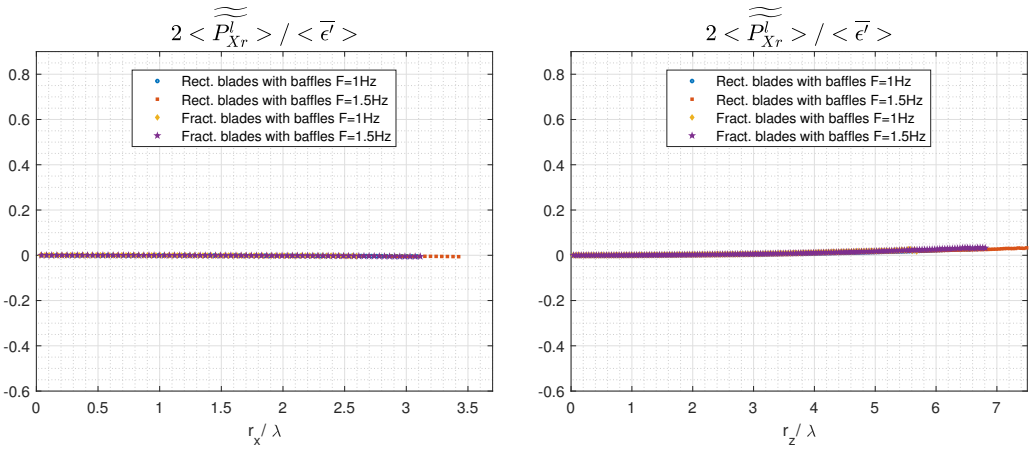

(a) r_x direction (b) r_z direction

Figure 4.5: Production surrogate defined in equation 4.20 along two radial directions

4.6 Small scale linear transport terms

Given the previous section's conclusion which encourages us to neglect two-point production in the small-scale energy equation 4.2 but not in the large-scale energy equation 4.4, we now focus on equation 4.2 and ask whether we can justify simplifying it further by neglecting the linear transport rate $(\overline{\boldsymbol{u_X}}.\boldsymbol{\nabla_X} + \boldsymbol{\delta\overline{u}}.\boldsymbol{\nabla_r})\,\frac{1}{2}\overline{|\boldsymbol{\delta u'}|^2}$. Once again, with our 2D2C PIV data, we can only consider a truncation and a surrogate estimate. The truncation is $\left(\overline{u_{Xx}}\frac{\partial}{\partial X_x} + \overline{u_{Xz}}\frac{\partial}{\partial X_z} + \delta\overline{u_x}\frac{\partial}{\partial r_x} + \delta\overline{u_z}\frac{\partial}{\partial r_z}\right)\frac{1}{2}\left(\overline{\delta u_x'^2 + \delta u_z'^2}\right)$ and the surrogate estimate is obtained by making the assumptions $\overline{\delta u_x'^2} = \overline{\delta u_y'^2}$, $\overline{u_{Xx}}\frac{\partial}{\partial X_x}\frac{1}{2}\overline{|\boldsymbol{\delta u'}|^2} = \overline{u_{Xy}}\frac{\partial}{\partial X_y}\frac{1}{2}\overline{|\boldsymbol{\delta u'}|^2}$ and $\delta\overline{u_x}\frac{\partial}{\partial r_x}\frac{1}{2}\overline{|\boldsymbol{\delta u'}|^2} = \delta\overline{u_y}\frac{\partial}{\partial r_y}\frac{1}{2}\overline{|\boldsymbol{\delta u'}|^2}$. Our surrogate estimate of $(\overline{\boldsymbol{u_X}}.\boldsymbol{\nabla_X} + \boldsymbol{\delta\overline{u}}.\boldsymbol{\nabla_r})\,\frac{1}{2}\overline{|\boldsymbol{\delta u'}|^2}$ is therefore $\left(2\overline{u_{Xx}}\frac{\partial}{\partial X_x} + \overline{u_{Xz}}\frac{\partial}{\partial X_z} + 2\delta\overline{u_x}\frac{\partial}{\partial r_x} + \delta\overline{u_z}\frac{\partial}{\partial r_z}\right)\frac{1}{2}\left(\overline{2\delta u_x'^2 + \delta u_z'^2}\right)$.

We calculate space-averages of the truncation and the surrogate estimate in two parts: i.e. $\langle\left(\overline{u_{Xx}}\frac{\partial}{\partial X_x} + \overline{u_{Xz}}\frac{\partial}{\partial X_z}\right)\frac{1}{2}\left(\overline{\delta u_x'^2 + \delta u_z'^2}\right)\rangle$ and $\langle\left(\delta\overline{u_x}\frac{\partial}{\partial r_x} + \delta\overline{u_z}\frac{\partial}{\partial r_z}\right)\frac{1}{2}\left(\overline{\delta u_x'^2 + \delta u_z'^2}\right)\rangle$ for the truncation, and for the surrogate estimate $\langle\left(2\overline{u_{Xx}}\frac{\partial}{\partial X_x} + \overline{u_{Xz}}\frac{\partial}{\partial X_z}\right)\frac{1}{2}\left(\overline{2\delta u_x'^2 + \delta u_z'^2}\right)\rangle$ and $\langle\left(2\delta\overline{u_x}\frac{\partial}{\partial r_x} + \delta\overline{u_z}\frac{\partial}{\partial r_z}\right)\frac{1}{2}\left(\overline{2\delta u_x'^2 + \delta u_z'^2}\right)\rangle$. Both parts of the space-average truncation and of the space-average surrogate are relatively small compared to $\langle\overline{\epsilon'}\rangle/2$ over a significant range of scales in all four configurations, increasing slowly in magnitude with increasing $|\boldsymbol{r}|$ and reaching at $r_z = 6.8\lambda \approx 0.3R$ a value of $0.23\langle\overline{\epsilon'}\rangle/2$ for the conservative surrogate estimate and of $0.14\langle\overline{\epsilon'}\rangle/2$ for the truncation. In figures 4.6a, 4.6b, 4.7a and 4.7b we plot the two space-average surrogate parts normalised by $\langle\overline{\epsilon'}\rangle/2$ versus r_x and r_z.

There are therefore grounds to support the additional hypothesis that $(\overline{\boldsymbol{u_X}}.\boldsymbol{\nabla_X} + \boldsymbol{\delta\overline{u}}.\boldsymbol{\nabla_r})\,\frac{1}{2}\overline{|\boldsymbol{\delta u'}|^2}$ might also be neglected from the small-scale energy equation 4.2 at small enough scales. We therefore consider the following simplified form of this equation for the turbulent flow region studied here:

$$\boldsymbol{\nabla_X}.(\overline{\boldsymbol{u_X}'|\boldsymbol{\delta u'}|^2}) + \boldsymbol{\nabla_r}.(\overline{\boldsymbol{\delta u'}|\boldsymbol{\delta u'}|^2}) + 2\boldsymbol{\nabla_X}.\overline{(\boldsymbol{\delta u'}\delta p')} \approx \frac{\nu}{2}(\boldsymbol{\nabla_X}^2 + \boldsymbol{\nabla_r}^2)\overline{|\boldsymbol{\delta u'}|^2} - \frac{1}{2}\left(\overline{\epsilon'^+} + \overline{\epsilon'^-}\right) \tag{4.21}$$

where $\overline{\epsilon'^+}$ and $\overline{\epsilon'^-}$ are $\overline{\epsilon'}$ at $\boldsymbol{\zeta}^+$ and $\boldsymbol{\zeta}^-$ respectively. Note, however, that this additional hypothesis concerning $(\overline{\boldsymbol{u_X}}.\boldsymbol{\nabla_X} + \boldsymbol{\delta\overline{u}}.\boldsymbol{\nabla_r})\,\frac{1}{2}\overline{|\boldsymbol{\delta u'}|^2}$ is in fact not crucial because the conclusions of the following two sections can also be obtained without it (with the only potential exception of the last sentence of subsection 4.8.4 which may need to be qualified).

It is worth pointing out that a careful look at all figures 4.2, 4.3, 4.4 and 4.5 as well as figure 4.6a, 4.6b, 4.7a and 4.7b suggests that the approximation 4.21 does not necessarily hold for large enough values of r_x and/or r_z. We chose to normalise r_x and r_z by λ in all these figures for comparison with Apostolidis, Laval, and Vassilicos 2023 who found, in a very different non-homogeneous turbulent flow (namely the intermediate region of fully developed turbulent channel flow), that equation 4.21 is not a good approximation at scales comparable to and larger than λ whereas we do assume it to be a good approximation at such scales (if

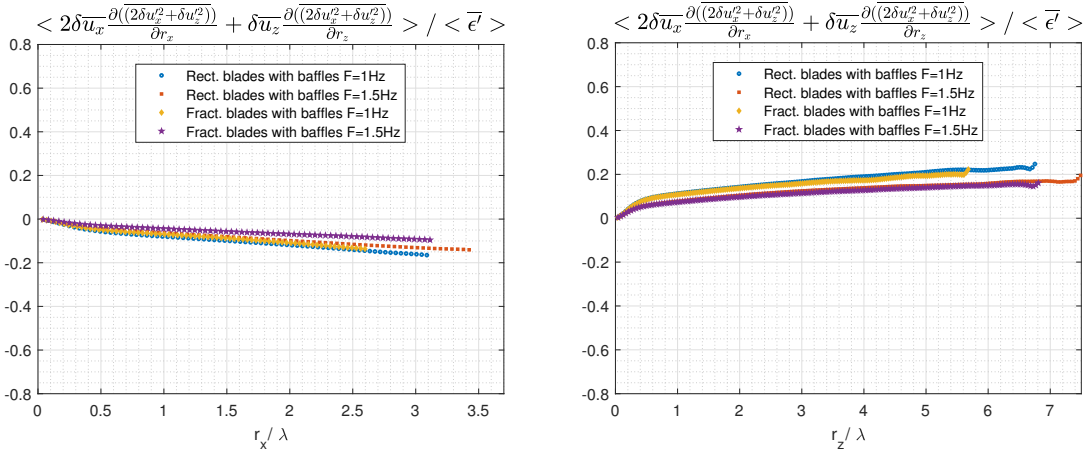

(a) r_x direction (b) r_z direction

Figure 4.6: Surrogate of rate of linear transport in scales in equation 4.2

they are not too large) in the flow region of the non-homogeneous turbulent flows considered here.

4.7 Second order structure functions

We now adopt the approach of Chen and Vassilicos 2022 which is based on inner and outer similarity. In effect, we assume that regions of space exist in the flow where the non-linear and non-local dynamics of the small-scale turbulence are similar at different places within the region. We therefore start with an hypothesis of inner and outer similarity for the second order structure function $\overline{|\boldsymbol{\delta u'}|^2}$, namely

$$\overline{|\boldsymbol{\delta u'}|^2} = V_{O2}^2(\boldsymbol{X}) f_{O2}\left(\frac{\boldsymbol{r}}{l_O}\right) \tag{4.22}$$

for $|\boldsymbol{r}| \gg l_I$ and

$$\overline{|\boldsymbol{\delta u'}|^2} = V_{I2}^2(\boldsymbol{X}) f_{I2}\left(\frac{\boldsymbol{r}}{l_I}\right) \tag{4.23}$$

for $|\boldsymbol{r}| \ll l_O$, where the inner length-scale l_I depends on viscosity and is much smaller than the outer length-scale l_O which does not depend on viscosity, i.e. $l_I = l_I(\boldsymbol{X}) \ll l_O = l_O(\boldsymbol{X})$ for large enough Reynolds number. The outer length scale can be thought of as an integral length of the order of the blade size $R = D/2$ and is assumed to be smaller than the extent of the similarity region where (4.22) and (4.23) hold. Statistical homogeneity is a special case of our inner and outer similarity hypotheses where V_{O2}, V_{I2}, l_O and l_I are independent of $\boldsymbol{X}$. In the following section we apply the approach of Chen and Vassilicos 2022 to the small-scale energy balance 4.21.

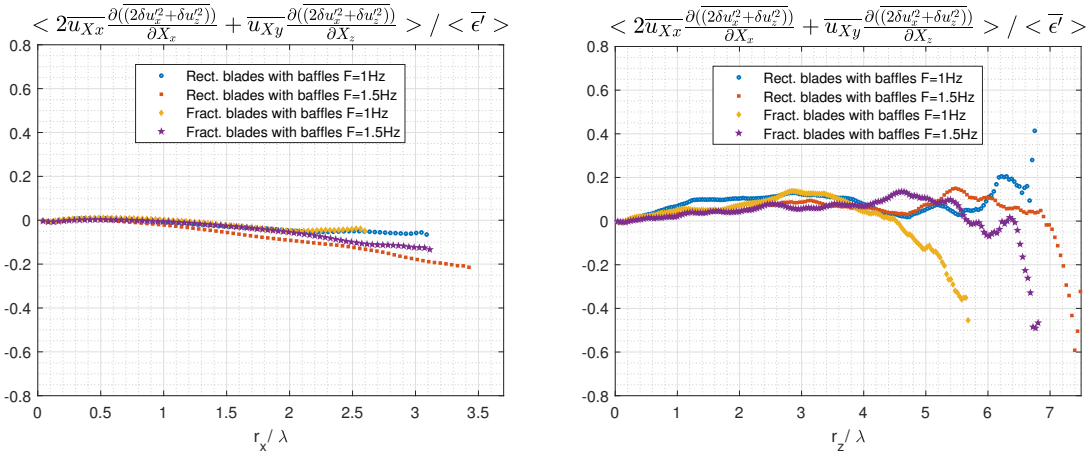

(a) r_x direction (b) r_z direction

Figure 4.7: Surrogate of rate of linear transport in space in equation 4.2

It is natural to expect the outer characteristic velocity V_{O2} to be independent of viscosity but the inner characteristic velocity V_{I2} to depend on it. The ratios V_{I2}/V_{O2} and l_I/l_O must therefore be functions of a local Reynolds number $Re_O = V_{O2}l_O/\nu$ and we write $V_{I2}/V_{O2} = g_2(Re_O, \boldsymbol{X})$, $l_I/l_O = g_l(Re_O, \boldsymbol{X})$, these two functions having to tend to zero as Re_O tends to infinity.

The inner and outer similarity forms overlap in the range $l_I \ll |\boldsymbol{r}| \ll l_O$, hence

$$f_{O2}\left(\frac{\boldsymbol{r}}{l_O}\right) = g_2^2(Re_O, \boldsymbol{X}) f_{I2}\left(\frac{\boldsymbol{r}}{l_O} g_l^{-1}\right) \tag{4.24}$$

in this intermediate range. Given that the left hand side of this equation does not depend on Re_O, the derivative with respect to Re_O of the right hand side cancels and we obtain

$$g_l \frac{dg_2^2}{dRe_O} f_{I2}(\boldsymbol{\rho}) = g_2^2 \frac{dg_l}{dRe_O} \rho_j \frac{\partial}{\partial \rho_j} f_{I2}(\boldsymbol{\rho}) \tag{4.25}$$

where there is an implicit sum over $j = 1, 2, 3$ and $\boldsymbol{\rho} = (\rho_1, \rho_2, \rho_3) = \boldsymbol{r}/l_I$. It follows that $\rho_j \frac{\partial}{\partial \rho_j} f_{I2}(\boldsymbol{\rho})$ is proportional to $f_{I2}(\boldsymbol{\rho})$. To solve for f_{I2} we adopt spherical coordinates (ρ, θ, ϕ) for $\boldsymbol{\rho}$, where θ varies from 0 to π and vanishes if $\boldsymbol{\rho}$ is aligned with the y axis and where ϕ varies from 0 to 2π and is equal to 0 or $\pi/2$ if $\boldsymbol{\rho}$ is aligned with the x or the z axis respectively. The proportionality between $\rho_j \frac{\partial}{\partial \rho_j} f_{I2}(\boldsymbol{\rho})$ and $f_{I2}(\boldsymbol{\rho})$ becomes

$$n f_{I2}(\rho, \theta, \phi) = \rho \frac{\partial}{\partial \rho} f_{I2}(\rho, \theta, \phi) \tag{4.26}$$

in terms of a dimensionless proportionality constant n and the solution to this equation is

$$f_{I2} = \rho^n F(\theta, \phi) \tag{4.27}$$

where F is an unknown function of angles θ and ϕ. Note that 4.27 holds in the intermediate range $l_I \ll |\boldsymbol{r}| \ll l_O$. Returning to 4.24, we get

$$g_2^2(Re_O, \boldsymbol{X}) g_l^{-n}(Re_O, \boldsymbol{X}) = A_1 \tag{4.28}$$

where the dimensionless coefficient A_1 is independent of Re_O and $\boldsymbol{X}$.

At this stage we follow Chen and Vassilicos 2022 and use their hypothesis of inner-outer equivalence for dissipation according to which there is an inner and an outer way to estimate the turbulence dissipation rate: $\overline{\epsilon'} \sim V_{O2}^3/l_O \sim V_{I2}^3/l_I$ where the proportionality coefficients are independent of Re_O but can depend on $\boldsymbol{X}$. We actually derive this hypothesis in subsection 4.8.3, and our derivation shows clearly that it has nothing to do with Kolmogorov's scale-by-scale equilibrium. At this stage, it provides the additional constraint $g_2^3(Re_O) g_l^{-1}(Re_O) = A_2$ where the coefficient A_2 is independent of Re_O. Combined with this additional constraint, 4.28 yields $n = 2/3$ (and $A_3 = A^{3/2}$, which means that A_2 is also independent of $\boldsymbol{X}$) and therefore

$$\overline{|\boldsymbol{\delta u'}|^2} = C(\overline{\epsilon'} r)^{2/3} F(\theta, \phi) \tag{4.29}$$

in the intermediate range $l_I \ll r = |\boldsymbol{r}| \ll l_O$. Note that, reflecting the dimensionless coefficients in $\overline{\epsilon'} \sim V_{O2}^3/l_O \sim V_{I2}^3/l_I$, the dimensional coefficient C can vary in space but is independent of Reynolds number. This is an obvious difference from Kolmogorov's prediction for the second order structure function which is limited to statistically homogeneous turbulence. This difference highlights the underlying difference in the way that our result 4.29 was obtained compared to Kolmogorov's derivation of his corresponding prediction which resembles 4.29 in the scaling $(\overline{\epsilon'} r)^{2/3}$ but is otherwise different (see Frisch 1995, Pope 2000 and section 2 of Chen and Vassilicos 2022)

We can refine our hypothesis of similarity by replacing it with an hypothesis of isotropic similarity which is an hypothesis of similarity for each component of $\boldsymbol{\delta u'}$, namely

$$\overline{(\delta u_j')^2} = V_{O2}^2(\boldsymbol{X}) f_{O2,j}\left(\frac{\boldsymbol{r}}{l_O}\right) \tag{4.30}$$

for $|\boldsymbol{r}| \gg l_I$ and

$$\overline{(\delta u_j')^2} = V_{I2}^2(\boldsymbol{X}) f_{I2,j}\left(\frac{\boldsymbol{r}}{l_I}\right) \tag{4.31}$$

for $|\boldsymbol{r}| \ll l_O$ for every $j = 1, 2, 3$. This is not an assumption of isotropy because neither the functions $f_{O2,j}$ nor the functions $f_{I2,j}$ are necessarily the same for different $j = 1, 2, 3$. The

argument leading to 4.29 can be repeated for every $j = 1, 2, 3$ yielding

$$\overline{(\delta u'_j)^2} = C_j(\overline{\epsilon'}r)^{2/3}F_j(\theta, \phi) \tag{4.32}$$

in the intermediate range $l_I \ll r = |\boldsymbol{r}| \ll l_O$. The dimensionless coefficient C_j may vary with j and with $\boldsymbol{X}$ and the dimensionless function F_j, which is independent of $\boldsymbol{X}$ and of $r \equiv |\boldsymbol{r}|$, may also vary with j.

The determination of the inner length scale l_I requires the small-scale energy balance 4.21. This is done in section 4.8. We complete the present section by confronting prediction 4.32 with our PIV data.

This prediction is similar to Kolmogorov's prediction for second order structure functions but it was derived without the homogeneity assumption required by Kolmogorov's theory and without Kolmogorov's scale-by-scale equilibrium which forms the physical basis of Kolmogorov's dimensional analysis.

4.7.1 Second order structure function measurements

We compute the normalised structure functions $\langle\overline{(\delta u'_j)^2}/\overline{\epsilon'}^{2/3}\rangle$ for $j = 1$ (velocity fluctuations along the x-axis) and $j = 3$ (velocity fluctuations along the z-axis) by averaging over time, i.e. over our 150, 000 samples (which correspond to 50, 000 uncorrelated samples) and also averaging over $\boldsymbol{X}$, i.e. over the planar space of our field of view. The additional averaging over space is necessary for convergence of our statistics (see Appendix A.1). The normalised structure functions $\overline{(\delta u'_j)^2}/\overline{\epsilon'}^{2/3}$ are therefore calculated by averaging over available points in the field of view in $150,000$ velocity field samples in this field of view. For two-point statistics, there are between 1.2×10^7 and 1.9×10^9 points available for convergence, depending on two-point separation vector, using both space and time averaging as explained in section 3.8.

Given that 4.32 implies $\langle\overline{(\delta u'_j)^2}/\overline{\epsilon'}^{2/3}\rangle = \langle C_j\rangle r^{2/3}F_j(\theta, \phi)$, we plot in figures 4.8a, 4.8b, 4.8c and 4.8d the compensated structure functions $\langle\overline{(\delta u'_x)^2}/\overline{\epsilon'}^{2/3}\rangle r^{-2/3}$ ($j = 1$) versus r_x/D (figure 4.8a) and versus r_z/D (figure 4.8b) and $\langle\overline{(\delta u'_z)^2}/\overline{\epsilon'}^{2/3}\rangle r^{-2/3}$ ($j = 3$) versus r_x/D (figure 4.8c) and versus r_z/D (figure 4.8d). This is the intermediate range data collapse suggested by 4.32 for all four configurations considered here. The dependence on r_x represents the dependence on r for $\theta = \pi/2$ and $\phi = 0$ whereas the dependence on r_z represents the dependence on r for $\theta = \pi/2$ and $\phi = \pi/2$. The average turbulence dissipation rate $\langle\overline{\epsilon'}\rangle$ varying by a factor larger than 4 across our four different configurations (see Table 4.2), figure 4.8 suggests that the collapse of the compensated structure functions in figure 4.8 is satisfactory. The exponent of the power law dependence of these structure functions on r_x and r_z (in an expected intermediate range of scales much smaller than $R = D/2$) appears close to but not exactly 2/3 and seems to vary a little around 2/3 from plot to plot in figure 4.8. The theory

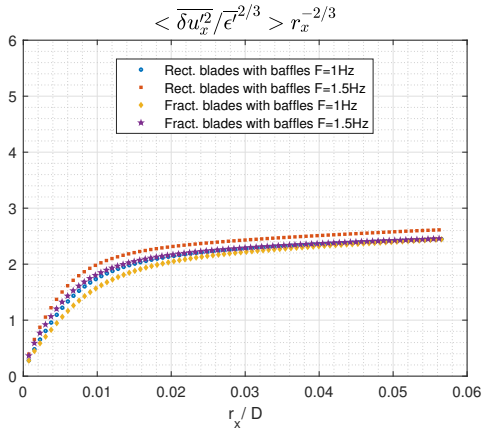

(a) Compensated $\overline{\delta u_x'^2}$ in r_x direction

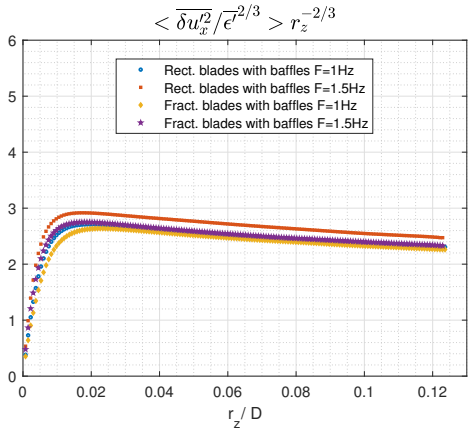

(b) Compensated $\overline{\delta u_x'^2}$ in r_z direction

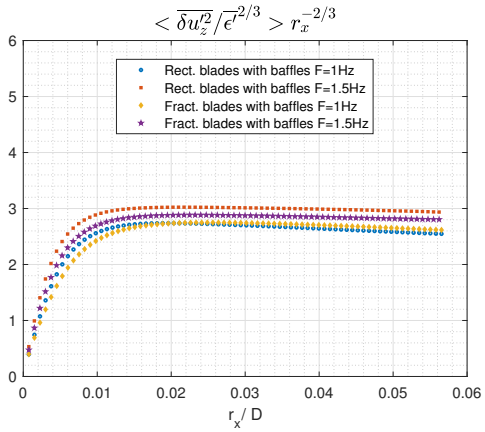

(c) Compensated $\overline{\delta u_z'^2}$ in r_x direction

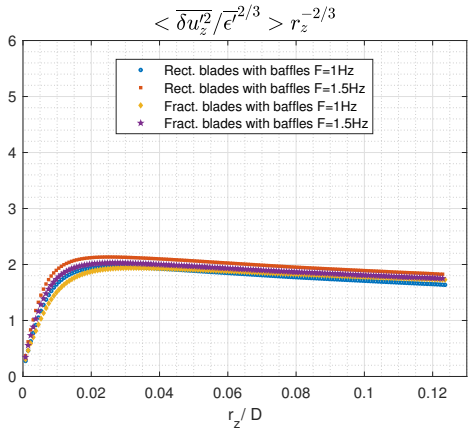

(d) Compensated $\overline{\delta u_z'^2}$ in r_z direction

Figure 4.8: Compensated structure functions

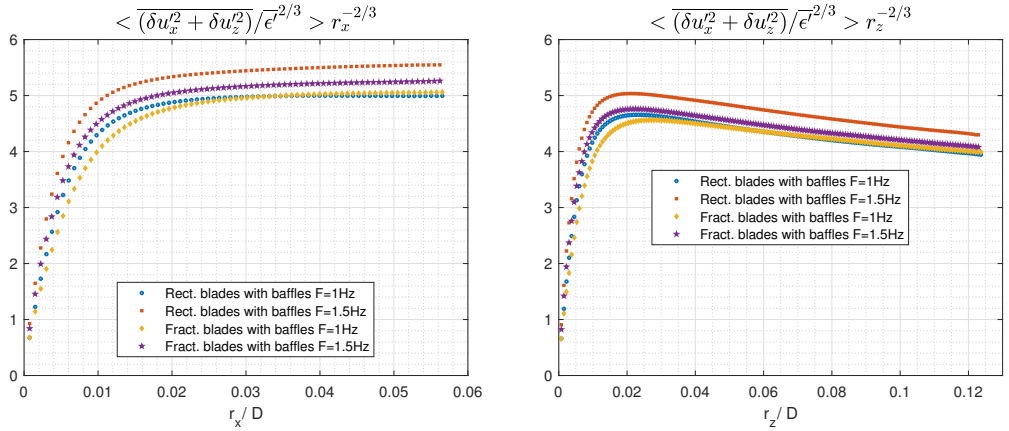

(a) r_x direction (b) r_z direction

Figure 4.9: Compensated structure function $\overline{(\delta u_x'^2 + \delta u_z'^2)}$

presented above and yielding equations 4.29 and 4.32 may be a leading order theory with different higher order corrections for different j components. Such corrections are beyond the scope of the present chapter, but noting from the plots in figure 4.8 that there may be opposite corrections to the 2/3 scaling, we now consider the r_x and r_z dependencies of the normalized structure function $\langle \overline{(\delta u_x'^2 + \delta u_z'^2)}/\overline{\epsilon'}^{2/3} \rangle$. Equation 4.32 implies

$$\langle \overline{(\delta u_x'^2 + \delta u_z'^2)}/\overline{\epsilon'}^{2/3} \rangle = r^{2/3}[\langle C_1 \rangle F_1(\theta, \phi) + \langle C_3 \rangle F_3(\theta, \phi)]. \tag{4.33}$$

This compensated normalised structure function is presented in figure 4.9 as a function of r_x/D (i.e. r/D for $\theta = \pi/2$ and $\phi = 0$) in one plot and of r_z/D (i.e. r/D for $\theta = \pi/2$ and $\phi = \pi/2$) in the other. Once again, the resulting collapse of the structure functions for the four different configurations is acceptable given the wide variation of $< \overline{\epsilon'} >$ from one configuration to the other. To look at the power law scaling more finely, we estimate the logarithmic slopes of $S \equiv \langle \overline{(\delta u_x'^2 + \delta u_z'^2)}/\overline{\epsilon'}^{2/3} \rangle$ versus both r_x and r_z, i.e. $\frac{dlogS}{dlogr_x}$ and $\frac{dlogS}{dlogr_z}$, which we plot versus r_x and r_z respectively in figures 4.10a and 4.10b. A well-defined plateau appears in both directions for $r_x, r_z \ll R = D/2$ which confirms the power-law behavior of S. The value of the plateau is the power-law exponent and it is slightly different in the two directions: it lies between $2/3 \approx 0.66$ and 0.7 in the r_x direction, which is very close to the theory's prediction but between 0.5 and 0.6 in the r_z direction which is further away from it.

We must leave it for future study to determine whether the deviation from $n = 2/3$ that we observe in the vertical r_z direction is a finite Reynolds number effect or whether it results from deviations from outer and/or inner isotropic similarity of second order structure functions. The good agreement with $n = 2/3$ in the r_x direction is nevertheless encouraging and so, in the following section, we use $n = 2/3$ in conjunction with an analysis of the small-scale energy

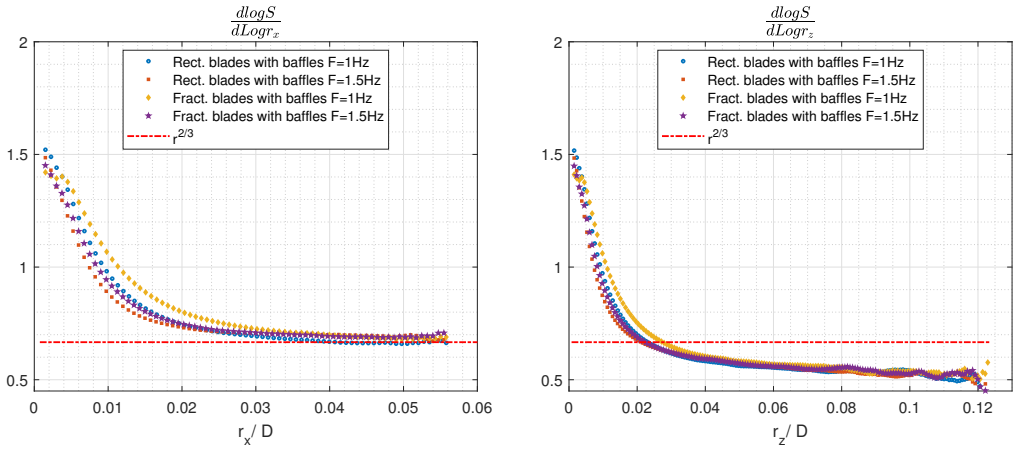

(a) r_x direction (b) r_z direction

Figure 4.10: Logarithmic slope of $S \equiv \langle \overline{(\delta u_x'^2 + \delta u_z'^2)} / \overline{\epsilon'}^{2/3} \rangle$

budget to predict the relations between l_I and l_O and between V_{I2} and V_{O2}. Perhaps more importantly, though, this analysis also leads to predictions concerning non-linear interscale and interspace turbulent energy transfer rates which do not critically depend on the value of the exponent n and which we also subject to experimental checks.

4.8 Small-scale turbulent energy budgets

Following Chen and Vassilicos 2022 who assume that regions exist in the flow where the non-linear and non-local dynamics of the small scale turbulence are similar at different places within the region, we now introduce, for such a region, inner and outer similarity forms for every term on the left hand side of equation 4.21.

Outer similarity for $|\boldsymbol{r}| >> l_I$*:*

$$\boldsymbol{\nabla_X}.(\overline{\boldsymbol{u_X}'|\boldsymbol{\delta u}'|^2}) = \frac{V_{OX}^3(\boldsymbol{X})}{l_O} f_{OX}\left(\frac{\boldsymbol{r}}{l_O}\right) \tag{4.34}$$

$$\boldsymbol{\nabla_r}.(\overline{\boldsymbol{\delta u}'|\boldsymbol{\delta u}'|^2}) = \frac{V_{O3}^3(\boldsymbol{X})}{l_O} f_{O3}\left(\frac{\boldsymbol{r}}{l_O}\right) \tag{4.35}$$

$$2\boldsymbol{\nabla_X}.(\overline{\boldsymbol{\delta u}'\delta p'}) = \frac{V_{Op}^3(\boldsymbol{X})}{l_O} f_{Op}\left(\frac{\boldsymbol{r}}{l_O}\right) \tag{4.36}$$

Inner similarity for $|\boldsymbol{r}| << l_O$*:*

$$\boldsymbol{\nabla_X}.(\overline{\boldsymbol{u_X}'|\boldsymbol{\delta u}'|^2}) = \frac{V_{IX}^3(\boldsymbol{X})}{l_I} f_{IX}\left(\frac{\boldsymbol{r}}{l_I}\right) \tag{4.37}$$

$$\boldsymbol{\nabla}_{\boldsymbol{r}}.(\overline{\boldsymbol{\delta u'}|\boldsymbol{\delta u'}|^2}) = \frac{V_{I3}^3(\boldsymbol{X})}{l_I} f_{I3}\left(\frac{\boldsymbol{r}}{l_I}\right) \tag{4.38}$$

$$2\boldsymbol{\nabla}_{\boldsymbol{X}}.\overline{(\boldsymbol{\delta u'}\delta p')} = \frac{V_{Ip}^3(\boldsymbol{X})}{l_I} f_{Ip}\left(\frac{\boldsymbol{r}}{l_I}\right) \tag{4.39}$$

The characteristic velocities V_{OX}, V_{O3}, V_{Op}, V_{IX}, V_{I3}, V_{Ip} depend explicitly on $\boldsymbol{X}$ but are independent of $\boldsymbol{r}$ and f_{OX}, f_{O3}, f_{Op}, f_{IX}, f_{I3}, f_{Ip} are dimensionless functions which do not depend explicitly on $\boldsymbol{X}$ within the similarity region. Statistical homogeneity is the special case where $f_{OX} = f_{Op} = f_{IX} = f_{Ip} = 0$ and the characteristic velocities are independent of $\boldsymbol{X}$.

As in the previous section, we expect the outer characteristic velocities to be independent of viscosity but the inner characteristic velocities to depend on it. The ratios of outer to inner characteristic velocities are therefore functions of local Reynolds number Re_O, i.e. $V_{IX}/V_{OX} = g_X(Re_O, \boldsymbol{X})$, $V_{I3}/V_{O3} = g_3(Re_O, \boldsymbol{X})$, $V_{Ip}/V_{Op} = g_p(Re_O, \boldsymbol{X})$, these functions approaching zero as Re_O tends to infinity.

Following the approach we took in section 4.7, we can replace the hypothesis of similarity by a hypothesis of isotropic similarity for terms on the left hand side of equation 4.21. For the two terms not involving pressure fluctuations, this refined hypothesis states that $\overline{u'_{Xi}\frac{\partial}{\partial X_i}(\delta u'_j)^2}$ and $\overline{\delta u'_i\frac{\partial}{\partial r_i}(\delta u'_j)^2}$ (without summation over i and without summation over j) have an inner and an outer similarity form for every $i, j = 1, 2, 3$. Only $i, j = 1, 3$ are accessible to our 2D2C PIV measurements and we therefore decompose the interscale transfer rate in two sub-terms, both of which have an inner and an outer similarity form: $\overline{\delta u'_x\frac{\partial}{\partial r_x}(\delta u'^2_x + \delta u'^2_z)} + \overline{\delta u'_z\frac{\partial}{\partial r_z}(\delta u'^2_x + \delta u'^2_z)}$ which is accessible to our 2D2C PIV and $\overline{\delta u'_x\frac{\partial}{\partial r_x}(\delta u'^2_y)} + \overline{\delta u'_z\frac{\partial}{\partial r_z}(\delta u'^2_y)} + \overline{\delta u'_y\frac{\partial}{\partial r_y}(\delta u'^2_x + \delta u'^2_y + \delta u'^2_z)}$ which is not. For example,

$$\overline{\delta u'_x\frac{\partial}{\partial r_x}(\delta u'^2_x + \delta u'^2_z)} + \overline{\delta u'_z\frac{\partial}{\partial r_z}(\delta u'^2_x + \delta u'^2_z)} = \frac{V_{O3}^3(\boldsymbol{X})}{l_O} F_{O3}\left(\frac{\boldsymbol{r}}{l_O}\right) \tag{4.40}$$

for $|\boldsymbol{r}| \gg l_I$ and

$$\overline{\delta u'_x\frac{\partial}{\partial r_x}(\delta u'^2_x + \delta u'^2_z)} + \overline{\delta u'_z\frac{\partial}{\partial r_z}(\delta u'^2_x + \delta u'^2_z)} = \frac{V_{I3}^3(\boldsymbol{X})}{l_I} F_{I3}\left(\frac{\boldsymbol{r}}{l_I}\right) \tag{4.41}$$

for $|\boldsymbol{r}| \ll l_O$. The function F_{O3} is not the same as the function f_{O3} and the function F_{I3} is not the same as the function f_{I3}.

We do the same for the interspace transfer rate $\boldsymbol{\nabla}_{\boldsymbol{X}}.(\overline{\boldsymbol{u_X}'|\boldsymbol{\delta u}'|^2})$ which we also decompose in two sub-terms, both of which have an inner and an outer similarity form. For the sub-term which is accessible to our 2D2C PIV, for example, we therefore write

$$\overline{u'_{Xx}\frac{\partial}{\partial X_x}(\delta u'^2_x + \delta u'^2_z)} + \overline{u'_{Xz}\frac{\partial}{\partial X_z}(\delta u'^2_x + \delta u'^2_z)} = \frac{V_{OX}^3(\boldsymbol{X})}{l_O} F_{OX}\left(\frac{\boldsymbol{r}}{l_O}\right) \tag{4.42}$$

for $|\boldsymbol{r}| \gg l_I$ and

$$\overline{u'_{Xx}\frac{\partial}{\partial X_x}(\delta u_x'^2+\delta u_z'^2)}+\overline{u'_{Xz}\frac{\partial}{\partial X_z}(\delta u_x'^2+\delta u_z'^2)}=\frac{V_{IX}^3(\boldsymbol{X})}{l_I}F_{IX}\left(\frac{\boldsymbol{r}}{l_I}\right) \tag{4.43}$$

for $|\boldsymbol{r}| \ll l_O$. Again, the function F_{OX} is not the same as the function f_{OX} and the function F_{IX} is not the same as the function f_{IX}.

4.8.1 Outer balance

Using the outer similarity forms 4.34, 4.35 and 4.36, Chen and Vassilicos 2022 have shown that the outer form of the small-scale energy balance 4.21 for $|\boldsymbol{r}| \gg l_I$ tends to

$$\frac{V_{OX}^3}{V_{O2}^3}f_{OX}(\boldsymbol{r}/l_O)+\frac{V_{O3}^3}{V_{O2}^3}f_{O3}(\boldsymbol{r}/l_O)+\frac{V_{Op}^3}{V_{O2}^3}f_{Op}(\boldsymbol{r}/l_O)=-C_\epsilon \tag{4.44}$$

as $Re_O \to \infty$, where the dissipation coefficient C_ϵ is defined on the basis of the turbulence dissipation scaling $\overline{\epsilon'} \sim V_{O2}^3/l_O$. This scaling follows from the hypothesis (often refered to as zeroth law of turbulence) that the turbulence dissipation rate is independent of the fluid's viscosity at large enough Reynolds number, hence $\overline{\epsilon'}=C_\epsilon V_{O2}^3/l_O$ where C_ϵ is independent of Reynolds number but can depend on $\boldsymbol{X}$ and boundary/forcing conditions. It follows from 4.44 that

$$V_{OX} \sim V_{O3} \sim V_{Op} \sim C_\epsilon^{1/3}V_{O2} \tag{4.45}$$

which means that all three velocities V_{OX}, V_{O3} and V_{Op} are the same function of $\boldsymbol{X}$ as $C_\epsilon^{1/3}V_{O2}$. The independence of C_ϵ on $\boldsymbol{r}$ which is required to go from (4.44) to (4.45) is valid without any restriction on spatial gradients of turbulent dissipation: the only requirement is that the second order spatial derivative of turbulent dissipation should be small compared to $\overline{\epsilon'}/l_O^2$.

4.8.2 Inner balance

Using the inner similarity forms 4.37, 4.38 and 4.39, Chen and Vassilicos 2022 have shown that the inner form of the small-scale energy balance 4.21 for $|\boldsymbol{r}| \ll l_O$ tends to

$$g_X^3 g_l^{-1}f_{IX}(\boldsymbol{r}/l_I)+g_3^3 g_l^{-1}f_{I3}(\boldsymbol{r}/l_I)+g_p^3 g_l^{-1}f_{Ip}(\boldsymbol{r}/l_I)=-1+C_\epsilon^{-1}Re_O^{-1}g_2^2 g_l^{-2}\boldsymbol{\nabla}^2_{\mathbf{r}/l_I}f_{I2}(\boldsymbol{r}/l_I) \tag{4.46}$$

as $Re_O \to \infty$, where $\boldsymbol{\nabla}^2_{\mathbf{r}/l_I}$ is the Laplacian with respect to $\boldsymbol{r}/l_I$ and where $Re_O^{-1}g_2^2 g_l^{-2}$ is independent of Reynolds number. They obtained this result without considering the possibility of explicit dependencies of the functions g_X, g_3, g_p, g_l on $\mathbf{X}$ but it can be checked that their result remains intact if such dependencies are taken into account. Writing

$$g_2^2(Re_O,\boldsymbol{X})g_l^{-2}(Re_O,\boldsymbol{X})=A_3(\boldsymbol{X})Re_O \tag{4.47}$$

in terms of a dimensionless coefficient A_3 which can depend on $\boldsymbol{X}$ (but not on $\boldsymbol{r}$ and viscosity), we note that equation 4.46 is viable only if $g_X^3 g_l^{-1}$, $g_3^3 g_l^{-1}$, $g_p^3 g_l^{-1}$ and A_3/C_ϵ are all independent of $\boldsymbol{X}$. Incidentally, the explicit $\mathbf{X}$-dependence of the functions g_2 and g_l and the constraint $A_3/C_\epsilon = Const$ independent of $\boldsymbol{X}$ cancel the need for the theoretical readjustments in the Appendix of Chen and Vassilicos 2022.

With 4.28 and the exponent $n = 2/3$ obtained theoretically in section 4.7, equation 4.47 implies $g_l \sim Re_O^{-3/4}$, therefore

$$l_I \sim l_O Re_O^{-3/4} \tag{4.48}$$

where the coefficient of proportionality can, in principle, be a function of $\boldsymbol{X}$. Using equation 4.47 once again leads to

$$V_{I2} \sim V_{O2} Re_O^{-1/4} \tag{4.49}$$

where the coefficient of proportionality is also, in principle, a function of $\boldsymbol{X}$. One notes the resemblance of l_I and V_{I2} with the Kolmogorov length and velocity scales. However, these forms of l_I and V_{I2} have been obtained in an explicitely non-homogeneous context with hypotheses which, unlike those of Kolmogorov (see Frisch 1995, Pope 2000 and section 2 of Chen and Vassilicos 2022), are adapted to non-homogeneous non-equilibrium turbulence. Note that we use the value 2/3 of the exponent n only to derive 4.48 and 4.49, nothing else in this chapter, and that 4.48 and 4.49 are not used to derive anything in the chapter either.

4.8.3 Intermediate scalings

The turbulence dissipation scaling $\overline{\epsilon'} = C_\epsilon V_{O2}^3/l_O$ and 4.45 imply

$$\overline{\epsilon'} \sim V_{O3}^3/l_O \sim V_{OX}^3/l_O \sim V_{Op}^3/l_O \tag{4.50}$$

where the proportionality coefficients are independent of $\boldsymbol{X}$ (and of course also independent of Re_O). One expects the non-linear terms to be part of the small-scale energy balance 4.46 which means that $g_X^3 g_l^{-1}$, $g_3^3 g_l^{-1}$ and $g_p^3 g_l^{-1}$ should be independent of Re_O in the limit $Re_O \to \infty$ and so we write, in this limit, $g_X^3 g_l^{-1} = B_X$, $g_3^3 g_l^{-1} = B_3$ and $g_p^3 g_l^{-1} = B_p$ where the dimensionless constants B_X, B_3, B_p are independent of $\boldsymbol{X}$, $\boldsymbol{r}$ and Re_O. With 4.50, the implication is

$$\overline{\epsilon'} \sim V_{I3}^3/l_I \sim V_{IX}^3/l_I \sim V_{Ip}^3/l_I \tag{4.51}$$

where, once again, the porportionality coefficients are independent of $\boldsymbol{X}$ and Re_O. Hence, in the intermediate range $l_I \ll |\boldsymbol{r}| \ll l_O$ where equation 4.34 matches equation 4.37, equation 4.35 matches equation 4.38 and equation 4.36 matches equation 4.39, we get $f_{OX}(\boldsymbol{r}/l_O) = B_X f_{IX}(\boldsymbol{r}/l_I)$, $f_{O3}(\boldsymbol{r}/l_O) = B_3 f_{I3}(\boldsymbol{r}/l_I)$ and $f_{Op}(\boldsymbol{r}/l_O) = B_p f_{Ip}(\boldsymbol{r}/l_I)$. These functions are therefore asymptotic constants in the intermediate range $l_I \ll |\boldsymbol{r}| \ll l_O$ as $Re_O \to \infty$, and therefore:

$$\boldsymbol{\nabla_X}.(\overline{\boldsymbol{u_X}'|\boldsymbol{\delta u}'|^2}) \sim \overline{\epsilon'}, \tag{4.52}$$

$$\boldsymbol{\nabla_r}.(\overline{\boldsymbol{\delta u}'|\boldsymbol{\delta u}'|^2}) \sim \overline{\epsilon'} \tag{4.53}$$

and

$$2\boldsymbol{\nabla_X}.\overline{(\boldsymbol{\delta u}'\delta p')} \sim \overline{\epsilon'} \tag{4.54}$$

in that range.

The dimensionless coefficients of proportionality in 4.52, 4.53 and 4.54 are independent of $\boldsymbol{r}$, independent of Reynolds number and independent of $\boldsymbol{X}$ in the similarity region of the flow considered, and add up to -1 asymptotically as $Re_O \to \infty$.

The same procedure applied to equations 4.40 and 4.41 on the one hand and equations 4.42 and 4.43 on the other yields

$$\overline{\boldsymbol{\nabla_X}.\widetilde{(\boldsymbol{u_X}'|\boldsymbol{\delta u}'|^2)}} \equiv \overline{u'_{Xx}\frac{\partial}{\partial X_x}(\delta u_x'^2 + \delta u_z'^2)} + \overline{u'_{Xz}\frac{\partial}{\partial X_z}(\delta u_x'^2 + \delta u_z'^2)} \sim \overline{\epsilon'} \tag{4.55}$$

and

$$\overline{\boldsymbol{\nabla_r}.\widetilde{(\boldsymbol{\delta u}'|\boldsymbol{\delta u}'|^2)}} \equiv \overline{\delta u'_x\frac{\partial}{\partial r_x}(\delta u_x'^2 + \delta u_z'^2)} + \overline{\delta u'_z\frac{\partial}{\partial r_z}(\delta u_x'^2 + \delta u_z'^2)} \sim \overline{\epsilon'} \tag{4.56}$$

in the intermediate range $l_I \ll |\boldsymbol{r}| \ll l_O$ as $Re_O \to \infty$. The dimensionless coefficients of proportionality in these two relations are also independent of $\boldsymbol{r}$, Reynolds number and $\boldsymbol{X}$.

Note that our analysis does not reveal the signs of the various constants of proportionality in the five proportionality relations above. These signs are important, in particular for the interscale transfer rate as its sign can discriminate between transfer from small to large scales (forward cascade) or from large to small scales (inverse cascade). The last two proportionalities are the ones which are accessible to our 2D2C PIV measurements. For them, our measurements can establish whether the proportionality constants are well defined and, if they are, whether they are negative or positive.

Before moving to our energy transfer measurements, we note that the hypothesis of inner-outer equivalence for turbulence dissipation introduced by Chen and Vassilicos 2022 and used in section 4.7 can now be seen to be a consequence of Reynolds number-independence of turbulence dissipation, outer and inner similarities and the natural assumption $V_{I3} = C_I(\mathbf{X})V_{I2}$ where the dimensionless coefficient $C_I(\mathbf{X})$ is independent of Re_O and $\boldsymbol{r}$. Using $\overline{\epsilon'} = C_\epsilon(\mathbf{X})V_{O2}^3/l_O$ and the first proportionality in 4.51 (which follows from inner and outer similarities), one then obtains the inner-outer equivalence in the form $C_\epsilon(\mathbf{X})V_{O2}^3/l_O \sim C_I^3(\mathbf{X})V_{I2}^3/l_I$ with a proportionality coefficient that is independent of $\mathbf{X}$ and Re_O. (It also follows that $C_\epsilon(\mathbf{X})/C_I^3(\mathbf{X})$ is independent of $\mathbf{X}$.

4.8.4 Energy transfer rate measurements

The quantities obtained from our 2D2C PIV and presented in this sub-section require high spatial resolution, in particular for the estimation of the turbulence dissipation rate, and a high number of samples for convergence of third order statistics.

Averaging over time is not enough for such convergence (see Appendix A.1). We therefore calculate spatial averages of both sides of proportionalities 4.55 and 4.56 given that they are the consequences of our theory that can be tested by our 2D2C PIV. In figures 4.11 and 4.12 we plot the normalised interscale transfer rate term $\langle \boldsymbol{\nabla_r}.(\widetilde{\overline{\boldsymbol{\delta u'}|\boldsymbol{\delta u'}|^2}})\rangle/\langle\overline{\epsilon'}\rangle$ and the normalised interspace transfer rate term $\langle \boldsymbol{\nabla_X}.(\widetilde{\overline{\boldsymbol{u_X'}|\boldsymbol{\delta u'}|^2}})\rangle/\langle\overline{\epsilon'}\rangle$ (we recall that the brackets $\langle ...\rangle$ are averages over $\boldsymbol{X}$ in the plane of our field of view). Our theory predicts that an intermediate range of scales exists where these two normalised terms are about constant, this constant being the same for different Reynolds numbers. The spread of Taylor length-based Reynolds numbers across our four experimental configurations is from 480 to 650, and the average turbulence dissipation rate varies by a factor of 4 across these configurations. The Taylor length λ depends on the turbulence dissipation rate and in chapter 3 we explain how we calculate both of them and how we denoise the PIV data for this purpose. The value of the average turbulence dissipation rate is probably slightly underestimated and this uncertainty is not taken into account in the error bars shown in figures 4.11 and 4.12. The spatial resolutions for all four configurations are given in Table 1.

The normalised energy transfer terms are plotted versus r_x/λ in figures 4.11a and 4.12a and versus r_z/λ in figures 4.11b and 4.12b. We normalise the components r_x and r_z of the vector $\mathbf{r}$ by λ because of the important role that λ has been shown to play in the separation length scale dependence of the interscale transfer rate in decaying homogeneous turbulence (Obligado and Vassilicos 2019, Meldi and Vassilicos 2021) and in fully developed turbulent channel flow (Apostolidis, Laval, and Vassilicos 2023). We find (figure 4.11) that the interscale transfer rate is negative for all observed scales in both directions r_x and r_z and all four configurations. This suggests a non-linear interscale turbulent energy transfer that is perdominantly from large to small scales, i.e. that the turbulence cascade is forward on average. The 2D2C PIV measurements also appear to support our theory's prediction that a range of scales exists where the interscale transfer rate is proportional to the turbulence dissipation rate and independent of two-point separation length. Indeed, for the four configurations, $\langle \boldsymbol{\nabla_r}.(\widetilde{\overline{\boldsymbol{\delta u'}|\boldsymbol{\delta u'}|^2}})\rangle/\langle\overline{\epsilon'}\rangle$ appear to collapse within error bars around a constant value between 0.35 and 0.45 in the range $\lambda/2 \leq r_x \leq 2\lambda$ and around a constant value between 0.4 and 0.5 in the range $\lambda/2 \leq r_z \leq 5\lambda$. Beyond these values of r_x and r_z statistical convergence visibly weakens. The Taylor length takes values between $3.7mm$ and $4.9mm$ across our four configurations and the field of view of our PIV is $27mm \times\ 28mm$, hence we cannot access values of r_x/λ and r_z/λ larger than those in the plots of figure 4.11 and 4.12 (to avoid symmetry

problems, we only used the right half of our field of view in the x-direction).

Whilst the negative sign of the average interscale transfer rate and its proportionality with the average turbulence dissipation rate over a range of scales are similar to Kolmogorov's prediction for the average interscale transfer rate in high Reynolds number statistically homogeneous stationary turbulence (Frisch 1995, Pope 2000, section 2 of Chen and Vassilicos 2022), the constant of proportionality is not Kolmogorov equilibrium's -1 but significantly smaller. This difference may of course be accounted for by the difference between $\langle \boldsymbol{\nabla_r}.(\widetilde{\overline{\boldsymbol{\delta u'}|\boldsymbol{\delta u'}|^2}}) \rangle / \langle \overline{\epsilon'} \rangle$ and $\boldsymbol{\nabla_r}.(\langle \overline{\boldsymbol{\delta u'}|\boldsymbol{\delta u'}|^2} \rangle) / \langle \overline{\epsilon'} \rangle$ and/or the Reynolds number not being large enough in case that this constant of proportionality has finite Reynolds number corrections. However, the results in figures 4.12a and 4.12b make it clear that the turbulence studied here is significantly non-homogeneous at the scales where $\langle \boldsymbol{\nabla_r}.(\widetilde{\overline{\boldsymbol{\delta u'}|\boldsymbol{\delta u'}|^2}}) \rangle / \langle \overline{\epsilon'} \rangle$ is about constant. Indeed, these figures show that the normalised interspace transfer rate term $\langle \boldsymbol{\nabla_X}.(\widetilde{\overline{\boldsymbol{u_X'}|\boldsymbol{\delta u'}|^2}}) \rangle / \langle \overline{\epsilon'} \rangle$ is very significantly non-zero and in fact positive over all accessible length-scales in both directions r_x and r_z for all four configurations. These consistent positive values mean that there is a leaving average turbulent flux which takes small-scale turbulent kinetic energy out of the field of view at all accessible length scales. In fact, $\langle \overline{u'_{Xx} \frac{\partial}{\partial X_x}(\delta u_x'^2 + \delta u_z'^2)} \rangle / \langle \overline{\epsilon'} \rangle$ dominates this interspace transfer rate (see figure 4.13) and $\langle \overline{u'_{Xz} \frac{\partial}{\partial X_z}(\delta u_x'^2 + \delta u_z'^2)} \rangle / \langle \overline{\epsilon'} \rangle$ is negligible if slightly negative. The small-scale turbulence energy is therefore transported out of the field of view by the turbulence predominantly in the horizontal direction.

For all four configurations, $\langle \boldsymbol{\nabla_X}.(\widetilde{\overline{\boldsymbol{u_X'}|\boldsymbol{\delta u'}|^2}}) \rangle / \langle \overline{\epsilon'} \rangle$, and $\langle \overline{u'_{Xx} \frac{\partial}{\partial X_x}(\delta u_x'^2 + \delta u_z'^2)} \rangle / \langle \overline{\epsilon'} \rangle$ which dominates it, appear to collapse within error bars around a constant value between about 0.05 and 0.15 in the range $\lambda/2 \leq r_x \leq 2\lambda$ and around a similar constant value in the range $\lambda/2 \leq r_z \leq 5\lambda$ (see figures 4.12a and 4.12b and 4.13). We stress once again, that larger two-point separation scales are not accessible to our PIV and statistical convergence weakens at the larger values of r_x and r_z that we can access. Nevertheless, the results in figures 4.12a and 4.12b and figure 4.13 do not invalidate and may even arguably offer some support to our theory's prediction 4.55 for the interspace turbulence transfer rate.

To summarise, the parts of the interscale and of the interspace average turbulent transfer rates that we can access appear to be independent of two-point separation scale and are proportional to the average turbulence dissipation rate over a more or less overlapping range of scales. The average turbulence dissipation rate and the Taylor length-scale collapse the two-point separation scale dependence of the accessible parts of the energy transfer rates for all four configurations tried here.

The average interscale transfer rate is negative, suggesting forward cascade, and the average interspace transfer rate is positive, suggesting outward turbulent transport of small-scale turbulence. This outward spatial turbulent flux is overwhelmingly in the x-direction. The non-homogeneity that it represents is present even at the smallest scales

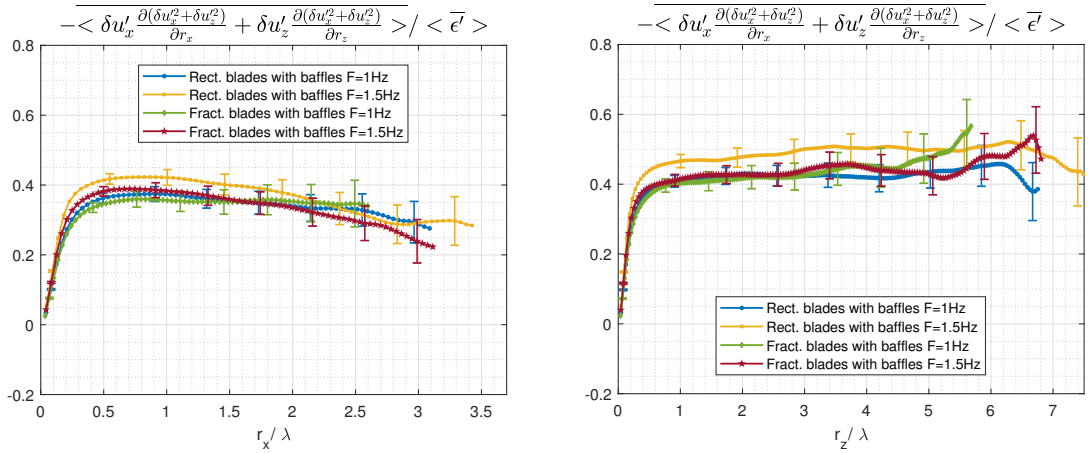

(a) r_x direction (b) r_z direction

Figure 4.11: Interscale transfer rate estimate

of the turbulence, in particular scales between $\lambda/2$ and 5λ. It is therefore not possible to apply the Kolmogorov equilibrium theory to the small scales of the present turbulent flows. However our non-equilibrium theory of non-homogeneous small-scale turbulence is able to account for some of our observations.

One can also analyse sub-terms of the part of the average interscale transfer rate that we measure. In figure 4.14, we plot $\langle\overline{\delta u'_x \frac{\partial}{\partial r_x}(\delta u'^2_x + \delta u'^2_z)}\rangle/\langle\overline{\epsilon'}\rangle$ and $\langle\overline{\delta u'_z \frac{\partial}{\partial r_z}(\delta u'^2_x + \delta u'^2_z)}\rangle/\langle\overline{\epsilon'}\rangle$ separately and see that they are both constant over the range of scales where their sum is constant and that they both contribute significantly to that sum but that the latter term is also significantly larger in magnitude than the former.

The magnitude of the accessible average interscale transfer rate is roughly 4 times larger than the magnitude of the accessible average interspace transfer rate. Considering our measurements, our theory (in particular equation 4.54) and the small-scale energy balance 4.21 averaged over the field of view of our PIV, it is highly likely that the pressure-velocity term in that balance plays a dominant role at scales $|\mathbf{r}|$ larger than $\lambda/2$.

4.9 Large-scale turbulent energy budget

We do not apply the previous section's theoretical approach to the large-scale turbulent energy budget, equation 4.4, given that the two-point turbulence production rate P_X tends to the one-point turbulence production rate in the limit $\boldsymbol{r} \to 0$ and given the PIV evidence of section 4.5 suggesting that it is significantly non-zero at the smallest scales and does not collapse with the average turbulence dissipation rate. Indeed, figure 4.4 shows that $\langle\widetilde{\widetilde{P_X}}\rangle/\langle\overline{\epsilon'}\rangle$ differs substantially for the regular and the fractal-like blades.

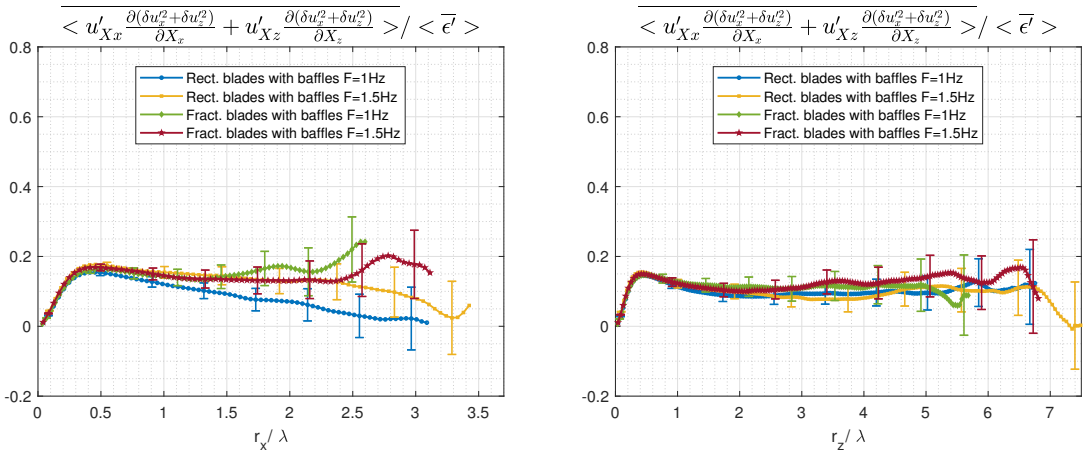

(a) r_x direction (b) r_z direction

Figure 4.12: Interspace transport rate estimate

Furthermore, the spatio-temporal average of the part of the interspace turbulent transport rate of large-scale turbulence energy that is accessible to our 2D2C PIV, i.e. $\langle \overline{u'_{Xx}\frac{\partial}{\partial X_x}(u'^2_{Xx}+u'^2_{Xz})} \rangle + \langle \overline{u'_{Xz}\frac{\partial}{\partial X_z}(u'^2_{Xx}+u'^2_{Xz})} \rangle$, does not collapse with the average turbulence dissipation rate $\langle \overline{\epsilon'} \rangle$. This is clear in figures 4.15a and 4.15b which also show that the normalised spatio-temporal average $\langle \overline{u'_{Xx}\frac{\partial}{\partial X_x}(u'^2_{Xx}+u'^2_{Xz})} \rangle / \langle \overline{\epsilon'} \rangle + \langle \overline{u'_{Xz}\frac{\partial}{\partial X_z}(u'^2_{Xx}+u'^2_{Xz})} \rangle / \langle \overline{\epsilon'} \rangle$ may depend linearly on r_z for $r_z \geq \lambda/2$ and may be constant or linear with r_x for $r_x \geq \lambda/2$ depending on type of blade. This is very different behaviour from the average interspace turbulent transport rate of small-scale energy in figure 4.12.

Another important difference is the non vanishing value when $\boldsymbol{r} \to 0$ of the average interspace turbulent transport rate of large-scale energy (see figure 4.15). Indeed, when $\boldsymbol{r} \to 0$, this term converges to the space-time averaged one-point turbulent energy transport rate $< \overline{\boldsymbol{\nabla}.\boldsymbol{u}'|\boldsymbol{u}'|^2} >$. This one-point turbulence transport rate reflects the non-homogeneity of each particular configuration and there is no reason to expect it to collapse when normalised by dissipation. There is therefore no reason either to expect such a collapse for the average two-point interspace turbulent transport rate of large-scale energy at the smallest two-point separations. Consistently, the measurements suggest that such a collapse is in fact absent at all two-point separations tested (figure 4.15).

The indications are, therefore, that the large-scale turbulent energy budget 4.4 is very different from the small-scale turbulent energy budget and that a theory of the type developed in the previous section for the small-scale turbulent energy budget cannot be developed for the large-scale turbulent energy budget. Nevertheless, there is a kinematic relation between the rate with which large scales gain or lose turbulent energy to the small scales via non-linear turbulence interactions and the rate with which small scales gain or lose turbulent energy via such interactions. This is equation 4.6. Neglecting mean flow velocity differences and

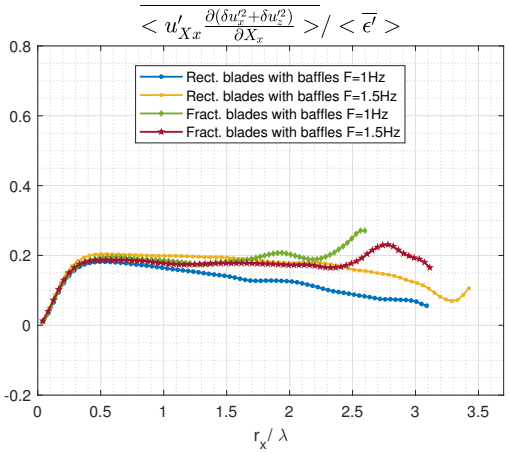

(a) Interspace transport rate $\frac{\partial}{X_x}$ contribution in r_x direction

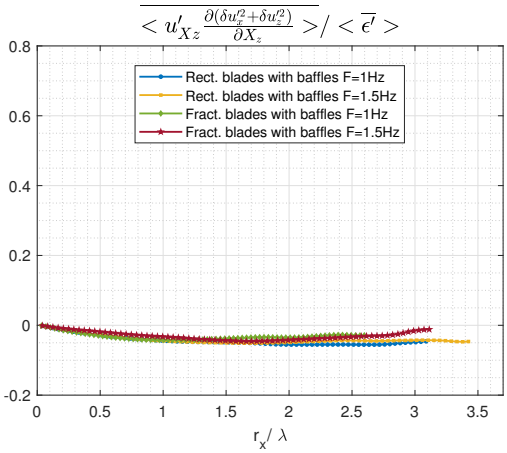

(b) Interspace transport rate $\frac{\partial}{X_z}$ contribution estimate in r_x direction

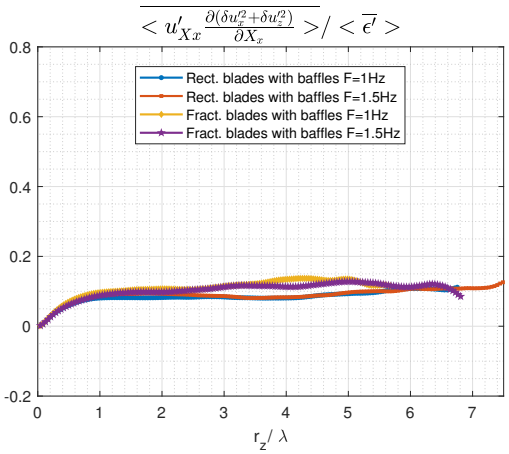

(c) Interspace transport rate $\frac{\partial}{X_x}$ contribution estimate in r_z direction

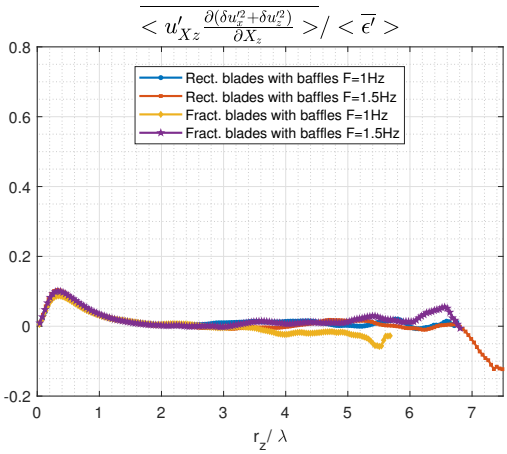

(d) Interspace transport rate $\frac{\partial}{X_z}$ contribution estimate in r_z direction

Figure 4.13: Interspace transport rate

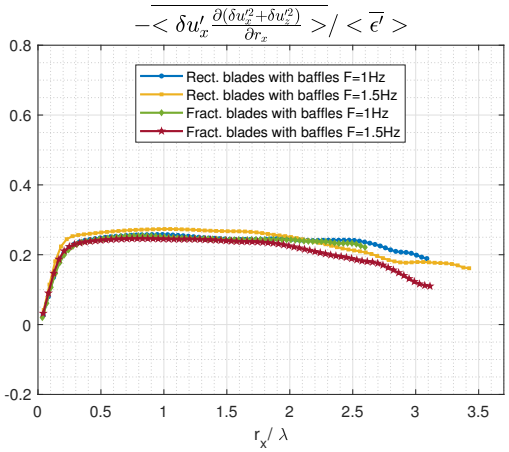

(a) Interscale transfer rate $\frac{\partial}{r_x}$ contribution in r_x direction

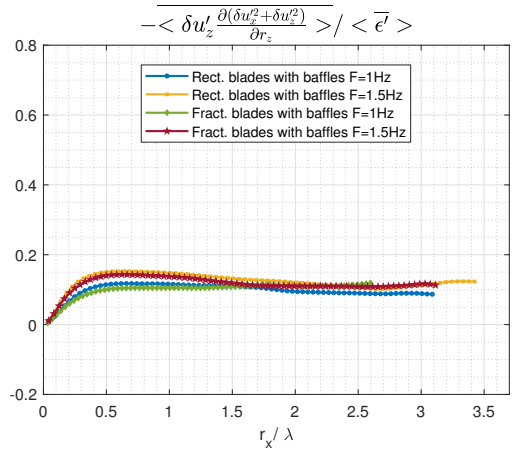

(b) Interscale transfer rate $\frac{\partial}{r_z}$ contribution estimate in r_x direction

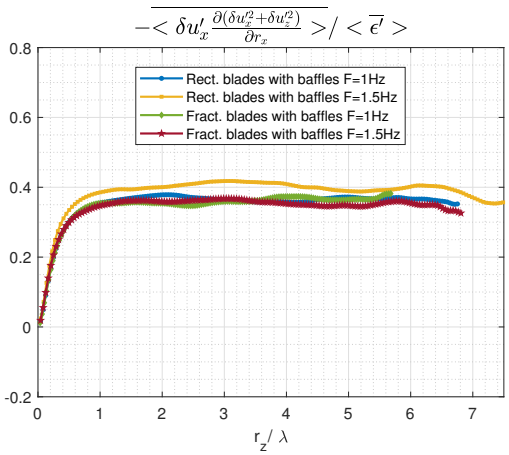

(c) Interscale transfer rate $\frac{\partial}{r_x}$ contribution estimate in r_z direction

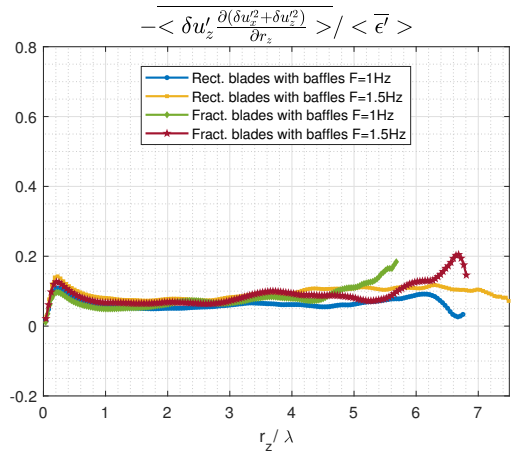

(d) Interscale transfer rate $\frac{\partial}{r_z}$ contribution estimate in r_z direction

Figure 4.14: Interscale transfer rate

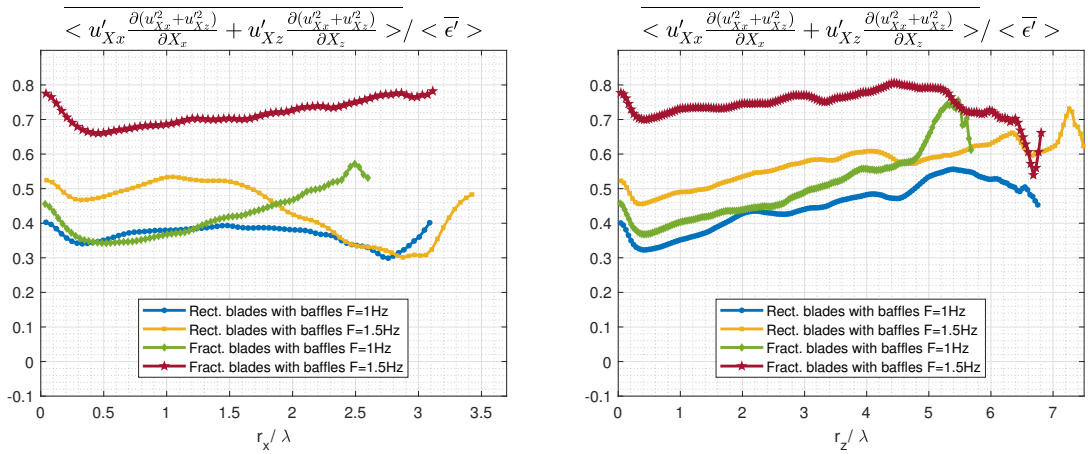

(a) r_x direction (b) r_z direction

Figure 4.15: Interspace transfer estimate of $\boldsymbol{u_X}^2$

two-point turbulence production rates P_r and P^l_{Xr}, as appears to be possible in our PIV's field of view for small two-point separation lengths, equation 4.6 becomes

$$\boldsymbol{\nabla_r} \cdot (\overline{\boldsymbol{\delta u'}|\boldsymbol{\delta u'}|^2}) + \boldsymbol{\nabla_r} \cdot (\overline{\boldsymbol{\delta u'}|\boldsymbol{u_X}'|^2}) = 2\boldsymbol{\nabla_X} \cdot (\overline{\boldsymbol{\delta u'}(\boldsymbol{\delta u'} \cdot \boldsymbol{u'_X})}) \tag{4.57}$$

where $\boldsymbol{\nabla_r} \cdot (\overline{\boldsymbol{\delta u'}|\boldsymbol{u_X}'|^2})$ represents the rate with which large scales lose or gain turbulent energy to or from the small scales and $\boldsymbol{\nabla_r} \cdot (\overline{\boldsymbol{\delta u'}|\boldsymbol{\delta u'}|^2})$ represents the rate with which small-scales gain or lose turbulent energy by the non-linear turbulence interactions (see also the complementary description of these transfer rates under equation 4.6). In general, and in the present flow in particular, the passage of turbulent energy from large to small scales (or vice versa) is not necessarily "impermeable" as energy can leak out of this cascade process because of non-homogeneities, in the present case by the spatial gradient term on the right hand side of 4.57.

In figures 4.16a and 4.16b we plot the spatio-temporal average of the part of $\boldsymbol{\nabla_r} \cdot (\overline{\boldsymbol{\delta u'}|\boldsymbol{u_X}'|^2})$ that is accessible to our 2D2C PIV, namely $\langle \overline{\delta u'_x \frac{\partial}{\partial r_x}(u'^2_{Xx} + u'^2_{Xz})} \rangle + \langle \overline{\delta u'_z \frac{\partial}{\partial r_z}(u'^2_{Xx} + u'^2_{Xz})} \rangle$. We plot it normalised by $\langle \overline{\epsilon'} \rangle$ versus both r_x/λ and r_z/λ and we note that it collapses well for the four different configurations. Furthermore, it appears to have a constant value across the same ranges $\lambda/2 \leq r_x \leq 2\lambda$ and $\lambda/2 \leq r_z \leq 5\lambda$ where the part of the spatio-temporal average of $\boldsymbol{\nabla_r} \cdot (\overline{\boldsymbol{\delta u'}|\boldsymbol{\delta u'}|^2})$ that is accessible to our PIV has an approximately collapsed constant value (figure 4.11). This suggests a strong link between these two turbulent energy transfer rates.

The positive constant value of $\langle \overline{\delta u'_x \frac{\partial}{\partial r_x}(u'^2_{Xx} + u'^2_{Xz})} \rangle / \langle \overline{\epsilon'} \rangle + \langle \overline{\delta u'_z \frac{\partial}{\partial r_z}(u'^2_{Xx} + u'^2_{Xz})} \rangle / \langle \overline{\epsilon'} \rangle$ (see figure 4.16) is slightly lower than the magnitude of the negative constant value of $\langle \overline{\delta u'_x \frac{\partial}{\partial r_x}(\delta u'^2_x + \delta u'^2_z)} \rangle / \langle \overline{\epsilon'} \rangle + \langle \overline{\delta u'_z \frac{\partial}{\partial r_z}(\delta u'^2_x + \delta u'^2_z)} \rangle / \langle \overline{\epsilon'} \rangle$ (see figure 4.11). If this experimental

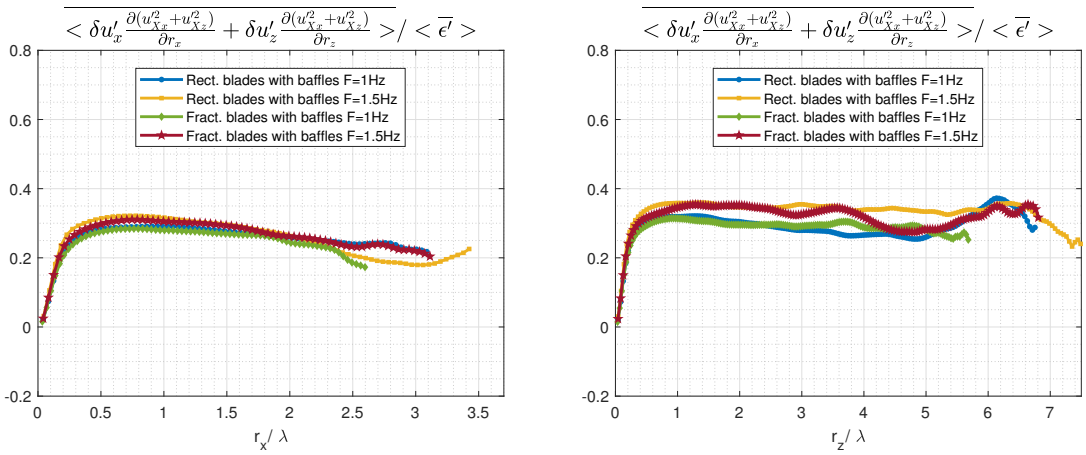

(a) r_x direction (b) r_z direction

Figure 4.16: Interscale transfer estimate of $\boldsymbol{u_X}^2$

observation reflects a similar difference between $\boldsymbol{\nabla_r}.(\overline{\boldsymbol{\delta u'}|\boldsymbol{u_X}'|^2})$ and $\boldsymbol{\nabla_r}.(\overline{\boldsymbol{\delta u'}|\boldsymbol{\delta u}'|^2})$ then the interpretation will have to be that large scales lose energy to small scales but that the small scales receive more of the energy lost by the large ones because some energy is transported from elsewhere in physical space without changing scale. In the kinematic equation 4.57, this energy leak away from the interscale turbulent energy transfer process is accounted for by $2\boldsymbol{\nabla_X}.(\overline{\boldsymbol{\delta u'}(\boldsymbol{\delta u'}.\boldsymbol{u'_X})})$ which can be non-zero in non-homogeneous turbulence (or, more generally, by all the other terms present in equation 4.6 if they cannot be neglected).

The experimental results presented in figures 4.16a and 4.16b may be reflecting a proportionality

$$\boldsymbol{\nabla_r}\cdot < \boldsymbol{\delta u'}|\boldsymbol{u_X}'|^2 > \sim < \epsilon' > \tag{4.58}$$

which cannot be confirmed or invalidated with our 2D2C PIV. This proportionality concerns interscale energy transfer within the large-scale turbulent energy budget and is additional to the proportionalities 4.52, 4.53, 4.54 obtained in the previous section on the basis of the small-scale turbulent energy budget. The previous section's theory does not give the proportionality coefficients of these relations. In the following section we present an hypothesis which has the power, if and when valid, to determine some such proportionality coefficients.

4.10 A local small-scale homogeneity hypothesis

We consider statistically stationary non-homogeneous turbulence by comparison to the case of statistically homogeneous non-stationary turbulence which we addressed in section 4.3 (equations 4.7 to 4.12). Statistical stationarity is meant in the Lagrangian sense of

following the mean flow, i.e. $\overline{\boldsymbol{u_X}}.\boldsymbol{\nabla_X}\frac{1}{2}\overline{|\boldsymbol{\delta u'}|^2} = 0 = \overline{\boldsymbol{u_X}}.\boldsymbol{\nabla_X}\frac{1}{2}\overline{|\boldsymbol{u'_X}|^2}$. This is indeed the case in the present flows because the mean flow velocity is vertical (i.e. in the z direction) and the turbulence varies mainly in the horizontal direction. With this statistical stationarity and by considering scales $|\mathbf{r}|$ large enough to neglect viscous diffusion, fluctuating energy equations 4.2 and 4.4 become, respectively,

$$\begin{aligned}&\boldsymbol{\delta\overline{u}}.\boldsymbol{\nabla_r}\frac{1}{2}\overline{|\boldsymbol{\delta u'}|^2} - P_r - P^s_{Xr} + \boldsymbol{\nabla_X}\cdot\left(\overline{\boldsymbol{u_X}'\frac{1}{2}|\boldsymbol{\delta u'}|^2} + \overline{\boldsymbol{\delta u'}\delta p'}\right)\\ &\approx -\boldsymbol{\nabla_r}.(\overline{\boldsymbol{\delta u}'\frac{1}{2}|\boldsymbol{\delta u'}|^2}) - \frac{\nu}{4}\overline{\frac{\partial u_i'^+}{\partial\zeta_k^+}\frac{\partial u_i'^+}{\partial\zeta_k^+}} - \frac{\nu}{4}\overline{\frac{\partial u_i'^-}{\partial\zeta_k^-}\frac{\partial u_i'^-}{\partial\zeta_k^-}}\end{aligned} \tag{4.59}$$

and

$$\begin{aligned}&\boldsymbol{\delta\overline{u}}.\boldsymbol{\nabla_r}\frac{1}{2}\overline{|\boldsymbol{u'_X}|^2} - P_X - P^l_{Xr} + \boldsymbol{\nabla_X}\cdot\left(\overline{\boldsymbol{u_X}'\frac{1}{2}|\boldsymbol{u_X}'|^2} + \overline{\boldsymbol{u_X}'p'_X}\right)\\ &\approx -\boldsymbol{\nabla_r}.(\overline{\boldsymbol{\delta u}'\frac{1}{2}|\boldsymbol{u_X}'|^2}) - \frac{\nu}{4}\overline{\frac{\partial u_i'^+}{\partial\zeta_k^+}\frac{\partial u_i'^+}{\partial\zeta_k^+}} - \frac{\nu}{4}\overline{\frac{\partial u_i'^-}{\partial\zeta_k^-}\frac{\partial u_i'^-}{\partial\zeta_k^-}}\end{aligned} \tag{4.60}$$

We formulate an hypothesis of local homogeneity as a parallel to Kolmogorov's small-scale stationarity hypothesis (see section 3). Whereas most terms on the left hand side of equation 4.60 do not tend to 0 as $\boldsymbol{r}$ tends to 0, the left hand side of 4.59 does tend to 0 in that limit. The local small-scale homogeneity hypothesis that we make is the hypothesis that in the limit of increasing Reynolds number, the magnitude of $\boldsymbol{\delta\overline{u}}.\boldsymbol{\nabla_r}\frac{1}{2}\overline{|\boldsymbol{\delta u'}|^2} - P_r - P^s_{Xr} + \boldsymbol{\nabla_X}\cdot\left(\overline{\boldsymbol{u_X}'\frac{1}{2}|\boldsymbol{\delta u'}|^2} + \overline{\boldsymbol{\delta u'}\delta p'}\right)$ is increasingly smaller than the local time-averaged turbulence dissipation rate at small enough scales $|\boldsymbol{r}|$. With this hypothesis, and with the approximation $\frac{\nu}{4}\overline{\frac{\partial u_i'^+}{\partial\zeta_k^+}\frac{\partial u_i'^+}{\partial\zeta_k^+}} + \frac{\nu}{4}\overline{\frac{\partial u_i'^-}{\partial\zeta_k^-}\frac{\partial u_i'^-}{\partial\zeta_k^-}} \approx \overline{\epsilon'}$ which is acceptable at small enough $|\boldsymbol{r}|$, the small-scale turbulent energy balance 4.59 simplifies to

$$\boldsymbol{\nabla_r}.(\overline{\boldsymbol{\delta u}'|\boldsymbol{\delta u'}|^2}) \approx -\overline{\epsilon'} \tag{4.61}$$

in an intermediate range of scales large enough to neglect viscous diffusion but small enough to neglect small-scale non-homogeneity. This balance incorporates the proportionality 4.53 but also sets the proportionality constant to -1. The similarity hypotheses required to obtain 4.53 are weaker than the local small-scale homogeneity hypothesis introduced here. A priori, they can be valid even if and when the local small-scale homogeneity hypothesis is not. When $\boldsymbol{\delta\overline{u}}$, P_r and P^s_{Xr} are negligible at small enough $|\boldsymbol{r}|$, as appears to be the case in the flow regions considered here, the local small-scale homogeneity hypothesis implies that the magnitude of $\boldsymbol{\nabla_X}\cdot\left(\overline{\boldsymbol{u_X}'\frac{1}{2}|\boldsymbol{\delta u'}|^2} + \overline{\boldsymbol{\delta u'}\delta p'}\right)$ is increasingly small compared to $\overline{\epsilon'}$ with increasing Reynolds number for small enough values of $|\boldsymbol{r}|$. It may be that, as the Reynolds number tends to infinity, 4.53 tends to 4.61 thereby recovering Kolmogorov's scale-by-scale equilibrium for homogeneous turbulence at small enough scales and implying that

this Kolmogorov equilibrium is a very particular case of 4.53. However, it is not clear how such a statement could be established at the current time and the foreseeable future.

We now use the kinematic relation 4.57, but we could also use its more general form 4.6 if we did not want to neglect $\boldsymbol{\delta\overline{u}}$, P_r and P^l_{Xr} from the outset. From 4.57 and 4.61 follows

$$\boldsymbol{\nabla_r}.\overline{\boldsymbol{\delta u'}|\boldsymbol{u'_X}|^2} \approx \overline{\epsilon'} + 2\boldsymbol{\nabla_X}\cdot(\overline{\boldsymbol{\delta u'}(\boldsymbol{\delta u'}\cdot\boldsymbol{u'_X})}) \tag{4.62}$$

which is the analogue for stationary non-homogeneous turbulence of the Germano-Hosokawa relation 4.11 for homogeneous non-stationary (in fact freely decaying) turbulence.

Finally, the analogue of 4.12 for stationary non-homogeneous turbulence is obtained from 4.62 and 4.60 and it is

$$-P_X - P^l_{Xr} + \boldsymbol{\nabla_X}\cdot\left(\overline{\boldsymbol{u_X}'\frac{1}{2}|\boldsymbol{u_X}'|^2} + \overline{\boldsymbol{u_X}'p'_X} + \overline{\boldsymbol{\delta u'}(\boldsymbol{\delta u'}\cdot\boldsymbol{u'_X})}\right) \approx -\overline{\epsilon'}. \tag{4.63}$$

Like equation 4.61, equations 4.62 and 4.63 hold in an intermediate range of scales large enough to neglect viscous diffusion and small enough to neglect small-scale non-homogeneity. Note that equation 4.63 identifies a statistic characterising non-homogeneity which is proportional to $\overline{\epsilon'}$ with proportionality coefficient -1. This statistic is not captured by the non-equilibrium theory of non-homogeneous turbulence of section 4.8. In this case, the hypothesis of local small-scale homogeneity makes a prediction concerning turbulence non-homogeneity which is not accessible to the theory of section 4.8.

In appendix A.2, a detailed picture of Kolmogorov-like turbulence in non-homogeneous flows is derived in a more theoretical framework (without Reynolds decomposition) to relate the physical understanding of these new results with the theoretical introduction in chapter 2. These side results are not part of the submitted publication.

4.11 Chapter conclusion

We have studied a turbulent flow region under rotating blades in a baffled container where the baffles break the rotation in the flow. The evidence from our 2D2C PIV supports the view that, within our PIV's field of view, two-point production makes a negligible contribution to the small-scale energy equation 4.2 over a range of small two-point separation lengths. In the absence of such production, we may assume the non-linear and non-local dynamics of the small-scale turbulence to be effectively the same at different places. We have therefore made the similarity hypothesis that every term in the non-homogeneous but statistically stationary scale-by-scale (two-point) small-scale energy balance 4.21 has the same dependence on two-point separation at different positions $\mathbf{X}$ if rescaled by $\mathbf{X}$-local velocity and length scales. Following the theory of Chen and Vassilicos 2022 we have introduced such similarity hypotheses for both inner and outer scales and have considered intermediate matchings. We

have also improved the theory (i) by deriving the inner-outer equivalence hypothesis of Chen and Vassilicos 2022 for turbulence dissipation from a more intuitively natural hypothesis and (ii) by taking explicit account of non-homogeneity in the inner to outer velocity ratios, thereby extending the theory's applicability range and removing the need for the theoretical adjustments in the Appendix of Chen and Vassilicos 2022.

This non-equilibrium theory of non-homogeneous small-scale turbulence predicts that an intermediate range of length-scales exists where the interscale turbulence transfer rate, the two-point interspace turbulence transport rate and the two-point pressure gradient velocity correlation term in equation 4.21 are all proportional to the turbulence dissipation rate. Given the limitations of 2D2C PIV we have been able to measure only parts (truncations) of the interscale turbulence transfer rate and the two-point interspace turbulence transport rate in equation 4.21. This has forced us to introduce inner and outer hypotheses of isotropic similarity applicable to the truncations accessible to our measurements. With these hypotheses (which should not be confused with hypotheses of isotropy) the theory leads to the same predictions for the 2D2C PIV-truncated interscale turbulence transfer rate and two-point interspace turbulence transport rate in equation 4.21. Our 2D2C PIV measurements suggest that these truncations may indeed be independent of two-point separation scale and be proportional to the average turbulence dissipation rate over a more or less overlapping range of scales as predicted by the theory. The PIV-truncated two-point interspace turbulence transport rate is significantly non-zero, thereby reflecting both the presence of small-scale non-homogeneity and the absence of Kolmogorov scale-by-scale equilibrium. Its proportionality with the turbulence dissipation rate is evidence that small-scale non-homogeneity and non-equilibrium do actually obey general rules.

The PIV-truncated average interscale transfer rate of small-scale turbulent energy is negative, suggesting forward cascade if the corresponding full (non-truncated) average interscale transfer rate has the same sign, and the PIV-truncated average interspace turbulent transfer rate of small-scale turbulence energy is positive, suggesting outward turbulent transport of small-scale turbulence if the corresponding full (non-truncated) average interspace turbulent transfer rate is also positive.

We have also applied hypotheses of inner and outer similarity as well as inner and outer isotropic similarity to second order structure functions of turbulent fluctuating velocities. Inner-outer intermediate matching has led to the prediction of power law dependencies on turbulence dissipation rate and two-point separation length with power law exponent $n = 2/3$. The 2D2C PIV has provided support for this Kolmogorov-like value of the exponent in the r_x direction but not in the r_z direction where the PIV suggests an exponent n between 0.5 and 0.6. Future studies should investigate whether rotation, even if effectively faint within our field of view because of the rotation-breaking effect of the baffles, may require similarity forms in terms of more than one outer length scale l_O and more than one inner length scale

l_I, depending on direction. The value of the exponent n impacts only the Reynolds number dependencies of l_I/l_O and V_I/V_O and has no direct impact on the other predictions of the theory. The exponent $n = 2/3$ implies the Kolmogorov-like scalings 4.48 and 4.49.

The large-scale turbulent energy budget 4.4 is very different from the small-scale turbulent energy budget 4.2 both in terms of production and interspace turbulence transport which are both non-zero in the limit of zero two-point separation lengths when the turbulence is inhomogeneous. We have therefore not applied to 4.4 the similarity approach that we applied to 4.2. However, we have taken advantage of the kinematic relation which exists between the rate with which large scales gain or lose turbulent energy to the small scales via non-linear turbulence interactions (present in 4.4) and the rate with which small scales gain or lose turbulent energy via such interactions (present in 4.2). The PIV-truncated part of the rate with which large scales gain or lose turbulent energy to the small scales has turned out to be approximately independent of two-point separation scale and proportional to the average turbulence dissipation rate over the same range of scales where the PIV-truncated interscale transfer rate in 4.2) exhibites the same behaviour. However, these two transfer rates do not balance, which suggests that the transfer of turbulent energy from large to small scales (or vice versa) may not be "impermeable" in the sense that energy may be leaking out of this cascade process because of non-homogeneities, in the present case by the spatial gradient term on the right hand side of 4.57.

Our non-equilibrium theory of non-homogeneous turbulence does not give the proportionality coefficients in 4.52, 4.53 and 4.54. We have therefore introduced a local small-scale homogeneity hypothesis in section 4.10 as a space analogue of Kolmogorov's small-scale stationarity hypothesis but do not have criteria, at this stage, for the validity of this small-scale homogeneity hypothesis. If and when this new hypothesis may hold (perhaps in the limit of infinite Reynolds numbers?) the coefficient of proportionality in 4.53 will be -1.

Chapter 5

Non-Kolmogorov turbulence in non-homogeneous rotating flow

5.1 Introduction

In chapter 4, the Chen and Vassilicos 2022 theory is improved and used to explain the Kolmogorov-like results measured in non-homogeneous (non-rotating) turbulence inside a mixer where Kolmogorov theory is not expected to hold. This theory provides predictions for the structure functions and for the energy terms present in the two-point Kármán-Howarth-Monin-Hill equation. In the following chapter, a rotating flow inside the same mixer is analyzed experimentally. The rotation effect is evaluated in comparison with the results and theory of chapter 4. First, the structure functions are characterized and the differences between rotating and non-rotating results are analyzed in light of the Chen and Vassilicos 2022 theory assumptions when possible. Then, the two-point statistics of the two-point equations are presented to characterize the rotation effect on the energy cascade and more generally on all the energy terms measured.

5.2 Experimental measurements

The experimental set-up and measurements are presented in detail in chapter 3. Both baffle and non-baffle configurations results are used in this chapter.

Defining parameters

The defining parameters of the experiment are presented in table 5.1. The rotation frequency F is between 1Hz and 3Hz. The global Reynolds number is $Re = \frac{2\pi F R^2}{\nu}$. where $R = D/2 \approx 11.25cm$ is an estimate of the rotor radius. Re is large, higher than 8.10^4 in all

cases, and the flow is therefore turbulent.

The Rossby number is defined in section 3.7.5. Our values of Ro range between 0.12 and 0.15 for non-baffled configurations and between 0.32 and 0.4 for baffled configurations. The smaller Rossby number for the non-baffled cases means that the rotation affects the turbulence more for these configurations than for the baffled configurations. Moreover, the rotor rotation speed Ω is not representative of the flow rotation in the case of the baffled configurations because the baffles break the flow rotation as explained in Nagata 1975. Therefore, the nominal Rossby number is most probably significantly underestimated for these configurations. The difference between baffled and non-baffled configurations is therefore much greater than the nominal Rossby number values suggest.

Basic turbulent flow properties

The main turbulent parameters are presented in table 5.2. They include the turbulence dissipation rate $\langle\overline{\epsilon'}\rangle$ averaged over time (overbar) and over the space in our field of view (brackets), the resulting Kolmogorov length-scale η and the Taylor length λ. These parameters are provided as reference and are used in this chapter to non-dimensionalise results.

The Taylor length-based Reynolds number Re_λ is higher than 410 in all configurations. All the eight flows that we study are therefore highly turbulent. Re_λ values are comparable between most baffled and non-baffled configurations, so no significant Reynolds effect is expected in the comparison between baffled and non-baffled results.

In figure 5.2a, we plot the mean flow velocity for one of our four non-baffled configurations but the plot is representative of the four configurations. The mean flow velocity is oriented horizontally from right to left and is very small in magnitude. These observations evidence the solid body rotation identified in Nagata 1975 and shown schematically in figure 5.1a. The solid body rotation appears in the measurement domain because of the small measurement offset in y direction previously described in section 3.5. In figure 5.2b, we plot the mean flow velocity of one representative baffled configuration. The mean flow velocity is oriented vertically from bottom to top and is significant. This observation is consistent with the mean

	F (Hz)	Re	vel rms (m/s)	Ro	Mean torque (N.m)
Rectangular blades	2	1.6×10^5	6.0×10^{-2}	0.12	0.42
Rectangular blades	3	2.5×10^5	9.2×10^{-2}	0.12	0.74
Fractal blades	2	1.6×10^5	7.8×10^{-2}	0.15	0.40
Fractal blades	2.5	2.0×10^5	9.6×10^{-2}	0.15	0.54
Rectangular blades with baffles	1	9.8×10^4	1.0×10^{-1}	0.36	0.53
Rectangular blades with baffles	1.5	1.3×10^5	1.6×10^{-1}	0.40	1.1
Fractal blades with baffles	1	8.6×10^4	9.1×10^{-2}	0.32	0.41
Fractal blades with baffles	1.5	1.2×10^5	1.4×10^{-1}	0.34	0.81

Table 5.1: Main parameters of the experiment: vel rms (m/s) stands for $\sqrt{< u_x'^2 > + < u_z'^2 >}$

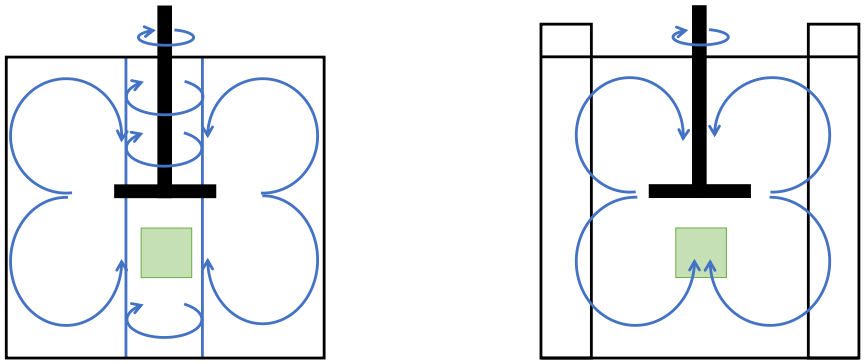

(a) Flow without baffles (b) Flow with baffles

Figure 5.1: Schematic of mean flow in a mixer with and without baffles (Nagata 1975). The measurement plane is shown as a green square.

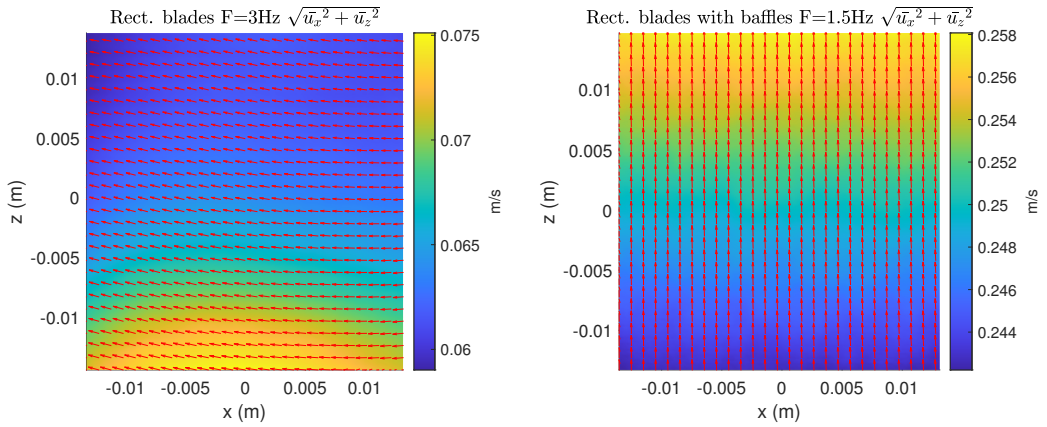

(a) Rectangular blade without baffles (b) Rectangular blade with baffles

Figure 5.2: Mean flow measurement within the measurement planes shown in figure 5.1

flow structure described in Nagata 1975 and shown in figure 5.1b.

5.3 Results

5.3.1 Second order structure functions: measurements

We start with the analysis of the structure functions to compare the turbulence properties of the flow with baffles (non-rotating flow) and without baffles (rotating flow). We compute the normalized structure functions $\langle \overline{(\delta u_j')^2} / \overline{\epsilon'}^{2/3} \rangle$ for $j = 1$ (velocity fluctuations along the x-axis) and $j = 3$ (velocity fluctuations along the z-axis) by averaging over time, i.e. over our 150,000 samples (which correspond to 50,000 uncorrelated samples) and also averaging over $\boldsymbol{X}$, i.e. over the planar space of our field of view. The additional averaging over space

	$F(Hz)$	$\langle\overline{\epsilon'}\rangle$ (m^2/s^3)	$\eta(m)$	$\lambda(m)$	Re_λ
Rectangular blades	2	6.0×10^{-4}	2.0×10^{-4}	6.6×10^{-3}	4.1×10^2
Rectangular blades	3	2.1×10^{-3}	1.4×10^{-4}	5.3×10^{-3}	5.2×10^2
Fractal blades	2	1.3×10^{-3}	1.6×10^{-4}	5.8×10^{-3}	4.6×10^2
Fractal blades	2.5	2.3×10^{-3}	1.5×10^{-4}	5.5×10^{-3}	5.3×10^2
Rectangular blades with baffles	1	3.6×10^{-3}	1.1×10^{-4}	4.1×10^{-3}	5.1×10^2
Rectangular blades with baffles	1.5	1.2×10^{-2}	8.8×10^{-5}	3.7×10^{-3}	6.5×10^2
Fractal blades with baffles	1	2.4×10^{-3}	1.3×10^{-4}	4.9×10^{-3}	4.8×10^2
Fractal blades with baffles	1.5	8.2×10^{-3}	1.0×10^{-4}	4.1×10^{-3}	5.8×10^2

Table 5.2: Main turbulence parameters. The Kolmogorov length scale is calculated as $\eta \equiv (\nu^3/\langle\overline{\epsilon'}\rangle)^{1/4}$.

is necessary for very good convergence of our statistics but these statistics are also computed without space averaging in this section.

In figure 5.3 we plot the compensated structure functions $\langle\overline{(\delta u'_x)^2}/\overline{\epsilon'}^{2/3}\rangle$ $(j = 1)$ versus r_x/D (figure 5.3a) and versus r_z/D (figure 5.3b) and $\langle\overline{(\delta u'_z)^2}/\overline{\epsilon'}^{2/3}\rangle$ $(j = 3)$ versus r_x/D (figure 5.3c) and versus r_z/D (figure 5.3d). The average turbulence dissipation rate $\langle\overline{\epsilon'}\rangle$ varies by a factor larger than 4 across our four different baffled configurations and by a factor larger than 3 across the four non-baffled configurations (see table 5.2). Therefore, figure 5.3 suggests some tendency toward a collapse of the compensated structure functions in both groups but it is more visible for the baffled configurations. However, the collapse is not very sensitive to the exponent of $\overline{\epsilon'}$ so the exact value of the exponent cannot be estimated with certainty just with these results.

A significantly different evolution with r is observed in figure 5.3 between configurations with and without baffles. A close to $r^{2/3}$ power-law behavior is identified for the baffled configurations results with a close to plateau or a slowly varying linear slope measured for $\langle\overline{(\delta u'_x)^2}/\overline{\epsilon'}^{2/3}\rangle.r^{-2/3}$ and $\langle\overline{(\delta u'_z)^2}/\overline{\epsilon'}^{2/3}\rangle.r^{-2/3}$ in both r_x and r_z directions. This behavior is described in more detail in chapter 4. The non-baffled configuration normalized structure functions have a very different behavior, clearly far from a $r^{2/3}$ power-law. Indeed, a significantly non-constant and non linear behavior is detected for $\langle\overline{(\delta u'_x)^2}/\overline{\epsilon'}^{2/3}\rangle.r^{-2/3}$ and $\langle\overline{(\delta u'_z)^2}/\overline{\epsilon'}^{2/3}\rangle.r^{-2/3}$ in the r_x and r_z directions (see figure 5.3). Therefore, the flow rotation seems to affect significantly the turbulence properties. This is not a Reynolds number effect as Re_λ values are comparable between baffled and non-baffled configurations (see table 5.2). The same results are obtained for $\langle\overline{(\delta u'_j)^2}\rangle/\langle\overline{\epsilon'}^{2/3}\rangle$ where the spatial averaging is applied to the individual terms (not shown for economy of space) which means the r dependence is the same for $\langle\overline{(\delta u'_j)^2}\rangle/\langle\overline{\epsilon'}^{2/3}\rangle$ and $\langle\overline{(\delta u'_j)^2}/\overline{\epsilon'}^{2/3}\rangle$.

To look at the power law scaling in more detail, we estimate the logarithmic slopes q of $\langle\overline{(\delta u'_x)^2}\rangle$ and $\langle\overline{(\delta u'_z)^2}\rangle$ versus both r_x and r_z, i.e. $\frac{dlog\langle\overline{(\delta u'_x)^2}\rangle}{dlogr_x}$, $\frac{dlog\langle\overline{(\delta u'_x)^2}\rangle}{dlogr_z}$, $\frac{dlog\langle\overline{(\delta u'_z)^2}\rangle}{dlogr_x}$ and $\frac{dlog\langle\overline{(\delta u'_z)^2}\rangle}{dlogr_z}$, which we plot versus r_x and r_z respectively in figures 5.4 and 5.5. For the baffled

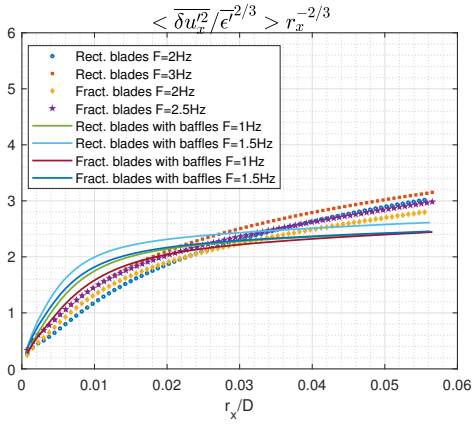

(a) Normalized $< \overline{\delta u_x'^2} >$ in r_x direction

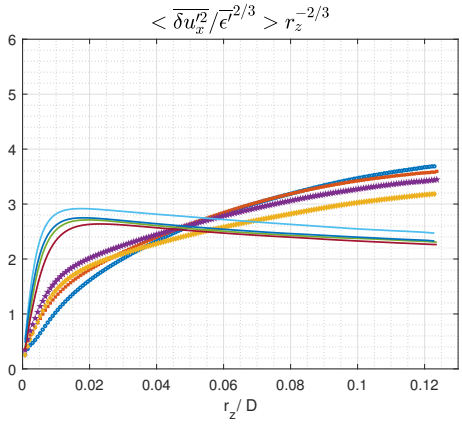

(b) Normalized $< \overline{\delta u_x'^2} >$ in r_z direction

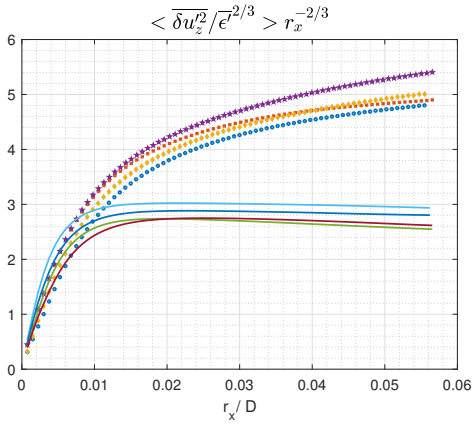

(c) Normalized $< \overline{\delta u_z'^2} >$ in r_x direction

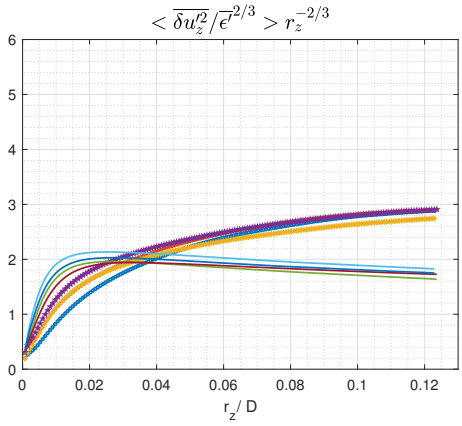

(d) Normalized $< \overline{\delta u_z'^2} >$ in r_z direction

Figure 5.3: Normalized structure functions $< \overline{\delta u_x'^2} >$ and $< \overline{\delta u_z'^2} >$ compensated by $r^{-2/3}$ versus r_x/D in (a) and (c) and versus r_z/D in (b) and (d)

configurations, a well-defined plateau appears in both directions for $r_x, r_z \ll D$ with an exponent q between 0.5 and 0.8 (close to the theoretical value 2/3). More details about the baffled configurations are provided in chapter 4. For the configurations without baffles and with either fractal blades at 2Hz and 3Hz or rectangular blades at 3Hz, a plateau is observed for the logarithmic slopes of $\langle\overline{(\delta u'_x)^2}\rangle$ in the ranges $0.026 \leq r_x/D \leq 0.05$ and $0.02 \leq r_z/D \leq 0.06$ with a value of q close to 1 (between 0.9 and 1.1). Therefore, for these non-baffled configurations, a significantly clear power-law behavior is identified for $\langle\overline{(\delta u'_x)^2}\rangle$ but with a significantly steeper slope than for the baffled configurations. For the configuration without baffles and with rectangular blades at 2Hz, it is hard to detect the presence of a constant exponent q over a significant range of scales either in r_x or r_z directions. This difference from the other configurations is not clearly understood as neither are several other results in this chapter for this peculiar configuration. This configuration has the smallest Re_λ (see table 5.2) but not to much small to explain why it is so different. More practically, a more significant experimental noise may be present in the results for this configuration as the turbulence signal is weaker than in other configurations (the turbulence dissipation rate signal for example is much weaker).

The logarithmic slopes of $\langle\overline{(\delta u'_z)^2}\rangle$ for the non-baffled configurations have significant variations between 0.7 and 0.9 in both r_x and r_z directions and therefore no range of constant q value. These results mean these structure functions cannot be approximated by a power law as opposed to the results for $\langle\overline{(\delta u'_x)^2}\rangle$ which can (with the exception of the rectangular blades with $F = 2Hz$ configuration). A r^1 behavior of the structure functions $\langle\overline{(\delta u'_x)^2}\rangle$ is equivalent to a k^{-2} power-law behavior of the energy spectrum. Therefore, our results are consistent with the k^{-2} energy spectrum slope identified in Herbert et al. 2012 at 'low Reynolds' in the azimutal direction of the rotation plane in a Von-Kármán tank ($Re = \frac{2\pi f R^2}{\nu} \approx 10^4$, where f is the rotation frequency of the Von-Kármán flow and R the cylinder radius). No clear scaling is observed in their results for the vertical component similarly to our measurements results.

The identification of a power-law behavior questions the non-dimensionalisation previously used. Indeed, $\langle\overline{(\delta u'_x)^2}/\overline{\epsilon'}^{2/3}\rangle \sim r_j^q$ or $\langle\overline{(\delta u'_x)^2}\rangle/\langle\overline{\epsilon'}\rangle^{2/3} \sim r_j^q$ is not dimensionally correct for $q \neq 2/3$ so another variable with independent dimension should be introduced. The rotation frequency is likely to affect the turbulence properties as previously introduced so it is used to build a relation based on dimensional analysis which is consistent with a power-law behavior in rotating turbulence:

$$\langle\overline{(\delta u'_i)^2}.(\overline{\epsilon'})^{-1+q/2}\rangle F^{1-3q/2} \sim r_j^q \tag{5.1}$$

The results are presented in figures 5.6 and 5.7 where $q \approx 1$ and an acceptable collapse of the results is obtained for $\langle\overline{(\delta u'_x)^2}/\overline{\epsilon'}^{1/2}\rangle F^{-1/2}$ in figures 5.6a and 5.6b in both r_x and r_z directions. The linear behavior is also clearly visible in figure 5.6. The plots of $\langle\overline{(\delta u'_z)^2}/\overline{\epsilon'}^{1/2}\rangle F^{-1/2}$

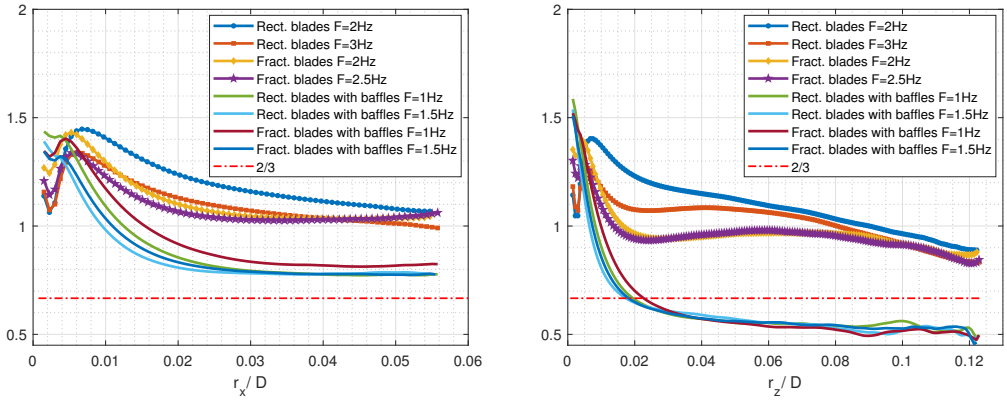

(a) r_x direction (b) r_z direction

Figure 5.4: Logaritmic slope q of the structure function $< \overline{\delta u_x'^2} >$ along two radial directions computed as $\frac{\partial log(<\overline{\delta u_x'^2}>)}{\partial log(r_j)} = f(r_j)$. $< \overline{\delta u_x'^2} >= f(r_j)$ is obtained by averaging $\delta u_x'^2$ over 150,000 samples in time corresponding to 50,000 uncorrelated and averaging over the spatial domain. The derivative is estimated with a centered scheme $\frac{log(<\overline{\delta u_x'^2}(r_j+dr_j)>)-log(<\overline{\delta u_x'^2}(r_j-dr_j)>)}{log(r_j+dr_j)-log(r_j-dr_j)}$.

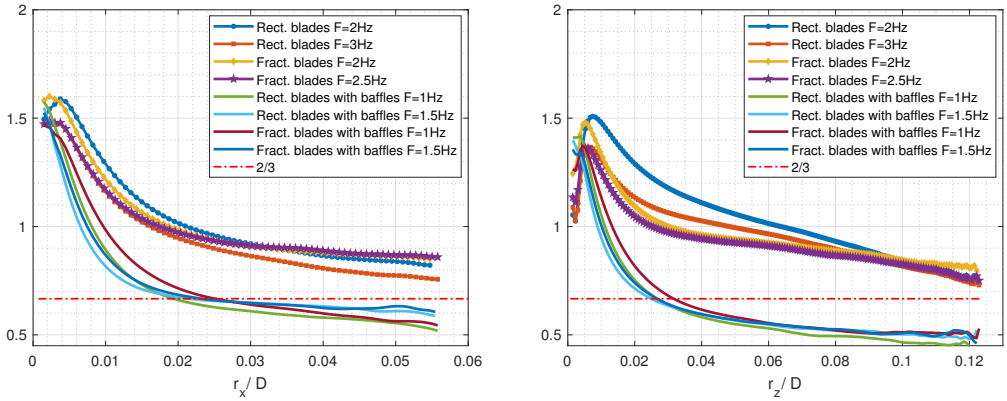

(a) r_x direction (b) r_z direction

Figure 5.5: Logaritmic slope q of the structure function $< \overline{\delta u_z'^2} >$ along two radial directions computed as $\frac{\partial log(<\overline{\delta u_z'^2}>)}{\partial log(r_j)} = f(r_j)$. $< \overline{\delta u_z'^2} >= f(r_j)$ is obtained by averaging $\delta u_z'^2$ over 150,000 samples in time corresponding to 50,000 uncorrelated and averaging over the spatial domain. The derivative is estimated with a centered scheme $\frac{log(<\overline{\delta u_z'^2}(r_j+dr_j)>)-log(<\overline{\delta u_z'^2}(r_j-dr_j)>)}{log(r_j+dr_j)-log(r_j-dr_j)}$.

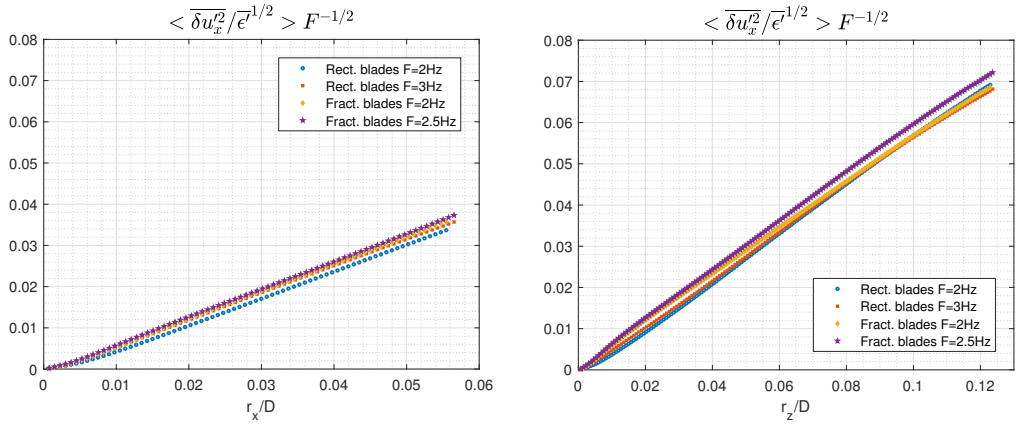

(a) r_x direction (b) r_z direction

Figure 5.6: Structure function $< \overline{\delta u_x'^2} >$ normalized by $\left(F\overline{\epsilon'}\right)^{1/2}$ along two radial directions.

in figures 5.7a and 5.7b do not show a good collapse of the fractal and the rectangular blades results. Moreover, the shape is not perfectly linear (particularly for rectangular blades) as anticipated with the previous $\overline{(\delta u_z')^2}$ logarithmic slope results. This explains also why this normalization does not collapse the $\overline{(\delta u_z')^2}$ results as it is only adapted for linear structure functions where $q \approx 1$.

Overall, a clear difference of structure function behaviors is identified and quantified between baffled and non-baffled configurations and it can be associated to flow rotation. The baffled results are explained in chapter 4 with a theory initially introduced in Chen and Vassilicos 2022 and improved here. Therefore, in the next section, the main steps of this theory are revisited to see which assumption is broken by the rotation effect causing the structure functions not to have the $r^{2/3}$ power law behavior that is present in the baffled configuration.

5.3.2 Second order structure functions: Chen and Vassilicos 2022 theory

For the baffled configurations, we have assumed that the non-linear and non-local dynamics of the small-scale turbulence are similar at different places within a local region. The approach of Chen and Vassilicos 2022 has been adopted which is based on inner and outer self-similarity. This theory (and our improvement of it) is described in section 4.7 of chapter 4. The derivation assumes inner/outer similarity of the structure functions and inner outer equivalence for dissipation (which we actually derived from a more basic hypothesis in section 4.8.3). The following second order structure functions behavior is derived without assuming homogeneity:

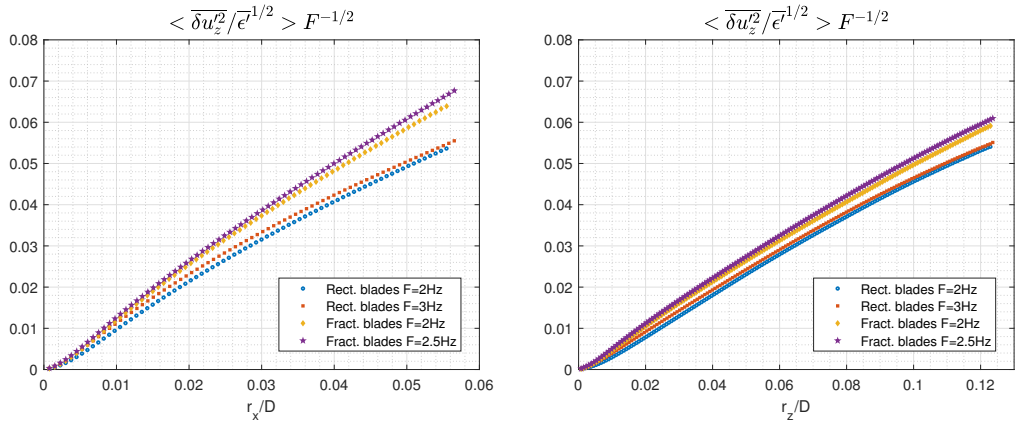

(a) r_x direction (b) r_z direction

Figure 5.7: Structure function $< \overline{\delta u_z'^2} >$ normalized by $\left(F\overline{\epsilon'}\right)^{1/2}$ along two radial directions.

$$\overline{(\delta u_j')^2} = C_j(\overline{\epsilon'}r)^{2/3}F_j(\theta,\phi) \tag{5.2}$$

in the intermediate range $l_I \ll r = |\boldsymbol{r}| \ll l_O$. The dimensionless coefficient C_j may vary with j and with $\boldsymbol{X}$ and the dimensionless function F_j, which is independent of $\boldsymbol{X}$ and of $r \equiv |\boldsymbol{r}|$, may also vary with j.

The structure function results obtained in non-baffled configurations are different from equation 5.2 so the question is to know at which step the theory is no longer applicable in the non-baffled cases? First, are inner and outer similarity in equations 4.22 and 4.23 valid in rotating turbulence? Second, does the inner-outer equivalence for dissipation hold?

The inner and outer similarity equations 4.22 and 4.23 cannot be used without modification in the non-baffled configurations as the flow is highly anisotropic so that we expect to have two inner (resp. outer) scales: l_{Iz} (resp. l_{Oz}) in the vertical direction and l_{Ixy} (resp. l_{Oxy}) in the equivalent rotation plane directions. Therefore, equation 4.27 cannot *a priori* be derived for non-baffled configurations in the same way as for baffled configurations. In the next paragraph, we test the inner similarity of the structure function components to see if inner/outer similarity assumptions can be applied to $\overline{(\delta u_j')^2}$ for each direction so that an equivalent equation to 4.27 may be re-derived for each component in each direction.

The field of view is of limited size in order to have a good spatial resolution so the outer region is not expected to be accessible with our dataset. We expect to see in our measurements the inner range and the inner-outer asymptotic overlap range which is classically observed for $r > \lambda$ (Alves Portela, Papadakis, and Vassilicos 2017) so we focus on the inner region.

The time averaged structure functions at different space locations of one baffled and one non-baffled configuration are plotted in figures 5.8, 5.9 and 5.10. These results are representative of all configurations which are plotted in appendix B.2. The two-point separation vector is limited in size depending on the spatial location so that all the plots do not end at the same point. The largest error bar of all spatial locations is evaluated and assigned to the mean value in red to show an estimate of statistical convergence.

Inspired by the theory in chapter 4, we use the inner scales $l_I = D.Re_O^{-3/4}$ and $V_I = \sqrt{\overline{u_x'^2} + \overline{u_z'^2}}.Re_O^{-1/4}$ where $Re_O = \frac{\sqrt{\overline{u_x'^2}+\overline{u_z'^2}}D}{\nu}$ to non-dimensionalize results. For these configurations, the results collapse within error bars for different space locations in our PIV field of view as $\overline{\delta u_x'^2}/V_I^2 = f(r_x/l_I)$ in figure 5.8a, $\overline{\delta u_x'^2}/V_I^2 = f(r_z/l_I)$ in figure 5.8b and $\overline{\delta u_z'^2}/V_I^2 = f(r_x/l_I)$ in figure 5.9a. Only the baffled results collapse acceptably well for $\overline{\delta u_z'^2}/V_I^2 = f(r_z/l_I)$ in figure 5.9b. For these results, the spatial dependence remains small or negligible (variation of l_I and V_I between 1% and 8%). This means that these second order structure functions are close to homogeneous in the inner region but this might not be the case in the outer region. Moreover, the quasi-homogeneity of these results does not mean that the turbulent flow is homogeneous as some non-negligible non-homogeneity is measured for other statistics in sections 5.5, 5.6, 5.7 and 5.8. On the other hand, the scales l_I and V_I do not return a particularly good collapse $\overline{\delta u_z'^2}/V_I^2 = f(r_z/l_I)$ for the non-baffled configurations. Another spatially dependent normalization is tested for these results: $\widetilde{l_I} = D.\widetilde{Re_O}^{-3/4}$ and $\widetilde{V_I} = \sqrt{\overline{u_z'^2}}.\widetilde{Re_O}^{-1/4}$ where $\widetilde{Re_O} = \frac{\sqrt{\overline{u_z'^2}}D}{\nu}$. The results of $\overline{\delta u_z'^2}/\widetilde{V_I}^2 = f(r_z/\widetilde{l_I})$ collapse very well for the non-baffled configurations, see figure 5.10 and appendix B.2. Therefore, it is possible to assume that inner similarity holds for each separate contribution $\overline{\delta u_i'^2}$ in each separate direction r_j for baffled and non-baffled configurations:

$$\overline{\delta u_i'^2}(r_j) = V_{I2ij}^2(\boldsymbol{X}) f_{I2ij}\left(\frac{r_j}{l_{Iij}}\right) \tag{5.3}$$

for $|\boldsymbol{r}| \ll l_O$ where V_{I2ij}, f_{I2ij} and l_{Iij} are defined for each component and each direction. This assumption is not very restrictive as it allows for the presence of non-homogeneity such as the one measured for $\overline{\delta u_z'^2}$ in the r_z direction (e.g. figure 5.9b). We can also define a similar outer similarity of the structure function even though we cannot verify this assumption experimentally because of the restricted size of the field of view. We introduce therefore V_{O2ij}, f_{O2ij} and l_{Oij} so that:

$$\overline{\delta u_i'^2}(r_j) = V_{O2ij}^2(\boldsymbol{X}) f_{O2ij}\left(\frac{r_j}{l_{Oij}}\right) \tag{5.4}$$

for $|\boldsymbol{r}| \gg l_I$.

We define $Re_{Oij} = V_{O2ij} l_{Oij}/\nu$, $V_{I2ij}/V_{O2ij} = g_{2ij}(Re_{Oij}, Ro_{ij}, \boldsymbol{X})$ and $l_{Iij}/l_{Oij} = g_{lij}(Re_{Oij}, Ro_{ij}, \boldsymbol{X})$ where the dependence on the Rossby number $Ro_{ij} = V_{I2ij}/(4\pi F l_{Oij})$ is new compared to chapter 4 and takes into account rotation effects. Note that we assume

that f_{Iij} and f_{Oij} do not depend on Re_{Oij} and Ro_{ij} explicitly. This assumption might not be true in all situations and can lead to some uncertainty in the predictions.

Assuming that the outer similarity holds and following our baffled configuration derivation in equations 4.24, 4.25 and 4.27, we can write the inner outer matching in the inner outer region ($l_I \ll |\boldsymbol{r}| \ll l_O$):

$$f_{O2ij}\left(\frac{r_j}{l_{Oij}}\right) = g_{2ij}^2 f_{I2ij}\left(\frac{r_j}{l_{Oij}} g_{lij}^{-1}\right) \tag{5.5}$$

and differentiate with respect to Re_{Oij} to find:

$$n_{ij} f_{I2ij}\left(\rho_{ij}\right) = \rho_{ij} \frac{\partial}{\partial \rho_{ij}} f_{I2ij}\left(\rho_{ij}\right) \tag{5.6}$$

(without implicit summation) where $\rho_{ij} = \frac{r_j}{l_{Oij}} g_{lij}^{-1}$ and where n_{ij} is a dimensionless exponent which can be different for each contribution in each direction. Therefore, a power-law behavior can be derived for f_{I2ij}:

$$f_{I2ij} = r_j^{n_{ij}} \tag{5.7}$$

Note that differentiating with respect to Ro_{ij} gives the same results so n_{ij} is not constrained at that point. We identified a power law behavior for $\overline{\delta u_x'^2}$ in both r_x and r_z directions, so we may expect outer similarity to hold for this component in both r_x and r_z directions which could explain the non-Kolmogorov power-law behavior identified experimentally as resulting from an inner/outer asymptotic matching. This is less clear for $\overline{\delta u_z'^2}$ as a power law behavior is not clearly identified for it. We expect therefore, the outer similarity assumption 5.4 to describe only approximately the behavior of $\overline{\delta u_z'^2}$ which would explain why a non-power law behavior is evidenced in the expected inner/outer matching region for this component. The non-verification of equation 5.4 might be related to a non-negligible Reynolds or Rossby dependence of f_{Oij}. The confirmation of these conjectures is left for future work.

The theory can be derived until equation 5.7 for $\overline{\delta u_x'^2}$. However, the inner-outer equivalence for dissipation: $\overline{\epsilon'} \sim V_{O2ij}^3 / L_{Oij} \sim V_{I2ij}^3 / L_{Iij}$, where $i = 1$, cannot hold for the non-baffle configurations because it can implies $n_{ij} = 2/3$ which is not measured in the non-baffled results. This inner/outer equivalence for dissipation is derived in chapter 4 based on the scale by scale analysis of the small scale two-points Navier-Stokes equations 4.2. Therefore, we investigate the possible causes which can explain why the inner-outer equivalence hypothesis can break.

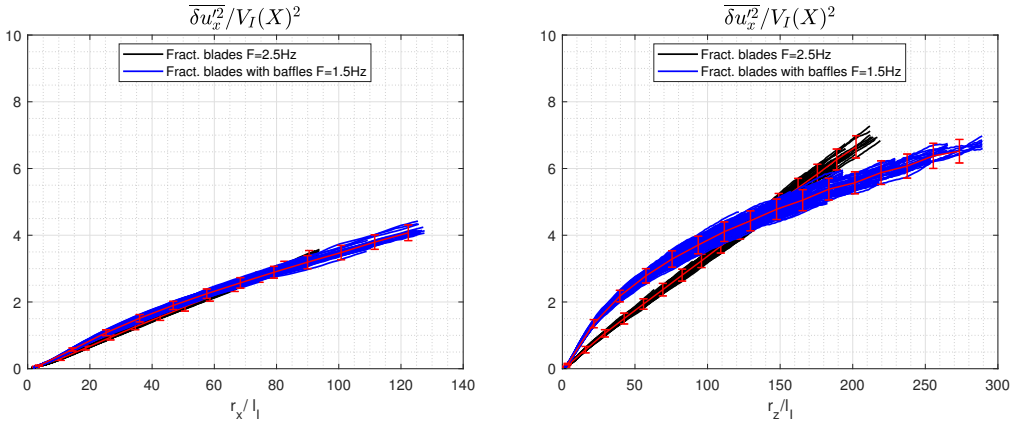

(a) r_x direction (b) r_z direction

Figure 5.8: Time averaged structure function $\overline{\delta u_x'^2}$ at different space locations in two radial directions and normalized by l_I, $V_I^2 = (\overline{u_x'^2} + \overline{u_z'^2}).Re_O^{-1/2}$ where $Re_O = \frac{\sqrt{\overline{u_x'^2}+\overline{u_z'^2}}D}{\nu}$.

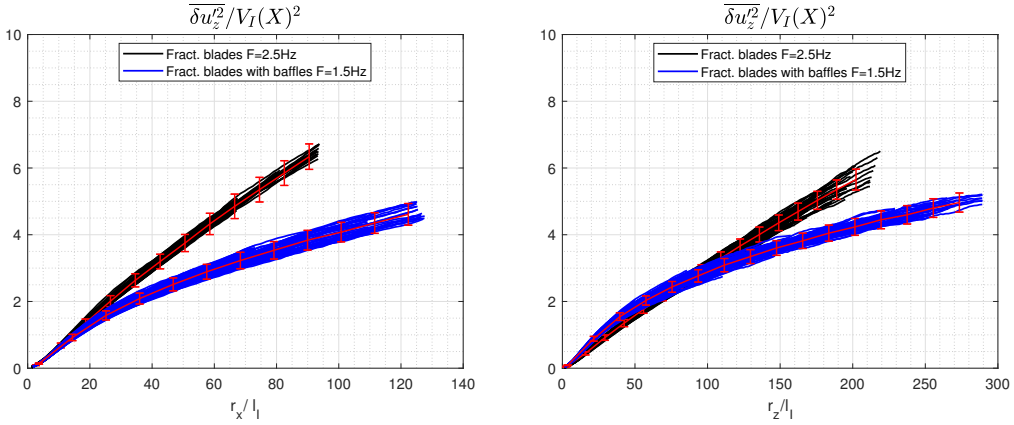

(a) r_x direction (b) r_z direction

Figure 5.9: Time averaged structure function $\overline{\delta u_z'^2}$ at different space locations in two radial directions and normalized by l_I, $V_I^2 = (\overline{u_x'^2} + \overline{u_z'^2}).Re_O^{-1/2}$ where $Re_O = \frac{\sqrt{\overline{u_x'^2}+\overline{u_z'^2}}D}{\nu}$.

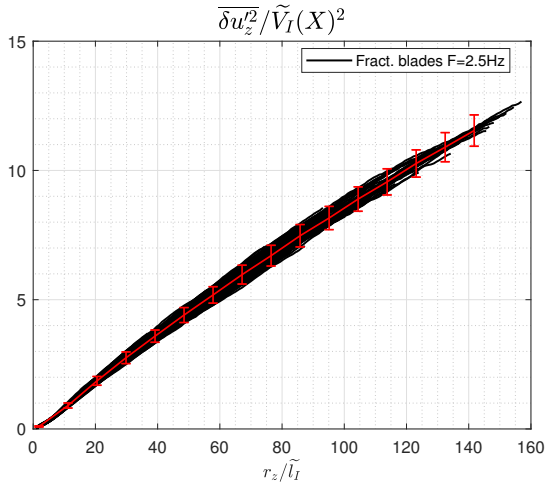

Figure 5.10: Time averaged structure function $\overline{\delta u_z'^2}$ at different space locations as function of r_z and normalized by $\widetilde{l_I}$, $\widetilde{V_I}^2 = (\overline{u_z'^2}).\widetilde{Re_O}^{-1/2}$ where $\widetilde{Re_O} = \frac{\sqrt{\overline{u_z'^2}}D}{\nu}$.

5.4 Inner-outer dissipation equivalence

The inner-outer dissipation equivalence hypothesis is derived in chapter 4 but the main steps (*i*, *ii*, *iii* and *iV*) of this derivation are reminded to identify the reason why it can fail in non-baffled configurations. This hypothesis is derived based on the small scale fluctuating two-point equation introduced in chapter 4 and recalled here:

$$\begin{aligned}&(\overline{\boldsymbol{u_X}}.\boldsymbol{\nabla_X} + \boldsymbol{\delta\overline{u}}.\boldsymbol{\nabla_r})\,\frac{1}{2}\overline{|\boldsymbol{\delta u'}|^2} - P_r - P^s_{Xr} + \boldsymbol{\nabla_X}.(\overline{\boldsymbol{u_X}'\frac{1}{2}|\boldsymbol{\delta u'}|^2}) + \boldsymbol{\nabla_r}.(\overline{\boldsymbol{\delta u}'\frac{1}{2}|\boldsymbol{\delta u'}|^2})\\ &= -2\boldsymbol{\nabla_X}.\overline{(\boldsymbol{\delta u'}\delta p')} + \frac{\nu}{2}{\boldsymbol{\nabla_X}}^2\frac{1}{2}\overline{|\boldsymbol{\delta u'}|^2} + \frac{\nu}{2}{\boldsymbol{\nabla_r}}^2\frac{1}{2}\overline{|\boldsymbol{\delta u'}|^2} - \frac{\nu}{4}\overline{\frac{\partial u_i'^+}{\partial\zeta_k^+}\frac{\partial u_i'^+}{\partial\zeta_k^+}} - \frac{\nu}{4}\overline{\frac{\partial u_i'^-}{\partial\zeta_k^-}\frac{\partial u_i'^-}{\partial\zeta_k^-}}\end{aligned} \tag{5.8}$$

where $P_r = -\overline{\delta u_j'\delta u_i'}\frac{\partial\delta\overline{u}_i}{\partial r_j}$ and $P^s_{Xr} = -\overline{u'_{Xj}\delta u_i'}\frac{\partial\delta\overline{u}_i}{\partial X_j}$ are small scale two-point production terms.

(*i*) In Chen and Vassilicos 2022 and chapter 4, inner similarity is assumed for $r << l_O$ and outer similarity is assumed for $r >> l_I$ for the terms: $\boldsymbol{\nabla_X}.(\overline{\boldsymbol{u_X}'|\boldsymbol{\delta u'}|^2})$, $\boldsymbol{\nabla_r}.(\overline{\boldsymbol{\delta u}'|\boldsymbol{\delta u'}|^2})$ and $2\boldsymbol{\nabla_X}.\overline{(\boldsymbol{\delta u'}\delta p')}$ (equations 4.34, 4.35, 4.36, 4.37, 4.38 and 4.39).

The inner similarity of the structure functions was confirmed previously in this chapter but the third order statistics similarity cannot be evaluated because of lack of convergence. The inner and/or the outer similarity of the third order statistics can conceptually fail in flows with significant rotation which would explain why the inner-outer dissipation hypothesis fails in non-baffled configurations. This is therefore, the first possible cause of failure of this

hypothesis in rotating flows.

(*ii*) It is assumed that $V_{I3} = C_I(\mathbf{X})V_{I2}$ where the dimensionless coefficient $C_I(\mathbf{X})$ is independent of Re_O and $\boldsymbol{r}$. This assumption relates the second order structure function scaling velocity with the interscale energy transfer rate scaling velocity and cannot be tested accurately because of the low convergence of third order quantities without space averaging.

(*iii*) It is also assumed that $\overline{\epsilon'} = C_\epsilon(\mathbf{X})V_{O2}^3/l_O$ where C_ϵ is independent of viscosity. This scaling follows from the hypothesis (often referred to as zeroth law of turbulence) that the turbulence dissipation rate is independent of the fluid's viscosity at large enough Reynolds number. This assumption is questionable in rotating flow according to Favier 2020. Indeed, rotating flow in the limit of zero Rossby number may be associated with two-dimensional turbulence where the zeroth-law does not hold. In our case, the Rossby number values are between 0.12 and 0.15 for the rotating configurations which is an intermediate regime between infinitely fast rotating turbulence and non-rotating turbulence. Therefore, the zeroth law of turbulence might not hold in our flow which can also explain the breakdown of the inner-outer dissipation equivalence hypothesis.

(*iV*) The inner and outer balance of equation 5.8 is used to derive $C_\epsilon(\mathbf{X})V_{O2}^3/l_O \sim C_I^3(\mathbf{X})V_{I2}^3/l_I$ with a proportionality coefficient that is independent of $\mathbf{X}$ and Re_O. The inner (resp. outer) balance results from injecting the inner (resp. outer) similarity forms of the energy terms into equation 5.8 and this then leads to a space and scale matching between the different terms in the equation.

This inner and outer balance are derived for turbulence where there is no two-point production at small scales (Chen and Vassilicos 2022). The production term can be seen as an internal turbulent energy injection rate, which interacts with the interscale /interspace turbulent energy transfers. Therefore, this term is not expected to follow turbulence universal laws but instead impose more strongly non-homogeneity specificities which might break or modify the inner and the outer balances. More generally, the Corrsin length $l_C = \overline{\epsilon}^{3/2}/S^{3/2}$ has been used previously in Corrsin 1958 to distinguish between scales above l_C where the mean shear S is significant, and scales below l_C where it may not be (but can nevertheless be significant in term of two-point production). This estimate gives a rough idea about the scales where there is significant one point production. This scale is a way to detect mean flow non-homogeneity as opposed to turbulence non-homogeneity which will be also evaluated later in this chapter.

Linear transport terms can also be affected by mean flow non-homogeneity when it survives at small scales and is strong enough to impact the scale dependence. Indeed, the linear transport terms: $(\overline{\boldsymbol{u_X}}.\boldsymbol{\nabla_X} + \boldsymbol{\delta}\overline{\boldsymbol{u}}.\boldsymbol{\nabla_r})\,\overline{|\boldsymbol{\delta u'}|^2}$ can be affected, for example, by the mean flow

non-homogeneity when $\overline{\boldsymbol{u_X}}$ and/or $\boldsymbol{\delta}\overline{\boldsymbol{u}}$ affect significantly the scale dependence so that it can break the inner/outer balance. This term can also transport in space/scale the quantity $\overline{|\boldsymbol{\delta u'}|^2}$ from a flow region affected by production at small scale into a region without mean flow non-homogeneity so that it can contaminates this new region. Therefore, both production and linear transport terms should be analyzed because they can break or at least modify the inner and outer balances.

5.5 Mean flow non-homogeneity

First, estimates of the Corrsin length are presented in table 5.3 to have an overview of the mean flow non-homogeneity. As introduced previously, this estimate is used to estimate the scale of the mean flow non-homogeneity which may give some hints about the one point production scale. We define the surrogate estimate: $\widetilde{l_C} =< \overline{\epsilon'} >^{1/2} / < S >^{3/2}$, where

$$< S >= \sqrt{2\left(\frac{\partial \overline{u_x}}{\partial x}\right)^2 + 2\left(\frac{\partial \overline{u_x}}{\partial z}\right)^2 + 2\left(\frac{\partial \overline{u_z}}{\partial x}\right)^2 + \left(\frac{\partial \overline{u_z}}{\partial z}\right)^2}; \tag{5.9}$$

the assumptions $\left(\frac{\partial \overline{u_x}}{\partial x}\right) \approx \left(\frac{\partial \overline{u_y}}{\partial y}\right)$, $\left(\frac{\partial \overline{u_x}}{\partial z}\right)^2 \approx \left(\frac{\partial \overline{u_y}}{\partial z}\right)^2$, $\left(\frac{\partial \overline{u_z}}{\partial x}\right)^2 \approx \left(\frac{\partial \overline{u_z}}{\partial y}\right)^2$ are used; and the missing terms $\left(\frac{\partial \overline{u_x}}{\partial y}\right)^2$ and $\left(\frac{\partial \overline{u_y}}{\partial x}\right)^2$ are neglected. $\widetilde{l_C}$ is expected to be overestimated because of the missing contributions but this estimate should be robust enough to compare baffled and non-baffled results. The estimates of $\widetilde{l_C}$ are presented normalized by λ similarly to the two-point results in the previous chapter and by l_I to compare with previous plots. The Corrsin length scale is very small for the non-baffled configurations: between 3λ and 6λ (or between $130l_I$ and $240l_I$) even though the results are overestimated which suggests the mean flow non-homogeneity exists at very small scales when the flow is rotating (as expected).

This small scale mean flow non-homogeneity might break the inner and the outer scale by scale balance of equation 5.8 described in Chen and Vassilicos 2022 and chapter 4. Indeed, the mean flow non-homogeneity scale is of the order of magnitude of λ where one often finds a Kolmogorov-like approximate scale-by-scale equilibrium balance (Meldi and Vassilicos 2021, Apostolidis, Laval, and Vassilicos 2023). The Corrsin length scale estimates are much larger for the baffled configuration, in fact higher than 26λ (or $1000l_I$), which suggests that the mean flow non-homogeneity is only contained at large scales for these configurations allowing inner and outer balances of the type of Chen and Vassilicos 2022 to exist for a large range of scales smaller than l_C. Another non-homogeneity scale ratio based on Chen and Vassilicos 2022 theory can be derived, namely:

$$l_{CV22,O}/l_O = (\frac{\epsilon}{V_{O2}^2 S})^{3/2} \tag{5.10}$$

where the ratio should be large so that the mean flow non-homogeneity does not affect

	F (Hz)	$\widetilde{l_C}/\lambda$	$\widetilde{l_C}/l_I$	$\widetilde{l_{CV22,O}}/\lambda$
Rectangular blades	2	3.5	133	1.1
Rectangular blades	3	5.1	217	1.5
Fractal blades	2	5.2	207	1.7
Fractal blades	2.5	5.5	239	1.6
Rectangular blades with baffles	1	26.4	1037	9.3
Rectangular blades with baffles	1.5	39.5	1816	13.4
Fractal blades with baffles	1	25.8	1017	8.3
Fractal blades with baffles	1.5	38.6	1673	13.3

Table 5.3: Corrsin length scale estimate $\widetilde{l_C} = <\bar{\epsilon}>^{1/2} / <S>^{3/2}$ with $<S>$ defined in 5.9

the inner-outer balance. The estimate: $\frac{\widetilde{l_{CV22,O}}}{\lambda} = \frac{l_O}{\lambda}\left(\frac{<\bar{\epsilon}>}{<V_{O2}>^2<S>}\right)^{3/2}$ is evaluated where $V_{O2} = \sqrt{2\overline{u_x'^2} + \overline{u_z'^2}}$ and l_O is approximated by D. These results are presented in table 5.3. The values of $\frac{\widetilde{l_{CV22,O}}}{\lambda}$ are different to the Corrsin values because of the change of definition and the approximation $l_O = D$ but the variation between baffled and non baffled results is of the same order of magnitude which confirms the previous results. As opposed to the results of Chen and Vassilicos 2022 where the Corrsin length scale does not seem to predict well where the theory holds and where it does not, our results are very explicit. This might be due to the fact that the Corrsin length should be compared to the Taylor scale or to the inner scale instead of the integral scale to know if the mean flow non-homogeneity is present at scales small enough to affect the inner-outer matching region as it is done this chapter.

In the next sections, we present the production and linear transport estimates to see if it can explain the breakdown of the inner/outer balance forms of (5.8), possibly related to mean flow non-homogeneity at small scales. Then, the other two-point statistics are compared between baffled and non-baffled configurations to have an exhaustive description of the rotation effect on two-point statistics.

5.6 Two-point turbulence production rates

We start our data analysis with an assessment of the two-point turbulence production rates. The sums defining $P_r = -\overline{\delta u_j' \delta u_i'}\frac{\partial \delta \overline{u_i}}{\partial r_j}$ and $P^s_{Xr} = -\overline{u'_{Xj}\delta u_i'}\frac{\partial \delta \overline{u_i}}{\partial X_j}$ are sums of nine terms of which our 2D2C PIV has access to four. Our data therefore allow only truncations to be calculated directly (defined in section 4.5).

We calculate space averages over the field of view of the two truncated two-point production rates ($\langle\widetilde{P_r}\rangle$ and $\langle\widetilde{P^l_{Xr}}\rangle$ and we plot them in figures 5.11 and 5.12 versus $r_1 \equiv r_x$ and $r_3 \equiv r_z$. We plot them normalised by $\langle\overline{\epsilon'}\rangle/2$ where $\epsilon' \equiv \frac{\partial u_i'}{\partial \zeta_j}\frac{\partial u_i'}{\partial \zeta_j}$ is estimated on the basis of our 2D2C PIV data using its axisymmetric formulation (see chapter 3).

We can see from the plots in figures 5.11 and 5.12 that for baffled configurations, $\langle\widetilde{P_r}\rangle$ and

$\langle\widetilde{P^s_{Xr}}\rangle$ collapse and are relatively small for most values of r_x and r_z that our field of view allows us to access. The non-baffled configurations results are different and non negligible values are obtained, in particular for the configurations with rectangular blades (see figure 5.12). For example, the values of $\langle\widetilde{P^s_{Xr}}\rangle$ are significant in r_z direction for the configurations with rectangular blades at 2Hz, 3Hz and fractal blades at 2Hz. No collapse of the results is found for the non-baffled individual production terms so the results depend on the non-homogeneity specificity of each configuration.

However, the results collapse reasonably well for the non-baffled configurations of specific blades when we sum both small scale production terms ($\langle\widetilde{P_r}\rangle + \langle\widetilde{P^s_{Xr}}\rangle$) as function of r_x and r_z given the large dissipation variation (see figure 5.13). The total small scale production's contribution is negligible for the non-baffled fractal blades configurations in r_x and r_z direction and significant for the non-baffled rectangular blades configurations. The difference between these results might be associated with the break of the coherent structures expected with fractal blades (Başbuğ, Papadakis, and Vassilicos 2018). Therefore, if the missing production contributions behave in a similar way as the measured contributions, the small scale production in equation 5.8 cannot explain alone the breakdown of the inner/outer balance through mean flow non-homogeneity at small scale. In particular, not for the fractal blade configurations where the configurations without baffles have similar total production results as configurations with baffles while their structure functions do not follow a $r^{2/3}$ power-law. Therefore, either the missing production contributions are non-negligible or the mean flow non-homogeneity at small scale disturbs the inner and/or outer balances with another term than the production so that the dissipation hypothesis fails and the structure functions behave differently.

Overall, our results suggest that the two-point productions in the small-scale energy equation 5.8 are significantly affected by the mean flow non-homogeneity but this cannot explain on its own the structure function behavior differences identified in previous sections of this chapter between baffled and non-baffled configurations.

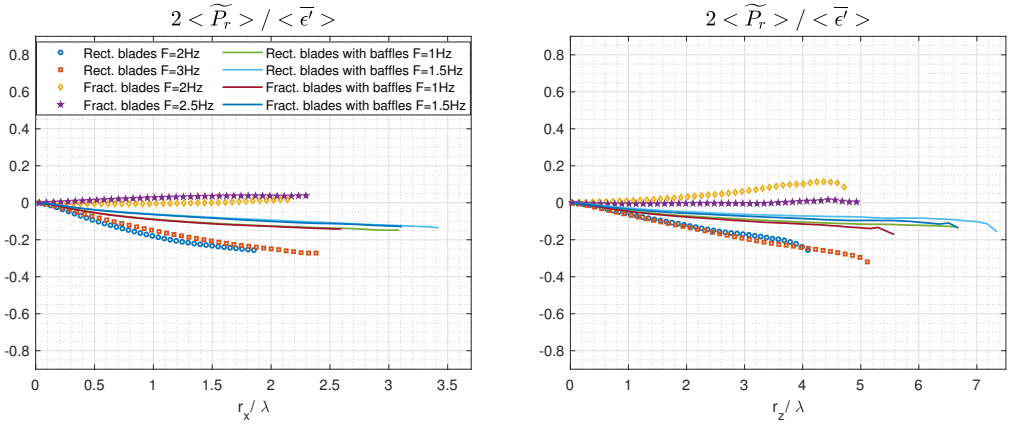

(a) r_x direction (b) r_z direction

Figure 5.11: Production truncate estimate $\widetilde{P_r}$ introduced in equation 5.8, normalized by dissipation and along two radial directions.

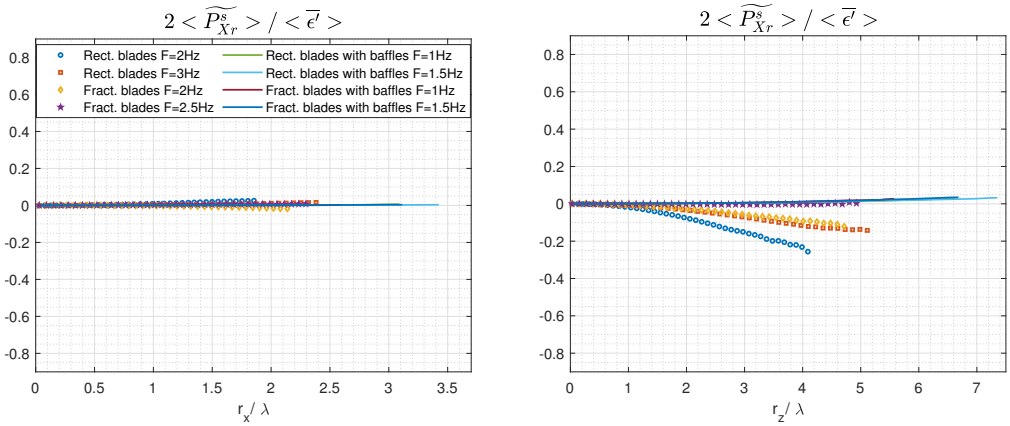

(a) r_x direction (b) r_z direction

Figure 5.12: Production truncate estimate $\widetilde{P^S_{Xr}}$ introduced in equation 5.8, normalized by dissipation and along two radial directions.

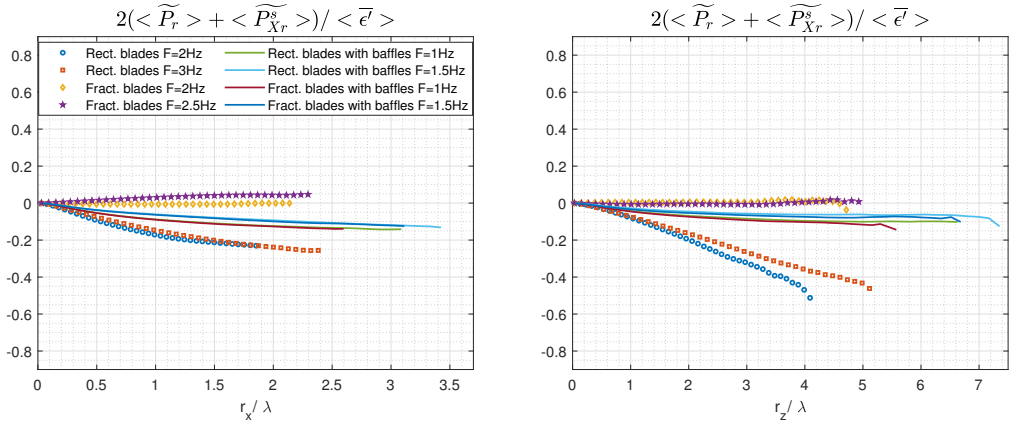

(a) r_x direction

(b) r_z direction

Figure 5.13: Total production truncate estimate $\widetilde{P_r} + \widetilde{P^S_{Xr}}$ introduced in equation 5.8, normalized by dissipation and along two radial directions.

5.7 Small scale linear transport

We now focus on the linear transport $(\overline{\boldsymbol{u_X}}.\boldsymbol{\nabla_X} + \boldsymbol{\delta\overline{u}}.\boldsymbol{\nabla_r})\,\frac{1}{2}\overline{|\boldsymbol{\delta u'}|^2}$ to see if the results differ between baffled and non-baffled configurations and check if it can explain the break of the inner-outer dissipation equivalence hypothesis. Once again, with our 2D2C PIV data, we can only consider a truncation estimate. The truncation averaged over the field of view is $<\left(\overline{u_{Xx}}\frac{\partial}{\partial X_x} + \overline{u_{Xz}}\frac{\partial}{\partial X_z} + \delta\overline{u}_x\frac{\partial}{\partial r_x} + \delta\overline{u}_z\frac{\partial}{\partial r_z}\right)\frac{1}{2}\left(\overline{\delta u_x'^2 + \delta u_z'^2}\right)>$.

We calculate space-averages of the truncation estimate in two parts: i.e. $\langle\left(\overline{u_{Xx}}\frac{\partial}{\partial X_x} + \overline{u_{Xz}}\frac{\partial}{\partial X_z}\right)\frac{1}{2}\left(\overline{\delta u_x'^2 + \delta u_z'^2}\right)\rangle$ which represents the spatial linear transport and $\langle\left(\delta\overline{u}_x\frac{\partial}{\partial r_x} + \delta\overline{u}_z\frac{\partial}{\partial r_z}\right)\frac{1}{2}\left(\overline{\delta u_x'^2 + \delta u_z'^2}\right)\rangle$ which represents the scale linear transport. In figures 5.15 and 5.14, we plot the space-average truncated parts normalized by $\langle\overline{\epsilon'}\rangle/2$ versus r_x and r_z. The baffled results of the spatial and scale linear transport are relatively small compared to $\langle\overline{\epsilon'}\rangle/2$ in r_x and r_z direction as described in chapter 4 with a very small dependence to the two-point separation length. Regarding the non-baffled configurations, the results do not collapse and depend of the non-homogeneity of each configuration. For the non-baffled configurations with fractal blades at 2Hz, 2.5Hz and rectangular blades at 2Hz, the spatial linear transport (figures 5.14a and 5.14b) return values significantly larger than the baffled configurations in both r_x and r_z directions with significantly non constant dependencies on two-point separation length. The same results are obtained for the non-baffled configuration with rectangular blades at 3Hz in the r_x direction but not in r_z direction where they are comparable to baffled results. However, for this configuration in the r_z direction, the scale linear transport (figures 5.15a and 5.15b) has a non constant dependance on r_z. Therefore, for all non-baffled configurations, the spatial linear transport

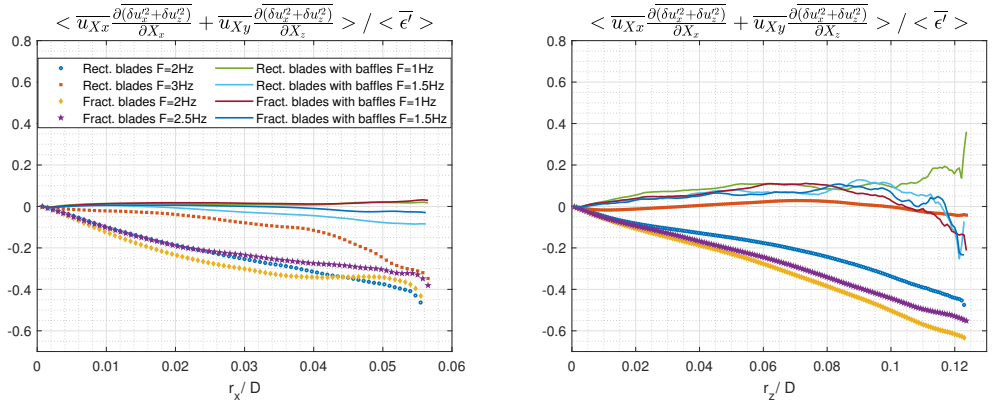

(a) r_x direction (b) r_z direction

Figure 5.14: Truncation estimate of the linear transport $(\overline{\boldsymbol{u_X}}.\boldsymbol{\nabla_X})\,\frac{1}{2}\overline{|\boldsymbol{\delta u'}|^2}$ introduced in equation 5.8, normalized by dissipation and along two radial directions.

estimate and/or the scale linear transport estimate have a non-constant evolution with r and values are significantly larger than for the baffled configurations. Practically, the non-zero linear transport at small scales means some energy ($\frac{1}{2}\overline{|\boldsymbol{\delta u'}|^2}$) enters or leaves the domain at small scales with the mean flow. This energy may come from highly non-homogeneous regions with high production at small scales so that the turbulence results inside the field of view are contaminated through the linear transport terms.

In Chen and Vassilicos 2022, the advection term is derived to be negligible in the inner balance when the Reynolds number is large on the basis of the inner similarity hypotheses and this is needed for the inner/outer dissipation equivalence hypothesis to hold. We observe experimentally that the rotation in the non-baffled configurations can produce a flow with large Reynolds number but non-negligible advection at small scales with significant dependence on two-point separation length. This rotation effect breaks the inner and outer balance of the small scale equation 5.8 in Chen and Vassilicos 2022. This significant difference can explain the breakdown of the inner-outer dissipation equivalence, so that the measured structure functions do not follow a $r^{2/3}$ power law behavior. In the following sections we continue to characterize the turbulence properties of the non-baffled configurations in comparison to the baffled ones by studying the other energy terms of equation 5.8.

5.8 Energy transfer rate measurements

The theory in chapter 4 predicts, for the baffled configurations, that an intermediate range of scales exists ($l_I \ll |\boldsymbol{r}| \ll l_O$) where, for $Re_O \to \infty$:

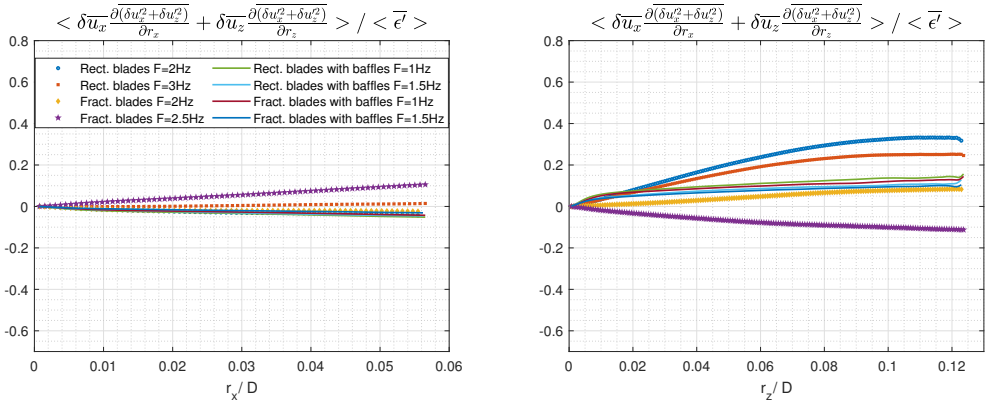

(a) r_x direction (b) r_z direction

Figure 5.15: Truncation estimate of the linear transport $(\boldsymbol{\delta\overline{u}}.\boldsymbol{\nabla_r})\,\frac{1}{2}\overline{|\boldsymbol{\delta u'}|^2}$ introduced in equation 5.8, normalized by dissipation and along two radial directions.

$$\boldsymbol{\nabla_r}.(\overline{\boldsymbol{\delta u'}|\boldsymbol{\delta u'}|^2}) \sim \overline{\epsilon'}, \tag{5.11}$$

$$\boldsymbol{\nabla_X}.(\overline{\boldsymbol{u_X}'|\boldsymbol{\delta u'}|^2}) \sim \overline{\epsilon'} \tag{5.12}$$

and

$$2\boldsymbol{\nabla_X}.\overline{(\boldsymbol{\delta u'}\delta p')} \sim \overline{\epsilon'}. \tag{5.13}$$

These results were derived assuming inner/outer similarity of these energy terms as introduced in Chen and Vassilicos 2022 and inner-outer equivalence for dissipation. The dimensionless coefficients of proportionality in 5.11, 5.12 and 5.13 are independent of $\boldsymbol{r}$, independent of Reynolds number and independent of $\boldsymbol{X}$ but add up to -1 asymptotically for large enough Reynolds numbers. These results are also generalized in chapter 4 to truncated estimates of the two-point quantities based on isotropic similarity assumptions (which is not an isotropic assumption):

$$\overline{\delta u'_x \frac{\partial}{\partial r_x}(\delta u'^2_x + \delta u'^2_z)} + \overline{\delta u'_z \frac{\partial}{\partial r_z}(\delta u'^2_x + \delta u'^2_z)} \sim \overline{\epsilon'} \tag{5.14}$$

and

$$\overline{u'_{Xx} \frac{\partial}{\partial X_x}(\delta u'^2_x + \delta u'^2_z)} + \overline{u'_{Xz} \frac{\partial}{\partial X_z}(\delta u'^2_x + \delta u'^2_z)} \sim \overline{\epsilon'}. \tag{5.15}$$

In this chapter, we focus on the non-baffled results but the baffled results are also plotted for comparison. The breakdown of the inner/outer balances of equation 5.8 identified previously in non-baffled configurations should be visible in the energy transfer results by the invalidity of equations 5.14 and 5.15.

The spread of Taylor length-based Reynolds numbers across our four non-baffled configurations is from 410 to 530. The Taylor length-based Reynolds number of the baffled configurations is from 480 to 650 and several values are comparable to the ones of the non-baffled configurations allowing comparison for similar Reynolds number. The spatial resolutions for all eight configurations are given in table 3.1. We normalise the two-point separation length components r_x and r_z by λ similarly to chapter 4. The Taylor length takes values between $5.3mm$ and $6.6mm$ across our four non-baffled configurations and the field of view of our PIV is $27mm \times\ 28mm$, hence we cannot access values of r_x/λ and r_z/λ larger than those in the plots of figures 5.16a and 5.16b for non-baffled configurations. The convergence is analyzed in appendix B.1 and seems to be acceptable for $r_x < 1.3\lambda$ and $r_z < 3\lambda$ for non-baffled configurations. Beyond these values of r_x and r_z statistical convergence visibly weakens. The baffled results are better converged for the same r_x/λ and r_z/λ ratio because of the smaller Taylor scale for these configurations. These results are acceptably converged over the ranges r_x and r_z presented in figures 5.16a and 5.16b.

In figures 5.16 and 5.17, we plot the normalised truncated interscale transfer rate term $\langle \boldsymbol{\nabla_r}.(\widetilde{\overline{\boldsymbol{\delta u'}|\boldsymbol{\delta u'}|^2}})\rangle/\langle\overline{\epsilon'}\rangle$ and the normalised truncated interspace transfer rate term $\langle \boldsymbol{\nabla_X}.(\widetilde{\overline{\boldsymbol{u_X}'|\boldsymbol{\delta u'}|^2}})\rangle/\langle\overline{\epsilon'}\rangle$.

The interscale transfer rate estimate is found to be negative for all baffled configurations for the scales observed in both r_x and r_z directions. The same sign is found for the non-baffled configurations in the range of scales measured. These results suggest a non-linear interscale turbulent energy transfer that is predominantly from large to small scales, i.e. that the turbulence cascade is forward on average. This result cannot be confirmed definitively with our dataset for the non-baffled configurations because several interscale transfer contributions cannot be computed and the turbulence is strongly anisotropic for these configurations.

For the baffled configurations, the interscale transfer estimate is found to be proportional to the turbulence dissipation rate and independent of the two-point separation length for $\frac{\lambda}{2} \leq r_x \leq 2\lambda$ and $\frac{\lambda}{2} \leq r_z \leq 5\lambda$ as predicted in equation 5.14. Non-constant interscale transfer rates are observed for the non-baffled configurations with a slow decrease in the r_x direction and a significant linearly decreasing variation in the r_z direction (see figure 5.16). Also, the results do not collapse well for these non-baffled configurations as particularly visible in r_z direction (see figure 5.16). These experimental results contradict the prediction (5.14) and are in agreement with the breakdown of the inner and outer balances of equation 5.8 as already suggested. These results are obtained for comparable Re_λ so the root cause for the difference is the flow rotation.

The interspace transport estimates, presented in figures 5.17a and 5.17b, are also significantly different between baffled and non-baffled configurations. These contributions are positive on average and nearly independent of the two-point separation length for the baffled configurations as predicted by equation 5.15. The sign suggests that there is an average

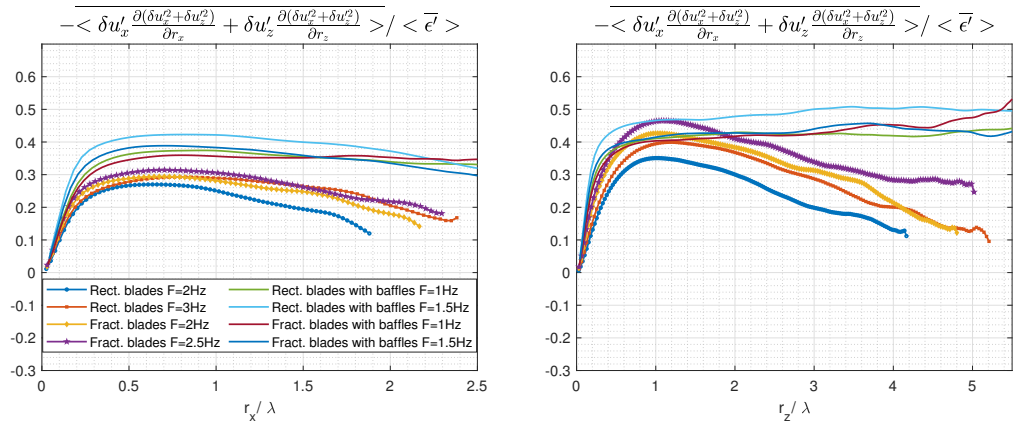

(a) r_x direction

(b) r_z direction

Figure 5.16: Space and time averaged truncation estimate of the small scale interscale transfer $\boldsymbol{\nabla_r}.(\overline{\boldsymbol{\delta u'}|\boldsymbol{\delta u'}|^2})$ introduced in equation 5.8, normalized by dissipation and along two radial directions.

turbulent flux which takes small-scale turbulent kinetic energy out of the field of view. The non-baffled interspace transport estimates do not collapse well with mean dissipation. This is particularly visible in the r_z direction where the fractal blade results are close to zero while the rectangular blade results are decreasing and negative. Therefore, the non-homogeneity contributions differ among different non-baffled configurations. For these configurations, a significant dependence with two-point separation length is found and is particularly visible in the r_x direction. Therefore, equation 5.15 is not valid for non-baffled configurations which confirms once again the breakdown of the inner and outer balances Chen and Vassilicos 2022. There is a change of sign of the interspace transport rate estimate at $r_x/\lambda \approx 1$ for the non-baffled configurations with fractal blade results at 2Hz and 2.5Hz and rectangular blades at 2Hz (see figure 5.17a). This change of sign suggests the non-homogeneity does not behave similarly at all scales and in all directions: outgoing flux of energy for positive values and incoming flux for negative ones.

The change of behavior between baffled and non-baffled configurations for the interspace energy transfer rates might be related to the mean flow non-homogeneity previously identified with the small Corrsin length scale (resp. Chen and Vassilicos 2022 length scale) for the non-baffled cases. Indeed, this mean flow non-homogeneity scale has values between 3λ and 6λ, for the non-baffle configurations, even after overestimation (resp. between 1λ and 1.7λ for the Chen and Vassilicos 2022 length scale). Therefore, the mean flow non-homogeneity may affect the turbulence in the range of scales presented in figures 5.17a and 5.17b.

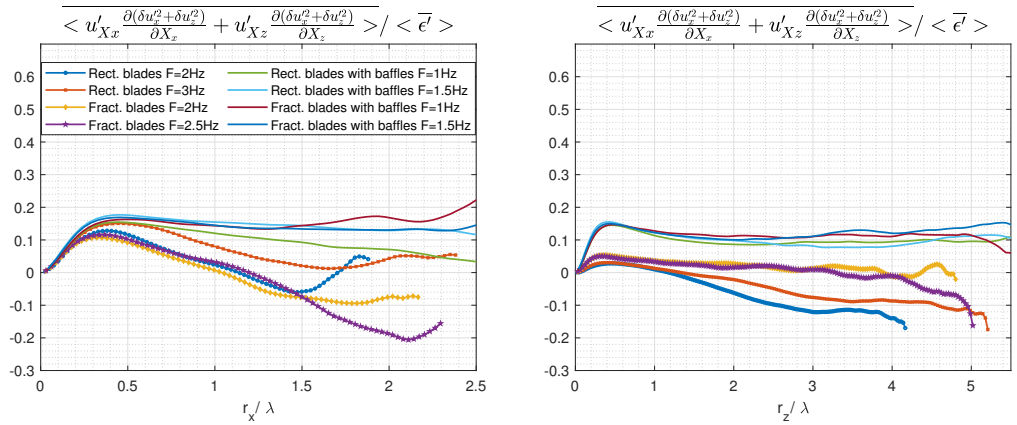

(a) r_x direction (b) r_z direction

Figure 5.17: Space and time averaged truncation estimate of the small scale interspace transport $\boldsymbol{\nabla_X}.(\overline{\boldsymbol{u_X}'|\boldsymbol{\delta u}'|^2})$ introduced in equation 5.8, normalized by dissipation and along two radial directions.

5.9 Large-scale turbulent energy budget

A RANS decomposition is applied to the Germano 2007b equation as introduced in chapter 4 to obtain the large scale fluctuating equation reproduced here:

$$\begin{aligned}&(\overline{\boldsymbol{u_X}}.\boldsymbol{\nabla_X} + \boldsymbol{\delta\overline{u}}.\boldsymbol{\nabla_r})\,\frac{1}{2}\overline{|\boldsymbol{u'_X}|^2} - P_X - P^l_{Xr} + \boldsymbol{\nabla_X}.(\overline{\boldsymbol{u_X}'\frac{1}{2}|\boldsymbol{u_X}'|^2}) + \boldsymbol{\nabla_r}.(\overline{\boldsymbol{\delta u}'\frac{1}{2}|\boldsymbol{u_X}'|^2})\\ &= -2\boldsymbol{\nabla_X}.(\overline{\boldsymbol{u_X}'p'_X}) + \frac{\nu}{2}\boldsymbol{\nabla_X}^2\frac{1}{2}\overline{|\boldsymbol{u'_X}|^2} + \frac{\nu}{2}\boldsymbol{\nabla_r}^2\frac{1}{2}\overline{|\boldsymbol{u'_X}|^2} - \frac{\nu}{4}\overline{\frac{\partial u_i'^+}{\partial\zeta_k^+}\frac{\partial u_i'^+}{\partial\zeta_k^+}} - \frac{\nu}{4}\overline{\frac{\partial u_i'^-}{\partial\zeta_k^-}\frac{\partial u_i'^-}{\partial\zeta_k^-}}\end{aligned} \tag{5.16}$$

where $P_X = -\overline{u'_{Xj}u'_{Xi}}\frac{\partial\overline{u}_{Xi}}{\partial X_j}$ and $P^l_{Xr} = -\overline{\delta u'_j u'_{Xi}}\frac{\partial\delta\overline{u}_i}{\partial X_j}$ are large scale production terms.

As mentioned in chapters 2 and 4, this equation describes the large scale velocity energy $(\boldsymbol{u_X}'^2)$ evolution as opposed to equation 5.8 which describes the small scale velocity energy $(\boldsymbol{\delta u}'^2)$ evolution.

We also remind the reader that the small scale interscale transfer rate $\boldsymbol{\nabla_r}.(\overline{\boldsymbol{\delta u}'|\boldsymbol{\delta u}'|^2})$ is related to the large scale interscale transfer rate $\boldsymbol{\nabla_r}.(\overline{\boldsymbol{\delta u}}\overline{|\boldsymbol{u_X}'|^2})$ through the equation:

$$\begin{aligned}&\boldsymbol{\nabla_r}.(\overline{\boldsymbol{\delta u}}|\overline{\boldsymbol{\delta u}}|^2) + \boldsymbol{\nabla_r}.(\overline{\boldsymbol{\delta u}}\overline{|\boldsymbol{\delta u}'|^2}) + \boldsymbol{\nabla_r}.(\overline{\boldsymbol{\delta u}'|\boldsymbol{\delta u}'|^2}) + 2\boldsymbol{\nabla_r}.(\overline{\boldsymbol{\delta u}'(\boldsymbol{\delta u}'\overline{\boldsymbol{\delta u}})})\\ &+ \boldsymbol{\nabla_r}.(\overline{\boldsymbol{\delta u}}|\overline{\boldsymbol{u_X}}|^2) + \boldsymbol{\nabla_r}.(\overline{\boldsymbol{\delta u}}\overline{|\boldsymbol{u_X}'|^2}) + \boldsymbol{\nabla_r}.\overline{(\boldsymbol{\delta u}'|\boldsymbol{u_X}'|^2)} - 2P^l_{Xr}\\ &= 2\boldsymbol{\nabla_X}.(\overline{\boldsymbol{\delta u}(\boldsymbol{\delta u}.\overline{\boldsymbol{u_X}})}) + 2\boldsymbol{\nabla_X}.(\overline{\overline{\boldsymbol{\delta u}}(\boldsymbol{\delta u}'.\boldsymbol{u'_X})})\\ &+ 2\boldsymbol{\nabla_X}.(\overline{\boldsymbol{\delta u}'(\boldsymbol{\delta u}'.\boldsymbol{u'_X})}) + 2\boldsymbol{\nabla_X}.(\overline{\boldsymbol{\delta u}'(\overline{\boldsymbol{\delta u}}.\boldsymbol{u'_X})}) - 2P_r\end{aligned} \tag{5.17}$$

In this section we present the results of the large scale equation to see how the small scale results are related to the large scale results and to characterize the flow rotation through this framework.

In figures 5.18a and 5.18b we plot the spatio-temporal average of the truncated estimate of $\boldsymbol{\nabla_r} \cdot (\overline{\boldsymbol{\delta u'} |\boldsymbol{u_X}'|^2})$ that is accessible to our 2D2C PIV, namely $\langle \overline{\delta u'_x \frac{\partial}{\partial r_x}(u'^2_{Xx} + u'^2_{Xz})} \rangle + \langle \overline{\delta u'_z \frac{\partial}{\partial r_z}(u'^2_{Xx} + u'^2_{Xz})} \rangle$. We plot it normalised by $\langle \overline{\epsilon'} \rangle$ versus both r_x/λ and r_z/λ and we note a significant difference between baffled and non-baffled configurations. The results collapse relatively well for the four different baffled configurations (where the mean dissipation changes by a ratio of four). This is definitively not the case for non-baffled configurations in the r_z direction where the fractal blade results and the rectangular blade results are significantly different. This difference can be attributed to a different non-homogeneity type related to the type of blade which would explain why the results differ for different blades but collapse a little better for same blades results at different rotation speeds. The fractal blade are expected for example to break the coherent structures of the flow compared to rectangular blades (Başbuğ, Papadakis, and Vassilicos 2018) which may explain the difference in the results.

Furthermore, the baffled configuration results appear to have a constant value across the same ranges $\lambda/2 \leq r_x \leq 2\lambda$ and $\lambda/2 \leq r_z \leq 5\lambda$ where the parts of the spatio-temporal average of $\boldsymbol{\nabla_r}.(\overline{\boldsymbol{\delta u'} |\boldsymbol{\delta u'}|^2})$ that is accessible to our PIV has an approximately collapsed constant value. For the non baffle configurations, there is a significant dependence to the two-point separation length which is particularly visible in r_z direction and plotted in figure 5.18b. This linear dependence is comparable to the one already observed for the truncate estimate of $\boldsymbol{\nabla_r}.(\overline{\boldsymbol{\delta u'} |\boldsymbol{\delta u'}|^2})$ in figure 5.16b. There is a link between the small scale and large scale interscale transfer derived mathematically in equation 5.17 but it involves many non-homogeneous terms. These non homogeneous terms affect significantly the relation between these two terms but some behavior similarity remains regarding the two-point separation length dependence.

The large scale interscale energy transfer estimates are positive for baffled configurations but a significant change of sign is observed for non-baffled configurations with rectangular blades for $r_z > 2\lambda$. The sign of the full quantity $\boldsymbol{\nabla_r}.(\overline{\boldsymbol{\delta u'} |\boldsymbol{u_X}'|^2})$ cannot be inferred from the truncated estimate results because of the strong anisotropy of the flow but we cannot exclude the presence of an inverse large scale interscale transfer rate ($\boldsymbol{\nabla_r}.(\overline{\boldsymbol{\delta u'} |\boldsymbol{u_X}'|^2})<0$, Germano 2007b) while having a direct small scale interscale transfer rate ($\boldsymbol{\nabla_r}.(\overline{\boldsymbol{\delta u'} |\boldsymbol{\delta u'}|^2})<0$) over a non-negligible range of scales for these configurations. The distinction between small scale interscale transfer and large scale interscale transfer is interesting in non-homogeneous flows as it allows the co-existence of both direct small scale interscale transfer rate and inverse large scale interscale transfer rate through the injection of energy with non-homogeneous terms in 5.17. It might be the case for the non-baffled configurations with rectangular blades but more generally it would be interesting to check this results in future work in non-homogeneous flows where for example P_r and P^l_{Xr} are large compared to $< \epsilon' >$.

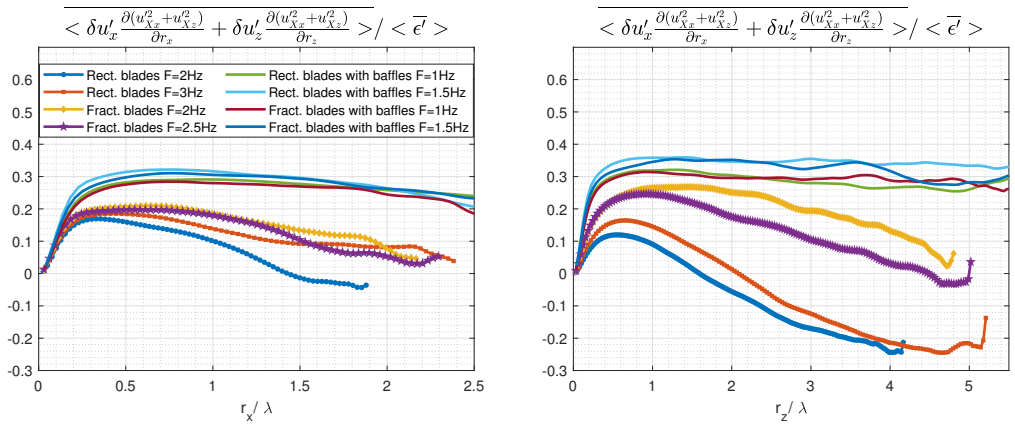

(a) r_x direction (b) r_z direction

Figure 5.18: Space and time averaged truncation estimate of the large scale interscale transfer $\boldsymbol{\nabla_r}.(\overline{\boldsymbol{\delta u'}|\boldsymbol{u_X}'|^2})$ introduced in equation 5.16, normalized by dissipation and along two radial directions.

In figures 5.19a and 5.19b, we plot the spatio-temporal average of the large scale interspace transport truncate estimate $\langle\overline{u'_{Xx}\frac{\partial}{\partial X_x}(u'^2_{Xx}+u'^2_{Xz})}\rangle + \langle\overline{u'_{Xz}\frac{\partial}{\partial X_z}(u'^2_{Xx}+u'^2_{Xz})}\rangle$ normalized by $\langle\overline{\epsilon'}\rangle$ versus both r_x/λ and r_z/λ. Non-negligible values are obtained which do not vanish when $r \to 0$. The results do not collapse with mean dissipation for both baffle and non-baffle configurations. Therefore, the large scale interspace transport seems to mainly depend on the non-homogeneity properties of each configuration. The spread of the non-baffle results is even more important than for baffle results which can be explained by larger non-homogeneity differences between these configurations. The dependence with r_x and r_z is small for the baffle configurations and more important for non-baffle configurations as observed in figures 5.19a and 5.19b.

Overall, no significant qualitative difference is observed between baffled and non-baffled configurations regarding large scale interspace transport except the stronger dependence with r_x and r_z for non-baffle configurations. This quantity seems to be mainly driven by large scale non-homogeneity and does not seems to be related to small scale quantities.

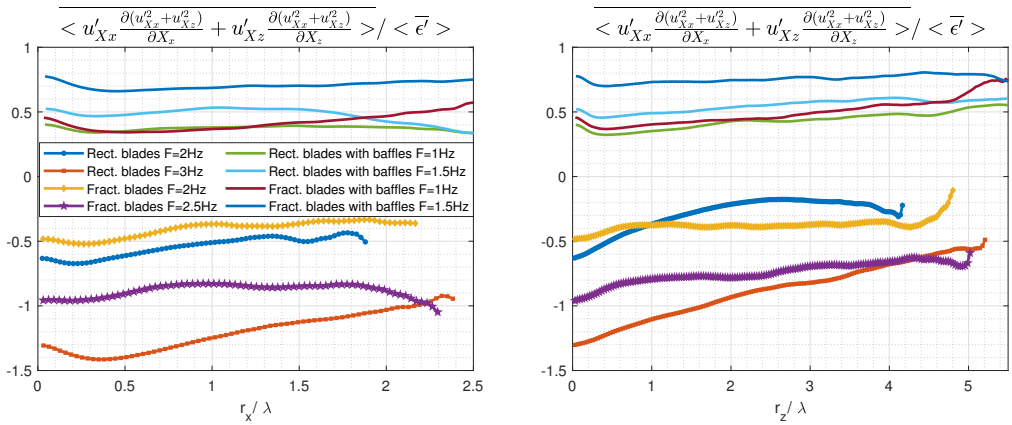

(a) r_x direction

(b) r_z direction

Figure 5.19: Space and time averaged truncation estimate of the large scale interspace transport $\boldsymbol{\nabla_X}.(\overline{\boldsymbol{u_X}'|\boldsymbol{u_X}'|^2})$ introduced in equation 5.16, normalized by dissipation and along two radial directions.

5.10 Chapter conclusions

Kolmogorov-like structure functions are measured in a turbulent flow generated by a mixer with baffles (vertical bars which break the global rotation) where the flow is non-homogeneous but not rotating. These results are presented and explained in chapter 4 through an improved Chen and Vassilicos 2022 theory. In this chapter, rotating turbulence generated by the same mixer without baffles is analyzed in comparison to the previous results. Non-Kolmogorov structure functions are measured for these configurations. These results mean that rotation breaks one or more assumptions of the Chen and Vassilicos 2022 theory. A power law/ linear behavior of $\overline{\delta u_x'^2}$ is however identified with an exponent $q \approx 1 > 2/3$. This behavior suggests that the beginning of the Chen and Vassilicos 2022 theory remains applicable once modified to take into account the anisotropy of the inner and outer length scales expected with rotation. We identified different Chen and Vassilicos 2022 theory hypotheses which might fail in rotating turbulence but the root cause might be the mean flow non-homogeneity present at small scales ([3λ, 6λ]) in the non-baffled configurations while it is at much larger scales ([29λ, 39λ]) in baffled configurations. As a result, the production and linear transport terms break the inner and outer scale-by-scale two-point energy balances which Chen and Vassilicos 2022 derived from the small scale fluctuating two-point energy equation 5.8. These results break in turn the inner-outer dissipation hypothesis needed to derive the $r^{2/3}$ structure function behavior.

The other two-point energy statistics of the small scale equation are quantified for non-baffled configurations and non constant evolutions with two-point separation length $\boldsymbol{r}$ are observed as well as an absence of collapse of interscale/interspace transfer rate with dissipation. These results are different from the baffled configurations results which follow the

predictions of Chen and Vassilicos 2022 theory. This difference confirms, once again, the breakdown of the inner and outer scale-by-scale balance of the small scale two-point energy equation. Eventually, large scale statistics introduced in chapter 4 are measured suggesting the existence of an inverse large scale interscale transfer rate coexisting with a direct small scale interscale transfer rate for non-baffled configurations with rectangular blades. This result cannot be confirmed definitively with our dataset but is allowed mathematically through the injection of non-homogeneous energy at small scales: for example with the non-homogeneous mean flow identified previously. The confirmation of these results is left for future work with experiments where all the contributions of the two-point statistics may be measured while ensuring a good convergence.

Chapter 6

Application to Large Eddy Simulation

6.1 Introduction

Large Eddy Simulations are simulations where only the 'large scales' or more precisely, the low-pass filtered velocity field is resolved. It reduces significantly the number of mesh points as long as a representative model predicts well the effect of the residual scales on the filtered scales. A lot of research has been carried out to find a representative model for different flows (for example: Smagorinsky 1963, Clark, Ferziger, and Reynolds 1977, Bardina, Ferziger, and Reynolds 1980, Métais and Lesieur 1992 and Dairay et al. 2017).

One model based on the concept of turbulent viscosity was defined by Smagorinsky (in Smagorinsky 1963). This rather simple model captures unexpectedly well the small scale dissipation so that simulations in 'homogeneous turbulence' reproduce partly the dissipation existing at high wavenumbers despite important limitations having been identified (Dairay et al. 2017, Vicente Cruz and Lamballais 2023). However, this model, when evaluated on real turbulent flows, is known not to be representative of local physical effects (Meneveau and Katz 2000). The fact that part of turbulence dissipation can be captured without capturing the local physical effects outlines the complexity of LES modeling where physical relevance seems to be dissociated, at first glance, from model accuracy.

However, the Germano 2007b equation might give an avenue towards some potential resolution of this contradiction. This exact equation 2.8 in chapter 2 describes exactly the larger scale behavior. To our knowledge, this equation was not analyzed physically by other researchers than Germano before the work of our group. However, various studies exist (Hill 2002a, Hill 2002b, Danaila et al. 2012, Alves Portela, Papadakis, and Vassilicos 2017, Chen and Vassilicos 2022, Knutsen et al. 2020) of its complementary small scale equation: the Kármán-Howarth-Monin-Hill (KHMH) equation introduced in chapter 2. The KHMH equa-

tion is very useful to understand and quantify turbulence in non-homogeneous flows without assumptions. In the recently submitted publication Yao et al. 2023, the authors analyze the relations between the interscale energy transfer rate of the KHMH equation (integrated in scale) and the rate of energy transferred between LES filtered scales and residual scales. This analysis is based on numerical computations in a DNS of isotropic turbulence at high Taylor Reynolds number ($Re_\lambda = 1250$). The analysis shows that both quantities share many properties but are not identical. The use of the larger scale Germano equation 2.8 in our study instead of the KHMH equation 2.7 may allow to explain these common and different properties. This equation is also likely to be a powerful tool for understanding some physical constraints in subfilter scale models for use in LES. In this chapter, a new LES model is developed which shows that the research in the previous chapters can be applied to simulation and modeling. The two-point equations research has the potential for direct, practical, applications for engineering flow simulations.

6.2 Two-point statistics theory

The two-point statistics theory is introduced in chapter 2. In chapter 4, the small scale and large scale interscale transfer rates averaged in space and time have been found to collapse with dissipation over a significant range of scales. However, Yasuda and Vassilicos 2018 quantified the small scale interscale transfer spatio-temporal fluctuations in a Direct Numerical Simulation of homogeneous turbulence. These fluctuations are very large with rare extreme events much larger than the mean dissipation value. These results are reminiscent of the backscatter already described in Piomelli et al. 1991, Domaradzki and Saiki 1997, Cerutti and Meneveau 1998, Aoyama et al. 2005 Goto 2008, Ishihara, Gotoh, and Kaneda 2009. Moreover, in Yasuda and Vassilicos 2018, these rare event contributions cannot be neglected as they contribute significantly to the mean interscale transfer rate value (50% of the mean value is contributed by events of less than $4.10^{-2}P_{max}$, where P_{max} is the maximal probability density value of the PDF for $|\boldsymbol{r}| \approx \lambda$ in one of their cases).

Similar results are obtained in our experiments as observed with the probability distribution function of the truncated estimate of the small scale interscale transfer normalized by dissipation in figure 6.1a. Very large tails of the PDF are measured, with positive and negative events much larger than dissipation (larger than $1000\langle\overline{\epsilon}'\rangle$ for $r_z > \lambda$). The local behavior is therefore very different from its mean value which is of the order of magnitude of the mean dissipation (see chapter 4). These results confirm that, locally, the turbulence behavior is far from the Kolmogorov picture with both direct and backward energy transfers across scales much larger than dissipation. The spatio-temporal probability distribution function of the large scale interscale transfer rate is also measured and plotted in figure 6.1b. The fluctuations of this term are similar and even larger than for the small scale interscale transfer rate with very large tails and values larger than $1500\langle\overline{\epsilon}'\rangle$ for the various separation

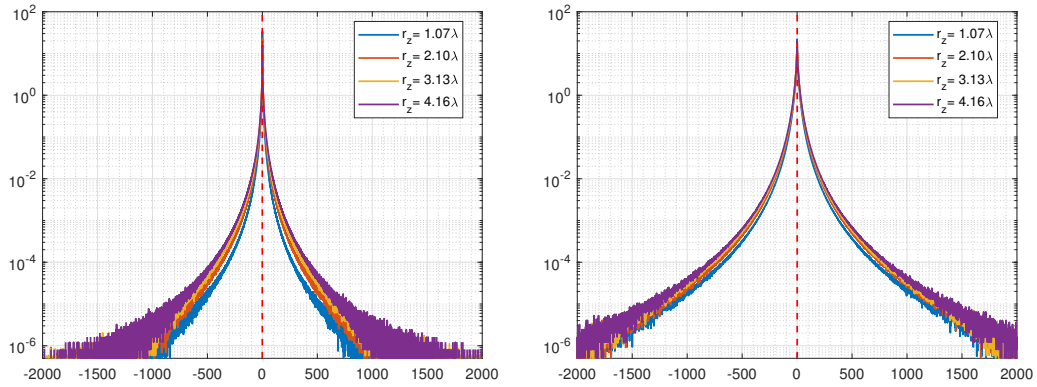

(a) Truncate estimate of the small scale interscale transfer rate normalized by dissipation locally averaged in space and in time: $\frac{\frac{\partial}{\partial r_x}[\delta u'_x(\delta u'^2_x+\delta u'^2_z)]+\frac{\partial}{\partial r_z}[\delta u'_z(\delta u'^2_x+\delta u'^2_z)]}{\langle\overline{\epsilon'}\rangle}$

(b) Truncate estimate of the large scale interscale transfer rate normalized by dissipation locally averaged in space and in time: $\frac{\frac{\partial}{\partial r_x}[\delta u'_x(u'^2_{Xx}+u'^2_{Xz})]+\frac{\partial}{\partial r_z}[\delta u'_z(u'^2_{Xx}+u'^2_{Xz})]}{\langle\overline{\epsilon'}\rangle}$

Figure 6.1: Spatio-temporal probability distribution function of the normalized small scale and large scale interscale transfer rate truncate estimates at different separation length r_z. These results are measured in the experiment with baffles, with rectangular blades and with a rotation frequency of 1Hz as presented in chapter 4. The red dashed line corresponds to the theoretical mean value in homogeneous turbulence: -1 in figure (a) and $+1$ in figure (b).

lengths plotted. In this chapter, we study the close link between the large scale interscale transfer and Large Eddy Simulation. The very large fluctuations of the large scale interscale transfer, both direct and backward, needs to be reproduced by a model which captures some turbulence physics that really happen locally.

6.3 Statement of the Large Eddy Simulation problem

In the Large Eddy Simulation concept described in Reynolds 1990, Pope 2000 and Dairay et al. 2017, model design and numerical resolution are two distinct problems. LES is seen as a numerical resolution of a filtered equation 2.24 whose residual terms are replaced by a model (2.25). This means that the modelling errors are associated with the difference between exact filtered equation 2.24 and modelled filtered equation 2.25. On the other hand, the numerical error comes from the numerical resolution of the modelled filtered equation 2.25. It can be evaluated through mesh convergence for example. In this study we focus mainly on the modelling error.

An energy equation for the filtered velocity can be derived from equation 2.24:

$$\frac{\partial}{\partial t}\left(\frac{|\widetilde{u_i}|^2}{2}\right)+\widetilde{u_j}\frac{\partial}{\partial x_j}\left(\frac{|\widetilde{u_i}|^2}{2}\right)=-\widetilde{u_i}\frac{\partial \tau_{ij}}{\partial x_j}-\frac{1}{\rho}\frac{\partial(\widetilde{u_i}\widetilde{p})}{\partial x_i}+\nu\widetilde{u_i}\nabla^2_{\boldsymbol{x}}\widetilde{u_i} \tag{6.1}$$

where $-\widetilde{u_i}\frac{\partial \tau_{ij}}{\partial x_j}$ is the rate of energy exchange between filtered scales and residual scales and represents a subfilter stress energy contribution to equation 6.1. The subfilter stress gradient $\frac{\partial \tau_{ij}}{\partial x_j}$ is modelled by $\widehat{\frac{\partial \tau_{ij}}{\partial x_j}}$ so that equation 6.1 is approximated by

$$\frac{\partial}{\partial t}\left(\frac{|\widetilde{u_i}|^2}{2}\right)+\widetilde{u_j}.\frac{\partial}{\partial x_j}\left(\frac{|\widetilde{u_i}|^2}{2}\right)\approx-\widetilde{u_i}\widehat{\frac{\partial \tau_{ij}}{\partial x_j}}-\frac{1}{\rho}\frac{\partial(\widetilde{u_i}\widetilde{p})}{\partial x_i}+\nu\widetilde{u_i}\nabla^2_{\boldsymbol{x}}\widetilde{u_i}. \tag{6.2}$$

where $-\widetilde{u_i}\widehat{\frac{\partial \tau_{ij}}{\partial x_j}}$ is the modelled subfilter stress energy contribution to the equation 6.2. In this chapter, we compare the rate of energy term $-\widetilde{u_i}\frac{\partial \tau_{ij}}{\partial x_j}$ with $-\widetilde{u_i}\widehat{\frac{\partial \tau_{ij}}{\partial x_j}}$ to know how close the modelled subfilter stress gradient contribution to (6.2) is to the exact subfilter stress gradient contribution to (6.1).

6.4 Links between two-point equations and LES modelling

In the next section, the mathematical links between the two-point equations framework and Large Eddy Simulation are derived following Germano 2007a.

6.4.1 Derivation of an exact form of the subfilter stress following Germano 2007a

The notations of $\boldsymbol{u_X}$ and $\boldsymbol{\delta u}$, defined in section 2.1.3, are slightly different to the ones used in Germano 2007a. Therefore, all the Germano's results are converted into our set of notation to be consistent with the previous chapters of this thesis.

Subfilter stress derived from u_X equation

The large scale two-point equation introduced in chapter 2 is used:

$$\frac{\partial \boldsymbol{u_X}}{\partial t}+(\boldsymbol{u_X}.\boldsymbol{\nabla_X})\boldsymbol{u_X}+(\boldsymbol{\delta u}.\boldsymbol{\nabla_r})\boldsymbol{u_X}=-\frac{1}{\rho}\boldsymbol{\nabla_X}P_X+\frac{\nu}{2}\nabla^2_X\boldsymbol{u_X}+\frac{\nu}{2}\nabla^2_r\boldsymbol{u_X} \tag{6.3}$$

and is rewritten as equation:

$$\frac{\partial \boldsymbol{u_X}}{\partial t}+(\boldsymbol{u_X}.\boldsymbol{\nabla_X})\boldsymbol{u_X}+(\boldsymbol{\delta u}.\boldsymbol{\nabla_r})\boldsymbol{u_X}=-\frac{1}{\rho}\boldsymbol{\nabla_X}P_X+\nu\nabla^2_X\boldsymbol{u_X} \tag{6.4}$$

using the fourth of the following relations (see Germano 2007b) :

$$\begin{cases} \dfrac{\partial \delta u_i}{\partial r_k} = \dfrac{\partial u_{Xi}}{\partial X_k} \\ \dfrac{\partial \delta u_i}{\partial X_k} = \dfrac{\partial u_{Xi}}{\partial r_k} \\ \dfrac{\partial^2 \delta u_i}{\partial X_k^2} = \dfrac{\partial^2 \delta u_i}{\partial r_k^2} \\ \dfrac{\partial^2 u_{Xi}}{\partial X_k^2} = \dfrac{\partial^2 u_{Xi}}{\partial r_k^2} \end{cases} \tag{6.5}$$

The term $(\boldsymbol{\delta u}.\boldsymbol{\nabla_r})\boldsymbol{u_X}$ can also be rewritten as $\frac{\partial(\delta u_i \delta u_j)}{\partial X_j}$ using the second of the relations 6.5 to derive:

$$\frac{\partial u_{Xi}}{\partial t} + u_{Xj}\frac{\partial u_{Xi}}{\partial X_j} = -\frac{\partial\left(\delta u_i \delta u_j\right)}{\partial X_j} - \frac{1}{\rho}\frac{\partial P_X}{\partial X_i} + \nu\frac{\partial^2 u_{Xi}}{\partial X_k \partial X_k} \tag{6.6}$$

According to Germano 2007c, $-\frac{\partial(\delta u_i \delta u_j)}{\partial X_j}$ represents the subfilter stress gradient associated to the two-point filter:

$$\boldsymbol{u_X} = \frac{\boldsymbol{u}(\boldsymbol{X}+\boldsymbol{r}) + \boldsymbol{u}(\boldsymbol{X}-\boldsymbol{r})}{2} = \int G_0(\boldsymbol{X}-\boldsymbol{\xi})\boldsymbol{u}(\boldsymbol{\xi})d\boldsymbol{\xi} \tag{6.7}$$

where

$$G_0(\boldsymbol{X}-\boldsymbol{\xi}) = 0.5\delta(\boldsymbol{X}+\boldsymbol{r}-\boldsymbol{\xi}) + 0.5\delta(\boldsymbol{X}-\boldsymbol{r}-\boldsymbol{\xi}), \tag{6.8}$$

and δ is the Dirac delta function $\delta(\boldsymbol{x}-\boldsymbol{\xi}) = \Pi_{k=1}^{3}\delta(x_k - \xi_k)$.

Therefore, for this basic filter, an exact form of the subfilter stress (which can, however, not be used as a subfilter stress model) is derived from the two-point large scale equation 6.6.

This subfilter stress formulation is directly related to

$$\tau_{ij} = \delta u_i \delta u_j \tag{6.9}$$

which is the basis of second-order structure functions. This basic filter is local in real space and non-local in Fourier space. It cannot be used directly for Large Eddy Simulation because it does not filter out all the energy at high wave numbers. Therefore, the results of this paragraph are generalized to more general filters.

Subfilter stress derived by Germano

A more practically useful equation for the subfilter stress is derived in Germano 2007a and Germano 2007c. The derivation is done directly from the Reynolds stress formulation. The subfilter stress explicit form is now written in the form obtained by Germano 2007a and Germano 2007c:

$$\begin{aligned}\tau_{ij} &= \widetilde{u_i u_j} - \widetilde{u}_i \widetilde{u}_j \\ &= \int G(\boldsymbol{x}-\boldsymbol{\xi}) u_i(\boldsymbol{\xi}) u_j(\boldsymbol{\xi}) d\boldsymbol{\xi} - \int_{-\infty}^{\infty} G(\boldsymbol{x}-\boldsymbol{\xi}) u_i(\boldsymbol{\xi}) d\boldsymbol{\xi} \int_{-\infty}^{\infty} G(\boldsymbol{x}-\boldsymbol{\xi'}) u_j(\boldsymbol{\xi'}) d\boldsymbol{\xi'} \\ &= 2 \int_{-\infty}^{\infty} \int_{-\infty}^{\infty} G(\boldsymbol{x}-\boldsymbol{\xi}) G(\boldsymbol{x}-\boldsymbol{\xi'}) d_{ij}(\boldsymbol{\xi},\boldsymbol{\xi'}) d\boldsymbol{\xi} d\boldsymbol{\xi'}\end{aligned} \tag{6.10}$$

where, $d_{ij}(\boldsymbol{\xi},\boldsymbol{\xi'}) = (\frac{u_i(\boldsymbol{\xi})-u_i(\boldsymbol{\xi'})}{2})(\frac{u_j(\boldsymbol{\xi})-u_j(\boldsymbol{\xi'})}{2})$ and where the discrete weight function

$$G(\boldsymbol{x}-\boldsymbol{\xi}) = \Sigma_\alpha g_\alpha \delta(\boldsymbol{x}+\boldsymbol{r}_\alpha-\boldsymbol{\xi}) \tag{6.11}$$

is used, with the weights g_α such that $\Sigma_\alpha g_\alpha = 1$. Hence $\int G(\boldsymbol{r}) d\boldsymbol{r} = 1$. The filtered velocity $\widetilde{\boldsymbol{u}}$ is obtained by

$$\widetilde{u_i} = \int_{-\infty}^{\infty} G(\boldsymbol{x}-\boldsymbol{\xi}) u_i(\boldsymbol{\xi}) d\boldsymbol{\xi}. \tag{6.12}$$

Following Germano 2007c (with change of notations), the change of variables $\boldsymbol{r} = \frac{\boldsymbol{\xi}-\boldsymbol{\xi'}}{2}$ and $\boldsymbol{s} = \frac{\boldsymbol{\xi}+\boldsymbol{\xi'}}{2}$ is used to derive the exact subfilter stress formula:

$$\tau_{ij}(\boldsymbol{x}) = \int_{-\infty}^{\infty} \int_{-\infty}^{\infty} G(\boldsymbol{x}-\boldsymbol{s}-\boldsymbol{r}) G(\boldsymbol{x}-\boldsymbol{s}+\boldsymbol{r}) d_{ij}(\boldsymbol{r},\boldsymbol{s}) d\boldsymbol{r} d\boldsymbol{s}. \tag{6.13}$$

The associated subfilter force is also derived (see Germano 2007b)

$$\frac{\partial \tau_{ij}}{\partial x_j}(\boldsymbol{x}) = \int_{-\infty}^{\infty} \int_{-\infty}^{\infty} G(\boldsymbol{x}-\boldsymbol{s}-\boldsymbol{r}) G(\boldsymbol{x}-\boldsymbol{s}+\boldsymbol{r}) \frac{\partial d_{ij}}{\partial s_j}(\boldsymbol{r},\boldsymbol{s}) d\boldsymbol{r} d\boldsymbol{s}. \tag{6.14}$$

Eventually, equation 6.14 can be rewritten, using equation 6.5, as:

$$\frac{\partial \tau_{ij}}{\partial x_j} = \int_{-\infty}^{\infty} \int_{-\infty}^{\infty} G(\boldsymbol{x}-\boldsymbol{s}-\boldsymbol{r}) G(\boldsymbol{x}-\boldsymbol{s}+\boldsymbol{r}) \boldsymbol{\nabla}_{\boldsymbol{r}}.(u_{Xi}\boldsymbol{\delta u}) d\boldsymbol{r} d\boldsymbol{s} \tag{6.15}$$

so that the term $\boldsymbol{\nabla}_{\boldsymbol{r}}.(u_{Xi}\boldsymbol{\delta u})$ which is at the origin of the large scale interscale transfer rate $\boldsymbol{\nabla}_{\boldsymbol{r}}.(\boldsymbol{\delta u}|\boldsymbol{u_X}|^2)$ introduced in the previous chapters appears explicitly.

Observations from this formulations

The exact result (6.13) is very meaningful to understand the properties of the subfilter stress of LES equations. The main points are summarized below:

- The subfilter stress has a direct link with the structure functions which are analyzed in many flows and for which the K41 theory is developed. It can therefore have a direct connection with turbulence physical understanding and some of its significant results.

- The term $\boldsymbol{\nabla_r}.(u_{X_i}\boldsymbol{\delta u})$ present in the exact subfilter stress gradient formulation 6.15 is closely related to the large scale interscale transfer rate as already mentioned. Again, the physical understanding developed with the small scale $\boldsymbol{\delta u}^2$ two-point equation and large scale $\boldsymbol{u_X}^2$ two-point equation are directly related to the subfilter stress and link the study of this chapter with the studies in the previous chapters 4 and 5.

- If compact filtering is used (gaussian filtering for example), then $g_\alpha > 0$. It can then be deduced from 6.10 that, $\tau_{ii} \geq 0$ (without implicit summation) $\forall x, t$. This result is obtained for the discrete filter used to obtain 6.10 and is not obvious when looking at the relation $\tau_{ii} = \widetilde{u_i u_i} - \widetilde{u_i}\widetilde{u_i}$.

A second exact formulation is derived in appendix C.3 which details more precisely the links between equation 6.4 and the subfilter stress gradient. This new formulation questions the contribution of the spatial transport term $(\boldsymbol{u_X}.\boldsymbol{\nabla_X})\boldsymbol{u_X}$ to the subfilter stress gradient.

6.4.2 Existing LES models close to Germano exact subfilter stress equation

Some models exist which are close to the Germano formulation 6.13 and can be used for comparison. For instance, the following *increment* model was introduced by Brun, Friedrich, and Da Silva 2006:

$$\frac{\partial \tau_{ij}}{\partial x_j} \sim \frac{\partial \left(\delta\check{u}_i \delta\check{u}_j \right)}{\partial x_j} \tag{6.16}$$

where

$$\delta\check{\boldsymbol{u}}_i = \sum_{k \in [\![1,3]\!]} \left(\widetilde{\boldsymbol{u}}_i(\boldsymbol{x} + \frac{1}{2}\boldsymbol{r}_k) - \widetilde{\boldsymbol{u}}_i(\boldsymbol{x} - \frac{1}{2}\boldsymbol{r}_k) \right), \tag{6.17}$$

$\boldsymbol{r}_k = 2m\Delta_k \boldsymbol{e}_k$ (in our case $\Delta_k = \Delta$ for all k), m is an integer number and $\boldsymbol{e}_k$ is the unit vector in direction k.

This large eddy simulation model is not explicitly inspired by Germano 2007c as it was published earlier but it has a striking similarity with the exact Germano equation 6.13. A dynamic procedure was defined by the authors to compute the model coefficient in 6.16. The model was applied to a channel flow and tested both *a priori* and *a posteriori*. Very good prediction of the probability distribution function of $\tau_{ij}\widetilde{S}_{ij}$ ($\widetilde{S_{ij}}$ is defined in (2.27)), including backscatter, is observed in *a priori* analyses in the buffer layer of a channel flow where $Re_\tau = 180$. However, the filtering was weak compared to classical LES resolution (top hat filter of $4\Delta_{DNS}$, where Δ_{DNS} is the mesh resolution size of the simulation). In *a posteriori* results, the model led to good predictions of mean quantities such as mean velocity profile and mean RMS profile.

A similar model was defined by Fang et al. 2009 with a slightly different formulation:

$$\frac{\partial \tau_{ij}}{\partial x_j} \sim \frac{\partial \widetilde{Q}_{ij}}{\partial x_j} \tag{6.18}$$

where:

$$\widetilde{Q}_{ij}(\boldsymbol{x}, \Delta) = \frac{1}{2}\left[\left(\widetilde{\boldsymbol{u}}_i(\boldsymbol{x}+\Delta \boldsymbol{e_i}) - \widetilde{\boldsymbol{u}}_i(\boldsymbol{x})\right)\left(\widetilde{\boldsymbol{u}}_j(\boldsymbol{x}+\Delta \boldsymbol{e_j}) - \widetilde{\boldsymbol{u}}_j(\boldsymbol{x})\right) + \left(\widetilde{\boldsymbol{u}}_i(\boldsymbol{x}) - \widetilde{\boldsymbol{u}}_i(\boldsymbol{x}-\Delta \boldsymbol{e_i})\right)\left(\widetilde{\boldsymbol{u}}_j(\boldsymbol{x}) - \widetilde{\boldsymbol{u}}_j(\boldsymbol{x}-\Delta \boldsymbol{e_j})\right)\right] \tag{6.19}$$

A model coefficient was derived for the model 6.18 under several assumptions but a dynamic procedure was also tested. The model predictions *a posteriori* in a channel flow about mean velocity, mean turbulent kinetic energy and mean Reynolds stress were in agreement with DNS predictions. Moreover, the non-dimensionalized subfilter dissipation tensor components

$$\Upsilon_{ij} = \frac{< \widetilde{Q_{ij}}', \widetilde{S}_{ij}' >}{RMS(\widetilde{Q_{ij}}')RMS(\widetilde{S}_{ij}')} \tag{6.20}$$

computed *a priori* are in agreement with *a posteriori* results, where $\widetilde{Q_{ij}}$ is defined in 6.19, $\widetilde{S}_{ij}$ in 2.27 and the notation: ' signifies the mean is removed for the computation of these quantities. The LES results contain mean backscatter in some specific directions and regions of the flow where it is supposed to exist according to the DNS results from Härtel et al. 1994. This is a promising result as mean backscatter is expected in specific flow regions or directions of non-homogeneous flows but classical dissipative models do not capture it.

More recently, Cimarelli and De Angelis 2014 introduced the mixed model:

$$\tau_{ij} = C_\Delta \, \overline{\overline{\delta u_i}}\,\overline{\overline{\delta u_j}} - 2\nu_T \widetilde{S_{ij}} \tag{6.21}$$

This model was inspired by the model of Brun, Friedrich, and Da Silva 2006 and the small scale KHMH energy equation. The first difference with the model of Brun, Friedrich, and Da Silva 2006 is the definition of

$$\overline{\overline{\delta u_i}} = \left(\widetilde{\boldsymbol{u}}_i(\boldsymbol{x}+\frac{1}{2}\boldsymbol{r}_k) - \widetilde{\boldsymbol{u}}_i(\boldsymbol{x}-\frac{1}{2}\boldsymbol{r}_k)\right), \tag{6.22}$$

where $\boldsymbol{r}_k = 2m\Delta_k \boldsymbol{e}_k$ (in our case $\Delta_k = \Delta$ for all k) and m is an integer number, instead of $\delta\check{u}_i$ defined in 6.17. The second difference is the combination with the Smagorinsky model in (6.21). The exact subfilter stress formulation (equation 6.10) which involves d_{ij} was also used to justify the first term of the right hand side of the model (6.21) but only as an inspiration: it was not derived from (6.13). The *increment* model is expected to capture backscatter events and the Smagorinsky model, the dissipative effects.

A dynamic procedure was set to compute C_Δ (and the Germano et al. 1991a, Germano et

al. 1991b, Lilly 1992 dynamic procedure is used for C_S). Very good results were obtained for the averaged subfilter dissipation in a channel flow compared to filtered DNS results. Again, some regions of the flow contain mean bakscatter and this is well predicted by the model. In this publication, the Smagorinsky model added to the modified Brun, Friedrich, and Da Silva 2006 model seems to be important to capture the right energy transfer values. The proposed model gives better results than classical mixed models such as the Bardina, Ferziger, and Reynolds 1980 similarity model used in combination with the Smagorinsky model. This is especially true for backscatter predictions. The model 6.21 is also close to but not exactly the same as the Clark, Ferziger, and Reynolds 1977 model, analyzed in Vreman, Geurts, and Kuerten 1995 and also called the mixed gradient model:

$$\tau_{ij} = \frac{\Delta_k^2}{12} \frac{\partial \widetilde{u_i}}{\partial x_k} \frac{\partial \widetilde{u_j}}{\partial x_k} - 2\nu_T \widetilde{S_{ij}} \tag{6.23}$$

where Δ_k is the mesh size in direction k. This model is derived based on a Taylor expansion of the subfilter stress (which may be valid only for very small Δ_k) and is also known to allow backscatter through the gradient term.

Subfilter stress models based on d_{ij} seem to be promising for large eddy simulation because they can capture backscatter events both statistically (probability distribution function) and on average. The Brun, Friedrich, and Da Silva 2006, Fang et al. 2009 and Cimarelli and De Angelis 2014 models are also very interesting as they are close to the exact equation 6.14. However, the physical and mathematical links with two-point equations can be developed further to support physically the model and bring all the physical understanding of the two-point equations into LES modelling. Such analysis requires to use the large scale two-point equations introduced by Germano 2007b and analyzed in the previous chapters instead of the small scale KHMH equation. The models (6.16), (6.18) and (6.21) have only been tested extensively in channel flows (with subfilter stress analysis) and without local analysis. Therefore, future improvements might be needed when testing such type of model in other flows or differently. If there is no clear connection with the physics, these improvements will have to be adapted for each situation meaning that the model cannot be used as an universal model. The main goal of this study is to develop possibilities for links between LES modelling and physics so that future improvements can be done based on physical findings rather than adapted for each flow and each specific simulations.

A LES model based on 6.13 is developed here and tested in a Taylor Green turbulent flow. This flow is composed of unsteady turbulent eddies at many scales. Therefore, the flow is highly irregular and the turbulent model used during LES has a significant importance for reproducing the effect of the missing small scales on the filtered scales. In this study, results are also obtained locally to see how close the predictions are to real events happening locally and instantaneously. Such analysis was not done in the studies of Brun, Friedrich, and Da Silva 2006, Fang et al. 2009 and Cimarelli and De Angelis 2014 and is a very accurate method

to test LES models as it can be observed with the different models presented in Meneveau and Katz 2000. In this later publication, the analysis of the different models locally discriminates very explicitly their representativeness.

6.4.3 Simplification of the exact subfilter stress formulation

In the present subsection, the Germano exact subfilter stress gradient formulation 6.14 is used.

Usually, the subfilter stress is analyzed rather than its gradient. Indeed, it is usual to analyze the subfilter stress because of the intuitive view developed with the Smaorinsky model where turbulence is associated to a stress. The new association of the subfilter contribution with the interscale transfer rate suggests to model directly the gradient.

The change of variable $s \longleftarrow x - s$ is used in equation 6.15 (which follows directly from 6.14) to simplify computations:

$$\frac{\partial \tau_{ij}}{\partial x_j} = \int_{-\infty}^{\infty}\int_{-\infty}^{\infty} G(\boldsymbol{s}-\boldsymbol{r})G(\boldsymbol{s}+\boldsymbol{r})\boldsymbol{\nabla}_{\boldsymbol{r}}.(u_{Xi}(\boldsymbol{x}-\boldsymbol{s},\boldsymbol{r})\boldsymbol{\delta u}(\boldsymbol{x}-\boldsymbol{s},\boldsymbol{r}))d\boldsymbol{r}d\boldsymbol{s}. \tag{6.24}$$

The cube top hat filter is used to simplify computations:

$$\begin{aligned} G\colon \mathbb{R}^3 &\longrightarrow \mathbb{R} \\ \boldsymbol{x} &\longmapsto \begin{cases} 1\colon \text{ if } |\boldsymbol{x}|_\infty \leq \Delta \text{ with } |\boldsymbol{x}|_\infty = \max\{|x_1|,|x_2|,|x_3|\} \\ 0\colon \text{ otherwise} \end{cases} \end{aligned} \tag{6.25}$$

With this filter, equation 6.24 can be re-writen as:

$$\frac{\partial \tau_{ij}}{\partial x_j} = \frac{1}{V_{ref}} \int\limits_{V_{ref}} \boldsymbol{\nabla}_{\boldsymbol{r}}.(u_{Xi}(\boldsymbol{x}-\boldsymbol{s},\boldsymbol{r})\boldsymbol{\delta u}(\boldsymbol{x}-\boldsymbol{s},\boldsymbol{r}))d\boldsymbol{r}d\boldsymbol{s} \tag{6.26}$$

where:

$$V_{ref}\colon \begin{cases} -\Delta \leq s_i - r_i \leq \Delta \\ -\Delta \leq s_i + r_i \leq \Delta. \end{cases} \tag{6.27}$$

We define the 6-dimensional volume regions V_1 and V_2

$$V_1\colon \begin{cases} -\dfrac{\Delta}{2} \leq s_i \leq \dfrac{\Delta}{2} \\ -\dfrac{\Delta}{2} \leq r_i \leq \dfrac{\Delta}{2} \end{cases} \tag{6.28}$$

$$V_2\colon \begin{cases} -\Delta \leq s_i \leq \Delta \\ -\Delta \leq r_i \leq \Delta \end{cases} \tag{6.29}$$

so that $V_1 \in V_{ref} \in V_2$. This can be derived mathematically or deduced from figure 6.2.

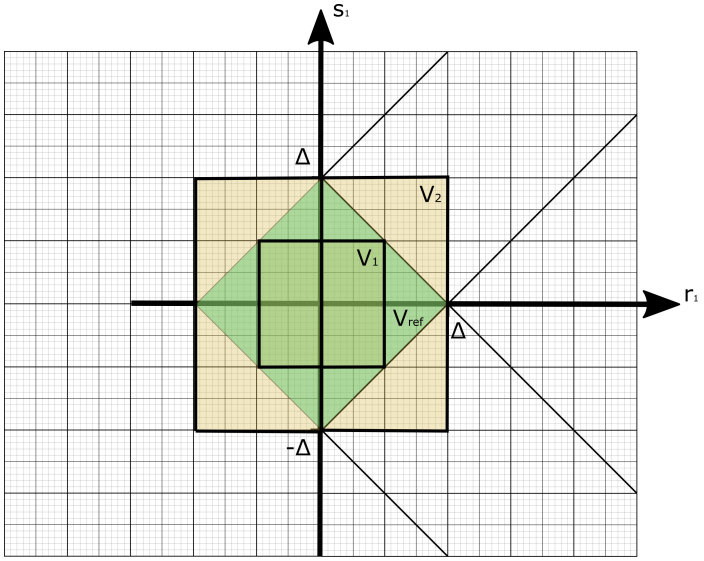

Figure 6.2: Volume representation of V_1, V_2 and V_{ref} in one dimension

V_{ref} is approximated by V_2 here which leads to an over-filtering compared to the initial top hat filter, and so we compute

$$\frac{\partial \tau_{ij}}{\partial x_j} \approx \frac{1}{V_2} \int_{V_2} \boldsymbol{\nabla_r}.(u_{Xi}(\boldsymbol{x}-\boldsymbol{s},\boldsymbol{r})\boldsymbol{\delta u}(\boldsymbol{x}-\boldsymbol{s},\boldsymbol{r}))d^3r d^3s \equiv \Gamma_i \tag{6.30}$$

The purpose of this approximation is the decoupling of the space filtering ($\boldsymbol{s}$ space) and the scale filtering ($\boldsymbol{r}$ space):

$$\Gamma_i = \frac{1}{(2\Delta)^3} \int_{V(\Delta)} \left(\frac{1}{(2\Delta)^3} \int_{V(\Delta)} \boldsymbol{\nabla_r}.(u_{Xi}(\boldsymbol{x}-\boldsymbol{s},\boldsymbol{r})\boldsymbol{\delta u}(\boldsymbol{x}-\boldsymbol{s},\boldsymbol{r}))d^3r \right) d^3s \tag{6.31}$$

where $\int_{V(\Delta)}(.)d^3s = \int_{-\Delta}^{\Delta}\int_{-\Delta}^{\Delta}\int_{-\Delta}^{\Delta}(.)d^3s$.

This first approximation 6.30 is quantified later in this chapter (in subsection 6.5.2). The decoupling that is introduced is useful because the divergence theorem can now be used in $\boldsymbol{r}$ space:

$$\Gamma_i = \frac{1}{(2\Delta)^3} \int_{V(\Delta)} \frac{1}{(2\Delta)^3} \left[\oint_{|\boldsymbol{r}|_\infty=\Delta} (u_{Xi}(\boldsymbol{x}-\boldsymbol{s},\boldsymbol{r})\boldsymbol{\delta u}(\boldsymbol{x}-\boldsymbol{s},\boldsymbol{r})).\boldsymbol{n} d^2r \right] d^3s \tag{6.32}$$

where $\boldsymbol{n}$ is the outward pointing unit normal at each point on the closed surface of integration. Therefore, after this point, during the closed surface integration in 6.32, for all j, in the direction n_j, the value of the component of $\boldsymbol{r}$ in this direction is: $r_j = \Delta$. This is interesting as only quantities with a separation distance of Δ or larger (in multiples of Δ) can be

evaluated on the LES resolution mesh. However, the values of the other components of $\boldsymbol{r}$, $r_i \leq \Delta$ where $i \neq j$ (n_j is the direction of projection) are still needed during the surface integration in 6.32 but are neglected later in the derivation. The integration in physical space (d^3s) of equation 6.34 should also be analyzed because it requires values not available during LES computations. The filtered quantities available with cube top hat filter LES resolution are:

$$\begin{aligned} \widetilde{u}_{Xi}(\boldsymbol{x},\boldsymbol{r}) &= \frac{1}{(2\Delta)^3}\int_{V(\Delta)} u_{Xi}(\boldsymbol{x}-\boldsymbol{s},\boldsymbol{r})d^3s \\ \boldsymbol{\delta}\widetilde{\boldsymbol{u}}(\boldsymbol{x},\boldsymbol{r}) &= \frac{1}{(2\Delta)^3}\int_{V(\Delta)} \boldsymbol{\delta u}(\boldsymbol{x}-\boldsymbol{s},\boldsymbol{r})d^3s \end{aligned} \tag{6.33}$$

which suggests to rewrite equation 6.32 as follows:

$$\begin{aligned} \Gamma_i = &\frac{1}{(2\Delta)^3}\oint_{|\boldsymbol{r}|_\infty=\Delta} (\widetilde{u}_{Xi}(\boldsymbol{x},\boldsymbol{r})\boldsymbol{\delta}\widetilde{\boldsymbol{u}}(\boldsymbol{x},\boldsymbol{r})).\boldsymbol{n}d^2r \\ &+ \frac{1}{(2\Delta)^3}\left[\oint_{|\boldsymbol{r}|_\infty=\Delta}\left(\frac{1}{(2\Delta)^3}\int_{V(\Delta)} u_{Xi}(\boldsymbol{x}-\boldsymbol{s},\boldsymbol{r})\boldsymbol{\delta u}(\boldsymbol{x}-\boldsymbol{s},\boldsymbol{r})d^3s - \widetilde{u}_{Xi}(\boldsymbol{x},\boldsymbol{r})\boldsymbol{\delta}\widetilde{\boldsymbol{u}}(\boldsymbol{x},\boldsymbol{r})\right).\boldsymbol{n}d^2r\right]. \end{aligned} \tag{6.34}$$

Equation 6.34 can also be written as:

$$\begin{aligned} \Gamma_i = &\frac{1}{(2\Delta)^3}\oint_{|\boldsymbol{r}|_\infty=\Delta} (\widetilde{u}_{Xi}(\boldsymbol{x},\boldsymbol{r})\boldsymbol{\delta}\widetilde{\boldsymbol{u}}(\boldsymbol{x},\boldsymbol{r})).\boldsymbol{n}d^2r \\ &+ \frac{1}{(2\Delta)^3}\left[\oint_{|\boldsymbol{r}|_\infty=\Delta}\left(\frac{1}{(2\Delta)^3}\int_{V(\Delta)} u'_{Xi}(\boldsymbol{x}-\boldsymbol{s},\boldsymbol{r})\boldsymbol{\delta u}'(\boldsymbol{x}-\boldsymbol{s},\boldsymbol{r})d^3s\right).\boldsymbol{n}d^2r\right] \end{aligned} \tag{6.35}$$

where $u'_{Xi}(\boldsymbol{x}-\boldsymbol{s},\boldsymbol{r}) = u_{Xi}(\boldsymbol{x}-\boldsymbol{s},\boldsymbol{r}) - \widetilde{u}_{Xi}(\boldsymbol{x},\boldsymbol{r})$ and $\boldsymbol{\delta u}'(\boldsymbol{x}-\boldsymbol{s},\boldsymbol{r}) = \boldsymbol{\delta u}(\boldsymbol{x}-\boldsymbol{s},\boldsymbol{r}) - \widetilde{\boldsymbol{\delta u}}(\boldsymbol{x},\boldsymbol{r})$.

The first part is the resolved part because it is computed with the resolved velocity field. The second part of the equation cannot be evaluated during LES resolution. Later in this chapter (subsection 6.5.2), it is found that the second part of the equation is much smaller than the first part in our flow but it should not be neglected as it probably contains important turbulent behavior properties. Indeed, this term is associated to small scale behavior so it is expected to be related to dissipation: we call it the residual term.

6.4.4 Interpretation of (6.35) and formulation of a new LES model

Justification of mixed model configuration

The small scale interscale transfer rates discussed in the previous chapters have highly non-gaussian PDFs with heavy tails which correspond to large / extreme events (see section

6.2). These events are by definition extremely energetic. On the other hand, the mean interscale transfer balances dissipation in very high Reynolds number, statistically stationary and homogeneous turbulence for $r >> \lambda$ (also observed sometimes in non-homogeneous flows as in Alves Portela, Papadakis, and Vassilicos 2017). The mean interscale transfer is very small compared to the large local fluctuations and is mostly associated to small scales through dissipative effects. The same behavior is expected for energy transfers between filtered and residual scales in LES because of the strong connection between interscale transfer and subfilter stress energy transfer introduced at the beginning of this chapter. This results is observed for a long time (Piomelli et al. 1991) but it is now related to the interscale transfer rate used in Physics.

The resolved term is expected to capture the local behavior of the energy transfer with large fluctuations mainly driven by the resolved scales but it probably does not capture the average dissipation associated to small scales. As mentioned previously, the dissipation is likely to be related to the residual term of equation 6.35. This interpretation may only be valid when the filtering width $\Delta >> \eta$ so that the dissipative scales are present in the residual term. This latter term can be modelled with existing dissipative models such as the Smagorinsky model or more accurately, with a spectral vanishing viscosity model which can be implemented in physical space as in Dairay et al. 2017. In this study, the Smagorinsky model is used to model dissipation for simplicity. Some limitations of this model are well known but the dissipative model is not the main object of the present study. The conclusions about the resolved part are not expected to be significantly dependent on the choice of dissipation model.

The separation of the LES model into two terms, one taking into account the local dynamics and a second term modeling the dissipation has been argued here with physical arguments. However, the result is equivalent to existing mixed models derived and commonly used in LES modelling. This is for example the case of the similarity model (Bardina, Ferziger, and Reynolds 1980) which is often used in combination with a dissipative model such as Smagorinsky or of the Cimarelli and De Angelis 2014 model described in subsection 6.4.2.

Definition of the model used in this study

We introduce and use the following LES model in our study:

$$\frac{\partial \tau_{ij}}{\partial x_j} = \frac{C_1}{(2\Delta)^3} \oint_{|\boldsymbol{r}|_\infty=\Delta} (\widetilde{u}_{Xi}(\boldsymbol{x},\boldsymbol{r})\boldsymbol{\delta}\widetilde{\boldsymbol{u}}(\boldsymbol{x},\boldsymbol{r})).\boldsymbol{n}d^2r + \frac{\partial\left(-2C_s\Delta^2|\widetilde{S}|\widetilde{S}_{ij}\right)}{\partial x_j} \tag{6.36}$$

where C_1 is a dimensionless model constant which may depend on Δ and is introduced to rescale the resolved part of the model if needed after the approximations done. This coefficient is evaluated by *a priori* DNS tests (see Appendix C.1) and $C_S = \frac{1}{\pi}\left(\frac{2}{3C_k}\right)^{3/4}$ following Lilly 1967 so that $C_S \approx 0.18$ for $C_k = 1.4$. This coefficient is used in our mixed

model assuming the resolved part of our model does not produce any dissipation.

The first part is an approximation and the second part a model which should partly reproduce neglected physical effects. The first part is called the resolved term/model and the second the dissipative model.

Galilean invariance

The resolved term has the same form as the exact term $(\boldsymbol{\delta u}.\boldsymbol{\nabla_r})\boldsymbol{u_X}$ in equation 6.4 once integrated in scale space. Therefore, the invariance properties of the Navier-Stokes equation are expected to be also applicable for the resolved term. However, the Galilean invariance property is derived here for clarity. Note that the Smagorinsky model is Galilean (Oberlack 1997).

We introduce a new reference system moving at a constant speed $\boldsymbol{U}$ compared to our previous reference system: $t' = t$, $\boldsymbol{x'} = \boldsymbol{x} - \boldsymbol{U}t$ and $\boldsymbol{u'} = \boldsymbol{u} - \boldsymbol{U}$ and we evaluate the model

$$\oint_{|\boldsymbol{r}|_\infty=\Delta} (\widetilde{u}_{Xi}(\boldsymbol{x},\boldsymbol{r})\boldsymbol{\delta}\widetilde{\boldsymbol{u}}(\boldsymbol{x},\boldsymbol{r})).\boldsymbol{n}d^2r \tag{6.37}$$

in that system. We start with the two-point velocity quantities:

$$\begin{cases} \boldsymbol{\delta}\widetilde{\boldsymbol{u}}(\boldsymbol{x},\boldsymbol{r},t) \rightarrow \boldsymbol{\delta}\widetilde{\boldsymbol{u}}(\boldsymbol{x'},\boldsymbol{r'},t') = \boldsymbol{\delta}\widetilde{\boldsymbol{u}}(\boldsymbol{x}-\boldsymbol{U}t,\boldsymbol{r},t) \\ \widetilde{\boldsymbol{u}}_{\boldsymbol{X}}(\boldsymbol{x},\boldsymbol{r},t) \rightarrow \widetilde{\boldsymbol{u}}_{\boldsymbol{X}}(\boldsymbol{x'},\boldsymbol{r'},t') = \widetilde{\boldsymbol{u}}_{\boldsymbol{X}}(\boldsymbol{x}-\boldsymbol{U}t,\boldsymbol{r},t) - \boldsymbol{U} \end{cases} \tag{6.38}$$

Using (6.38) and the property that $\boldsymbol{\nabla_r}.\boldsymbol{\delta}\widetilde{\boldsymbol{u}} = 0$ so that the closed surface integral of $\boldsymbol{\delta}\widetilde{\boldsymbol{u}}$ vanishes, the resolved term (6.37) can be written as follows in the reference frame moving with velocity U relative to the original frame.

$$\begin{aligned} &\oint_{|\boldsymbol{r}|_\infty=\Delta} (\widetilde{u}_{Xi}(\boldsymbol{x'},\boldsymbol{r'},t')\boldsymbol{\delta}\widetilde{\boldsymbol{u}}(\boldsymbol{x'},\boldsymbol{r'},t').\boldsymbol{n}d^2r' \\ &= \oint_{|\boldsymbol{r}|_\infty=\Delta} (\widetilde{u}_{Xi}(\boldsymbol{x}-\boldsymbol{U}t,\boldsymbol{r},t)\boldsymbol{\delta}\widetilde{\boldsymbol{u}}(\boldsymbol{x}-\boldsymbol{U}t,\boldsymbol{r},t)).\boldsymbol{n}d^2r - U_i \oint_{|\boldsymbol{r}|_\infty=\Delta} \boldsymbol{\delta}\widetilde{\boldsymbol{u}}(\boldsymbol{x}-\boldsymbol{U}t,\boldsymbol{r},t).\boldsymbol{n}d^2r \\ &= \oint_{|\boldsymbol{r}|_\infty=\Delta} (\widetilde{u}_{Xi}(\boldsymbol{x}-\boldsymbol{U}t,\boldsymbol{r},t)\boldsymbol{\delta}\widetilde{\boldsymbol{u}}(\boldsymbol{x}-\boldsymbol{U}t,\boldsymbol{r},t)).\boldsymbol{n}d^2r \end{aligned} \tag{6.39}$$

Therefore, the resolved model is Galilean invariant as expected.

6.4.5 Implementation of the model

Discrete form of the model

The resolved term in equation 6.36 is written with a closed surface integral over a mesh cell. However, all the points are not available with LES resolution so the implementation is an approximation of equation 6.36. In this chapter, the simplest option is used where only the available points are taken into account:

We define the list: $I_\Delta = \{-\Delta, 0, \Delta\}$.

$$
\begin{aligned}
&\frac{C_1}{(2\Delta)^3}\oint_{|\boldsymbol{r}|_\infty=\Delta}(\widetilde{u}_{Xi}(\boldsymbol{x},\boldsymbol{r})\boldsymbol{\delta\widetilde{u}}(\boldsymbol{x},\boldsymbol{r})).\boldsymbol{n}d^2r \\
\approx \frac{C_1}{(2\Delta)^3}\frac{6(2\Delta)^2}{6\times 9}\Big[&\sum_{r_y\in I_\Delta}\sum_{r_z\in I_\Delta}\widetilde{u}_{Xi}(\boldsymbol{x},r_x=\Delta,r_y,r_z)\delta\widetilde{u_x}(\boldsymbol{x},r_x=\Delta,r_y,r_z) \\
&-\sum_{r_y\in I_\Delta}\sum_{r_z\in I_\Delta}\widetilde{u}_{Xi}(\boldsymbol{x},r_x=-\Delta,r_y,r_z)\delta\widetilde{u_x}(\boldsymbol{x},r_x=-\Delta,r_y,r_z) \\
&+\sum_{r_x\in I_\Delta}\sum_{r_z\in I_\Delta}\widetilde{u}_{Xi}(\boldsymbol{x},r_x,r_y=\Delta,r_z)\delta\widetilde{u_y}(\boldsymbol{x},r_x,r_y=\Delta,r_z) \\
&-\sum_{r_x\in I_\Delta}\sum_{r_z\in I_\Delta}\widetilde{u}_{Xi}(\boldsymbol{x},r_x,r_y=-\Delta,r_z)\delta\widetilde{u_y}(\boldsymbol{x},r_x,r_y=-\Delta,r_z) \\
&+\sum_{r_x\in I_\Delta}\sum_{r_y\in I_\Delta}\widetilde{u}_{Xi}(\boldsymbol{x},r_x,r_y,r_z=\Delta)\delta\widetilde{u_z}(\boldsymbol{x},r_x,r_y,r_z=\Delta) \\
&-\sum_{r_x\in I_\Delta}\sum_{r_y\in I_\Delta}\widetilde{u}_{Xi}(\boldsymbol{x},r_x,r_y,r_z=-\Delta)\delta\widetilde{u_z}(\boldsymbol{x},r_x,r_y,r_z=-\Delta)\Big] \equiv \Psi
\end{aligned}
\tag{6.40}
$$

The available points are plotted in figure 6.3 where the black arrows represent the projections of $\widetilde{u}_{Xi}(\boldsymbol{x},\boldsymbol{r})\boldsymbol{\delta\widetilde{u}}(\boldsymbol{x},\boldsymbol{r})$ used during surface integration of 6.37.

The error introduced by replacing equation 6.32 with equation 6.40 is quantified later in this chapter (in subsection 6.5.2). The uncertainty introduced during this step is the discretization of the left hand side of equation 6.36 and the missing residual term. Interpolation might improve the results and could be used in future work. For simplicity, the mesh is considered here to be isotropic but the results can in principle be generalized if necessary (the uncertainty introduced might change).

Extrapolation to Large Eddy Simulation

Referring to the Large Eddy Simulation concept introduced at the start of section 6.3, the Smagorinsky model does to not converge to the right solution with mesh convergence as shown by Dairay et al. 2017. Other models such as vanishing spectral viscosity methods (and associated models) give better results. This is why the Smagorinsky model, used in this study for simplicity, is to be replaced in the future by a better dissipation model.

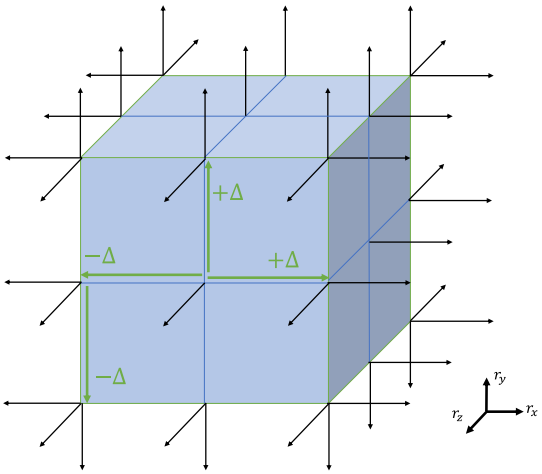

Figure 6.3: Integration points available in r space over a coarse LES mesh. Each arrow describes a point used during surface integration over the coarse mesh with the projection direction.

The resolved part is approximated from the exact subfilter stress based on a top hat filter. It might be possible to generalize the derivation for other compact filters. However, following the LES interpretation defined previously, any filter satisfying the right LES properties can be used to derive a LES subfilter scale model as long as the simulation's resolution is chosen accordingly. When, the mesh resolution size Δ approaches zero, the following properties are derived: $\lim_{\Delta\to 0} \widetilde{u}_{Xi} = u_{Xi}$ and $\lim_{\Delta\to 0} \boldsymbol{\delta\widetilde{u}} = \boldsymbol{\delta u}$ so that when Δ is small enough, we may approximate $\oint_{|\boldsymbol{r}|_\infty=\Delta}(\widetilde{u}_{Xi}(\boldsymbol{x},\boldsymbol{r})\boldsymbol{\delta\widetilde{u}}(\boldsymbol{x},\boldsymbol{r})).\boldsymbol{n}d^2r$ by $\oint_{|\boldsymbol{r}|_\infty=\Delta}(u_{Xi}(\boldsymbol{x},\boldsymbol{r})\boldsymbol{\delta u}(\boldsymbol{x},\boldsymbol{r})).\boldsymbol{n}d^2r$.

Therefore, as the filtering in physical space in equation 6.15 is expected to vanish when $\Delta \to 0$, we conjecture that the resolved part of the equation converges toward the exact solution when the mesh is refined. This result is not derived mathematically and may not hold when it is combined with the Smagorinsky model which does not converge toward the right solution according to Dairay et al. 2017.

6.5 Evaluation of the model

6.5.1 Presentation of the simulation

Presentation of the simulation code

An in-house pseudo-spectral code is used to solve the Navier-Stokes equations with Direct Numerical Simulation. The non-linear term $\boldsymbol{\omega} \times \boldsymbol{u}$ is computed in real space which allows the implementation of the LES models in real space even though the simulation is in Fourier space. A 2/3 truncation de-aliasing is used and a second order Runge-Kutta time step scheme is implemented. Periodic boundary conditions are used in all three dimensions. More

information about this code can be found in the paper of Vincent and Meneguzzi 1991.

Presentation of the Taylor-Green Direct Numerical Simulation

The Taylor-Green simulation is described in Brachet et al. 1983 Dairay et al. 2017. Kolmogorov-like results for the energy spectrum are usually observed for Re_λ large enough.

A $512 \times 512 \times 512$ forced Direct Numerical Simulation is carried out with periodicity conditions until energy is converged. The simulation parameters are described in table 6.1 where k_{trunck} is the de-aliasing truncation and where L, evaluated here as $\frac{\int E(k)/kdk}{\int E(k)dk}$, is the integral scale. The simulation is highly resolved (the mesh resolution, $\Delta x = \frac{2\pi}{2k_{max}} \approx 0.7\eta$) and Re_λ has a moderate value. We do not expect to observe a large inertial range with this moderate Reynolds number. It is not a problem for the model evaluation because no Kolmogorov or inertial range similarity assumption is used during the resolved part derivation. The CFL is initialized at 0.016 and then the simulation time step is modified dynamically to reach a CFL of 0.5.

Number of points	Size of the domain	Re_λ	$k_{trunck}\eta$	$k_{max}\eta$	ν
$512 \times 512 \times 512$	$7.1L \times 7.1L \times 7.1L$	91	3	4.5	2×10^{-3}

Table 6.1: DNS parameters

The flow is initialized with a random velocity field. A Taylor-Green flow is defined as follows:

$$\begin{aligned} u_x(x,y,z) &= sin(x)cos(y)cos(z) \\ u_y(x,y,z) &= -cos(x)sin(y)cos(z) \\ u_z &= 0 \end{aligned} \tag{6.41}$$

During the simulation, the Fourier modes associated to equation 6.41 are injected on the corresponding simulation wavenumbers at each time step to force the flow.

The energy evolution in time and energy spectrum at the final time (33τ, where $\tau = \frac{L}{\sqrt{(u-\overline{u})^2}}$ is the final turnover time) are presented in figure 6.4a and 6.4b. The simulation is long enough so that the turbulent kinetic energy fluctuates around a constant. A small inertial range with a slope close to $k^{-5/3}$ may be identified in the energy spectrum. The flow contains a wide range of scales so it is turbulent enough to be an acceptable test for LES modeling.

6.5.2 Presentation of the model's *a priori* results

A good LES model according to *a priori* analysis should succeed by at least the following two criteria. Firstly, it should inject dissipation and backscatter at the right space location

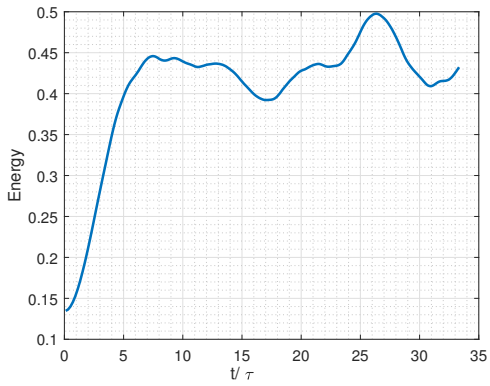

(a) Energy evolution in time. τ is the turnover time.

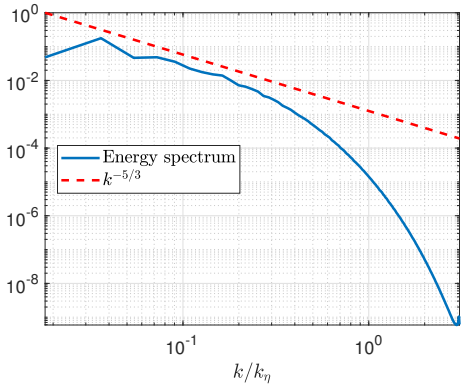

(b) Energy spectrum at the last time step. $k_\eta = \frac{1}{\eta}$

Figure 6.4: DNS simulation results

at the right time. Secondly, it should inject the right distribution of values of dissipation and backscatter. These two steps are processed differently during the design of our model. The *a priori* analysis is carried out first only qualitatively to check that the LES model predicts well the sign and the locations of the energy transfers between residual and filtered scales. Then, the analysis of the model coefficient is carried out based on the values predicted by the model and compared to exact values.

Qualitative comparison

The resolved part, defined in equation 6.40, is evaluated *a priori* on the DNS velocity field. The Smagorinsky model

$$\frac{\partial \tau_{ij}}{\partial x_j} = \frac{\partial \left(-2C_s\Delta^2|\widetilde{S}|\widetilde{S}_{ij}\right)}{\partial x_j} \tag{6.42}$$

where $C_S = 0.18$ and the model (6.16) introduced in Brun, Friedrich, and Da Silva 2006 are used for comparison. A $12 \times 12 \times 12$ points top-hat filter is used for filtering (6.12) which corresponds to around $8\eta \times 8\eta \times 8\eta$ ($\Delta \approx 8\eta$). The quantity: $-\widetilde{u}_i \frac{\partial \tau_{ij}}{\partial x_j}$, introduced in equation 6.1, is evaluated as function of space and time. It describes the full energy transfer between the residual scales and the filtered scales. In this work, negative values reduce the energy of $\widetilde{u}_i\widetilde{u}_i$ so they can be seen as dissipative values while positive values represent backscatter.

This definition is slightly different to the common one $\tau_{ij}\widetilde{S}_{ij}$ which does not take into account the full energy transfer. Indeed the total energy transfer is sometimes divided into a spatial term and a 'local energy flux of the turbulence energy cascade' (Vela-Martín 2022):

$$-\widetilde{u}_i \frac{\partial \tau_{ij}}{\partial x_j} = -\frac{\partial(\widetilde{u}_i \tau_{ij})}{\partial x_j} + \tau_{ij}\widetilde{S}_{ij} \tag{6.43}$$

The author of this latter publication shows that τ_{ij} can be chosen so that $\tau_{ij}\widetilde{S}_{ij}$ does not produce backscatter. However, this does not mean that the sign of the full contribution of the subfilter stress to equation 6.1: $-\widetilde{u}_i\frac{\partial\tau_{ij}}{\partial x_j}$, is negative. Indeed, positive and negative values are produced by the transport term $-\frac{\partial(\widetilde{u_i\tau_{ij}})}{\partial x_j}$ so that the full term $-\widetilde{u}_i\frac{\partial\tau_{ij}}{\partial x_j}$ has positive and negative contributions to (6.1) even when $\tau_{ij}\widetilde{S}_{ij}$ does not produce backscatter. Therefore, the backscatter defined in this chapter describes positive events of the full term: $-\widetilde{u}_i\frac{\partial\tau_{ij}}{\partial x_j}$. Note that, in a different framework, the mathematically exact equation C.6 derived in appendix C.3 suggests that spatial contribution to the subfilter stress cannot be dissociated from the energy transfer between filtered and residual scales in the same framework which questions the role of the spatial term in this energy transfer.

The PDF of the exact subfilter stress contribution to (6.1), noted $-\widetilde{u}_i\frac{\partial\tau_{ij}}{\partial x_j}$, is presented in figure 6.5. The model constants C_1 for (6.36) and C_2 for (6.16) are optimized based on the PDF of $-\widetilde{u}_i\frac{\partial\left(\delta\check{u}_i\delta\check{u}_j\right)}{\partial x_j}$ and $-\widetilde{u}_i\Psi$ (where Ψ is defined in 6.40) evaluated a priori on DNS results and compared to the PDF of $-\widetilde{u}_i\frac{\partial\tau_{ij}}{\partial x_j}$ for the same dataset. The numerical optimisation is described in appendix C.1. The mean values corresponding to these PDFs correspond to the mean contribution of the subfilter stress $-\widetilde{u_i}\widehat{\frac{\partial\tau_{ij}}{\partial x_j}}$ (expected to be negative). The tails correspond to the rare, very intense events.

The PDF of the Smagorinsky model subfilter stress contribution to (6.2) (i.e. $-\widetilde{u}_i\frac{\partial\left(-2C_s\Delta^2|\widetilde{S}|\widetilde{S}_{ij}\right)}{\partial x_j}$) has a significantly different shape compared to the PDF of $-\widetilde{u}_i\frac{\partial\tau_{ij}}{\partial x_j}$ obtained directly from the DNS with a skewness that is too negative. This is consistent with the known over-dissipative behavior of this model. There are only a few backscatter events and their values are relatively small.

The Brun, Friedrich, and Da Silva 2006 model contribution ($-\widetilde{u}_i\frac{\partial\left(\delta\check{u}_i\delta\check{u}_j\right)}{\partial x_j}$) has a more realistic shape with both dissipative and backscatter events but it doesn't fit very well the exact results $-\widetilde{u}_i\frac{\partial\tau_{ij}}{\partial x_j}$ even after optimization of the coefficient C_2 (see appendix C.1).

The subfilter stress resolved part contribution ($-\widetilde{u}_i\Psi$, Ψ defined in 6.40) has distribution values closer to exact results once the coefficient C_1 is well adjusted (see appendix C.1 where the coefficient C_1 is optimized and a value of 0.97 is obtained for the present filtering width). This may be expected as this model is derived from the exact subfilter stress but it confirms that the approximations done during the derivation process, and evaluated later in this chapter, do not introduce too much uncertainty. The results of the resolved part with the coefficient C_1 used for figure 6.5 combined with the Smagorinsky model are also presented in figure 6.6. The results are over dissipative with skewnesses of the probability distribution functions that are too negative compared to exact results. However, this part of the model does capture the large range of variation of the energy transfer rate and contains backscatter. Therefore, this model can in principle be used in large eddy simulation but there is also a need for future work to design a new dissipation model which would better complement the

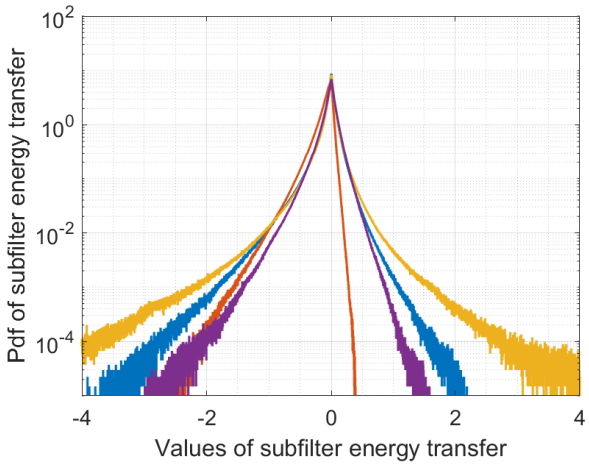

Figure 6.5: PDF of the subfilter stress contribution (exact: $-\widetilde{u}_i \frac{\partial \tau_{ij}}{\partial x_j}$ or modelled: $-\widetilde{u_i} \widehat{\frac{\partial \tau_{ij}}{\partial x_j}}$) evaluated *a priori* on DNS results with a $12 \times 12 \times 12$ top hat filter. In blue: exact results ($-\widetilde{u}_i \frac{\partial \tau_{ij}}{\partial x_j}$); red: Smagorinsky model ($-\widetilde{u}_i \frac{\partial\left(-2C_s\Delta^2|\widetilde{S}|\widetilde{S}_{ij}\right)}{\partial x_j}$); yellow: Brun, Friedrich, and Da Silva 2006 model (6.16) ($-\widetilde{u}_i \frac{\partial\left(\delta\check{u}_i\delta\check{u}_j\right)}{\partial x_j}$); purple: Present model with the resolved part only ($-\widetilde{u}_i\Psi$, where Ψ is defined in 6.40).

resolved part.

The subfilter stress contributions ($-\widetilde{u}_i \frac{\partial \tau_{ij}}{\partial x_j}$, $-\widetilde{u}_i \frac{\partial\left(-2C_s\Delta^2|\widetilde{S}|\widetilde{S}_{ij}\right)}{\partial x_j}$, $-\widetilde{u}_i \frac{\partial\left(\delta\check{u}_i\delta\check{u}_j\right)}{\partial x_j}$ and $-\widetilde{u}_i\Psi$) are now analyzed in space (figures 6.7a, 6.7b, 6.7c and 6.7d) to check the spatial correlation between exact and modeled values. The same adjusted constants as for the PDFs in figure 6.5 and 6.6 are used. In figure 6.7a, clear structures are identified in the exact subfilter stress contribution ($-\widetilde{u}_i \frac{\partial \tau_{ij}}{\partial x_j}$) with well identified large events and filaments in the background. Large dissipative events are often observed to be close to large backscatter events which is consistent with the theoretical analysis of interscale flux energy transfer in Chen and Vassilicos 2022. In figure 6.7b, the missing backscatter events when the Smagorinsky model is used are clearly visible in comparison to the exact results in figure 6.7a. Some correlation seems to exist for the large events and the filaments compared to exact ones but the sign is often wrong and large backscatter events are even sometimes replaced by large dissipative events. The results of the model Brun, Friedrich, and Da Silva 2006 in figure 6.7c contain both dissipative and backscatter events as wanted. The background filaments are comparable to the exact ones but the large events do not correlate well with exact ones except at specific locations. The best correlation with real values is observed with the subfilter stress resolved part (6.40) of our model (6.36) in figure 6.7d where most of large events predicted are representative of real events. The background filaments are also well representative of real ones. However, the exact large event locations and magnitudes can differ between predicted and exact values. This analysis is restricted to one snapshot in space so the correlation over the full domain is

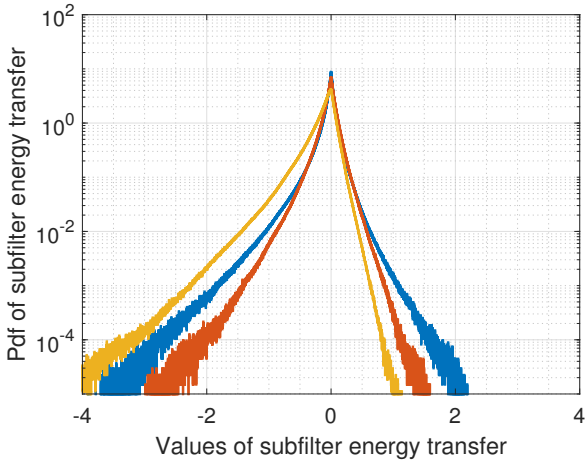

Figure 6.6: PDF of the subfilter stress contribution (exact: $-\widetilde{u}_i \frac{\partial \tau_{ij}}{\partial x_j}$ or modelled: $-\widetilde{u}_i \widehat{\frac{\partial \tau_{ij}}{\partial x_j}}$) evaluated *a priori* on DNS results with a $12 \times 12 \times 12$ top hat filter. In blue: exact results ($-\widetilde{u}_i \frac{\partial \tau_{ij}}{\partial x_j}$); red: Present model with the resolved part only ($-\widetilde{u}_i \Psi$, where Ψ is defined in 6.40); yellow: Present model including its Smagorinsky model part (i.e. $-\widetilde{u}_i(\Psi + \frac{\partial\left(-2C_s\Delta^2|\widetilde{S}|\widetilde{S}_{ij}\right)}{\partial x_j})$).

now analyzed for a more reliable conclusion.

The joint PDFs of the modelled subfilter stress contribution (Smagorinsky model: $-\widetilde{u}_i \frac{\partial\left(-2C_s\Delta^2|\widetilde{S}|\widetilde{S}_{ij}\right)}{\partial x_j}$, Brun, Friedrich, and Da Silva 2006 model (6.16): $-\widetilde{u}_i \frac{\partial\left(\delta\check{u}_i \delta\check{u}_j\right)}{\partial x_j}$ and resolved part of our model: $-\widetilde{u}_i \Psi$, where Ψ is defined in 6.40) with the exact contribution: $-\widetilde{u}_i \frac{\partial \tau_{ij}}{\partial x_j}$ are presented in figures 6.8a, 6.8b and 6.8c.

There is a good correlation if a linear shape is observed. This test is more sensitive than spatial map visualizations because a small position uncertainty of a well predicted structure (shape and magnitude) can lead to non linear shapes in figure 6.8.

The Smagorinsky model in figure 6.8a has nearly no local correlation with the exact values which confirms the impressions given in figures 6.7a, 6.7b. The Brun, Friedrich, and Da Silva 2006 model (6.16) in figure 6.8b has a small correlation but the values around the axes suggest also strong anti-correlation. These results are probably affected by the small position shift of the structures as a correlation seems to be observed when looking directly at the map in figure 6.7c. The resolved subfilter part (6.40), with C_1 optimized as explained in appendix C.1, in figure 6.8c has a better correlation compared to the other models. The results are not fully satisfactory and can probably be improved in future work. However, compared to existing LES models, this is a rather good result. Our approach being based on a progressive simplification of Germano's exact subfilter stress equation, it is possible to know where the errors are introduced by checking the main steps where approximations are introduced. For the *a priori* analysis, $\Delta \approx 8\eta$ is used. This value has been selected in order to use the same

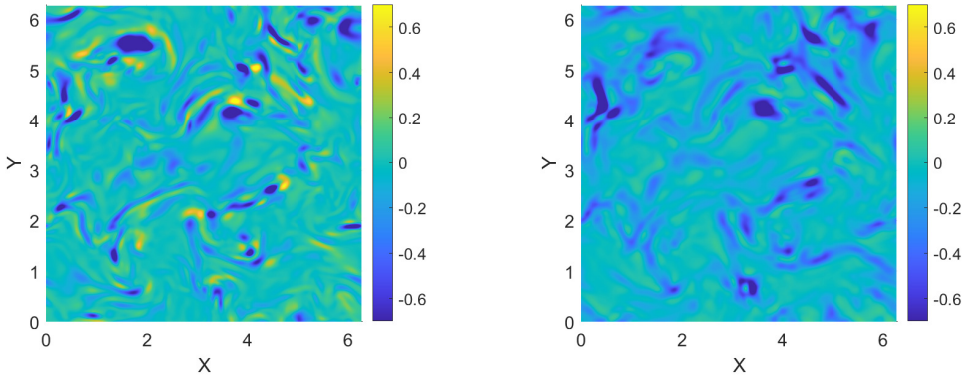

(a) $-\widetilde{u}_i \frac{\partial \tau_{ij}}{\partial x_j}$

(b) $-\widetilde{u}_i \frac{\partial\left(-2C_s\Delta^2|\widetilde{S}|\widetilde{S}_{ij}\right)}{\partial x_j}$

(c) $-\widetilde{u}_i \frac{\partial\left(\delta\check{u}_i\delta\check{u}_j\right)}{\partial x_j}$

(d) $-\widetilde{u}_i\Psi$ (where Ψ is defined in 6.40)

Figure 6.7: Subfilter stress contribution $-\widetilde{u_i}\widehat{\frac{\partial \tau_{ij}}{\partial x_j}}$, defined in (6.2): (a) exact contribution, (b) Smagorinsky contribution, (c) Brun, Friedrich, and Da Silva 2006 model (6.16) contribution, (d) present model (with the resolved part only) contribution. The results are plotted in space on a slice of the DNS dataset.

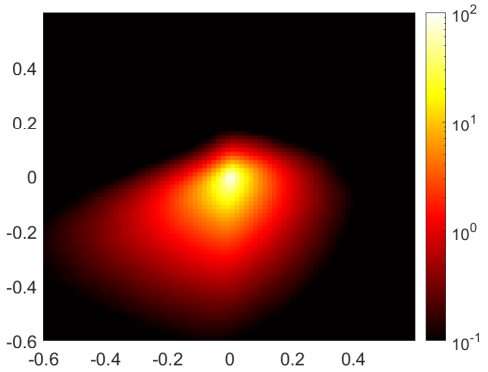

(a) Horizontal axis: exact subfilter contribution to (6.1): $-\widetilde{u}_i \frac{\partial \tau_{ij}}{\partial x_j}$. Vertical axis: Smagorinsky model contribution to (6.2): $-\widetilde{u}_i \frac{\partial \left(-2C_s\Delta^2|\widetilde{S}|\widetilde{S}_{ij}\right)}{\partial x_j}$.

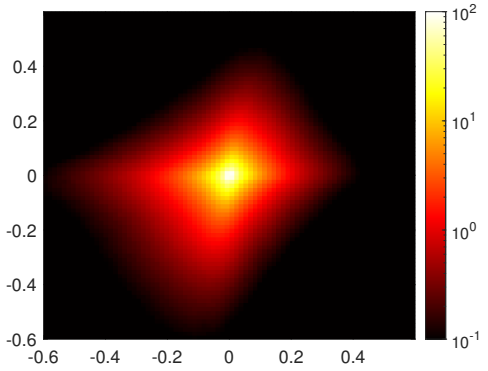

(b) Horizontal axis: exact subfilter stress contribution to (6.1): $-\widetilde{u}_i \frac{\partial \tau_{ij}}{\partial x_j}$. Vertical axis: Brun, Friedrich, and Da Silva 2006 model contribution to (6.2): $-\widetilde{u}_i \frac{\partial \left(\delta\check{u}_i \delta\check{u}_j\right)}{\partial x_j}$.

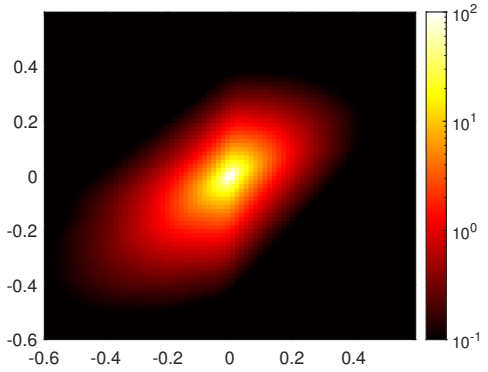

(c) Horizontal axis: exact subfilter stress contribution to (6.1): $-\widetilde{u}_i \frac{\partial \tau_{ij}}{\partial x_j}$. Vertical axis: Resolved part of the present model contribution to (6.2): $-\widetilde{u}_i \Psi$, where Ψ is defined in 6.40.

Figure 6.8: Joint PDFs of modelled subfilter stress contributions to (6.2): $-\widetilde{u_i} \widehat{\frac{\partial \tau_{ij}}{\partial x_j}}$ with exact subfilter stress energy contribution to (6.1): $-\widetilde{u_i} \frac{\partial \tau_{ij}}{\partial x_j}$ evaluated in the Taylor-Green DNS simulation with $\Delta \approx 8\eta$ and with scaling coefficient.

value of Δ in all the steps of the validation process. Indeed, the evaluation of the uncertainty (introduced when approximating (6.15)) done in the next section requires a lot of memory and computational resources. The size of Δ is the limiting parameter of this analysis because it is involved in the complex Germano filtering used in 6.15. $\Delta \approx 8\eta$ is maximized here to compute (6.15) over the domain with one node in a reasonable time. However, the analysis of the modelled subfilter stress contribution in (6.2) computed in this section is also done in appendix C.2 for $\Delta \approx 16\eta$ and the conclusions remain similar to the ones of this section.

Errors introduced with the different approximations

In this section, the errors introduced at each approximation step in our simplification procedure of subsections 6.4.3 and 6.4.5 are analyzed. This is the main advantage of this mathematically supported model: the numerical error introduced can be quantified. Therefore, some future improvements can be done and checked easily by refining the approximations done during the derivation process.

The analysis is only done with the first component of the subfilter stress gradient for simplicity. The joint PDF of the exact subfilter stress component ($\frac{\partial \tau_{1j}}{\partial X_j}$) with the corresponding approximated subfilter stress component at different steps of the derivation (exact equation: 6.24 with $i = 1$, first approximation: 6.30 with $i = 1$ and second approximation: 6.40 with $i = 1$) are evaluated *a priori* on the DNS dataset. Note that equations 6.24 and 6.30 are discretized to be evaluated over our DNS dataset as opposed to equation 6.40 which is already discrete. For the numerical implementation of the continuous terms, all the points of the DNS are used without interpolation and discrete centered scheme are used to compute derivatives. However, our DNS is highly resolved ($\Delta x = 0.7\eta$) so that the uncertainty introduced during the discretization of 6.24 and 6.30 may be negligible. When a linear shape is observed, there is a good correlation between the approximation and exact values. The results in figure 6.9a are presented to check the implementation of the exact equation 6.24 where the terms $\frac{\partial \tau_{1j}}{\partial X_j}$ and $\iiint_{-\infty}^{\infty} \iiint_{-\infty}^{\infty} G(s-r)G(s+r)\nabla_r.(u_{X1}\delta u)d^3r d^3s$ are discretized separately to evaluate the numerical uncertainty of the implementation. The results are very good with a linear shape as expected because the equation is exact.

The results in figure 6.9b are there to test the first approximation of equation 6.30. This approximation consists of a decoupling of space and scale coordinates and some uncertainty is introduced in the results as observed with the elliptical shape of the joint PDF. However, the correlation remains high as observed with the joint PDF results where the shape remains close to linear. This means the space-scale decoupling does not introduce significant error in the present case (Taylor-Green flow, $Re_\lambda \approx 91$ and $\Delta \approx 8\eta$). According to the results in figure 6.9c, where a large ellipse is observed, most of the numerical error is introduced when moving from equation 6.30 to equation 6.40 where the equation is discretized over the LES mesh and where the residual term is neglected. If a good dissipation model is

designed to reproduce the residual term behavior, the uncertainty will be reduced. Moreover, the numerical uncertainty might be reduced with a better numerical implementation of the resolved term: using interpolation for example. However, the correlation observed is already better than with other models tested and some large events are probably just slightly shifted in space. This shift in space can explain part of the uncertainty observed in figure 6.9c, while having the encouraging results of figure 6.7d.

Scaling coefficient analysis

The results of the Smagorinsky model and subfilter stress resolved part of the present model are presented in figure 6.10 with $C_S = 0.18$ and $C_1 = 1$ to check the accuracy of the predicted scaling coefficients (without correction). The Smagorinsky model coefficient is realistic because the left side of the PDF of $-\widetilde{u}_i \frac{\partial\left(-2C_s\Delta^2|\widetilde{S}|\widetilde{S}_{ij}\right)}{\partial x_j}$ evaluated with the coefficient $C_s = 0.18$, is close to the one of the exact subfilter stress contribution $-\widetilde{u_i}\frac{\partial \tau_{ij}}{\partial x_j}$. It is not possible to be more accurate on the Smagorinsky scaling coefficient as this model is too far from reality (see right side of the PDF in figure 6.10) to better adjust the coefficient based on the PDFs. The resolved subfilter stress coefficient is slightly underestimated according to the PDF results of $-\widetilde{u}_i\Psi$ (Ψ defined in 6.40) compared to exact results $-\widetilde{u_i}\frac{\partial \tau_{ij}}{\partial x_j}$ as observed with the tails which are too small. However, the shape of the PDF of $-\widetilde{u}_i\Psi$ is close to the one of $-\widetilde{u_i}\frac{\partial \tau_{ij}}{\partial x_j}$. Therefore, it is possible to estimate accurately the coefficient C_1 for this simulation based on PDFs. The model is tested in the Taylor-Green simulation with the coefficient C_1 evaluated *a priori* in appendix C.1. This coefficient cannot be used in other simulations than the one tested here so future work is needed to check the coefficient variation in other flows and implement a dynamic method if needed. The variation of this coefficient with mesh resolution is also analyzed in appendix C.1 and a linear dependence of C_1 on Δ is obtained for $\Delta > 4\eta$.

6.5.3 Presentation of the model's *a posteriori* results (LES)

Large Eddy Simulations of a Taylor-Green flow are carried out with the same forcing as the one of the DNS. A $64 \times 64 \times 64$ discretization is used over the domain $7.1L \times 7.1L \times 7.1L$ for the LES, with periodic conditions, which is 8 times coarser than the DNS. Similarly to the DNS simulation, $\nu = 2 \times 10^{-3}$. The time step is initialized for a CFL smaller than 0.1 and then it is adapted dynamically to reach a CFL of 0.5. The $12 \times 12 \times 12$ top hat filter used during the *a priori* analysis gives a -3dB cutoff wavenumber: $k_{cutoff} \approx 19$. In the LES, the truncation frequency is close to this value: $k_{trunck} = \frac{2}{3}k_{max} \approx 21$. Therefore, the LES is equivalent to the *a priori* analysis where a top hat filter is used so that we can compare the results.

The simulation is initialized with the DNS velocity field sub-sampled on a $64 \times 64 \times 64$ mesh. These initial conditions are selected so that the coefficients evaluated for the model

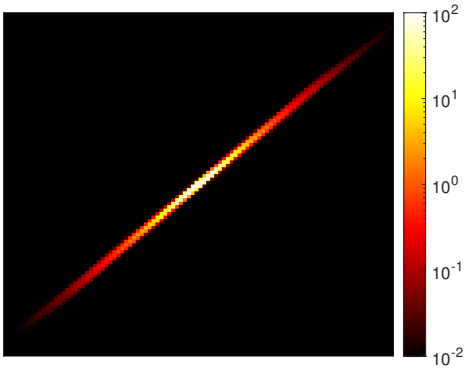

(a) Exact subfilter stress gradient computations. Horizontal axis: $\frac{\partial \tau_{1j}}{\partial X_j}$. Vertical axis: $\iiint_{-\infty}^{\infty} \iiint_{-\infty}^{\infty} G(s-r)G(s+r)\nabla_r.(u_{X1}\delta u)d^3rd^3s$.

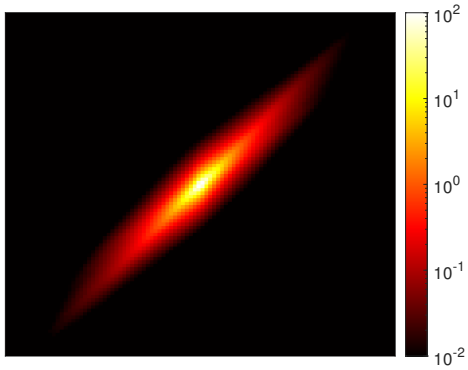

(b) Dissociation of scale and space integration. Horizontal axis: $\frac{\partial \tau_{1j}}{\partial X_j}$. Vertical axis: $\iiint_{-\Delta}^{\Delta} \oiint_{|r|=\Delta} u_{X1}\delta u.nd^2rd^3s$.

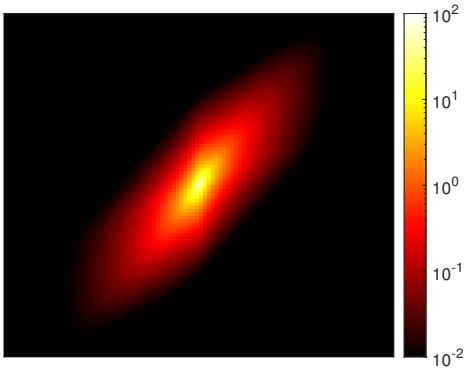

(c) Implementation over a LES mesh. Horizontal axis: $\frac{\partial \tau_{1j}}{\partial X_j}$. Vertical axis: Equation 6.40 with $i = 1$.

Figure 6.9: Two-dimensional probability distribution function of one component of the subfilter stress gradient with its different approximations evaluated in the Taylor-Green DNS simulation with $\Delta \approx 8\eta$.

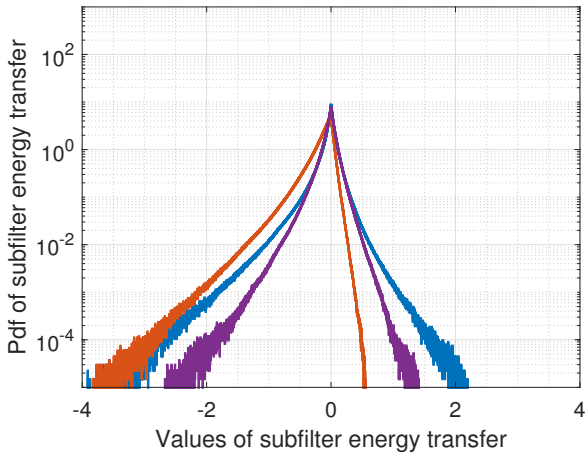

Figure 6.10: PDF of the subfilter stress contribution (exact: $-\widetilde{u}_i \frac{\partial \tau_{ij}}{\partial x_j}$ or modelled: $-\widetilde{u}_i \widehat{\frac{\partial \tau_{ij}}{\partial x_j}}$) evaluated *a priori* on DNS results with a $12 \times 12 \times 12$ top hat filter. In blue: exact subfilter stress energy contribution ($-\widetilde{u}_i \frac{\partial \tau_{ij}}{\partial x_j}$), red: Smagorinsky model energy contribution ($-\widetilde{u}_i \frac{\partial \left(-2C_s\Delta^2|\widetilde{S}|\widetilde{S}_{ij}\right)}{\partial x_j}$ with $C_S = 0.18$), purple: resolved model energy contribution ($-\widetilde{u}_i \Psi$, where Ψ is defined in 6.40 and $C_1 = 1$ for this plot only).

(6.16) and the resolved part of our model in appendix C.1 remain valid.

Models used

- The Smagorinsky model implemented is the classical one defined in equation 6.42 where $C_S = 0.18$. A second order central difference scheme is used for the derivatives so that the model is fully implemented in physical space.

- The model (6.16) implemented is the same as in Brun, Friedrich, and Da Silva 2006:

$$\frac{\partial \tau_{ij}}{\partial x_j} \approx C_2 \frac{\partial \left(\delta\check{u}_i \delta\check{u}_j\right)}{\partial x_j} \tag{6.44}$$

  where $C_2 = 0.152$ is evaluated *a priori* in this study for the Taylor-Green flow at the present resolution in appendix C.1. This model is tested alone and in combination with the Smagorinsky model with $C_S = 0.18$.

- The subfilter stress contribution resolved part is:

$$\frac{\partial \tau_{ij}}{\partial x_j} \approx \frac{C_1}{(2\Delta)^3} \oint_{|\boldsymbol{r}|_\infty = \Delta} (\widetilde{u}_{Xi}(\boldsymbol{x}, \boldsymbol{r}) \boldsymbol{\delta}\widetilde{\boldsymbol{u}}(\boldsymbol{x}, \boldsymbol{r})) \boldsymbol{n} d^2 r \tag{6.45}$$

where $C_1 = 0.97$ for the present resolution as computed in appendix C.1. The numerical implementation of this term is described in equation 6.40. The resolved part is tested alone and in association with the Smagorinsky model.

Large Eddy Simulations results

First, Large Eddy Simulations are carried out with the model (6.16) and the resolved part of our model but without dissipation model. The results are averaged in time over 24 turnover times and are compared to the DNS results and Large Eddy Simulations with Smagorinsky model alone.

The spatial energy spectrum averaged over 24 turnover times of the different simulations (DNS, LES without model, LES with Smagorinsky model, LES with model (6.16) and LES with resolved part of our model) are presented in figure 6.11a. It suggests that the model (6.16) and the resolved part of our model introduces little dissipation for this resolution as observed with the energy at high wavenumbers ($k/k_\eta > 0.2$ with $k_\eta = \pi/\eta$) that is too high and close to the simulation without model. This confirms the idea of Cimarelli and De Angelis 2014 to use a version of the model (6.16) in combination with a dissipation model and our strategy to combine the resolved part of our model with a dissipation model as anticipated in section 6.4.4. However, some small scale dissipation is nevertheless introduced by the resolved part of our model (and by model 6.16) as observed in figure 6.11a where the energy at high wavenumbers ($k/k_\eta > 0.2$) is slightly smaller than for the simulation without model. This suggests that the results of the resolved model associated to the Smagorinsky model will be over-dissipative compared to the Smagorinsky model alone.

The energy spectrum results of the different simulations with dissipation models are presented in figure 6.11b (Smagorinsky model 6.42, model 6.44 combined with Smagorinsky model 6.42 and resolved model 6.40 combined with Smagorinsky model 6.42). These results are compared to the results of DNS and LES without model. These results are highly dependent on the Smagorinsky coefficient $C_s = 0.18$ and the resolved model coefficient $C_1 = 0.97$ evaluated *a priori*. Indeed, a small variation affects significantly the results so the analysis is more qualitative than quantitative. All the large eddy simulations with a model are over-dissipative compared to the DNS results as observed with the too large drop of energy at high wavenumbers ($k/k_\eta > 0.2$) for the simulations with model in figure 6.11b. Among the different models, the resolved model with Smagorinsky is the most over-dissipative one as observed with the lowest energy at high wavenumbers compared to other simulations. This behavior is likely to come from the resolved scales. Indeed, the conceptual separation of the model into a dissipative and non-dissipative part is meaningful only if the filtered scales do not dissipate energy at all. This assumption depends on the filter but is obviously not fully respected in classical large eddy simulation especially when a top hat filter is used to design the model. Indeed, a top hat filter does not filter out all the energy at high wavenumbers

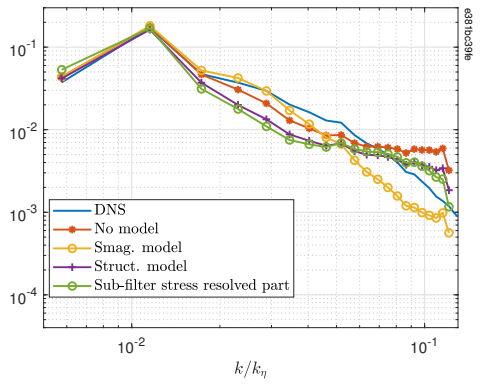

(a) Time averaged energy spectrum without dissipation model (except for the simulation with Smagorinsky model)

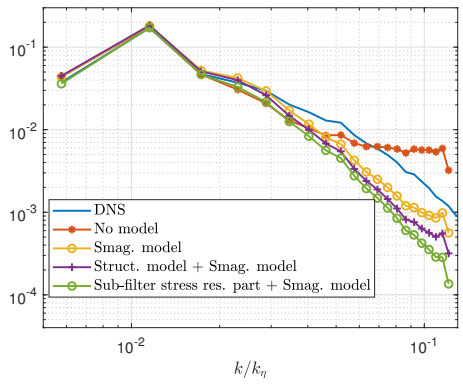

(b) Time averaged energy spectrum with dissipation model (except for the DNS and the simulation without model)

Figure 6.11: Comparison of large eddy simulation results with different models. $k_\eta = \pi/\eta$ and $\frac{\eta}{\Delta} \approx 0.13$.

so that some small scale effect is expected to remain in the resolved model. Moreover, some dissipation can be present at low wavenumbers which will be captured by the resolved model. Therefore, the resolved part of the model adds some dissipation. It explains why this model is more dissipative than the Smagorinsky model alone. This over-dissipative behavior might be reduced by tuning the Smagorinsky model coefficient C_s but we do not focus on this point as we already know the strong limitations of this model (Dairay et al. 2017) so that this point is left for future work when a better dissipation model may be used. The shape of the energy spectrum seems to be mainly driven by the dissipation model as observed with the similar shapes between the three simulations with models (Smagorinsky model, model (6.16) combined with Smagorinsky model and resolved model combined with Smagorisnky model (6.36)). Therefore, large, local, backscatter and dissipative events do not play a significant role for the shape of the energy spectrum in periodic/homogeneous turbulence.

However, energy spectrum introduces a spatial averaging which can hide interesting flow properties. Indeed, the Fourier transform is non-local in space so that the energy computed at one wavenumber is only representative of the spatially averaged energy of the associated scale. This might explain why the effect of local backscatter is not seen in the *a posteriori* results. Indeed, the non-homogeneity does not contribute to the energy balance in Fourier space (see Lin equation) so that the impact of the resolved model might only be visible in non-homogeneous turbulence or locally in homogeneous turbulence. Therefore, the PDFs of the subfilter stress contribution in (6.2) for the different models, sampled in space and time during the LES simulations, are now analyzed to describe the local properties of the simulated turbulence.

These probability distribution functions are presented in figure 6.12. The events are sampled in space and time for all the time steps where the simulation is converged (24 turnover times) to improve convergence. The PDF of $-\widetilde{u_i}\frac{\partial \tau_{ij}}{\partial X_j}$ computed during the *a priori* analysis is used for reference. The Smagorinsky model alone produces mainly dissipation during the simulation similarly to the previous *a priori* results as observed with the highly negatively skewed PDF with small tails compared to the reference results. It means that most events of energy transfer are dissipative and that, the rare, and energetic events are not well predicted. The model 6.16 and the resolved model combined with the Smagorinsky model improve significantly the results by introducing rare energetic events (large backscatter and dissipative events) as observed with the near superposition of the PDFs of these simulations with the exact results $-\widetilde{u_i}\frac{\partial \tau_{ij}}{\partial X_j}$ computed during *a priori* analysis. These results also confirm the relevance of the *a priori* evaluation of the coefficient C_1 (see appendix C.1).

Therefore, as opposed to the conclusions from the energy spectrum where the results do not depend so much on the model 6.16 and the resolved part of our model, the local results of the different simulations are significantly affected by these models. Indeed, the physics of the energy transfer, between filtered and residual scales, happening locally in the simulations with the model 6.16 combined with Smagorinsky or with our model is completely different to the physics present in the simulation with the Smagorinsky model alone. These models capture the local non-homogeneity of the flow with large energy transfers between filtered and residual scales both positive and negative which do not seem to affect significantly global homogeneous quantities such as the energy spectrum in periodic/homogeneous turbulence.

However, the 6.16 model is found to affect global quantities such as mean flow or velocity RMS in non-homogeneous flows as observed in channel flows in Brun, Friedrich, and Da Silva 2006 and the other variants of this model in Fang et al. 2009 and Cimarelli and De Angelis 2014. Therefore, our model is to be tested in non-homogeneous turbulence in future work to see if the physics captured about local energy transfers between resolved and filtered scales, both *a priori* and *a posteriori*, improves the predictions of global quantities in Large Eddy Simulations of non-homogeneous turbulent flows.

6.6 Conclusion

The small scale Kármán-Howarth-Monin-Hill 2002b two-point equation and large scale Germano 2007b equation are used in fundamental research to develop turbulence physical knowledge and understanding. This mathematically exact framework allows the analysis of the turbulent energy cascade in non-homogeneous turbulent flows and in the dynamics of homogeneous turbulence. An exact formulation of the Large Eddy Simulation subfilter stress by Germano 2007c is used (6.14) related to this framework (Germano 2007b). This formulation depends on subfilter quantities which are unknown with LES resolution.

In this chapter, a new LES model is proposed based on approximations of the exact subfilter

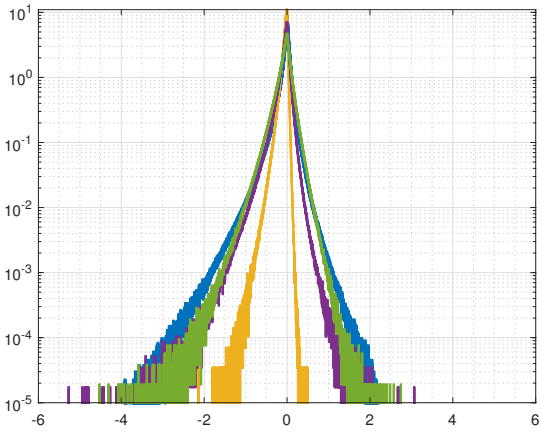

Figure 6.12: PDF of the modelled subfilter stress contribution ($-\widetilde{u_i}\widehat{\frac{\partial \tau_{ij}}{\partial x_j}}$) during large eddy simulation. In blue: a priori results plotted for reference ($-\widetilde{u}_i\frac{\partial \tau_{ij}}{\partial x_j}$), yellow: Smagorinsky model contribution ($-\widetilde{u}_i\frac{\partial\left(-2C_s\Delta^2|\widetilde{S}|\widetilde{S}_{ij}\right)}{\partial x_j}$), purple: structure model and Smagorinsky model contribution ($-\widetilde{u}_i\frac{\partial\left(\delta\check{u}_i\delta\check{u}_j\right)}{\partial x_j} - \widetilde{u}_i\frac{\partial\left(-2C_s\Delta^2|\widetilde{S}|\widetilde{S}_{ij}\right)}{\partial x_j}$), green: resolved model and Smagorinsky model contribution ($-\widetilde{u}_i\Psi - \widetilde{u}_i\frac{\partial\left(-2C_s\Delta^2|\widetilde{S}|\widetilde{S}_{ij}\right)}{\partial x_j}$, where Ψ is defined in 6.40).

stress formulation (6.14). The small scale and large scale interscale energy transfer rate knowledge (used in fundamental research) where large fluctuations are measured with both direct and backward energy transfers in scales, is used to justify the expected behavior of the Large Eddy Simulation model with large dissipative and backscatter events. A mixed configuration is proposed with a resolved part combined with a dissipation model. The resolved part of the model is compared to the Brun, Friedrich, and Da Silva 2006 LES model which is not far from the exact formulation (6.14).

A priori analysis of the resolved part of our model is carried out in a forced Taylor-Green flow and compared to exact results, Smagorinsky model results and Brun, Friedrich, and Da Silva 2006 model results. Rather good correlation with DNS of local energy transfers between filtered and residual scales is obtained with the resolved part of our model. Particularly, backscatter events are well predicted which is usually not the case with classical models such as the Smagorinsky one. The correlation of the exact subfilter stress contribution $-\widetilde{u}_i\frac{\partial \tau_{ij}}{\partial x_j}$ (see equation 6.1) with the modelled one $-\widetilde{u_i}\widehat{\frac{\partial \tau_{ij}}{\partial x_j}}$ (see equation 6.2) is better with the resolved part of our model than with the Brun, Friedrich, and Da Silva 2006 model in our flow.

In *a posteriori* simulations, the resolved part of our model does not capture well the mean dissipation (very small value compared to energy transfer fluctuations). This result was anticipated during the formulation of the model and this is why the resolved part is used

combined with a dissipation model in a mixed configuration. The Smagorinsky model used for this combination affects the *a priori* results which suggests the results can be improved with a more relevant dissipation model. This mixed model captures well, *a posteriori*, the PDF of the local energy transfers between filtered and residual scales, and particularly backscatter events. The good prediction of these results, which are related to real physical effects, does not affect significantly spatially averaged quantities such as the energy spectrum. The energy spectrum of the LES with the resolved part of our model combined with the Smagorinsky model is over dissipative compared to exact results suggesting again that the dissipative model used in combination with the resolved part should be modified in future work.

This mixed model is to be evaluated in other flows because it is expected to affect significantly the results in non-homogeneous turbulence and especially in regions of the flow where mean backscatter is measured such as regions with high mean flow gradients (for example channel flow as in Cimarelli and De Angelis 2014). This model should also be tested in flows at higher Reynolds number to test the Reynolds dependence of the resolved part of our model. Overall, this study is used as a proof of concept that new LES models can be approximated from exact equations which ensure the physical relevance of the models. The present model can be improved by refining the approximations done during the derivation process and also by using present and future physical results related to the Germano 2007b equation. It supports therefore, the need for more research on the large scale Germano equation both experimentally and numerically.

Chapter 7

Conclusions and perspectives

7.1 Conclusions

The experimental set-up used during this thesis, with a water tank agitated by four rotating blades with or without baffles, is used to generate various non-homogeneous turbulent flows with or without rotation where Re_λ is between 410 and 580. Time resolved 2D2C PIV measurements, with interrogation window size between 2.3η and 5.1η (in order to have a good accuracy on velocity derivative terms), are carried out in different experimental configurations with high number of statistics ($150,000$ velocity fields per configuration corresponding to around $50,000$ decorrelated velocity fields).

Truncated estimates of terms in the Kármán-Howarth-Monin-Hill (KHMH) two-point equation are used to describe the small scale behavior. Moreover, larger scale quantities from the Germano two-point equation are evaluated for the first time to describe the larger scale behavior. Kolmogorov-like results of the two-point statistics are measured for the non-rotating results with $r^{2/3}$ power law behavior of the second order structure functions. Moreover, a collapse of the interscale transfer rate of energy with dissipation is measured without dependence on two-point separation length r. These results are not the consequences of the Kolmogorov theory which cannot be applied in these flows where non-negligible non-homogeneity is quantified. Indeed, a non-negligible interspace transport rate of energy is measured which corresponds to a non-zero spatial flux of energy.

The Chen and Vassilicos 2022 theory is improved and used to justify the Kolmogorov-like results in our non-homogeneous turbulent flows where the two-point production and linear transport are measured and found to be relatively small. This theory is based on the matching of an inner scale region with an outer scale region where a space and scale variable separation is assumed for the different time-averaged two-point energy quantities. In the matching region, called the inner-outer intermediate region, the truncated estimates of the main terms of the KHMH equation are predicted to collapse with dissipation without

dependence on two-point separation length r. These results are confirmed experimentally for the interscale transfer but also for the interspace transport which is a non-homogeneous quantity and whose collapse is not trivial. This later result strongly supports the validity of the predictions of the Chen and Vassilicos 2022 theory for these non-rotating flows.

Truncated estimates of the large scale Germano equation are also measured for the non-rotating configurations and the large scale interscale transfer defined in this equation is measured and found to behave similarly to the small scale interscale transfer defined in the KHMH equation. Indeed, it is found to collapse with dissipation and is independent of the two-point separation length in the inertial range. This result is not yet predicted theoretically but it suggests that the large scale interscale transfer rate remains connected to the already known small scale interscale transfer rate even in the non-homogeneous flows of our baffled experiments. The non-homogeneous terms of the large scale equation do not collapse with dissipation which underlines the peculiarity of the large scale interscale transfer rate in this equation. An analogue of the Kolmogorov homogeneity assumption is defined where the small scale non-homogeneous terms are individually non-zero but whose the sum is negligible compared to the dissipation. With this assumption, whose criteria of validity remain to be defined, a -1 coefficient is predicted between the interscale transfer rate and dissipation.

Non-Kolmogorov structure functions are measured for the configurations without baffles where the flow is strongly rotating. The structure function for δu_x^2 is measured to have a linear behavior with r which change with rotation frequency. These results do not follow the Chen and Vassilicos 2022 theory similarly to the small scale two-point energy terms which do not obey the theory's predictions. In these flows, the mean flow non-homogeneity at small scales (at the order of magnitude of λ) seems to break some assumptions of the theory. The analysis of the different terms of the KHMH equation suggests that the inner-outer dissipation equivalence introduced in Chen and Vassilicos 2022 fails in these flows which explains why the predictions do not hold.

Finally, the large scale two-point framework introduced by Germano is used to develop a new Large Eddy Simulation (LES) model in chapter 6. This model is composed of a resolved part combined with a dissipation model. The resolved part is approximated from exact equations so that the uncertainty introduced at each step is quantified in the case of a numerically integrated Taylor-Green flow. The connection of this model with the large scale equation, analyzed experimentally in chapters 4 and 5, is used to justify the physics captured by the model with very intense dissipative and backscatter events. Generally, the physical understanding obtained with the two-point equations can in principle be transferred to LES through this connection. We use a mixed model consistently with recent LES models where the first term (the resolved part) captures the large local energy transfer between filtered and residual scales while the second term is there to capture the mean dissipation. The resolved part of our model is found to capture well the local energy transfer, including large backscatter events, in an *a priori* analysis of a Taylor-Green turbulent flow. These

results are significantly better than the ones obtained with the Brun, Friedrich, and Da Silva 2006 model which is a model designed to capture the local and global backscatter in a channel flow. The Smagorinsky model is used for the second term of the mixed model configuration for ease of implementation. The present mixed model captures well the local energy transfer in *a posteriori* simulations of the same Taylor-Green flow with a coarse mesh. However, no improvement is observed for second order homogeneous quantities such as energy spectra which are classically used to evaluate LES models. Following the results of Brun, Friedrich, and Da Silva 2006 and Cimarelli and De Angelis 2014, the prediction of the energy transfer fluctuations and particularly backscatter may be of great interest in non-homogeneous turbulence where mean backscatter is expected in some specific regions or directions of the flow. Our model remains therefore to be tested in non-homogeneous turbulence.

7.2 Perspectives

The PIV measurements carried out during this thesis were done in two dimensions with two components instead of three dimensions with three components as needed to evaluate the full terms of the KHMH and Germano equations. These experiments would require to use Particules Tracking Velocimetry (4D PTV) and then convert the Lagrangian results into Eulerian results. The current technology does not allow the measurements of the same number of statistics as in the experiments presented in this thesis because of the huge amount of data to process. However, time resolved results are already of great interest especially in the case of the large scale equation. Indeed, it allows the local analysis of the large scale interscale transfer which is strongly related to LES modelling as developed in the last chapter of this thesis. The 4D PTV experiment datatset recorded during a collaboration between LMFL and CEA (Chaabo 2022, Debue 2019, Geneste 2023 and Cheminet et al. 2022) in a large Von-Kármán tank might be a good datatset for this analysis and it is already available (Re_λ between 150 and 1000 with Lagrangian resolution between 0.3η and 5η and measurement window size between 20η and 300η). 4D PTV experiments can also be conducted in a new mixing tank made of glass. These experiments may also be useful to better quantify the mean flow non-homogeneity in the non-baffled (rotating) configurations and maybe relate it explicitly to the rotation.

The evaluation of the Chen and Vassilicos 2022 theory in other locations of the mixer tank and more generally in other flows may be useful to test it in different classes of non-homogeneous turbulent flows. These tests are needed to classify better the differences between non-homogeneous turbulent flows and identify clearly the flow properties needed to apply the theory. The theory is to be tested extensively in turbulent flow regions of high production where it is not expected to hold to understand how the mean flow non-homogeneity may be included in the theory.

The main perspective emerging from the thesis is the crucial need for more information about the Germano energy equation. This equation should be evaluated in many flows both experimentally and numerically even with simplifications if needed. Particularly, the time-averaged large scale interscale transfer should be quantified and compared to the time-averaged small scale interscale transfer in different classes of non-homogeneous flows to identify when the connection between the large scale and small scale interscale transfer rate holds or when it is contaminated by non-homogeneity. This physical understanding is needed to go further in the direction of physically relevant Large Eddy Simulation modelling. This analysis should also be done about the fluctuations of the energy terms (equation 2.8) as well as for the momentum terms (equation 2.6) in the same spirit as the work of Yasuda and Vassilicos 2018 and Larssen and Vassilicos 2023. This analysis is directly relevant for LES modelling because the models should be designed to reproduce these fluctuations.

The entanglement of space and scale momentum terms identified for LES in section 6.4.1 might be related to the energy results in section A.2.2 where the Lamb decomposition shows that the energy exchanged between the large scale equation and the small scale equation is composed of a spatial term and a scale term. This entanglement should be analyzed to understand the role of the spatial transport term in the cascade process itself. The Lamb decomposition used to derive this results seems to capture important physical features of the equations so this decomposition should be analyzed in more details to understand better its role. Some mathematical research exists about Beltrami flows where the Lamb term is by definition zero. The analysis of the Lamb term energy contribution should provide the physical meaning of its importance and why turbulent flows are different to Beltrami flows. This research direction is also strongly related to the physical links between the small scale and the large scale equations which seems to be crucial as a physical point of view.

The implementation of the resolved part of the LES model designed in chapter 6 can be improved to reduce the uncertainty introduced. The impact of the filtering on the modelling results can also be investigated to check the robustness of the results to a stronger filtering. The derivation of the resolved term may also be generalized, if possible, to other filters than the top hat filter which would provide more efficient model formulation. This model remains also to be tested in non-homogeneous turbulence to see if it captures well the expected mean backscatter in some regions/ directions of the flow. The new model can be evaluated, for example, in a channel flow were it can be easily compared to the Brun, Friedrich, and Da Silva 2006, Fang et al. 2009 and Cimarelli and De Angelis 2014 results. The dissipation model should also be replaced by a better model than the Smagorinsky one for example with the Dairay et al. 2017 model. Practically, this can be done by implementing the resolved part of our model into the code Xcompact3d where the Dairay et al. 2017 model is already implemented. In that way, the model can be tested on existing simulation cases pre-implemented in Xcompact3d such as Taylor-Green flow to test the impact of the dissipation model on our results and in a channel flow to test the mean backscatter in

specific directions. In addition, the coefficient used in front of the resolved part of our model should be analyzed to see if a general formulation can be used or if a dynamic method should be implemented in the same spirit as in Brun, Friedrich, and Da Silva 2006, Fang et al. 2009 and Cimarelli and De Angelis 2014. Eventually, having in mind the practical use of this model, its numerical cost should also be investigated.

Finally, beyond the scope of this thesis, I think there is a need for more research to develop the transfer of knowledge in turbulence from theoretical world toward the practical world through the different disciplines at stake in the order: Mathematics $\rightarrow$ Physics $\rightarrow$ Numerical simulation $\rightarrow$ Engineering applications. Indeed, turbulence research has the potential to change the way we predict and understand our surrounding fluid world with direct and practical applications in weather/climate forecast, transport and energy sectors. This is a highly topical issue, and the new mantra of the CNRS is precisely defined by Antoine Petit as: 'Fundamental research at the service of society'.

Appendix A

Chapter 4 appendices

A.1 Space averaging impact on results

Structure functions are averaged in space to improve convergence as the results collapse is very sensitive to convergence. Therefore, the results are plotted in figure A.1a, A.1b, A.1c and A.1d without space averaging to check if the results are affected. Only one configuration is presented but it is representative of the four configurations. $V_I = V_O.R_O^{-1/4}$ and $l_I = l_O.R_O^{-3/4}$ are defined arbitrarily where $l_O = D$ and $V_O = \sqrt{\overline{u_x'^2} + \overline{u_z'^2}}$. However, it is important to note that V_I and l_I are nearly constant over the spatial domain with a variation of less than 3% for the two quantities. The error bars for these results are computed with classical convergence formula. The largest error bar of all positions is used and centered on the spatially averaged structure function (in red). The results collapse within error bars for $\overline{\delta u_x'^2}/V_I^2 = f(r_x)$, $\overline{\delta u_x'^2}/V_I^2 = f(r_z)$, $\overline{\delta u_z'^2}/V_I^2 = f(r_x)$ and $\overline{\delta u_z'^2}/V_I^2 = f(r_z)$, which confirms that space averaging does not distort the results and can be therefore used to improve convergence. These results are also consistent with the inner region structure functions' similarity assumed in equation 4.23. The outer region is not accessible with our dataset.

Third order statistics are even more difficult to converge than second order statistics. Therefore, space averaging is mandatory to converge results. The most critical quantity is the interspace transport as it is computed with space derivatives which can be affected by space averaging. The interspace transport averaged in time and space is compared to the same quantity averaged in time and in space in only one direction (z) but at different x locations (figure A.2). The results are not well converged due to the reduction of the number of points. The shape of the non-converged functions at the different x positions seems to be consistent with the converged results averaged in space. Therefore, spatial averaging can be used to improve the results convergence without loss of information and without significant distortion of the results.

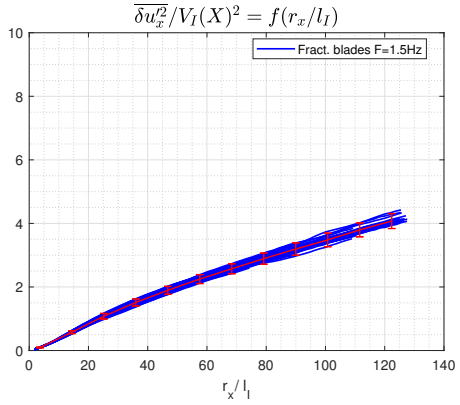

(a) Time averaged results of $\overline{\delta u_x'^2}/V_I^2$ in r_x direction at different spatial positions.
In red: $< \overline{\delta u_x'^2}/V_I^2 >$

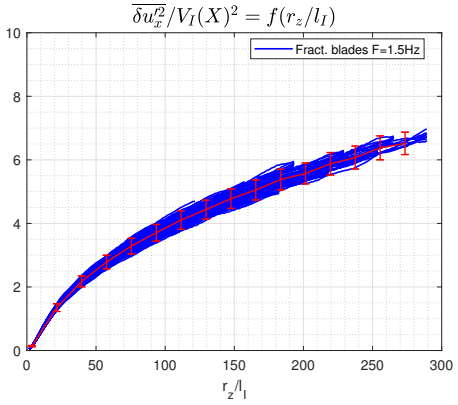

(b) Time averaged results of $\overline{\delta u_x'^2}/V_I^2$ in r_z direction at different spatial positions.
In red: $< \overline{\delta u_x'^2}/V_I^2 >$

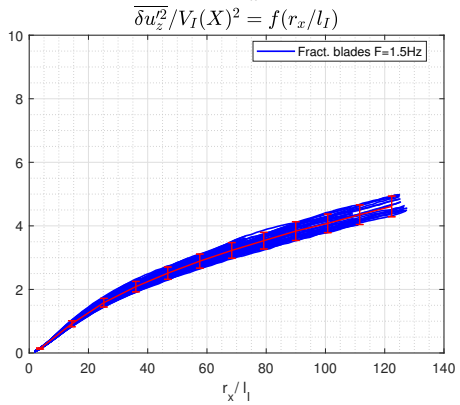

(c) Time averaged results of $\overline{\delta u_z'^2}/V_I^2$ in r_x direction at different spatial positions.
In red: $< \overline{\delta u_z'^2}/V_I^2 >$

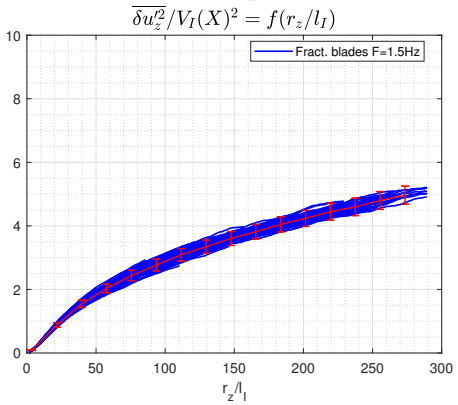

(d) Time averaged results of $\overline{\delta u_z'^2}/V_I^2$ in r_z direction at different spatial positions.
In red: $< \overline{\delta u_z'^2}/V_I^2 >$

Figure A.1: Time averaged structure functions at different spatial locations

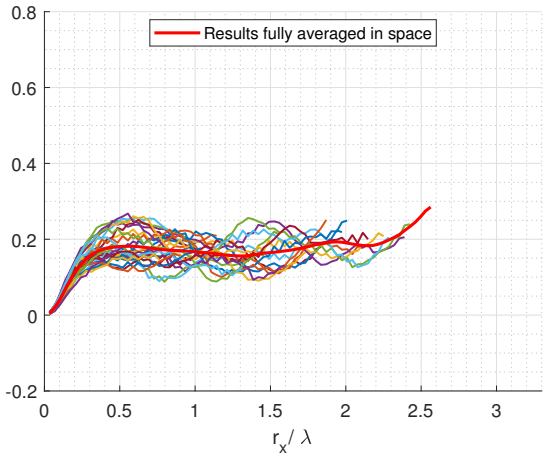

Figure A.2: Interspace transport truncate estimate at different x positions averaged over time and z direction. In red the same estimate averaged over time and all directions.

A.2 Large scale / small scale Kolmogorov-like turbulent picture

In this part, Kolmogorov-like assumptions are used to improve the understanding of the large scale equation and its contribution to the global turbulent picture. This part is not in the submitted publication but the results are close to the ones in the last section of chapter 4. In this section, Reynolds average decomposition is not used in the computations to keep it as simple as possible and simplify the discussion about the mean flow contribution. This work relates therefore the results of chapter 4 with the theoretical ones of chapter 2 where there is no Reynolds average decomposition.

A.2.1 Homogeneous turbulence

Most of the materials in this subsection are based on the turbulence lectures of Christos Vassilicos.

The small scale and large scale equations are first analyzed in theoretical homogeneous turbulence. This kind of turbulence is unlikely to exist in real world but it is a first step to give a simplified turbulent picture which will help for the understanding of non-homogeneous turbulence analyzed in the next section. Equations 2.7, 2.8 and 2.9 are averaged in space over a periodic domain to obtain equations:

$$\frac{\partial < |\boldsymbol{\delta u}| >^2}{\partial t} + \boldsymbol{\nabla_r}. < \boldsymbol{\delta u} |\boldsymbol{\delta u}|^2 > \approx - < \epsilon > \tag{A.1}$$

$$\frac{\partial < |\boldsymbol{u_X}|^2 >}{\partial t} + \boldsymbol{\nabla_r}. < \boldsymbol{\delta u}|\boldsymbol{u_X}|^2 > \approx - < \epsilon > \tag{A.2}$$

$$\boldsymbol{\nabla_r}. < \boldsymbol{\delta u}|\boldsymbol{u_X}|^2 > = -\boldsymbol{\nabla_r}. < \boldsymbol{\delta u}|\boldsymbol{\delta u}|^2 > \tag{A.3}$$

where diffusion is neglected for $r >> \lambda$ (Valente and Vassilicos 2015).

As already mentioned, equation A.3 describes an exact connection between the small and large scale interscale transfer in homogeneous turbulence. Therefore, the energy provided by larger scales is received and cascaded at smaller scales.

Using A.1, A.2 and A.3, a decay law is derived:

$$\frac{\partial < |\boldsymbol{\delta u}|^2 >}{\partial t} + \frac{\partial < |\boldsymbol{u_X}|^2 >}{\partial t} \approx -2 < \epsilon > \tag{A.4}$$

This two-point equation is actually the sum of two one point turbulent kinetic energy decay laws:

$$\frac{1}{2}\frac{\partial < \boldsymbol{u}^{+2} >}{\partial t} + \frac{1}{2}\frac{\partial < \boldsymbol{u}^{-2} >}{\partial t} = \frac{\partial < \boldsymbol{u}^2 >}{\partial t} \approx -2 < \epsilon > \tag{A.5}$$

where $\boldsymbol{u}^+ = \boldsymbol{u}(\boldsymbol{\zeta}^+)$ and $\boldsymbol{u}^- = \boldsymbol{u}(\boldsymbol{\zeta}^-)$. These decay laws are easily understood as there is no forcing.

$|\boldsymbol{\delta u}|^2$ is a small scale quantity and $|\boldsymbol{u_X}|^2$ is a large scale quantity, so for $r << L$, the small scale unsteadiness is assumed to be much smaller than the large scale unsteadiness. With this assumption, the Kolmogorov steady assumption at small scale is re-derived:

$$\frac{\partial < |\boldsymbol{\delta u}| >^2}{\partial t} \approx 0 \tag{A.6}$$

but the large scale remains non-stationary with a decay law because there is no forcing:

$$\frac{\partial < |\boldsymbol{u_X}|^2 >}{\partial t} \approx -2 < \epsilon > \tag{A.7}$$

Again, the flow cannot be both homogeneous and steady at large scale. It can also be derived that small scale steadiness assumption A.6 associated to equation A.5 implies a correlation decay at the dissipation rate:

$$\frac{1}{2}\frac{\partial < \boldsymbol{u}^+.\boldsymbol{u}^- >}{\partial t} \approx - < \epsilon > \tag{A.8}$$

This results means that, without forcing, the flow becomes more and more chaotic (less coherent) with time. This is probably due to the break of the large scale structures into smaller scale structures through the turbulent cascade. These results supports that the 'steadiness' assumption in decaying homogeneous flows: $\frac{\partial <|\boldsymbol{\delta u}|>^2}{\partial t} \approx 0$ represents actually a balance of time derivative terms $\frac{\partial <|\boldsymbol{\delta u}|>^2}{\partial t} = \frac{1}{2}\frac{\partial <\boldsymbol{u}^{+2}>}{\partial t} + \frac{1}{2}\frac{\partial <\boldsymbol{u}^{-2}>}{\partial t} - \frac{\partial <\boldsymbol{u}^+.\boldsymbol{u}^->}{\partial t} \approx -2 < \epsilon > +2 < \epsilon > \approx 0$. From these results the Kolmogorov cascade is derived where the energy

transfer across scale is constant and balances dissipation:

$$\boldsymbol{\nabla_r}.<\boldsymbol{\delta u}|\boldsymbol{u_X}|^2>=-\boldsymbol{\nabla_r}.<\boldsymbol{\delta u}|\boldsymbol{\delta u}|^2>\approx<\epsilon> \tag{A.9}$$

This situation remains theoretical but some analogy to these results is used in the next section for time averaged non-homogeneous flow which really exist.

A.2.2 Steady non-homogeneous turbulence

One point spatial balance equation

Steady turbulence is obtained by averaging equations in time. We start with the Navier-Stokes energy equation without forcing at one point:

$$\boldsymbol{\nabla}.\overline{\boldsymbol{u}(\frac{p}{\rho}+\frac{1}{2}\boldsymbol{u}^2)}=\nu\boldsymbol{\nabla}.\frac{\overline{\boldsymbol{\nabla u}^2}}{2}-\bar{\epsilon} \tag{A.10}$$

This equation is averaged in space over a finite domain Ω:

$$\frac{1}{\rho}\oiint_{\partial\Omega}\left(\overline{\boldsymbol{u}(p+\frac{1}{2}\rho\boldsymbol{u}^2)}-\nu\frac{\boldsymbol{\nabla}\overline{\boldsymbol{u}^2}}{2}\right)\boldsymbol{n}dS=-\iiint_{\Omega}\bar{\epsilon}dV \tag{A.11}$$

Equation A.11 is reminiscent of the Bernoulli equation once converted into energy equation (even more visible when diffusion is neglected). However, this equation is valid for time averaged turbulent flows without assumption. This equation describes a balance of spatial terms with dissipation. The spatial fluxes on the sides of the spatial domain bring the energy needed inside were it is consumed by dissipation. This fluxes balance sustain turbulence and prevents it to decay (because it is a steady flow without forcing).

It means also that a non-local law exist where non-homogeneous terms balance with dissipation so this idea is applied to two-point energy equations.

Time averaged two-point equations

The two-point small scale equation 2.7 and the two-point large scale equation 2.8 are rewritten in this section with time averaging:

$$\boldsymbol{\nabla_r}.\overline{(\boldsymbol{\delta u}|\boldsymbol{\delta u}|^2)}+\boldsymbol{\nabla_X}.\left[\overline{(\boldsymbol{u_X}|\boldsymbol{\delta u}|^2)}+\frac{2}{\rho}\overline{(\boldsymbol{\delta u}\delta p)}-\frac{\nu}{2}\boldsymbol{\nabla_X}\overline{\boldsymbol{\delta u}^2}\right]=\frac{\nu}{2}{\boldsymbol{\nabla_r}}^2\overline{|\boldsymbol{\delta u}|^2}-\bar{\epsilon} \tag{A.12}$$

and

$$\boldsymbol{\nabla_r}.\overline{(\boldsymbol{\delta u}|\boldsymbol{u_X}|^2)}+\boldsymbol{\nabla_X}.\left[\overline{(\boldsymbol{u_X}|\boldsymbol{u_X}|^2)}+\frac{2}{\rho}\overline{(\boldsymbol{u_X}P_X)}-\frac{\nu}{2}\boldsymbol{\nabla_X}\overline{\boldsymbol{u_X}^2}\right]=\frac{\nu}{2}{\boldsymbol{\nabla_r}}^2\overline{|\boldsymbol{u_X}|^2}-\bar{\epsilon}. \tag{A.13}$$

This latter equation can also be rewritten as:

$$\begin{aligned} &-\boldsymbol{\nabla_r}.\overline{(\boldsymbol{\delta u}|\boldsymbol{\delta u}|^2)}+\boldsymbol{\nabla_X}.\left[\overline{(\boldsymbol{u_X}|\boldsymbol{u_X}|^2)}+\frac{2}{\rho}\overline{(\boldsymbol{u_X}P_X)}+2\overline{(\boldsymbol{\delta u}(\boldsymbol{\delta u}.\boldsymbol{u_X}))}-\frac{\nu}{2}\boldsymbol{\nabla_X}\overline{\boldsymbol{u_X}^2}\right] \\ &=\frac{\nu}{2}\boldsymbol{\nabla_r}^2\overline{|\boldsymbol{u_X}|^2}-\overline{\epsilon} \end{aligned} \tag{A.14}$$

where, equation A.3 is used so that the small scale interscale transfer appears explicitly in the large scale equation and $\overline{\epsilon}=\frac{1}{2}(\overline{\epsilon^+}+\overline{\epsilon^-})$. These equations will be used later in this section.

Two-point spatial balance equation from lamb decomposition

In this section, the lamb decomposition is applied to the two-point equation.

The Lamb decomposition corresponds to the advection term decomposition: $(\boldsymbol{u}.\boldsymbol{\nabla})\boldsymbol{u}=\boldsymbol{\omega}\times\boldsymbol{u}+\frac{1}{2}\boldsymbol{\nabla}\boldsymbol{u}^2$. With this decomposition, the Navier-Stokes equation can be re-written:

$$\frac{\partial\boldsymbol{u}}{\partial t}+\boldsymbol{\omega}\times\boldsymbol{u}+\frac{1}{2}\boldsymbol{\nabla}\boldsymbol{u}^2=-\frac{\boldsymbol{\nabla}P}{\rho}+\nu\boldsymbol{\nabla}^2\boldsymbol{u} \tag{A.15}$$

The $\boldsymbol{\omega}\times\boldsymbol{u}$ term is often associated to the complexity of the Navier-Stokes equations (through the non-linear interactions) and therefore to the energy cascade (Speziale 1987). This term is not present in the one point kinetic energy equation because $\boldsymbol{u}.(\boldsymbol{\omega}\times\boldsymbol{u})=0$ which complicates its analysis. However, it is derived in appendices A.3 and A.4 that the lamb term energy contribution is present in the two-point energy equations which explains why these equations are so meaningful for the turbulence energy cascade analysis. The $|\boldsymbol{\delta u}|^2$ and $|\boldsymbol{u_X}|^2$ equations can be decomposed between the lamb and the gradient part of the advection contribution to the energy budget:

$$\frac{\partial|\boldsymbol{\delta u}|^2}{\partial t}+\underline{\left[\boldsymbol{\nabla_X}.(\boldsymbol{u_X}|\boldsymbol{\delta u}|^2)-\boldsymbol{\nabla_r}.(\boldsymbol{\delta u}|\boldsymbol{uX}|^2)\right]}+\frac{2}{\rho}\boldsymbol{\nabla_X}.(\boldsymbol{\delta u}\delta p^*)=D_{\boldsymbol{\delta u}^2}-\epsilon \tag{A.16}$$

$$\frac{\partial|\boldsymbol{u_X}|^2}{\partial t}-\underline{\left[\boldsymbol{\nabla_X}.(\boldsymbol{u_X}|\boldsymbol{\delta u}|^2)-\boldsymbol{\nabla_r}.(\boldsymbol{\delta u}|\boldsymbol{uX}|^2)\right]}+\frac{2}{\rho}\boldsymbol{\nabla_X}.(\boldsymbol{u_X}P_X^*)=D_{\boldsymbol{u_X}^2}-\epsilon \tag{A.17}$$

Where $\underline{\left[\boldsymbol{\nabla_X}.(\boldsymbol{u_X}|\boldsymbol{\delta u}|^2)-\boldsymbol{\nabla_r}.(\boldsymbol{\delta u}|\boldsymbol{uX}|^2)\right]}$ is the lamb energy contribution to both small scale and large scale two-point energy equations; $D_{\boldsymbol{\delta u}^2}=\frac{\nu}{2}\boldsymbol{\nabla_X}^2|\boldsymbol{\delta u}|^2+\frac{\nu}{2}\boldsymbol{\nabla_r}^2|\boldsymbol{\delta u}|^2$; $D_{\boldsymbol{u_X}^2}=\frac{\nu}{2}\boldsymbol{\nabla_X}^2|\boldsymbol{u_X}|^2+\frac{\nu}{2}\boldsymbol{\nabla_r}^2|\boldsymbol{u_X}|^2$; $\epsilon=\frac{1}{2}\epsilon^+ +\frac{1}{2}\epsilon^-$ and the change of variable $p^*\leftarrow p+\frac{1}{2}\rho\boldsymbol{u}^2$ is used. The derivations of these equations is done in appendices A.3 and A.4.

We can notice from these computations that the lamb contribution represents the energy

exchanged between the large scale two-point equation A.16 /A.12 and small scale two-point equation A.17 /A.13. Indeed, it is the same term appearing in both equations with a minus sign in the large scale equation and a positive sign in the small scale equation. The gradient contribution is a non-homogeneous term in both equations and can be hidden in the pressure term. The lamb part of the equation represents the two-point energy interactions because it is not present in the one point energy equation.

Note: the lamb contribution can also be written as:

$$\underline{\left[\boldsymbol{\nabla_X}.(\boldsymbol{u_X}|\boldsymbol{\delta u}|^2)+\boldsymbol{\nabla_r}.(\boldsymbol{\delta u}|\boldsymbol{\delta u}|^2)-2\boldsymbol{\nabla_X}.(\boldsymbol{\delta u}(\boldsymbol{\delta u}.\boldsymbol{u_X}))\right]} \tag{A.18}$$

where the small scale interscale transfer rate appears explicitly.

When the sum of both time averaged equations is done, the lamb contribution vanishes and we come back to the sum of the one point equations A.10 written for $\boldsymbol{u}^2(\boldsymbol{\zeta}^+)$ and $\boldsymbol{u}^2(\boldsymbol{\zeta}^-)$:

$$\frac{2}{\rho}\boldsymbol{\nabla_X}.\overline{(\boldsymbol{\delta u}\delta p^*)}+\frac{2}{\rho}\boldsymbol{\nabla_X}.\overline{(\boldsymbol{u_X}P_X^*)}=\nu\boldsymbol{\nabla_X}.\boldsymbol{\nabla_X}\overline{(\boldsymbol{u_X}^2+\boldsymbol{\delta u}^2)}-2\overline{\epsilon} \tag{A.19}$$

This exact spatial balance with dissipation (which can be derived without assumption) supports that non-local laws exist which relate non-homogeneous energy with dissipation. These non-local laws might explain why universal results seems to be measured for turbulence in numerous flows even though the non-homogeneity is non-zero.

As we noticed that equation A.19 is just the sum of the small scale equation A.12 and the large scale equation A.13 where the lamb term contribution vanishes, it is natural to rewrite equation A.19 as:

$$\begin{aligned}&\boldsymbol{\nabla_X}.\left[\overline{(\boldsymbol{u_X}|\boldsymbol{\delta u}|^2)}+\frac{2}{\rho}\overline{(\boldsymbol{\delta u}\delta p)}-\frac{\nu}{2}\boldsymbol{\nabla_X}\overline{\boldsymbol{\delta u}^2}\right]\\&+\boldsymbol{\nabla_X}.\left[\overline{(\boldsymbol{u_X}|\boldsymbol{u_X}|^2)}+\frac{2}{\rho}\overline{(\boldsymbol{u_X}P_X)}+2\overline{(\boldsymbol{\delta u}(\boldsymbol{\delta u}.\boldsymbol{u_X}))}-\frac{\nu}{2}\boldsymbol{\nabla_X}\overline{\boldsymbol{u_X}^2}\right]\\&\approx-2\overline{\epsilon}\end{aligned} \tag{A.20}$$

where the non-homogeneous parts of the small scale and large scale equations appear explicitly. The diffusion in r space is neglected for $r >> \lambda$ (Valente and Vassilicos 2015).

Local homogeneity

Similarly to the argumentation in section A.2.1, it is assumed for $r << L$ that the small scale spatial non-homogeneity is negligible compared to the large scale one:

$$\begin{aligned}&\boldsymbol{\nabla}_{\boldsymbol{X}}.\left[\overline{(\boldsymbol{u_X}|\boldsymbol{\delta u}|^2)}+\frac{2}{\rho}\overline{(\boldsymbol{\delta u}\delta p)}-\frac{\nu}{2}\boldsymbol{\nabla}_{\boldsymbol{X}}\overline{\boldsymbol{\delta u}^2}\right]\\&<<\boldsymbol{\nabla}_{\boldsymbol{X}}.\left[\overline{(\boldsymbol{u_X}|\boldsymbol{u_X}|^2)}+\frac{2}{\rho}\overline{(\boldsymbol{u_X}P_X)}+2\overline{(\boldsymbol{\delta u}(\boldsymbol{\delta u}.\boldsymbol{u_X}))}-\frac{\nu}{2}\boldsymbol{\nabla}_{\boldsymbol{X}}\overline{\boldsymbol{u_X}^2}\right]\end{aligned}\tag{A.21}$$

This assumption is similar to Kolmogorov idea of local homogeneity. However, the local homogeneity is not applied to each terms individually but for the sum. This assumption is consistent with a significantly non-zero small scale transport term as it is for example the case in our measurements. It is also analog to the non-zero sub-terms of the steady term $\frac{\partial<|\boldsymbol{\delta u}|>^2}{\partial t}\approx 0$ in section A.2.1.

Using equation A.20, the assumption A.21 can be rewritten for $\lambda << r << L$ as:

$$\begin{cases}\boldsymbol{\nabla}_{\boldsymbol{X}}.\left[\overline{(\boldsymbol{u_X}|\boldsymbol{\delta u}|^2)}+\frac{2}{\rho}\overline{(\boldsymbol{\delta u}\delta p)}-\frac{\nu}{2}\boldsymbol{\nabla}_{\boldsymbol{X}}\overline{\boldsymbol{\delta u}^2}\right]\approx 0\\\boldsymbol{\nabla}_{\boldsymbol{X}}.\left[\overline{(\boldsymbol{u_X}|\boldsymbol{u_X}|^2)}+\frac{2}{\rho}\overline{(\boldsymbol{u_X}P_X)}+2\overline{(\boldsymbol{\delta u}(\boldsymbol{\delta u}.\boldsymbol{u_X}))}-\frac{\nu}{2}\boldsymbol{\nabla}_{\boldsymbol{X}}\overline{\boldsymbol{u_X}^2}\right]\approx -2\overline{\epsilon}\end{cases}\tag{A.22}$$

These assumptions are integrated over a finite spatial domain to interpret it:

$$\begin{cases}\oiint_{\partial\Omega}\left(\overline{(\boldsymbol{u_X}|\boldsymbol{\delta u}|^2)}+\frac{2}{\rho}\overline{(\boldsymbol{\delta u}\delta p)}-\frac{\nu}{2}\boldsymbol{\nabla}_{\boldsymbol{X}}\overline{\boldsymbol{\delta u}^2}\right)\boldsymbol{n}dS\approx 0\\\oiint_{\partial\Omega}\left(\overline{(\boldsymbol{u_X}|\boldsymbol{u_X}|^2)}+\frac{2}{\rho}\overline{(\boldsymbol{u_X}P_X)}+2\overline{(\boldsymbol{\delta u}(\boldsymbol{\delta u}.\boldsymbol{u_X}))}-\frac{\nu}{2}\boldsymbol{\nabla}_{\boldsymbol{X}}\overline{\boldsymbol{u_X}^2}\right)\boldsymbol{n}dS\approx -2\iiint_{\Omega}\overline{\epsilon}dV\end{cases}\tag{A.23}$$

The small scale assumption describes a spatial volume which does not receive or provide energy in average to its neighborhood. On the other side, the large scale assumption describes spatial flux which provides in average the amount of energy consumed by dissipation inside the spatial domain. The large scale non-homogeneity is therefore mandatory to sustain turbulence.

This global picture is valid if no energy is produced inside the domain at small scale. Indeed, a production of energy directly at small scale would bypass the need to sustain turbulence with spatial flux as it is produced locally. In other world it is not possible to have small scale production or small scale mean flow non-homogeneity in this simplified picture.

Interscale transfer results

Using the local homogeneity defined previously, in a similar way to chapter 4, we can re-derive for $\lambda << r << L$:

$$\boldsymbol{\nabla}_{\boldsymbol{r}}.\overline{(\boldsymbol{\delta u}|\boldsymbol{\delta u}|^2)}\approx -\overline{\epsilon}\tag{A.24}$$

$$\boldsymbol{\nabla_r}.\overline{(\boldsymbol{\delta u}|\boldsymbol{u_X}|^2)} \approx \bar{\epsilon} + 2\boldsymbol{\nabla_X}.\overline{(\boldsymbol{\delta u}(\boldsymbol{\delta u}.\boldsymbol{u_X}))}. \tag{A.25}$$

Note that the separation of the small scale and large scale non-homogeneity in A.23 is ambiguous for the term: $2\boldsymbol{\nabla_X}.\overline{(\boldsymbol{\delta u}(\boldsymbol{\delta u}.\boldsymbol{u_X}))}$ which is related to both small scale and large scale equations. Other assumptions can lead to $\boldsymbol{\nabla_r}.\overline{(\boldsymbol{\delta u}|\boldsymbol{u_X}|^2)} \approx \bar{\epsilon}$ or even $2\boldsymbol{\nabla_r}.\overline{(\boldsymbol{\delta u}(\boldsymbol{u}^+.\boldsymbol{u}^-)} \approx \bar{\epsilon}$.

Overall, the results derived in this section support that Kolmogorov-like turbulence can exist when the local homogeneity defined previously holds but:

- It does not require that the small scale non-homogeneous terms are individually zero.
- The large scale non-homogeneity should be non-zero to sustain turbulence if there is no forcing.

A.3 Lamb decomposition of the δu^2 equation

$$\frac{\partial \boldsymbol{u}}{\partial t} + \boldsymbol{\omega} \times \boldsymbol{u} + \frac{1}{2}\boldsymbol{\nabla} \boldsymbol{u}^2 = -\frac{\boldsymbol{\nabla} P}{\rho} + \nu \boldsymbol{\nabla}^2 \boldsymbol{u} \tag{A.26}$$

The equation is written at $\boldsymbol{\zeta_+} = \boldsymbol{X} + \boldsymbol{r}$ and $\boldsymbol{\zeta_-} = \boldsymbol{X} - \boldsymbol{r}$ and the half difference is done to obtain:

$$\frac{\partial \boldsymbol{\delta u}}{\partial t} + \frac{1}{2}\left[\boldsymbol{\omega}^+ \times \boldsymbol{u}^+ - \boldsymbol{\omega}^- \times \boldsymbol{u}^-\right] + \boldsymbol{\nabla_X}(\boldsymbol{u_X}.\boldsymbol{\delta u}) = -\frac{\boldsymbol{\nabla_X}\delta p}{\rho} + \frac{\nu}{2}{\boldsymbol{\nabla_X}}^2 \boldsymbol{\delta u} + \frac{\nu}{2}{\boldsymbol{\nabla_r}}^2 \boldsymbol{\delta u} \tag{A.27}$$

After multiplication by $2\boldsymbol{\delta u}$, we obtain:

$$\begin{aligned} &\frac{\partial |\boldsymbol{\delta u}|^2}{\partial t} + \boldsymbol{\delta u}\left[\boldsymbol{\omega}^+ \times \boldsymbol{u}^+ - \boldsymbol{\omega}^- \times \boldsymbol{u}^-\right] + 2\boldsymbol{\nabla_X}.(\boldsymbol{\delta u}(\boldsymbol{u_X}.\boldsymbol{\delta u})) = \\ &-2\frac{\boldsymbol{\nabla_X}.(\boldsymbol{\delta u}\delta p)}{\rho} + \frac{\nu}{2}{\boldsymbol{\nabla_X}}^2|\boldsymbol{\delta u}|^2 + \frac{\nu}{2}{\boldsymbol{\nabla_r}}^2|\boldsymbol{\delta u}|^2 - \frac{1}{2}\epsilon^+ - \frac{1}{2}\epsilon^- \end{aligned} \tag{A.28}$$

Which can also be written as:

$$\begin{aligned} &\frac{\partial |\boldsymbol{\delta u}|^2}{\partial t} + \boldsymbol{\delta u}\left[\boldsymbol{\omega}^+ \times \boldsymbol{u}^+ - \boldsymbol{\omega}^- \times \boldsymbol{u}^-\right] + \boldsymbol{\nabla_r}.(\boldsymbol{\delta u}|\boldsymbol{\delta u}|^2) + \boldsymbol{\nabla_r}.(\boldsymbol{\delta u}|\boldsymbol{u_X}|^2) = \\ &-2\frac{\boldsymbol{\nabla_X}.(\boldsymbol{\delta u}\delta p)}{\rho} + \frac{\nu}{2}{\boldsymbol{\nabla_X}}^2|\boldsymbol{\delta u}|^2 + \frac{\nu}{2}{\boldsymbol{\nabla_r}}^2|\boldsymbol{\delta u}|^2 - \frac{1}{2}\epsilon^+ - \frac{1}{2}\epsilon^- \end{aligned} \tag{A.29}$$

The difference between these two equations is derived below using the relations $\frac{\partial u_{Xi}}{\partial X_j} = \frac{\partial \delta u_i}{\partial r_j}$ and $\frac{\partial u_{Xi}}{\partial r_j} = \frac{\partial \delta u_i}{\partial X_j}$ introduced in Germano 2007b:

$$\begin{aligned}
&2\boldsymbol{\nabla_X}.(\boldsymbol{\delta u}(\boldsymbol{u_X}.\boldsymbol{\delta u})) \\
&2\delta u_j \frac{\partial(u_{Xi}\delta u_i)}{\partial X_j} \\
&= 2\delta u_j \delta u_i \frac{\partial u_{Xi}}{\partial X_j} + 2\delta u_j u_{Xi} \frac{\partial \delta u_i}{\partial X_j} \\
&= 2\delta u_j \delta u_i \frac{\partial \delta u_i}{\partial r_j} + 2\delta u_j u_{Xi} \frac{\partial u_{Xi}}{\partial r_j} \\
&= \delta u_j \frac{\partial \delta u_i^2}{\partial r_j} + \delta u_j \frac{\partial u_{Xi}^2}{\partial r_j} \\
&= \boldsymbol{\nabla_r}.(\boldsymbol{\delta u}|\boldsymbol{\delta u}|^2) + \boldsymbol{\nabla_r}.(\boldsymbol{\delta u}|\boldsymbol{u_X}|^2)
\end{aligned} \tag{A.30}$$

The term $\boldsymbol{\delta u}\left[\boldsymbol{\omega}^+ \times \boldsymbol{u}^+ - \boldsymbol{\omega}^- \times \boldsymbol{u}^-\right]$ is difficult to simplify directly but it can be obtained through identification with the results of the global KHMH equation 2.7:

$$\boldsymbol{\delta u}\left[\boldsymbol{\omega}^+ \times \boldsymbol{u}^+ - \boldsymbol{\omega}^- \times \boldsymbol{u}^-\right] = \boldsymbol{\nabla_X}.(\boldsymbol{u_X}|\boldsymbol{\delta u}|^2) - \boldsymbol{\nabla_r}.(\boldsymbol{\delta u}|\boldsymbol{u_X}|^2) \tag{A.31}$$

Therefore the KHMH equation can be decomposed between the lamb and gradient part of the advection contribution to energy budget:

$$\begin{aligned}
\frac{\partial|\boldsymbol{\delta u}|^2}{\partial t} + \underline{\boldsymbol{\nabla_X}.(\boldsymbol{u_X}|\boldsymbol{\delta u}|^2)} - \underline{\boldsymbol{\nabla_r}.(\boldsymbol{\delta u}|\boldsymbol{uX}|^2)} + \underline{\underline{2\boldsymbol{\nabla_X}.(\boldsymbol{\delta u}(\boldsymbol{u_X}.\boldsymbol{\delta u}))}} \\
= -\frac{2}{\rho}\boldsymbol{\nabla_X}.(\boldsymbol{\delta u}\delta p) + \frac{\nu}{2}\boldsymbol{\nabla_X}^2|\boldsymbol{\delta u}|^2 + \frac{\nu}{2}\boldsymbol{\nabla_r}^2|\boldsymbol{\delta u}|^2 - \epsilon
\end{aligned} \tag{A.32}$$

This equation can also be written in a reduced form:

$$\frac{\partial|\boldsymbol{\delta u}|^2}{\partial t} + \left[\underline{\boldsymbol{\nabla_X}.(\boldsymbol{u_X}|\boldsymbol{\delta u}|^2) - \boldsymbol{\nabla_r}.(\boldsymbol{\delta u}|\boldsymbol{uX}|^2)}\right] + \frac{2}{\rho}\boldsymbol{\nabla_X}.(\boldsymbol{\delta u}\delta p^*) = D_{\boldsymbol{\delta u}^2} - \epsilon \tag{A.33}$$

where $p^* = p + \frac{1}{2}\rho u^2$ and $D_{\boldsymbol{\delta u}^2} = \frac{\nu}{2}\boldsymbol{\nabla_X}^2|\boldsymbol{\delta u}|^2 + \frac{\nu}{2}\boldsymbol{\nabla_r}^2|\boldsymbol{\delta u}|^2$.

A.4 Lamb decomposition of the u_X^2 equation

$$\frac{\partial \boldsymbol{u}}{\partial t} + \boldsymbol{\omega} \times \boldsymbol{u} + \frac{1}{2}\boldsymbol{\nabla u}^2 = -\frac{\boldsymbol{\nabla} P}{\rho} + \nu \boldsymbol{\nabla}^2 \boldsymbol{u} \tag{A.34}$$

The equation is written at $\boldsymbol{\zeta_+} = \boldsymbol{X} + \boldsymbol{r}$ and $\boldsymbol{\zeta_-} = \boldsymbol{X} - \boldsymbol{r}$ and the sum is done to obtain:

$$\frac{\partial \boldsymbol{u_X}}{\partial t} + \frac{1}{2}\left[\boldsymbol{\omega}^+ \times \boldsymbol{u}^+ + \boldsymbol{\omega}^- \times \boldsymbol{u}^-\right] + \frac{1}{2}\boldsymbol{\nabla_X}(\boldsymbol{u_X}^2 + \boldsymbol{\delta u}^2) = -\frac{\boldsymbol{\nabla_X} P_X}{\rho} + \frac{\nu}{2}\boldsymbol{\nabla_X}^2 \boldsymbol{u_X} + \frac{\nu}{2}\boldsymbol{\nabla_r}^2 \boldsymbol{u_X} \tag{A.35}$$

After multiplication by $2\boldsymbol{u_X}$, we obtain:

$$\begin{aligned} &\frac{\partial |\boldsymbol{u_X}|^2}{\partial t} + \boldsymbol{u_X}\left[\boldsymbol{\omega}^+ \times \boldsymbol{u}^+ + \boldsymbol{\omega}^- \times \boldsymbol{u}^-\right] + \boldsymbol{\nabla_X}.(\boldsymbol{u_X}(\boldsymbol{u_X}^2 + \boldsymbol{\delta u}^2)) = \\ &-2\frac{\boldsymbol{\nabla_X}.(\boldsymbol{u_X} P_X)}{\rho} + \frac{\nu}{2}\boldsymbol{\nabla_X}^2 |\boldsymbol{u_X}|^2 + \frac{\nu}{2}\boldsymbol{\nabla_r}^2 |\boldsymbol{u_X}|^2 - \frac{1}{2}\epsilon^+ - \frac{1}{2}\epsilon^- \end{aligned} \tag{A.36}$$

The term $\boldsymbol{u_X}\left[\boldsymbol{\omega}^+ \times \boldsymbol{u}^+ + \boldsymbol{\omega}^- \times \boldsymbol{u}^-\right]$ is obtained by identification to equation 2.8:

$$\boldsymbol{u_X}\left[\boldsymbol{\omega}^+ \times \boldsymbol{u}^+ + \boldsymbol{\omega}^- \times \boldsymbol{u}^-\right] = \boldsymbol{\nabla_r}.(\boldsymbol{\delta u}|\boldsymbol{u_X}|^2) - \boldsymbol{\nabla_X}.(\boldsymbol{u_X}|\boldsymbol{\delta u}|^2) \tag{A.37}$$

Therefore the KHMH equation can be decomposed between the lamb and gradient part of the advection contribution to energy budget:

$$\begin{aligned} &\frac{\partial |\boldsymbol{u_X}|^2}{\partial t} - \underline{\boldsymbol{\nabla_X}.(\boldsymbol{u_X}|\boldsymbol{\delta u}|^2) + \boldsymbol{\nabla_r}.(\boldsymbol{\delta u}|\boldsymbol{uX}|^2)} + \underline{\underline{\boldsymbol{\nabla_X}.(\boldsymbol{u_X}(\boldsymbol{u_X}^2 + \boldsymbol{\delta u}^2))}} \\ &= -\frac{2}{\rho}\boldsymbol{\nabla_X}.(\boldsymbol{u_X} P_X) + \frac{\nu}{2}\boldsymbol{\nabla_X}^2 |\boldsymbol{u_X}|^2 + \frac{\nu}{2}\boldsymbol{\nabla_r}^2 |\boldsymbol{u_X}|^2 - \frac{1}{2}\epsilon^+ - \frac{1}{2}\epsilon^- \end{aligned} \tag{A.38}$$

$$\frac{\partial |\boldsymbol{u_X}|^2}{\partial t} - \left[\underline{\boldsymbol{\nabla_X}.(\boldsymbol{u_X}|\boldsymbol{\delta u}|^2) - \boldsymbol{\nabla_r}.(\boldsymbol{\delta u}|\boldsymbol{uX}|^2)}\right] + \frac{2}{\rho}\boldsymbol{\nabla_X}.(\boldsymbol{u_X} P_X^*) = D_{\boldsymbol{u_X}^2} - \epsilon \tag{A.39}$$

where $p^* = p + \frac{1}{2}\rho u^2$ and $D_{\boldsymbol{u_X}^2} = \frac{\nu}{2}\boldsymbol{\nabla_X}^2 |\boldsymbol{u_X}|^2 + \frac{\nu}{2}\boldsymbol{\nabla_r}^2 |\boldsymbol{u_X}|^2$.

Appendix B

Chapter 5 appendices

B.1 Third order statistics convergence

The third order statistics convergence is evaluated on truncate estimates of the interscale transfer in figure B.1 and interspace transport in figure B.2. Only one baffle configuration and one non-baffle configuration are presented for clarity but the results of all other configurations are similar. Error bars are computed with a bootstrapping method. For both interscale and interspace energy transfer, the convergence is better in the r_z direction because of the more important number of spatial points available in this direction. The baffle results are also better converged than non-baffle results for the same r/λ because the values of λ are smaller. The baffle configurations results are well converged for all the separation length values used in the figures B.1 and B.2 i.e. $r_x < 2.5\lambda$ and $r_z < 5.5\lambda$. The convergence of the non-baffle configurations is acceptable for $r_x < 1.3\lambda$ and $r_z < 3\lambda$. For larger separation lengths, the results are significantly contaminated by convergence uncertainty and might have erratic behavior.

B.2 Structure functions at different space locations

In chapter 5, the inner similarity hypothesis 5.3 is evaluated. Only one baffled and one non-baffled configurations were plotted in the chapter so this appendix contains the results of all the other configurations. The reader can refer to chapter 5 for the comments about the results.

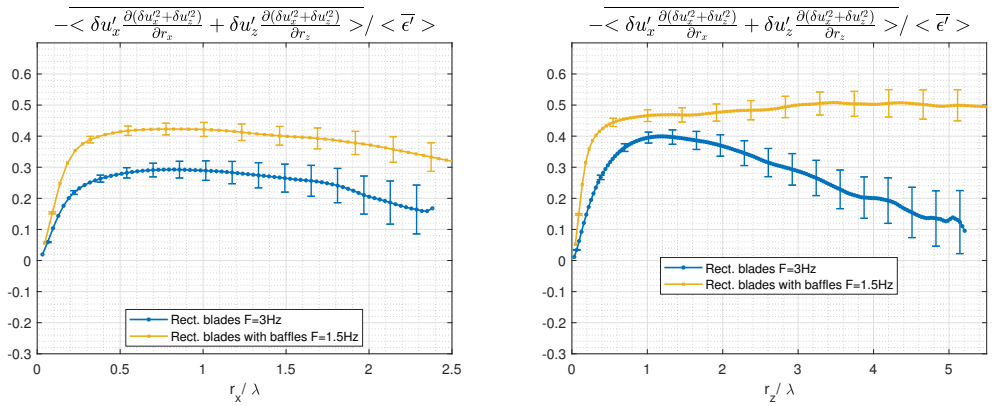

(a) r_x direction (b) r_z direction

Figure B.1: Interscale transfer truncate estimate convergence

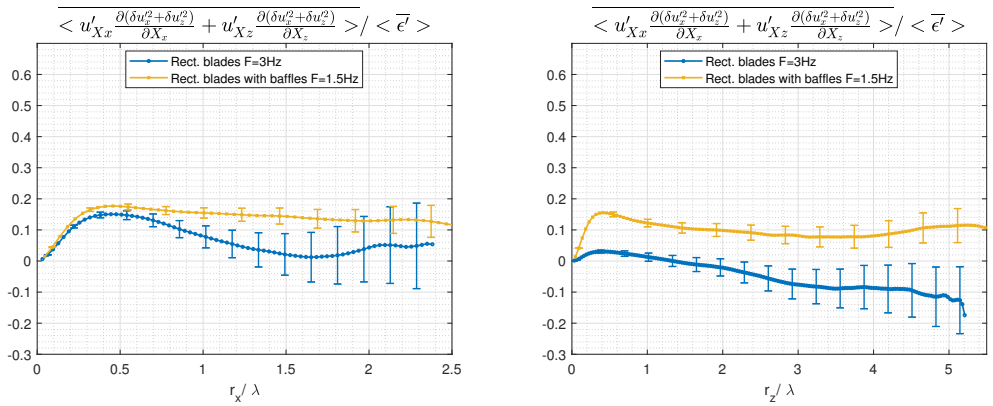

(a) r_x direction (b) r_z direction

Figure B.2: Interspace transport truncate estimate convergence

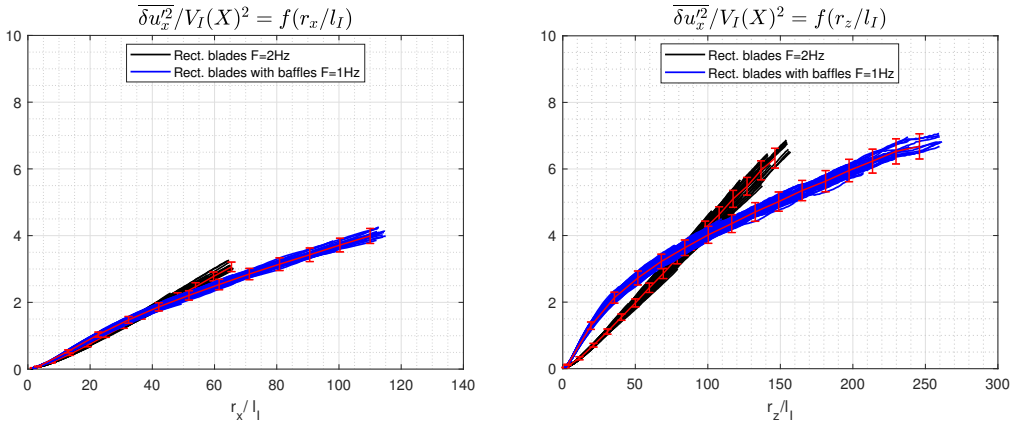

(a) r_x direction (b) r_z direction

Figure B.3: Configurations: rectangular blades at 2Hz without baffles and rectangular blades at 1Hz with baffles.Time averaged structure function $\overline{\delta u_x'^2}$ at different space locations in two radial directions and normalized by l_I, $V_I^2 = (\overline{u_x'^2} + \overline{u_z'^2}).Re_O^{-1/2}$ where $Re_O = \frac{\sqrt{\overline{u_x'^2}+\overline{u_z'^2}}D}{\nu}$.

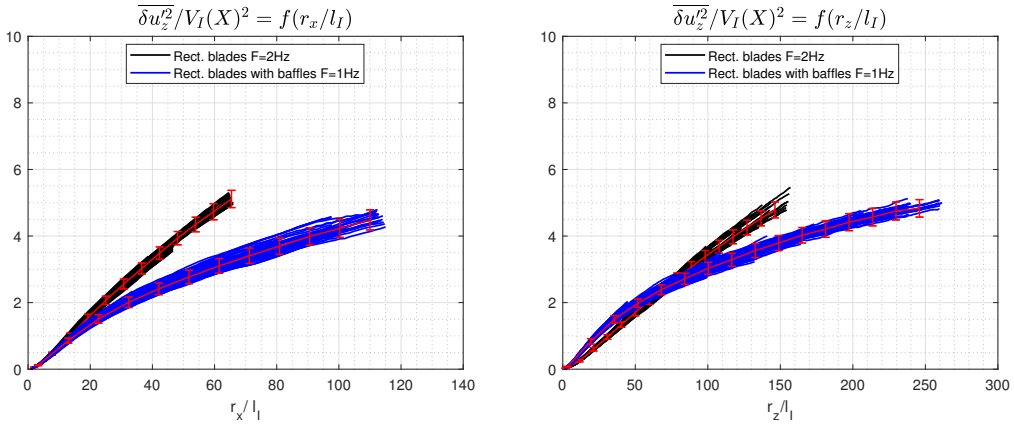

(a) r_x direction (b) r_z direction

Figure B.4: Configurations: rectangular blades at 2Hz without baffles and rectangular blades at 1Hz with baffles. Time averaged structure function $\overline{\delta u_z'^2}$ at different space locations in two radial directions and normalized by l_I, $V_I^2 = (\overline{u_x'^2} + \overline{u_z'^2}).Re_O^{-1/2}$ where $Re_O = \frac{\sqrt{\overline{u_x'^2}+\overline{u_z'^2}}D}{\nu}$.

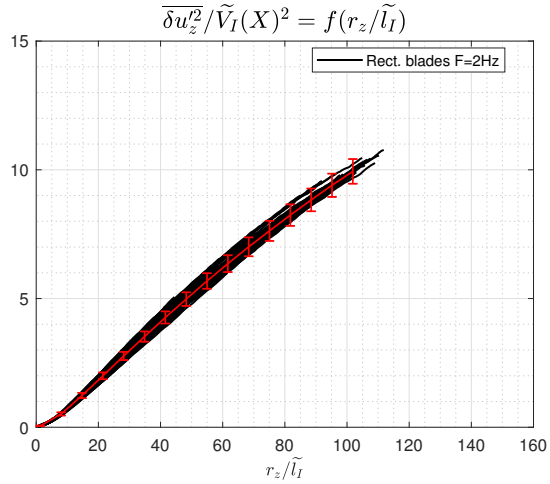

Figure B.5: Configurations: rectangular blades at 2Hz without baffles. Time averaged structure function $\overline{\delta u_z'^2}$ at different space locations as function of r_z and normalized by $\widetilde{l_I}$, $\widetilde{V_I}^2 = (\overline{u_z'^2}).\widetilde{Re_O}^{-1/2}$ where $\widetilde{Re_O} = \frac{\sqrt{\overline{u_z'^2}}D}{\nu}$.

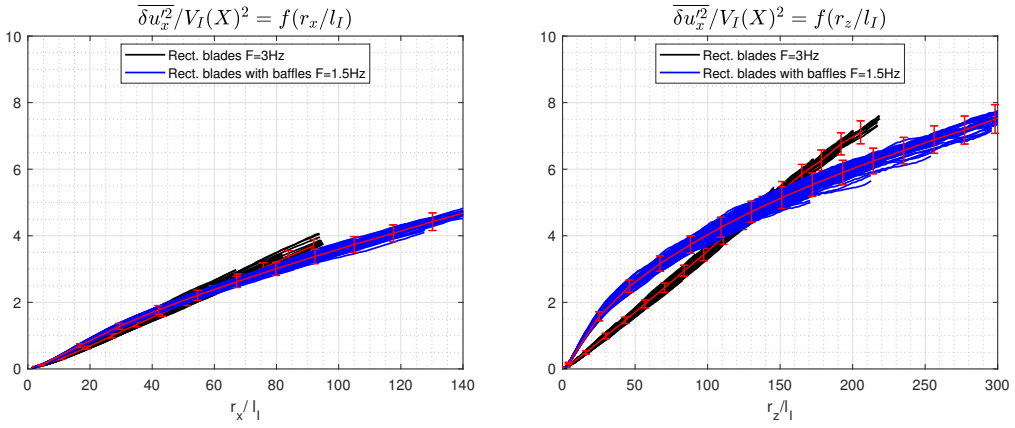

(a) r_x direction (b) r_z direction

Figure B.6: Configurations: rectangular blades at 3Hz without baffles and rectangular blades at 1.5Hz with baffles. Time averaged structure function $\overline{\delta u_x'^2}$ at different space locations in two radial directions and normalized by l_I, $V_I^2 = (\overline{u_x'^2} + \overline{u_z'^2}).Re_O^{-1/2}$ where $Re_O = \frac{\sqrt{\overline{u_x'^2}+\overline{u_z'^2}}D}{\nu}$.

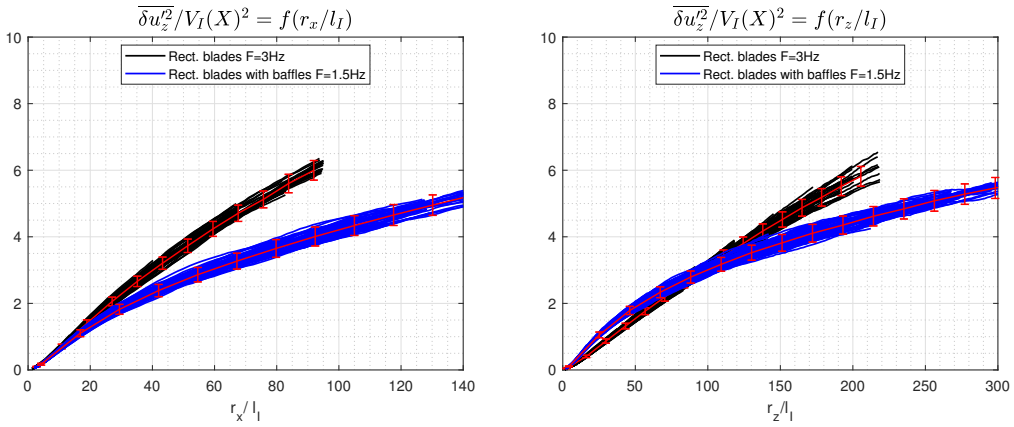

(a) r_x direction (b) r_z direction

Figure B.7: Configurations: rectangular blades at 3Hz without baffles and rectangular blades at 1.5Hz with baffles. Time averaged structure function $\overline{\delta u_z'^2}$ at different space locations in two radial directions and normalized by l_I, $V_I^2 = (\overline{u_x'^2} + \overline{u_z'^2}).Re_O^{-1/2}$ where $Re_O = \frac{\sqrt{\overline{u_x'^2}+\overline{u_z'^2}}D}{\nu}$.

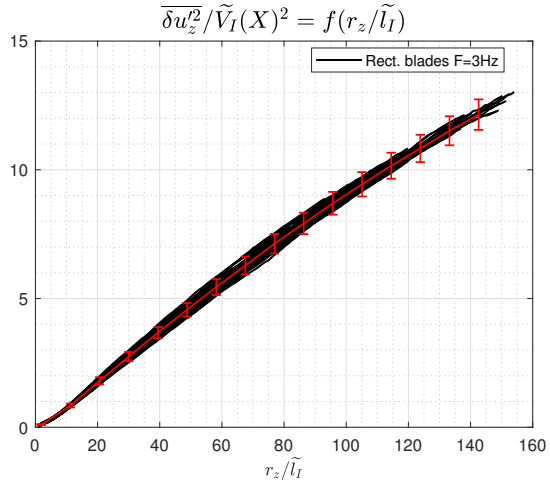

Figure B.8: Configurations: rectangular blades at 3Hz without baffles. Time averaged structure function $\overline{\delta u_z'^2}$ at different space locations as function of r_z and normalized by $\widetilde{l_I}$, $\widetilde{V_I}^2 = (\overline{u_z'^2}).\widetilde{Re_O}^{-1/2}$ where $\widetilde{Re_O} = \frac{\sqrt{\overline{u_z'^2}}D}{\nu}$.

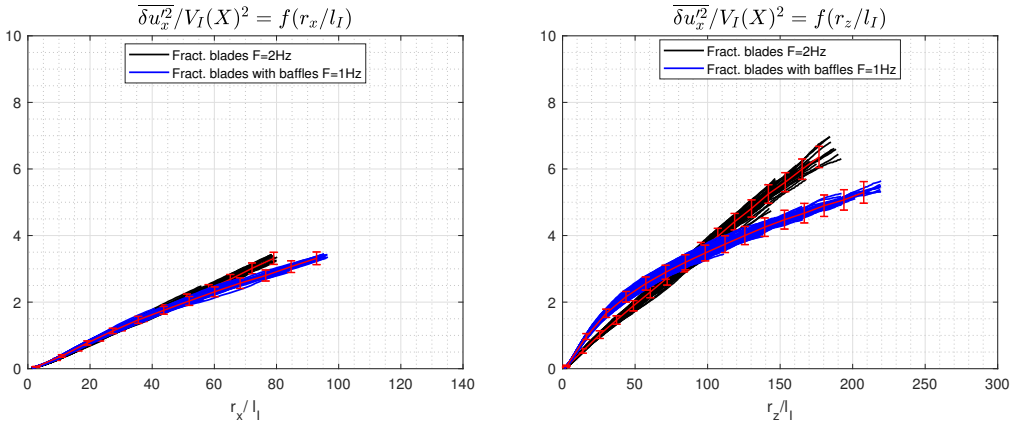

(a) r_x direction (b) r_z direction

Figure B.9: Configurations: fractal blades at 2Hz without baffles and fractal blades at 1Hz with baffles. Time averaged structure function $\overline{\delta u_x'^2}$ at different space locations in two radial directions and normalized by l_I, $V_I^2 = (\overline{u_x'^2} + \overline{u_z'^2}).Re_O^{-1/2}$ where $Re_O = \frac{\sqrt{\overline{u_x'^2}+\overline{u_z'^2}}D}{\nu}$.

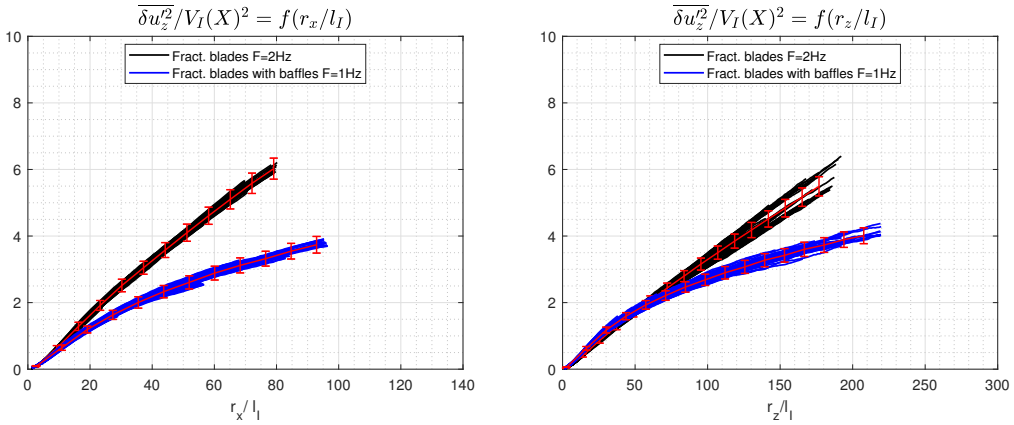

(a) r_x direction (b) r_z direction

Figure B.10: Configurations: fractal blades at 2Hz without baffles and fractal blades at 1Hz with baffles. Time averaged structure function $\overline{\delta u_z'^2}$ at different space locations in two radial directions and normalized by l_I, $V_I^2 = (\overline{u_x'^2} + \overline{u_z'^2}).Re_O^{-1/2}$ where $Re_O = \frac{\sqrt{\overline{u_x'^2}+\overline{u_z'^2}}D}{\nu}$.

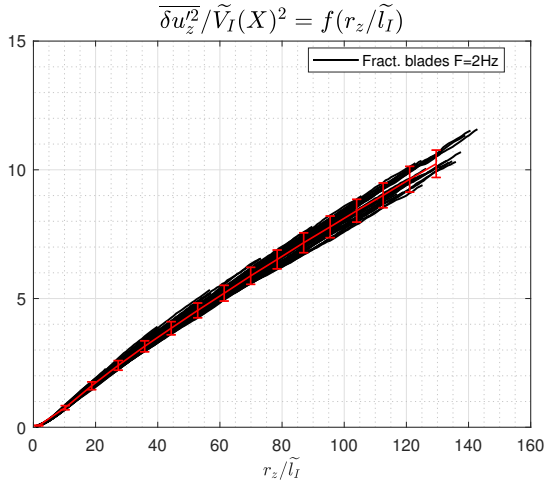

Figure B.11: Configurations: fractal blades at 2Hz without baffles. Time averaged structure function $\overline{\delta u_z'^2}$ at different space locations as function of r_z and normalized by $\widetilde{l_I}$, $\widetilde{V_I}^2 = (\overline{u_z'^2}).\widetilde{Re_O}^{-1/2}$ where $\widetilde{Re_O} = \frac{\sqrt{\overline{u_z'^2}}D}{\nu}$.

Appendix C

Chapter 6 appendix

C.1 Coefficient evaluation

The coefficient used in front of the resolved part of our model is not straightforward so a basic analysis is done with *an priori* test to evaluate it. This coefficient may be needed to rescale the resolved part of our model because of the uncertainty introduced during the approximations of the exact equation 6.10. The formulation tested is the equation 6.40 where the multiplying factor takes the form $\frac{C_1}{(2\Delta)^3}\frac{6(2\Delta)^2}{6\times 9} = \frac{C_1}{18\Delta}$ where C_1 is defined in equation 6.40 and is evaluated at different filtering widths: Δ. The coefficient is adjusted with an optimization to fit the model subfilter stress energy contribution PDF with exact results. The optimization is based on the following process:

- C_1 is initialized to 1
- The PDF of the modelled subfilter stress energy contribution $-\widetilde{u}_i\Psi$ (where Ψ is defined in 6.40) is evaluated on the Taylor-Green DNS dataset. We use the notation $Q_m = -\widetilde{u}_i\Psi$ to simplify notation. The PDF of the exact subfilter stress contribution $-\widetilde{u_i}\frac{\partial\tau_{ij}}{\partial x_j}$ is evaluated on the same dataset and we use the notation $Q_r = -\widetilde{u_i}\frac{\partial\tau_{ij}}{\partial x_j}$.
- The coefficient C_1 is updated: $C_1 \leftarrow C_1\langle\frac{Q_m * PDF(Q_m)}{Q_r * PDF(Q_r)}\rangle^{-1}$ where $(*)$ represents the term by term multiplication $(x * y = (x(i) * y(i))_i)$ and $< . >$ spatial averaging. This process tends to superimpose the PDF of Q_r over the one of Q_m (see figure C.1).
- We iterate on the process (without the initialization of C_1) until convergence.

The same optimization is carried out for the *increment* model coefficient C_2 defined in 6.44.

The optimization results are presented in figure C.1 with linear axes and in C.2 with logarithmic axes for one value of $\Delta \approx 8\eta$: the most probable events are well fitted, as observed in figure C.1, because of their dominant representation but the rare events are

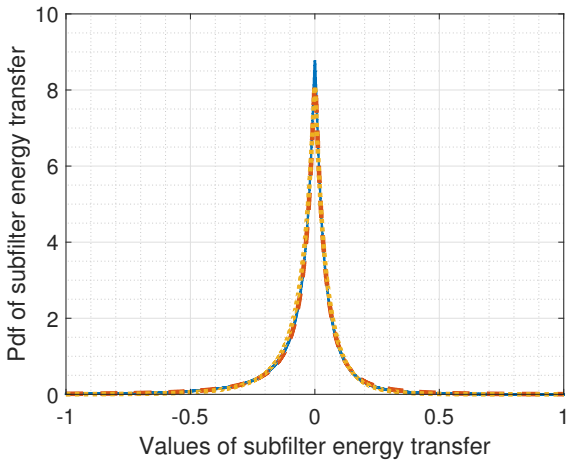

Figure C.1: PDF of the subfilter stress contribution with linear axes (exact: $-\widetilde{u}_i \frac{\partial \tau_{ij}}{\partial x_j}$ or modelled: $-\widetilde{u}_i \widehat{\frac{\partial \tau_{ij}}{\partial x_j}}$) evaluated *a priori* on DNS results with a $12 \times 12 \times 12$ top hat filter. The results are superimposed. In blue: the exact contribution ($-\widetilde{u}_i \frac{\partial \tau_{ij}}{\partial x_j}$), in red: Brun, Friedrich, and Da Silva 2006 model contribution ($-\widetilde{u}_i \frac{\partial \left(\delta \check{u}_i \delta \check{u}_j\right)}{\partial x_j}$) and in yellow: resolved part of the present model contribution ($-\widetilde{u}_i \Psi$, where Ψ is defined in 6.40)

overestimated with the model 6.44 and underestimated with resolved model as seen in figure C.2,. The resolved model coefficient results are presented in figure C.3 where a linear evolution is observed for $\Delta > 4\eta$. For a filtering over $12 \times 12 \times 12$ points ($\Delta \approx 8\eta$) which correspond to a LES simulation in $64 \times 64 \times 64$ domain, the value of C_1 is 0.97 and the value of C_2 is 0.152. Future work is needed to have a better computation method of this coefficient for general turbulence but the results obtained are sufficient to test the model in Taylor-Green simulations.

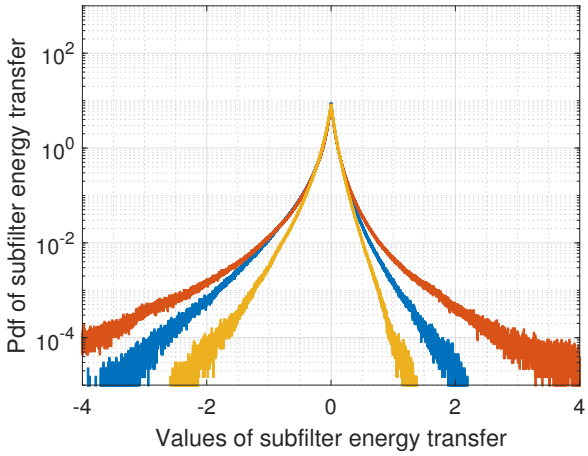

Figure C.2: PDF of the subfilter stress contribution with logarithmic axes (exact: $-\widetilde{u}_i \frac{\partial \tau_{ij}}{\partial x_j}$ or modelled: $-\widetilde{u}_i \widehat{\frac{\partial \tau_{ij}}{\partial x_j}}$) evaluated *a priori* on DNS results with a $12 \times 12 \times 12$ top hat filter. In blue: the exact contribution ($-\widetilde{u}_i \frac{\partial \tau_{ij}}{\partial x_j}$), in red: Brun, Friedrich, and Da Silva 2006 model contribution ($-\widetilde{u}_i \frac{\partial \left(\delta \check{u}_i \delta \check{u}_j\right)}{\partial x_j}$) and in yellow: resolved part of the present model contribution ($-\widetilde{u}_i \Psi$, where Ψ is defined in 6.40)

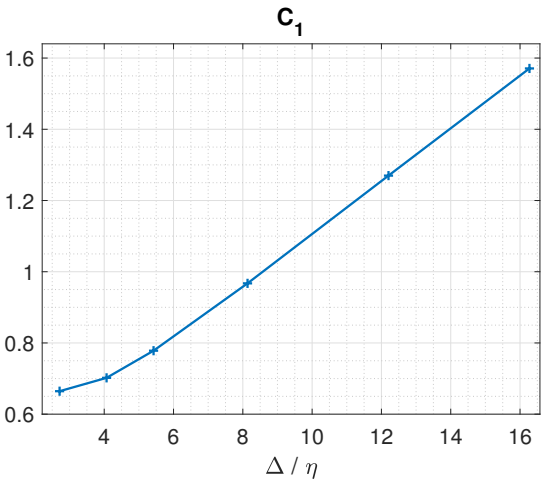

Figure C.3: Coefficient variation with filtering width

C.2 *A priori* analysis with $\Delta \approx 16\eta$

In subsection 6.5.2, the two-dimensional PDFs of the subfilter stress contributions (Smagorinsky model: $-\widetilde{u}_i \frac{\partial\left(-2C_s\Delta^2|\widetilde{S}|\widetilde{S}_{ij}\right)}{\partial x_j}$, Brun, Friedrich, and Da Silva 2006 model (6.16): $-\widetilde{u}_i \frac{\partial\left(\delta\check{u}_i\delta\check{u}_j\right)}{\partial x_j}$ and resolved part of our model: $-\widetilde{u}_i\Psi$ (where Ψ is defined in 6.40) with the exact contribution: $-\widetilde{u}_i \frac{\partial\tau_{ij}}{\partial x_j}$ are presented for a filtering width $\Delta \approx 8\eta$. In this appendix, a wider filtering is used ($\Delta \approx 16\eta$) to check the results remain valid for larger filtering. The Smagorinsky results in figure C.4a are close to the results in figure 6.8a with nearly no correlation between $-\widetilde{u}_i \frac{\partial\left(-2C_s\Delta^2|\widetilde{S}|\widetilde{S}_{ij}\right)}{\partial x_j}$ and $-\widetilde{u}_i \frac{\partial\tau_{ij}}{\partial x_j}$. The larger filtering does not improve the Smagorinsky model results as expected. The Brun, Friedrich, and Da Silva 2006 model results in figure C.4b are also close to the results at smaller filtering in figure 6.8b with a small correlation but also strong anti-correlation values around the axes. The main result of this appendix is the figure C.4c where we can observe that the correlation of $-\widetilde{u}_i\Psi$ (where $C_1 \approx 1.57$ accordingly to appendix C.1) with $-\widetilde{u}_i \frac{\partial\tau_{ij}}{\partial x_j}$ does not evolve significantly with the filtering width as the results at larger filtering ($\Delta \approx 16\eta$) are close to the results at smaller filtering ($\Delta \approx 8\eta$) in figure 6.8c. We can therefore conclude that the results of the *a priori* analysis done in chapter 6 does not depend significantly on the filter width at least until $\Delta \approx 16\eta$.

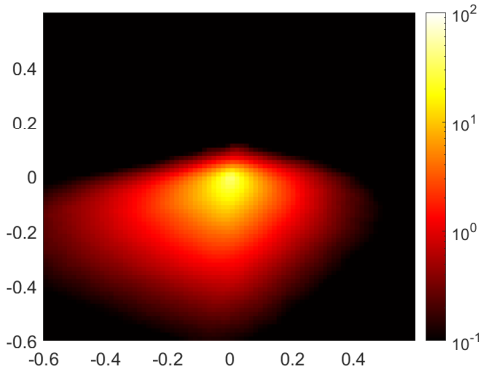

(a) Horizontal axis: exact subfilter contribution to (6.1): $-\widetilde{u}_i \frac{\partial \tau_{ij}}{\partial x_j}$. Vertical axis: Smagorinsky model contribution to (6.2): $-\widetilde{u}_i \frac{\partial \left(-2C_s\Delta^2|\widetilde{S}|\widetilde{S}_{ij}\right)}{\partial x_j}$.

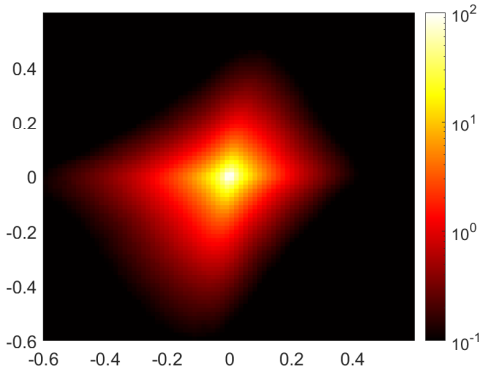

(b) Horizontal axis: exact subfilter stress contribution to (6.1): $-\widetilde{u}_i \frac{\partial \tau_{ij}}{\partial x_j}$. Vertical axis: Brun, Friedrich, and Da Silva 2006 model contribution to (6.2): $-\widetilde{u}_i \frac{\partial \left(\delta\check{u}_i \delta\check{u}_j\right)}{\partial x_j}$.

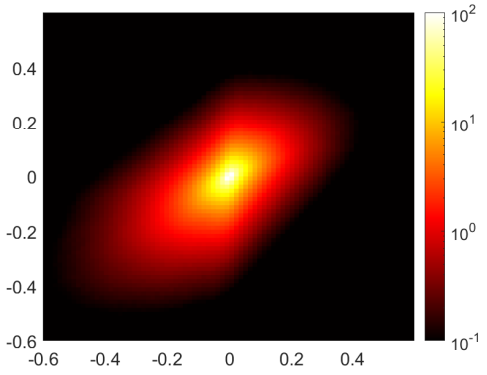

(c) Horizontal axis: exact subfilter stress contribution to (6.1): $-\widetilde{u}_i \frac{\partial \tau_{ij}}{\partial x_j}$. Vertical axis: Resolved part of the present model contribution to (6.2): $-\widetilde{u}_i \Psi$, where Ψ is defined in 6.40.

Figure C.4: Two-dimensional PDFs of modelled subfilter stress contributions to (6.2): $-\widetilde{u}_i \widehat{\frac{\partial \tau_{ij}}{\partial x_j}}$ with exact subfilter stress energy contribution to (6.1): $-\widetilde{u}_i \frac{\partial \tau_{ij}}{\partial x_j}$, with scaling coefficient, evaluated in the Taylor-Green DNS simulation with $\Delta \approx 16\eta$.

C.3 Derivation of a second exact form of the subfilter stress

A first exact subfilter stress exact equation 6.10 is derived in subsection 6.4.1. In this appendix a second exact form of the subfilter stress is derived and compared to the equation 6.10.

The basic filtering 6.8 does not filter enough to obtain a practically useful subfilter stress formula so a filter is applied to $\boldsymbol{u_X}$. Before applying a general discrete filtering to $\boldsymbol{u_X}$, a simple example is used in continuous form. $\boldsymbol{u_X}$ is averaged in $\boldsymbol{r}$ space over a volume $V(\Delta) = (2\Delta)^3$ (where Δ is the LES mesh width) similarly to two-point energy equations in chapter 2. This filtering is equivalent to a continuous top hat filter applied to the velocity field $\boldsymbol{u}$:

$$\begin{aligned}\widetilde{\boldsymbol{u}} = \frac{1}{V(\Delta)}\int_{V(\Delta)} \boldsymbol{u_X} d^3r &= \frac{1}{V(\Delta)}\int_{-\Delta}^{\Delta}\int_{-\Delta}^{\Delta}\int_{-\Delta}^{\Delta} \frac{\boldsymbol{u}(\boldsymbol{X}-\boldsymbol{r})+\boldsymbol{u}(\boldsymbol{X}+\boldsymbol{r})}{2} dr_3 dr_2 dr_1 \\ &= \frac{1}{(2\Delta)^3}\int_{-\Delta}^{\Delta}\int_{-\Delta}^{\Delta}\int_{-\Delta}^{\Delta} \boldsymbol{u}(\boldsymbol{X}-\boldsymbol{r}) dr_3 dr_2 dr_1\end{aligned} \tag{C.1}$$

The integration in scale space leads to an efficient filtering as opposed to the basic filtering defined in equation 6.8. Now, the filtering is generalized to any discrete filter with the discrete weight function 6.11, G, used in order to match the filtering used in Germano 2007a and subsection 6.4.1. This filter allows to filter in a different way than the continuous top hat filtering used in (C.1). A discrete filter is used for practical reasons of implementation but the same results can be derived for a continuous filter if the weight function defined is continuous. For example, C.1 is a specific case of a continuous filtering.

The filtered velocity $\widetilde{\boldsymbol{u}}$ is obtained by

$$\widetilde{\boldsymbol{u}} = \int G(\boldsymbol{r})\boldsymbol{u_X} d^3r \tag{C.2}$$

and is exactly equivalent to (6.12) when $G(-\boldsymbol{r}) = G(\boldsymbol{r})$. We assume from now that it is the case.

We restrict the filtering to compact filtering over $V(\Delta)$ to stay close to (C.1) formulation and obtain

$$\widetilde{\boldsymbol{u}} = \int_{V(\Delta)} G(\boldsymbol{r})\boldsymbol{u_X} d^3r \tag{C.3}$$

A possible example among many is discrete Gaussian filtering where G has a discretized gaussian shape. The residual velocity field is:

$$\boldsymbol{u'_X} = \boldsymbol{u_X} - \widetilde{\boldsymbol{u}} \tag{C.4}$$

The integration (C.3) in $\boldsymbol{r}$ space is applied to equation 6.4 to derive an exact equation for the filtered velocity $\widetilde{\boldsymbol{u}}$

$$\begin{aligned}&\frac{\partial \widetilde{\boldsymbol{u}}}{\partial t} + (\widetilde{\boldsymbol{u}}.\nabla_{\boldsymbol{X}})\widetilde{\boldsymbol{u}} + \int_{V(\Delta)} G(\boldsymbol{r})(\boldsymbol{u'_X}.\nabla_{\boldsymbol{X}})\boldsymbol{u'_X} d\boldsymbol{r}^3 + \int_{V(\Delta)} G(\boldsymbol{r})(\boldsymbol{\delta u}.\nabla_{\boldsymbol{r}})\boldsymbol{u_X} d\boldsymbol{r}^3 \\ &= -\frac{1}{\rho}\nabla_{\boldsymbol{X}}\widetilde{p} + \nu\nabla^2_{\boldsymbol{X}}\widetilde{\boldsymbol{u}}\end{aligned} \tag{C.5}$$

For this derivation we have used the property: $\int_{V(\Delta)} G(\boldsymbol{r})\boldsymbol{u'_X} d^3r = 0$ so that $\int_{V(\Delta)} G(\boldsymbol{r})(\boldsymbol{u_X}.\boldsymbol{\nabla_X})\boldsymbol{u_X} d^3r = (\widetilde{\boldsymbol{u}}.\nabla_{\boldsymbol{X}})\widetilde{\boldsymbol{u}} + \int_{V(\Delta)} G(\boldsymbol{r})(\boldsymbol{u'_X}.\nabla_{\boldsymbol{X}})\boldsymbol{u'_X} d^3r$. Note that we consider functions G which are independent of $\boldsymbol{X}$.

The terms $\int_{V(\Delta)} G(\boldsymbol{r})(\boldsymbol{u'_X}.\nabla_{\boldsymbol{X}})\boldsymbol{u'_X} d^3r$ and $\int_{V(\Delta)} G(\boldsymbol{r})(\boldsymbol{\delta u}.\nabla_{\boldsymbol{r}})\boldsymbol{u_X} d^3r$ in equation C.5 are the exact subfilter stress contributions that need to be modeled. This exact equation links explicitly the two-point equations used in fundamental research for physical understanding (equations (6.4) and (2.8)) with LES modeling. Indeed, the term $(\boldsymbol{\delta u}.\nabla_{\boldsymbol{r}})\boldsymbol{u_X}$ once multiplied by $\boldsymbol{u_X}$ is called the large scale interscale transfer rate $\boldsymbol{\nabla_r}.\boldsymbol{\delta u}|\boldsymbol{u_X}|^2$. This quantity is interpreted and measured experimentally in chapters 2, 4 and 5. Therefore, $\int_{V(\Delta)} G(\boldsymbol{r})(\boldsymbol{\delta u}.\nabla_{\boldsymbol{r}})\boldsymbol{u_X} d^3r$ can be interpreted as the scale contribution to the subfilter stress gradient.

Similarly, the term $(\boldsymbol{u'_X}.\nabla_{\boldsymbol{X}})\boldsymbol{u'_X}$ once multiplied by $\boldsymbol{u_X}$ looks similar to the large scale interspace transport which is also measured and analyzed in chapters 2, 4 and 5. Therefore, $\int_{V(\Delta)} G(\boldsymbol{r})(\boldsymbol{u'_X}.\nabla_{\boldsymbol{X}})\boldsymbol{u'_X} d^3r$ can be interpreted as the space contribution to the subfilter stress gradient. This specific formulation of the subfilter stress is derived for the first time. However, another formulation was previously derived in Germano 2007a and Germano 2007c. This formulation, presented in subsection 6.4.1, is more useful for large eddy simulation but the matching between the two formulations provides additional understanding about the contribution of the spatial term to the subfilter stress gradient. Moreover, the derivation steps of this appendix help understanding the links between the exact equation C.5 and the subfilter stress gradient.

Using both the Germano 2007c subfilter stress exact formulation 6.10 and the one derived in this appendix, the following result is derived from C.5 and 6.15.

$$\begin{aligned}\frac{\partial \tau_{ij}}{\partial x_j} &= \int_{-\infty}^{\infty}\int_{-\infty}^{\infty} G(\boldsymbol{x}-\boldsymbol{s}-\boldsymbol{r})G(\boldsymbol{x}-\boldsymbol{s}+\boldsymbol{r})\boldsymbol{\nabla_r}.(u_{Xi}\boldsymbol{\delta u}) d\boldsymbol{r} d\boldsymbol{s} \\ &= \int_{V(\Delta)} G(\boldsymbol{r})\boldsymbol{\nabla_X}.(u'_{Xi}\boldsymbol{u'_X}) d\boldsymbol{r} + \int_{V(\Delta)} G(\boldsymbol{r})\boldsymbol{\nabla_r}.(u_{Xi}\boldsymbol{\delta u}) d\boldsymbol{r}\end{aligned} \tag{C.6}$$

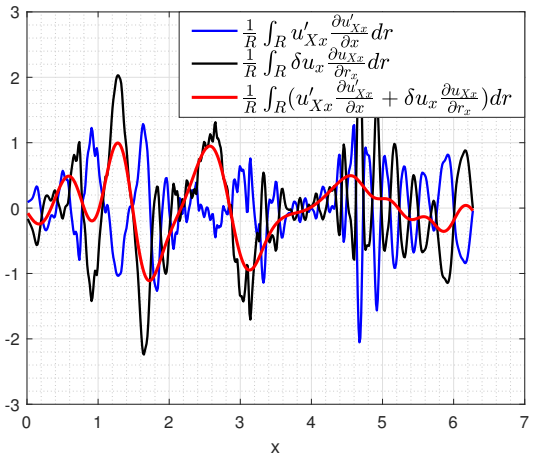

Figure C.5: Entanglement of space and scale contributions observed with filtering in 1 dimension. These results are evaluated with one velocity component from a DNS dataset of homogeneous turbulence ($8L \times 8L \times 8L$, where L is the integral scale, $Re_\lambda = 140$, $k_{max}\eta = 1.3$). blue: 1D space subfilter stress gradient contribution, black: 1D scale subfilter stress gradient contribution, red: 1D total subfilter stress gradient contribution

where G, is defined in equation 6.11.

In equation C.6, the total subfilter stress gradient is expected to be much smoother than the scale subfilter stress gradient contribution. Indeed, it is the same quantity filtered differently. The first term is filtered both in scale and space while the second is only filtered in space. Therefore, the contribution in equation C.6 of the fluctuating space subfilter stress gradient is to cancel out some fluctuations of scale subfilter stress gradient contribution so that the sum is a smooth quantity. This result is reminiscent of the work of Larssen and Vassilicos 2023 where some strong correlations/anti-correlations of KHMH energy terms are quantified in a DNS of homogeneous turbulence.

This result is confirmed experimentally with simple tests in one dimension (figure C.5). The total 1D subfilter stress (in red) is much smoother than the 1D scale subfilter stress gradient contribution (in black) because some fluctuations are canceled by fluctuations of the 1D space subfilter stress gradient contribution (in blue). This cancellation underlines the strong entanglement of the space and scale contributions. The analysis of the consequences of this effect on the associated energy terms, interspace energy transport and interscale energy transfer, would be a very interesting direction of future research. The physical understanding of these relations would improve both turbulence knowledge and modelling methods.

Bibliography

[1] F. Alves Portela, G. Papadakis, and J. C. Vassilicos. “The turbulence cascade in the near wake of a square prism”. In: *Journal of Fluid Mechanics* 825 (Aug. 25, 2017).

[2] Felipe Alves Portela. “Turbulence Cascade in an Inhomogeneous Turbulent Flow”. PhD thesis. Imperial College London, 2017.

[3] Tomohiro Aoyama et al. “Statistics of Energy Transfer in High-Resolution Direct Numerical Simulation of Turbulence in a Periodic Box”. In: *Journal of the Physical Society of Japan* 74.12 (Dec. 2005).

[4] A Apostolidis, J P Laval, and J C Vassilicos. “Turbulent cascade in fully developed 2 turbulent channel flow”. In: *Journal of Fluid Mechanics* (2023).

[5] J. Bardina, J. Ferziger, and W. Reynolds. “Improved subgrid-scale models for large-eddy simulation”. In: *13th Fluid and PlasmaDynamics Conference*. 13th Fluid and PlasmaDynamics Conference. Snowmass,CO,U.S.A.: American Institute of Aeronautics and Astronautics, July 14, 1980.

[6] Charles N. Baroud et al. “Anomalous Self-Similarity in a Turbulent Rapidly Rotating Fluid”. In: *Physical Review Letters* 88.11 (Feb. 28, 2002).

[7] S. Başbuğ, G. Papadakis, and J. C. Vassilicos. “Reduced power consumption in stirred vessels by means of fractal impellers”. In: *AIChE Journal* 64.4 (Apr. 2018).

[8] L. H. Benedict and R. D. Gould. “Towards better uncertainty estimates for turbulence statistics”. In: *Experiments in Fluids* 22.2 (Dec. 1, 1996).

[9] Marc E. Brachet et al. “Small-scale structure of the Taylor–Green vortex”. In: *Journal of Fluid Mechanics* 130 (May 1983). Publisher: Cambridge University Press.

[10] A. Brissaud et al. “Helicity cascades in fully developed isotropic turbulence”. In: *Physics of Fluids* 16.8 (1973).

[11] Christophe Brun, Rainer Friedrich, and Carlos B. Da Silva. “A Non-Linear SGS Model Based On The Spatial Velocity Increment: Application to LES of fully developed pipe flow and round turbulent jet”. In: *Theoretical and Computational Fluid Dynamics* 20.1 (Feb. 2006).

[12] Stefano Cerutti and Charles Meneveau. “Intermittency and relative scaling of subgrid-scale energy dissipation in isotropic turbulence”. In: *Physics of Fluids* 10.4 (Apr. 1, 1998).

[13] Tarek Chaabo. “Optimization of a 4D-PTV metrology for the characterization of a turbulent flow at very small scales”. PhD thesis. Ecole Centrale de Lille, 2022.

[14] Adam Cheminet et al. “Eulerian vs Lagrangian Irreversibility in an Experimental Turbulent Swirling Flow”. In: *Physical Review Letters* 129.12 (Sept. 14, 2022).

[15] J.G. Chen and J.C. Vassilicos. “Scalings of scale-by-scale turbulence energy in non-homogeneous turbulence”. In: *Journal of Fluid Mechanics* 938 (May 10, 2022).

[16] Murali R. Cholemari. “Modeling and correction of peak-locking in digital PIV”. In: *Experiments in Fluids* 42.6 (June 1, 2007).

[17] K. T. Christensen. “The influence of peak-locking errors on turbulence statistics computed from PIV ensembles”. In: *Experiments in Fluids* 36.3 (Mar. 1, 2004).

[18] Andrea Cimarelli and Elisabetta De Angelis. “The physics of energy transfer toward improved subgrid-scale models”. In: *Physics of Fluids* 26.5 (May 2014).

[19] R. A. Clark, J. H. Ferziger, and W. C. Reynolds. *Evaluation of subgrid-scale turbulence models using a fully simulated turbulent flow.* 1977.

[20] S. Corrsin. “Local isotropy in turbulent shear flow”. In: *Tech. Rep.. National Advisory Committee for Aeronautics.* (1958).

[21] Thibault Dairay et al. “Numerical dissipation vs. subgrid-scale modelling for large eddy simulation”. In: *Journal of Computational Physics* 337 (May 15, 2017).

[22] L. Danaila et al. “Turbulent energy scale budget equations in a fully developed channel flow”. In: *Journal of Fluid Mechanics* 430 (Mar. 2001). Publisher: Cambridge University Press.

[23] L. Danaila et al. “Yaglom-like equation in axisymmetric anisotropic turbulence”. In: *Physica D: Nonlinear Phenomena* 241.3 (Feb. 2012).

[24] Paul Debue. “Experimental approach to the problem of the Navier-Stokes singularities”. PhD thesis. Université Paris-Saclay, 2019.

[25] J.A. Domaradzki and E.M. Saiki. “Backscatter Models for Large-Eddy Simulations”. In: *Theoretical and Computational Fluid Dynamics* 9.2 (Oct. 30, 1997).

[26] L. Fang et al. “An improved velocity increment model based on Kolmogorov equation of filtered velocity”. In: *Physics of Fluids* 21.6 (June 2009). Publisher: American Institute of Physics.

[27] Benjamin Favier. “A Brief Introduction to Turbulence in Rotating and Stratified Fluids”. In: *Fluid Mechanics of Planets and Stars.* Ed. by Michael Le Bars and Daniel Lecoanet. Cham: Springer International Publishing, 2020.

[28] J. M. Foucaut, J. Carlier, and M. Stanislas. “PIV optimization for the study of turbulent flow using spectral analysis”. In: *Measurement Science and Technology* 15.6 (May 2004).

[29] Jean Marc Foucaut et al. “Optimization of a SPIV experiment for derivative moments assessment in a turbulent boundary layer”. In: *Experiments in Fluids* 62.12 (Dec. 2021).

[30] Uriel Frisch. *Turbulence: The Legacy of A. N. Kolmogorov*. Cambridge University Press, 1995.

[31] Damien Geneste. “Des évènements extrêmes de dissipation aux évènements extrêmes de dispersion, une empreinte des singularités: Approche expérimentale”. PhD thesis. Université Paris-Saclay, 2023.

[32] William K. George and Hussein J. Hussein. “Locally axisymmetric turbulence”. In: *Journal of Fluid Mechanics* 233 (Dec. 1991). Publisher: Cambridge University Press.

[33] M. Germano. “A direct relation between the filtered subgrid stress and the second order structure function”. In: *Physics of Fluids* 19.3 (Mar. 2007).

[34] M. Germano. “The elementary energy transfer between the two-point velocity mean and difference”. In: *Physics of Fluids* 19.8 (Aug. 1, 2007). Publisher: American Institute of Physics.

[35] Massimo Germano. “The two-point average and the related subgrid model”. In: TCFP. 2007.

[36] Massimo Germano et al. “A dynamic subgrid-scale eddy viscosity model”. In: *Physics of Fluids A: Fluid Dynamics* 3.7 (July 1991).

[37] Massimo Germano et al. “Erratum: “A dynamic subgrid-scale eddy viscosity model” [Phys. Fluids A 3, 1760 (1991)]”. In: *Physics of Fluids A: Fluid Dynamics* 3.12 (Dec. 1, 1991).

[38] R. Gomes-Fernandes, B. Ganapathisubramani, and J. C. Vassilicos. “The energy cascade in near-field non-homogeneous non-isotropic turbulence”. In: *Journal of Fluid Mechanics* 771 (May 25, 2015).

[39] Susumu Goto. “A physical mechanism of the energy cascade in homogeneous isotropic turbulence”. In: *Journal of Fluid Mechanics* 605 (June 2008). Publisher: Cambridge University Press.

[40] Susumu Goto and J. C. Vassilicos. “The dissipation rate coefficient of turbulence is not universal and depends on the internal stagnation point structure”. In: *Physics of Fluids* 21.3 (Mar. 1, 2009).

[41] E. Herbert et al. “Dual non-Kolmogorov cascades in a von Kármán flow”. In: *EPL (Europhysics Letters)* 100.4 (Nov. 1, 2012).

[42] Reginald J. Hill. “Equations relating structure functions of all orders”. In: *Journal of Fluid Mechanics* 434 (May 10, 2001).

[43] Reginald J. Hill. “Exact second-order structure-function relationships”. In: *Journal of Fluid Mechanics* 468 (Oct. 2002). Publisher: Cambridge University Press.

[44] Reginald J. Hill. “The Approach of Turbulence to the Locally Homogeneous Asymptote as Studied using Exact Structure-Function Equations”. In: (June 12, 2002).

[45] I. Hosokawa. “A Paradox concerning the Refined Similarity Hypothesis of Kolmogorov for Isotropic Turbulence”. In: *Progress of Theoretical Physics* 118.1 (July 1, 2007).

[46] Carlos Härtel et al. “Subgrid-scale energy transfer in the near-wall region of turbulent flows”. In: *Physics of Fluids* 6.9 (Sept. 1, 1994).

[47] Takashi Ishihara, Toshiyuki Gotoh, and Yukio Kaneda. “Study of High–Reynolds Number Isotropic Turbulence by Direct Numerical Simulation”. In: *Annual Review of Fluid Mechanics* 41.1 (2009).

[48] R. D. Keane and R. J. Adrian. “Optimization of particle image velocimeters: II. Multiple pulsed systems”. In: *Measurement Science and Technology* 2.10 (Dec. 1, 1991).

[49] Mouloud Kessar et al. “Non-Kolmogorov cascade of helicity-driven turbulence”. In: *Physical Review E* 92.3 (Sept. 28, 2015).

[50] Anna N. Knutsen et al. “The inter-scale energy budget in a von Kármán mixing flow”. In: *Journal of Fluid Mechanics* 895 (July 25, 2020).

[51] A. N. Kolmogorov. “Dissipation of Energy in the Locally Isotropic Turbulence”. In: *Doklady Akademii Nauk SSSR* 32.1941 (1941).

[52] A. N. Kolmogorov. “On the degeneration of isotropic turbulence in an incompressible viscous fluid”. In: *Doklady Akademii Nauk SSSR* 31.1941 (1941).

[53] A. N. Kolmogorov. “The Local Structure of Turbulence in Incompressible Viscous Fluid for Very Large Reynolds Numbers”. In: *Doklady Akademii Nauk SSSR* 30.1941 (1941). Publisher: The Royal Society.

[54] Robert H. Kraichnan. “On Kolmogorov’s inertial-range theories”. In: *Journal of Fluid Mechanics* 62.2 (Jan. 23, 1974).

[55] Susan Kurien, Mark A. Taylor, and Takeshi Matsumoto. “Cascade time-scales for energy and helicity in homogeneous isotropic turbulence”. In: *Physical Review E* 69.6 (June 18, 2004). arXiv: `nlin/0312034`.

[56] S. Laizet, J. Nedić, and J. C. Vassilicos. “Influence of the spatial resolution on fine-scale features in DNS of turbulence generated by a single square grid”. In: *International Journal of Computational Fluid Dynamics* 29.3 (Mar. 16, 2015).

[57] H. S. Larssen and J. C. Vassilicos. *Spatio-temporal fluctuations of interscale and interspace energy transfer dynamics in homogeneous turbulence.* Apr. 11, 2023.

[58] P. Lavoie et al. “Spatial resolution of PIV for the measurement of turbulence”. In: *Experiments in Fluids* 43.1 (July 1, 2007).

[59] B. Lecordier and M. Trinité. "Advanced PIV algorithms with Image Distortion Validation and Comparison using Synthetic Images of Turbulent Flow". In: *Particle Image Velocimetry: Recent Improvements*. Ed. by M. Stanislas, J. Westerweel, and J. Kompenhans. Berlin, Heidelberg: Springer, 2004.

[60] H. W. Liepmann. "Die Anwendung eines Satzes über die Nullstellen Stochastischer Funktionen auf Turbulenzmessungen". In: (Apr. 20, 1949).

[61] H. W. Liepmann and M. S. Robinson. *Counting methods and equipment for mean-value measurements in turbulence research.pdf*. 1952.

[62] D. K. Lilly. "A proposed modification of the Germano subgrid-scale closure method". In: *Physics of Fluids A: Fluid Dynamics* 4.3 (Mar. 1992).

[63] D K Lilly. "The representation of small-scale turbulence in numerical simulation experiments". In: *Proc. IBM Scient3c Computing Symp. on Environmental Sciences* (1967).

[64] N. Mazellier and J. C. Vassilicos. "The turbulence dissipation constant is not universal because of its universal dependence on large-scale flow topology". In: *Physics of Fluids* 20.1 (Jan. 2008).

[65] M. Meldi and J. C. Vassilicos. "Analysis of Lundgren's matched asymptotic expansion approach to the Kármán-Howarth equation using the eddy damped quasinormal Markovian turbulence closure". In: *Physical Review Fluids* 6.6 (June 3, 2021). Publisher: American Physical Society.

[66] Charles Meneveau and Joseph Katz. "Scale-Invariance and Turbulence Models for Large-Eddy Simulation". In: *Annual Review of Fluid Mechanics* 32.1 (Jan. 2000).

[67] Robert D. Moser, Sigfried W. Haering, and Gopal R. Yalla. "Statistical Properties of Subgrid-Scale Turbulence Models". In: *Annual Review of Fluid Mechanics* 53.1 (Jan. 5, 2021).

[68] Hideaki Mouri and Akihiro Hori. "Two-point velocity average of turbulence: Statistics and their implications". In: *Phys. Fluids* (2010).

[69] Olivier Métais and Marcel Lesieur. "Spectral large-eddy simulation of isotropic and stably stratified turbulence". In: *Journal of Fluid Mechanics* 239.-1 (June 1992).

[70] Shinji Nagata. *Mixing: Principles and Applications*. 1975.

[71] Michèle Neuilly and Claude Fréjacques. *Modélisation et estimation des erreurs de mesure*. Tec & doc-Lavoisier. 1998.

[72] Q. Nie and S. Tanveer. "A note on third–order structure functions in turbulence". In: *Proceedings of the Royal Society of London. Series A: Mathematical, Physical and Engineering Sciences* 455.1985 (May 8, 1999). Publisher: Royal Society.

[73] M Oberlack. "Invariant modeling in large-eddy simulation of turbulence". In: *Center for Turbulence Research Annual Research Briefs* (1997).

[74] M. Obligado and J. C. Vassilicos. “The non-equilibrium part of the inertial range in decaying homogeneous turbulence”. In: *Europhysics Letters* 127.6 (Oct. 2019). Publisher: EDP Sciences, IOP Publishing and Società Italiana di Fisica.

[75] Ugo Piomelli et al. “Subgrid-scale backscatter in turbulent and transitional flows”. In: *Physics of Fluids A: Fluid Dynamics* 3.7 (July 1991). Publisher: American Institute of Physics.

[76] Stephen B. Pope. *Turbulent Flows*. Cambridge: Cambridge University Press, 2000.

[77] Markus Raffel et al. *Particle Image Velocimetry: A Practical Guide*. Cham: Springer International Publishing, 2018.

[78] W. C. Reynolds. “The potential and limitations of direct and large eddy simulations”. In: *Whither Turbulence? Turbulence at the Crossroads*. Ed. by J. L. Lumley. Vol. 357. Series Title: Lecture Notes in Physics. Berlin, Heidelberg: Springer Berlin Heidelberg, 1990.

[79] Lewis F. Richardson. *Weather prediction by numerical process*. Cambridge University Press. 1922.

[80] Pierre Sagaut and Claude Cambon. *Homogeneous Turbulence Dynamics*. Springer. 2018.

[81] Fulvio Scarano. “Iterative image deformation methods in PIV”. In: *Measurement Science and Technology* 13 (Nov. 23, 2001).

[82] J. Smagorinsky. “General circulation experiments with the primitive equations: I. the basic equations”. In: *Monthly Weather Review* 91.3 (Mar. 1, 1963). Publisher: American Meteorological Society Section: Monthly Weather Review.

[83] Julio Soria. “An investigation of the near wake of a circular cylinder using a video-based digital cross-correlation particle image velocimetry technique”. In: *Experimental Thermal and Fluid Science* 12.2 (Feb. 1, 1996).

[84] C. G. Speziale. *Helicity fluctuations and the energy cascade in turbulence. Final report*. N-88-12028; NASA-CR-178403; ICASE-87-69; NAS-1.26:178403. National Aeronautics and Space Administration, Hampton, VA (USA). Langley Research Center, Nov. 1, 1987.

[85] K. Steiros et al. “Effect of blade modifications on the torque and flow field of radial impellers in stirred tanks”. In: *Physical Review Fluids* 2.9 (Sept. 11, 2017).

[86] K. Steiros et al. “Power consumption and form drag of regular and fractal-shaped turbines in a stirred tank”. In: *AIChE Journal* 63.2 (Feb. 2017).

[87] Geoffrey Ingram Taylor. “Statistical theory of turbulenc”. In: *Proceedings of the Royal Society of London. Series A - Mathematical and Physical Sciences* 151.873 (Sept. 2, 1935).

[88] P. C. Valente and J. C. Vassilicos. “The decay of turbulence generated by a class of multiscale grids”. In: *Journal of Fluid Mechanics* 687 (Nov. 25, 2011).

[89] P. C. Valente and J. C. Vassilicos. “The energy cascade in grid-generated non-equilibrium decaying turbulence”. In: *Physics of Fluids* 27.4 (Apr. 2015).

[90] Alberto Vela-Martín. “Subgrid-scale models of isotropic turbulence need not produce energy backscatter”. In: *Journal of Fluid Mechanics* 937 (Apr. 2022). Publisher: Cambridge University Press.

[91] R. Vicente Cruz and E. Lamballais. “Physical/numerical duality of explicit/implicit subgrid-scale modelling”. In: *Journal of Turbulence* 24.6 (July 3, 2023).

[92] A. Vincent and M. Meneguzzi. “The spatial structure and statistical properties of homogeneous turbulence”. In: *Journal of Fluid Mechanics* 225 (Apr. 1991).

[93] Bert Vreman, Bernard Geurts, and Hans Kuerten. “Large-eddy simulation of the temporal mixing layer using the Clark model”. In: *Theoretical and Computational Fluid Dynamics* (1995).

[94] C. E. Willert and M. Gharib. “Digital particle image velocimetry”. In: *Experiments in Fluids* 10.4 (Jan. 1, 1991).

[95] H. Yao et al. *Comparing local energy cascade rates in isotropic turbulence using structure function and filtering formulations*. 2023.

[96] Tatsuya Yasuda and J. Vassilicos. “Spatio-temporal intermittency of the turbulent energy cascade”. In: *Journal of Fluid Mechanics* 853 (2018).

[97] Y. Zhou and J. C. Vassilicos. “Energy cascade at the turbulent/nonturbulent interface”. In: *Physical Review Fluids* 5.6 (June 9, 2020).

Résumé vulgarisé en Français

Pourquoi étudier la turbulence ?

La turbulence décrit un comportement particulier d'un écoulement lorsqu'il se déplace rapidement ou qu'il est contraint par une grande ou complexe forme géométrique. L'écoulement peut être celui de n'importe quel fluide comme l'air ou l'eau. Les écoulements turbulents sont facilement identifiables par leur instationnarité et leur irrégularité. La plupart des écoulements qui nous entourent dans notre vie quotidienne sont turbulents. Si l'air n'était pas transparent, la turbulence serait visible partout.

Les écoulements turbulents sont aussi présents dans beaucoup d'applications industrielles : aéronautique (mécanique du vol, conception des aéronefs, conception des réacteurs, ...), industrie (mélangeurs industriels, turbines, ...), géophysique (prévisions météo, ...). Le comportement de ces écoulements est très difficile à comprendre et à prévoir à cause de la complexité de leurs équations. Cependant, leur compréhension et leur simulation sont critiques pour les applications mentionnées précédemment.

Par exemple, il y a un besoin d'une meilleure compréhension des équations des écoulements turbulents dans l'industrie aéronautique en raison de la tendance actuelle de créer des géométries très complexes (comme des nouveaux rotors ou fuselages) tout en utilisant un processus "model-based design". Cela nécessite des simulations fiables des écoulements pour modéliser les principaux effets aérodynamiques tels que la portance, la traînée, la poussée, en toutes circonstances.

L'industrie s'attaque aux problèmes de modélisation aérodynamique en utilisant des méthodes numériques appelées "Reynolds Averaging Navier Stokes simulation" ou plus récemment "Large Eddies Simulation" en collaboration avec la recherche. La recherche va encore plus loin en utilisant la méthode "Direct Numerical Simulation". Cette dernière approche numérique est beaucoup plus précise mais nécessite aussi beaucoup plus de puissance de calcul. Elle est limitée aux écoulements basse vitesse en raison de leur coût en calcul ou est réduite à des petites régions de l'écoulement. Aucune de ces méthodes n'est

pleinement satisfaisante car les méthodes numériques sont complexes, nécessitent trop de puissance de calcul ou nécessitent des processus de calibration pour chaque cas d'application. C'est pourquoi, des mesures expérimentales longues et coûteuses sont nécessaires avant de concevoir une nouvelle géométrie. La solution choisie contient souvent des simplifications importantes et des incertitudes.

C'est pourquoi la turbulence et ses conséquences sur les phénomènes aérodynamiques reste un problème non résolu à ce jour.

Une des principales directions pour résoudre ce problème est d'augmenter la connaissance et la compréhension des équations de la turbulence. Cela doit être fait dans des situations proches des situations pratiques : des écoulements perturbés dont les propriétés changent dans l'espace et où la vitesse évolue de faible à grande vitesse.

En pratique, une meilleure compréhension des équations de la turbulence, appelées les équations de Navier-Stokes, devrait conduire à :

- Des simulations plus efficaces des écoulements grâce à l'utilisation de simplifications basées sur la physique pour réduire le coût des calculs numériques
- De meilleures prédictions des effets aérodynamiques / hydrodynamiques grâce au développement de nouveaux modèles
- La conception de nouvelles géométries plus efficaces aérodynamiquement / hydrodynamiquement
- De nouvelles applications qui utilisent l'énergie et les propriétés des écoulements turbulents

Pourquoi étudier particulièrement la non-homogénéité dans la turbulence ?

Un consensus scientifique existe à propos d'une théorie autour de la turbulence développée par Kolmogorov en 1941. Cette théorie a été développée pour de la turbulence homogène en équilibre. C'est un état théorique des écoulements qui existe peut-être à très grand nombre de Reynolds (haute vitesse, grande géométrie, faible viscosité) quand la turbulence est complètement développée. Dans ce cas, les propriétés de l'écoulement ne varient pas en espace et en direction : c'est un écoulement homogène isotrope.

Cette théorie, doit encore être étendue pour les écoulements turbulents hors équilibre / non-homogènes. En effet, le cadre théorique utilisé pour démontrer la théorie de Kolmogorov

n'est pas applicable pour la plupart des écoulements complexes. C'est le cas par exemple pour les écoulements non-homogènes présents dans les mélangeurs, rotors, voiles, tempêtes, ...

Qu'est ce qui a été fait pendant ce doctorat ?

Premièrement, la turbulence est analysée avec un jeu de données expérimentales mesurées pendant le doctorat. Un écoulement est stimulé par quatre pales qui tournent dans un mélangeur rempli d'eau.

Ce montage expérimental génère un écoulement rotatif ou non-rotatif selon les configurations expérimentales. Ces écoulements générés sont non-homogènes en raison de la géométrie complexe du problème.

Cette expérience reproduit les propriétés spécifiques des écoulements turbulents qui existent dans les applications pratiques comme la turbulence très développée ou la turbulence en rotation stimulée par des pales. La compréhension des propriétés turbulentes dans cette expérience fournit des informations concernant la turbulence qui existe dans les applications pratiques tout en gardant une relative simplicité expérimentale.

Un récent cadre d'étude théorique (à deux points) est utilisé avec le jeu de données expérimentales et de nouveaux éléments de compréhension physique sont découverts. De plus, une extension de ce cadre d'étude théorique est analysée grâce aux expériences pour confirmer son intérêt physique. De manière simplifié, cette extension mathématique décrit principalement les grandes "échelles" des écoulements turbulents.

Dans ce dernier chapitre, les résultats théoriques obtenus dans les chapitres précédents sont utilisés d'une manière plus pratique. En effet, l'extension du cadre d'étude à deux points aux grandes échelles est utilisée pour construire un modèle de simulation "Large Eddy Simulation". Le but de cette partie est d'amener des connaissances de recherche fondamentale vers la recherche appliquée en améliorant la modélisation. Un nouveau modèle de simulation, justifié physiquement et mathématiquement, est développé à partir d'équations exactes grâce à des simplifications. Cette démarche permet que les précédentes et futures découvertes de recherche fondamentale concernant le cadre d'étude à deux points soit appliqué à la "Large Eddy Simulation" grâce à la connexion décrite dans cette étude.

Experimental analysis of two-point Navier-Stokes equations in non-homogeneous turbulence and application to Large Eddy Simulation

Time-resolved 2D2C PIV (Particle Image Velocimetry) measurements are carried out in a water tank agitated by four rotating blades. Different blade geometries with rectangular and fractal-like shapes are tested. In some runs, vertical bars (baffles) on the walls are used to break the rotation of the flow. This experimental set-up is used to generate and measure different non-homogeneous turbulent flows with different turbulent properties. The turbulent energy cascade is analyzed in a framework based on two-point Navier-Stokes equations which allows transfer rates of energy across scales and through space to be analysed in non-homogeneous flows without assumptions/approximations. For any length r, the Kármán-Howarth-Monin-Hill (KHMH) two-point equation is used to describe scales smaller than r and the Germano two-point equation is used for the first time to describe experimentally scales larger than r. In non-homogenous flows where baffles break overall rotation, the Chen and Vassilicos 2022 theory is improved and used to explain theoretically the Kolmogorov-like results measured in the presence of significant non-homogeneity down to scales smaller than the Taylor length. This theory predicts that an intermediate range of length-scales exists where the interscale turbulence transfer rate, the two-point interspace turbulence transport rate and the two-point pressure gradient velocity correlation term in the two-point KHMH equation are all proportional to the turbulence dissipation rate and independent of length-scale. The PIV measurements in these flows support these predictions. The PIV measurements also suggest that the rate with which scales larger than r lose energy to the scales smaller than r in the two-point Germano equation behaves in a similar way. This result suggests a strong physical connection between the KHMH equation (scales smaller than r) and the Germano equation (scales larger than r) in our flows. In non-homogeneous flows without baffles where the rotation is significant, structure function results are qualitatively different. Also, the two-point statistics from the KHMH and Germano equations are not proportional to the turbulence dissipation rate and not independent of length-scale. The assumptions of the Chen and Vassilicos 2022 theory are used in this case as a reference for identifying which assumptions fail and how under the action of rotation. Finally, Germano's exact subfilter stress equation, which is part of the Germano two-point framework used in this thesis to describe the physics at scales larger than a certain r, is used as the basis of a new Large Eddy Simulation (LES) model. As this model is a simplification/approximation and modeling of two different parts of an exact subfilter stress equations, it lends itself to controlled future improvements by refining the mathematical approximations and by implementing future physical findings into a preexisting mathematical framework. This new model is tested in a simulated Taylor-Green flow both *a priori* and *a posteriori*. It is found to capture well the large local energy transfer between filtered scales and residual scales including large backscatter and large forward transfer events.

Keywords: Turbulence, Non-homogeneous, Particle Image Velocimetry, Large Eddy Simulation

Analyse expérimentale des équations de Navier-Stokes à deux points dans la turbulence non homogène et application à la simulation numérique grandes échelles

Des expériences PIV (Particle Image Velocimetry) résolues en temps sont réalisées dans un réservoir mélangeur avec de l'eau agitée par quatre pales en rotation. Différents types de pales sont utilisés avec des formes rectangulaires ou fractales. Dans certains cas, des barres verticales sont fixées aux parois pour casser la rotation de l'écoulement. Ce montage expérimental est utilisé pour générer et mesurer différents écoulements non homogènes avec des propriétés turbulentes différentes. La cascade d'énergie turbulente est analysée grâce aux équations de Navier-Stokes à deux points qui permettent d'analyser sans approximation le taux d'énergie échangé entre les échelles et dans l'espace dans des écoulements non homogènes. Pour tout r, l'équation à deux points de Kármán-Howarth-Monin-Hill (KHMH) est utilisée pour décrire le comportement de la turbulence des échelles plus petites que r et l'équation à deux points de Germano est utilisée expérimentalement pour la première fois pour décrire le comportement des échelles plus grandes que r. Dans les écoulements non homogènes où des barres verticales stoppent la rotation globale, la théorie de Chen et Vassilicos 2022 est améliorée et utilisée pour justifier théoriquement les résultats de type Kolmogorov mesurés malgré la non-homogénéité présente jusqu'à des échelles plus petites que l'échelle de Taylor. Cette théorie prédit un intervalle d'échelles où le transfert interéchelles turbulent, le transport spatial à deux points et le terme de pression à deux points sont proportionnels à la dissipation. Les mesures PIV dans ces écoulements vont dans le sens de ces prédictions. Ces mesures suggèrent aussi que le taux d'énergie perdu aux échelles plus grandes que r vers les échelles plus petites que r dans l'équation de Germano ont un comportement similaire. Ce résultat suggère un lien physique fort entre l'équation de KHMH (échelles plus petites que r) et l'équation de Germano (échelles plus grandes que r) dans notre écoulement. Dans les écoulements non homogènes sans barre verticale et où la rotation est importante, les fonctions de structures ont des résultats qualitatifs différents. Par ailleurs, les statistiques à deux points des équations de KHMH et de Germano ne sont pas proportionnelles à la dissipation et pas indépendantes de l'échelle r. Les hypothèses de Chen et Vassilicos 2022 sont utilisées comme référence pour ces écoulements pour identifier les hypothèses qui ne sont pas valides et dans quelle mesure en raison de la rotation. Enfin, l'équation exacte du tenseur de sous-maille de Germano est utilisée. Cette équation fait partie du cadre théorique général de Germano utilisé dans cette thèse pour décrire physiquement les échelles plus grandes que r et est utilisé comme référence pour construire un nouveau modèle LES. Ce modèle est composé d'une simplification/approximation et d'une modélisation de deux différentes parties d'une équation exacte du tenseur de sous-maille. C'est pourquoi, il se prête aux améliorations en raffinant les approximations mathématiques faites et en incorporant les futurs résultats physiques dans ce cadre mathématique préexistant. Ce nouveau modèle est testé dans un écoulement simulé de Taylor-Green à la fois *a priori* et *a posteriori*. On observe que ce modèle reproduit bien les larges transferts d'énergie entre les échelles filtrées et les échelles résiduelles : ce qui inclut les événements de larges dissipations positives et négatives.

Mots-clés : Turbulence, non homogène, PIV, Simulation grandes échelles